ON THE CHEMICAL NATURE OF AEROSOL, CLOUDS, AND PRECIPITATION ALONG THE US WEST COAST

by

Lin Ma

A Dissertation Submitted to the Faculty of the

DEPARTMENT OF CHEMICAL AND ENVIRONMENTAL ENGINEERING

In Partial Fulfillment of the Requirements

For the Degree of

DOCTOR OF PHILOSOPHY

In the Graduate College

THE UNIVERSITY OF ARIZONA

2019

THE UNIVERSITY OF ARIZONA
GRADUATE COLLEGE

As members of the Dissertation Committee, we certify that we have read the dissertation prepared by ***Lin Ma***, titled ***On the Chemical Nature of Aerosol, Clouds, and Precipitation Along the US West Coast*** and recommend that it be accepted as fulfilling the dissertation requirement for the Degree of Doctor of Philosophy.

Armin Sorooshian, Chair Date: 4/19/2019

Farhang Shadman Date: 4/19/2019

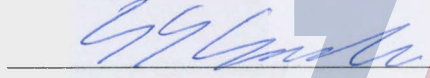

Steven Saavedra Date: 4/19/2019

Ara Philipossian Date: 4/19/2019

Final approval and acceptance of this dissertation is contingent upon the candidate's submission of the final copies of the dissertation to the Graduate College.

I hereby certify that I have read this dissertation prepared under my direction and recommend that it be accepted as fulfilling the dissertation requirement.

Date: 4/19/2019

Dissertation Director: Armin Sorooshian
Professor
Department of Chemical and Environmental Engineering

ACKNOWLEDGEMENTS

I want to give special thanks to Armin Sorooshian for accepting me in his research group and providing financial support during this study. I also want to thank Ara Philipossian, Farhang Shadman, and Scott Saavedra for being my committee members. I thank Nancy Rogers who advised me to switch advisors, prepared documents and accompanied me at meetings during the transition time. To all of them who made this dissertation possible, I am greatly thankful.

To Armin Sorooshian who restored me from a broken condition and gave me courage to complete my Ph.D. studies, I feel lucky to meet him. I thank him for being incredibly accessible. Armin taught me communication. I thank him for making my final year studying at University of Arizona such a wonderful and unforgettable experience.

I want to thank Anne Padias and Dee Belle-Oudry in the Chemistry and Biochemistry Department for offering me opportunities to teach general chemistry laboratory courses. I thank Mark for the teaching preparation training. I thank Tori, Laura, Peggy and everyone who worked closely at Teaching Support Office.

To Alex, Ali, Hossein, Rachel, Connor, Alberto, Abdulmonam, David, Mojtaba and Joe in the Sorooshian research group, I thank them for their help and discussion. I thank Hossein Dadashazar who generously taught me Positive Matrix Factorization and patiently answered numerous questions I asked.

I want to thank friends back in China who took care of my parents when I was not at home. I thank them for celebrating my parent's birthday and going on trips with my parents.

I want to acknowledge Xuezi Qin who I knew from English school for being a family friend of mine over many years. Through knowing her, I learned to relax and enjoy life. I thank her for always warmly welcoming me to LA.

I wish to thank my following friends: Cybil, Brina, Danlei, Fangyuan, Nancy, Scott, Jon, Macro, Yuliang, Henry, and Dezheng. I thank Nina for writing me letters and sharing fond stories with me. I thank Han, Yichen, Yingying and Gaby who offered me a place to stay when I was preparing for the Ph.D. qualifying exam. I thank Ruochen for inspiring me to learn computer coding and being a role model in many aspects of life. I thank Paul for teaching me electron microscopy and thank Jerry and Paul for analyzing aerosol and struvite samples for me. I thank my roommates Xiaoxiao and Evelyn for being loyal friends and giving me mental treatment day and night. I thank them for accompanying me and brainstorming solutions for me in life situations.

I thank Jeff, Adam, Barbara, Belinda, Nancy, Jenelle, Dean, Tom, Chris, Jason, Steven, and Mike, all of who helped Matt and me when we were working on a pilot project at Tres Rios WWTP. I thank Matthew Potzler for helping me open and close manhole and monitoring gas flow during extremely hot summer days.

Finally, I want to thank my parents for their love and support. I thank them for sending me abroad for studies and taking long flights to visit me.

DEDICATION

To my parents Lixin Ma and Junjun Gao

TABLE OF CONTENTS

LIST OF FIGURES

ABSTRACT

Particulate matter (PM) in ambient air affects visibility, climate, human health, and the hydrological cycle. The water-soluble fraction of PM is relevant to nucleation efficiency, atmospheric residence time and hygroscopicity. In regions such as coastal California (United States) and Metro Manila (Philippines), pollution comes from variety of sources. By analyzing water-soluble element data collected in Marina, California from two separate summertime field campaigns: the Nucleation in California Experiment (NiCE) in 2013 and the Fog and Stratocumulus Evolution (FASE) campaign in 2016, six characteristic sources were found: Marine Emissions (45.4% of total mass), Secondary Aerosol (24.4%), Biomass Burning (13.1%), Waste Facilities (8.7%), Vehicular Emissions (4.4%) and Crustal Emissions (3.9%). Temporally-resolved results showed higher PM levels associated with Vehicular Emissions (day/night mass concentration ratio = 31.3) in Marina, California. Similar source apportionment analysis was conducted using data collected in Metro Manila, Philippines through a year-long sampling campaign (the Cloud, Aerosol, and Monsoon Processes Philippines Experiment ($CAMP^2Ex$) weatHEr and CompoSition Monitoring (CHECSM) study) established in July 2018. It was observed that black carbon contributed a large fraction of PM in Metro Manila, exceeding what is found in most all other global regions. Positive Matrix Factorization (PMF) results revealed that the highest contribution to the study region was Aged/Transported pollution (48.0% of total mass) and followed by Sea Salt (22.5%), Combustion (18.7%), Vehicular/Resuspended Dust (5.6%) and Waste Processing (5.1%). In Metro Manila, secondarily produced inorganic species exhibited peaks in the submicrometer range (0.32–0.56 μm) while ions associated with primary emissions had peaks in the supermicrometer range (1.8–5.6 μm). Most of the water-soluble

elements exhibited bimodal behavior, with peaks in the submicrometer and supermicrometer range.

Pinnacles National Monument, ~65 km east of the coastline of California, is one of the few monitoring sites along the US western coast where aerosol and precipitation data are both available. At that site, seven pollution sources were identified by PMF: aged sea salt (25.7% of $PM_{2.5}$), biomass burning (24.2% of $PM_{2.5}$), fresh sea salt (8.2% of $PM_{2.5}$), secondary sulfate (11.7% of $PM_{2.5}$), dust (10.0% of $PM_{2.5}$), vehicular emissions (8.2% of $PM_{2.5}$) and secondary nitrate (5.2% of $PM_{2.5}$). Examining co-located aerosol and precipitation data provided insights into aerosol and precipitation interactions. Results revealed that the reduction of pH in precipitation is likely due to uptake of HNO_3 instead of acidic aerosols such as secondary sulfate and aged sea salt partitioning to rain drops. The positive correlation between Ca^{2+} in precipitation and two aerosol source factors (dust and aged sea salt) and PM_{Coarse} indicated that coarse particles promoted precipitation to some extent. The finding that sulfate was highly corelated with dust and aged sea salt source factors, suggested that secondary sulfate partitions to dust and sea salt particles.

Arid and semi-arid region such as Tucson, Arizona are experiencing water shortages, which promotes the development of advanced technologies that can improve process performance in water reclamation. UV/H_2O_2 advanced oxidation processes (AOPs) have been mostly used in destruction of organic compounds in tertiary wastewater treatment. The transformation mechanism of organic compound UV/H_2O_2 AOPs involves reaction with hydroxyl radical that is difficult to measure using analytical techniques. Existing models that have been developed to quantify and monitor the attenuation of organic compounds did not consider the scavenging effect between hydroxyl radical and reaction intermediates. In this study, a complete kinetic

model was developed to understand the full reaction mechanism of p-cresol in UV/H_2O_2 AOPs. Such a model can be employed to predict concentrations of target compound and intermediates.

Centrate is a supernatant of products produced in anaerobic digesters. Struvite is a relatively insoluble mineral that has been identified in sludge and anaerobic digestor associated pipelines. The formation of struvite clogs pipes and coats pumps and can significantly reduce process performance. Because the solubility of struvite is higher in low pH solution, carbon dioxide from an anaerobic digester was used to reduce pH of centrate for prevention of struvite formation. Bench experiments were conducted to validate an equilibrium model that was used to predict the steady state pH of centrate at the point of injection of carbon dioxide under atmospheric and elevated pressures. The equilibrium model was also used to determine pH, where struvite formation occurs. A pilot plant was constructed to investigate alternative operation modes. Results showed that mixing carbon dioxide pre-saturated centrate with a fresh centrate stream can reduce centrate pH to levels necessary to prevent struvite formation and is more effective than injection of gaseous carbon dioxide. This study provides a design protocol for wastewater treatment plants that experience struvite issues to implement proposed technologies for preventing struvite formation.

CHAPTER 1. INTRODUCTION

1.1. Background and motivation of aerosols

Aerosols (liquid or solid particles in a gaseous medium) range in size from nanometers to tens of micrometers and are comprised of myriad species. Among all environmental threats, aerosols are responsible for the most deaths globally, specifically being responsible for one out of every eight deaths and a total of 7 million deaths according to data available from 2012 (World Health Organization). Aerosol particles scatter and absorb solar radiation and serve as cloud condensation nuclei (CCN), thereby influencing cloud microphysics and radiative transfer. Consequently, aerosols influence climate, the hydrologic cycle, and atmospheric visibility. The Fifth Assessment Report of the Intergovernmental Panel on Climate Change (IPCC, 2013) identified aerosols and their interactions with radiation and clouds as the largest source of uncertainty in current estimates of the total anthropogenic radiative forcing. Therefore, aerosol particles arguably represent the weakest link in predictions of future climate change. Major uncertainty surrounds the nature of aerosols and the magnitude of their effects in the atmosphere partly because of their physicochemical complexity, short lifetime, and spatial inhomogeneity. The ability of aerosols to impact health, visibility, climate, and the hydrological cycle depends on their composition, size, and shape. To model and predict these aerosol properties it is necessary to deeply understand their sources, formation mechanisms, and atmospheric aging processes. The goal of this dissertation is to mainly characterize size-resolved aerosol properties in a variety of regions, but most especially the western United States. The following subsections outline the motivation and main points of different investigations that comprise this dissertation.

1.2. Characterization of size-resolved water-soluble metal elements in Marina, California

1.2.1. Background

The water-soluble fraction of elements is important to characterize because it represents the fraction of elements that are responsible for the dynamic of atmosphere via affecting nucleation efficiency, atmospheric residence time, particle growth/shrinkage mechanisms, bioavailability and human and environmental health. The central coast of California is a region of high interest because it is impacted by diverse pollution sources. Marine, shipping, biomass burning, dust and vehicular and agriculture emissions have been identified based on the data collected in Pinnacles National Monuments ~65km east of the Pacific coast (Dadashazar et al., 2019). This study analyzed data collected during two separate summertime field campaigns: the Nucleation in California Experiment (NiCE) in 2013 and the Fog and Stratocumulus Evolution (FASE) campaign in 2016. Analyzed data are used to gain knowledge on emission sources and size distributions of water-soluble elements.

Metals elements play an important role in ambient air as they can serve as tracers for pollution source identification (Blanco et al., 2003; Font et al., 2015) and promote aqueous phase chemical reactions such as the production of sulfate and low molecular organic acids (Alexander et al., 2009). Metal elements that originate inland from anthropogenic or natural emissions when transported to the ocean can become nutrients of organisms in the ocean and thus contribute to global biochemical cycling. In addition, metal elements are detrimental to human health, especially the smaller fraction that can penetrate deeper in the respiratory system (Baghurst et al., 1992; Mateos et al., 2018).

Natural and anthropogenic emissions are two major sources for the origination of metal elements in ambient air. Among natural sources such as sea spray, soil, crustal rock, vegetation and

volcano eruption, sea salt and crustal matter contribute the most to the natural emitted elements. Metal elements in ambient air can also come from variety of anthropogenic sources such as vehicular emissions, industrial combustion processes, smelting, power plant and ship emissions. Identifying the sources of elements and size distribution provide more insights on understanding aerosol physical and chemical properties that influence atmospheric cycling and climate change. Water-soluble elements impact human health and play an important role in wet deposition and global cycling of nutrients and contaminants. For example, elements can enter to the blood stream and stimulate inflammation responses due to their ability to elevate oxidative stress through generation of reactive oxygen species (ROS) inside the body (Li et al., 2008). Furthermore, water-soluble elements have been reported to cause severe damage to DNA and promote mutation of genes (Valavanidis et al., 2008). Despite the impacts of elements on human well-being, elements can also affect the environment. For example, iron that is associated with crustal matter and biomass burning can be transported from land to atmosphere and become part of droplets that finally deposit into the ocean or lakes through precipitation. The water-soluble fraction of the iron, when deposited in oceans, can become a fertilizing agent and provide nutrients for microorganisms. In the atmosphere, iron is also responsible for catalyzing in-cloud photochemical oxidation reactions that break down large organics into low molecular weight acids such as oxalate. The catalytic behavior of iron can alter chemical composition of atmospheric aerosols and thus affect the hygroscopic and optical properties of aerosols.

The goal of this study is to characterize water-soluble elements that are suspended in ambient air by examining their chemical composition, size distribution and source of emission. The results collected in this study provide information on size-resolved elemental composition for regions that share similarity of geological and meteorological conditions.

1.2.2. Positive Matrix Factorization (PMF)

PMF is a receptor model developed by Environmental Protection Agency (EPA) to identify source types in region of interest based on measured source profile information, and emissions or discharge inventories. It is a multivariate factor analysis tool that requires input of speciated sample data and yields factor contributions and factor profiles (Paatero and Tapper, 1994). Factor profiles must be interpreted by user to decide source names of each pollution source. Errors can be reduced by increasing uncertainties in the model. A species should not have large influence on solution, if it is given a high uncertainty. To minimize influence of missing value, increase uncertainty is a common practice to make a missing value truly missing. In other words, higher uncertainty provides model more freedom to make predictions. If one assumption does not work well, then model can make another assumption instead of being forced to reach a solution with a high Q value. Q is an important parameter in PMF as it measures goodness-of-fit of data points. Optimal solutions are identified by low Q values. PMF model offers an option to categorize species by “weak”, “strong” and “bad” based on signal to noise ratio. If a species is categorized as “bad” species, it is removed from the model. If a species is categorized as “weak” species, its uncertainty is tripled in the model, resulting a minimized impact on PMF solution. Uncertainty of “strong” species remind as input value (Norries et al., 2014). In addition, extra uncertainties can be added manually by user in data preparation step to improve model results. Bootstrapping (BS) and displacement (DISP) are both error estimation tools in PMF model. BS error intervals include random errors in input data and part of the errors from rotational ambiguity. In contrast, DISP error intervals do not include any random errors but strongly influenced by rotational ambiguity. BS resamples results from PMF base model results that are randomly located within rotationally accessible space. If BS results match base model results, it

is referred as mapped. User input sample uncertainties do not have significant impact on BS errors, however sample uncertainties have strong impact on DISP error estimates. DISP displaces base model results from predicted value and then performs factor swaps. DISP evaluates the probability for one factor to be reassigned to another factor. It provides user details about how factor solutions are sensitive to small changes. A robust base model solution should demonstrate small rotational ambiguity. BS-DISP are combination of BS and DISP. Since BS-DISP estimates both random errors and rotational ambiguity, BS-DISP is a more robust in error estimation than application of BS or DISP alone.

1.3. Characterization of size-resolved particulate matter in Manila, Philippines

1.3.1. Background

Southeast Asia has been a region of interest for aerosol size and chemical composition characterization because it is heavily polluted by anthropogenic activities due to rapid urbanization and increasing population, and it is also influenced by natural pollution. Properties of size-resolved aerosol particles have implications for human health, visibility, climate and hydrological cycle. The Philippines is a country in Southeast Asia that is susceptible to climate change. As a political and economic center of the Philippines, Metro Manila is composed of 16 cities and the most populated Quezon City has been chosen as the sampling location of this study.

Metro Manila is heavily polluted by vehicular emissions that can be attributed to personal cars, motorcycles, commercial trucks, and motorized public transportation such as powered tricycles and jeepneys along the roadway. Another unique feature of Metro Manila is that its pollution level is consistent in both the dry season (November – April) and wet season (May - October), which is a phenomenon that is rarely seen in other cities around the world. An increasing number

research studies have been undertaken in Metro Manila as the area is largely polluted by anthropogenic sources such as vehicular, industrial and domestic cooking. The region is also impacted by long-range transported pollution such as biomass burning. Research has found that the black carbon level is significantly higher in samples collected in Metro Manila; however, the rest of the aerosol fraction has not been thoroughly studied. As past studies have only focused on examining the composition of particulate matter by evaluating either $PM_{2.5}$ or PM_{10}, size-resolved composition information is missing.

The objective of this study is to characterize size-resolved aerosol in Metro Manila in order to fill this knowledge gap through a year-long sampling campaign: the Cloud, Aerosol, and Monsoon Processes Philippines Experiment ($CAMP^2Ex$) weatHEr and CompoSition Monitoring (CHECSM) study. The size-resolved characterization results are important for understanding the effect of ambient aerosol on the atmospheric conditions in Metro Manila. In addition, such size-resolved data can be used as a reference for future studies examining pollution in Southeast Asia.

1.3.2. Scanning Electron Microscopy (SEM)

Scanning electron microscopy (SEM) is an instrument that has been widely used in aerosol community to characterize morphology of particulate matters (Li et al., 2011; Morata et al., 2008; Srivastava et al., 2009). Compared with optical microscope that uses light to form image, SEM uses electron to produce image, which allows higher level of magnification. Below is a schematic of SEM (Figure 1.3-1).

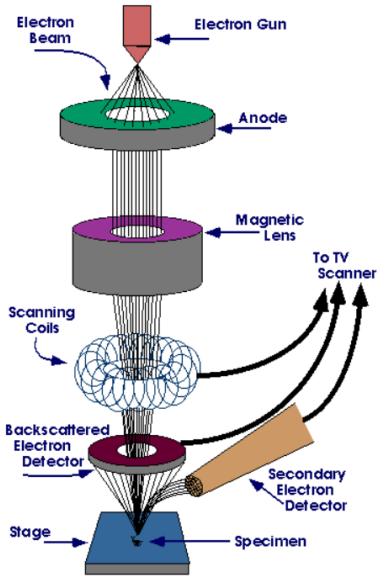

Figure 1.3-1 Schematics of Scanning Electron Microscopy (SEM)

(https://www.purdue.edu/ehps/rem/laboratory/equipment%20safety/Research%20Equipment/sem.html)

During SEM analysis, sample is placed in a vacuum chamber and electron beam is produced by an electron gun on top of the microscope. Electron beam travels through lenses and electromagnetic field and finally arrives at sample. X-rays, backscattered electrons and secondary electrons are ejected from sample after sample interacts with incident electron beam. Depending on the position of detector, different types of electron or electromagnetic wave can be collected and converted to signals that are used to produce high resolution images. Energy Dispersive X-ray Spectroscopy (EDX), a non-destructive tool is often equipped with SEM to examine chemical composition of aerosol sample. X-rays are emitted when inner shell electrons are removed from sample and the vacancy is filled by higher energy electron. To improve image quality, non-conductive aerosol samples are sometimes coated with thin layer of conductive material such as Au and Pt before SEM analysis (Csavina et al., 2011; Zeb et al., 2018).

1.3.3. Aerosol microscopy characterization

Bulk chemical analytical method is unable distinguish sources of particles that have similar chemical composition. However, microscopy analysis provides morphology information of single particle and this information has been helpful in understanding of sources, formation mechanisms and impact on climate and public health. Aluminosilicate and silica contribute to both anthropogenic and mineral dust emissions. The ones come from anthropogenic sources are spherical, but those from natural sources are non-spherical. Therefore, it is impossible to identify sources of aluminosilicate and silica if morphology information is unavailable. Tar ball and soot are both carbonaceous particles with O and C being dominated elements. Soot are primary associated with high temperature combustion processes. Tar balls are originated from biomass burning. It is impossible to distinguish them according to their chemical composition; however, they can be distinguished according to morphologies. Soot likes to form chain-like and cluster-like structures ranging from 20 to 100 nm in diameter (Hu et al., 2012), whereas tar balls are mostly spherical with diameters typically between 300 - 500 nm and are seldom agglomerate with other types of particles (Posfai et al., 2004).

In classification process, particles are often divided into groups according to morphology (Chen et al., 2017) or chemical composition (Li et al, 2013) or combination of the two (Hu et al., 2012). Shape factor such as aspect ratio and sphericity are calculated to assist with particle classification by morphology (Satsangi and Yadav, 2014), but strong conclusion can only be made if sufficient number of particles are analyzed. Naturally emitted particles are dominated by irregular morphology, whereas most particles with anthropogenic origins are spherical. Single particle analysis has been utilized to study aerosols in urban and roadside (Talbi et al., 2018) or indoor and outdoor (Conner et al., 2001) or under different weather conditions (Chen et al., 2017).

Transmission Electron Microscopy (TEM) has been used in combination with SEM in aerosol morphology characterization, especially when aerosol internal and external mixing states are examined (Chen et al., 2015; Li et al., 2013) to provide information on optical hygroscopic properties of aerosols (Fassi-Fihri et al., 1997).

1.4. Interrelationship between aerosol and precipitation

The interaction between aerosol and precipitation is difficult to study due to the interference of meteorology with clouds and precipitation, which often obfuscates the impact of particles. However, it is important to understand the impact of aerosol on precipitation as it can be used to improve accuracy of many atmospheric models. First, models that describe cloud and precipitation or models developed to study the influence of precipitation on aquatic and terrestrial ecosystems require aerosol and precipitation knowledge to be validated. Second, gases and particles in the air can be removed through precipitation (MacDonald et al., 2018), which may be used to improve chemical tracer transport models (Bobbink et al., 1998; Driscoll et al., 2003; Pardo et al., 2011). This research study overcomes the difficulties that in situ measurements and remote sensing have related to cost, statistics, temporal resolution and coverage; this work examined the interrelationship between aerosol and precipitation composition using long term ground measurement data collected at Pinnacles National Monument.

The objective of this work is to use long-term surface data collected in a unique location in California, where aerosol and precipitation chemistry monitoring instruments are both available, to understand the impact of aerosol on precipitation. Results presented in this study provide implications on pollution sources, gas particle interaction by uptake processes or wet scavenging and types of aerosol that affect precipitation.

1.5. UV/H_2O_2 Advanced oxidation processes (AOPs)

1.5.1. Background

In past decades, the increasing concerns about human activity on water resources has promoted numerous studies on water reclamation especially in arid and semi-arid regions such as Arizona. In Arizona, reclaimed wastewater has been underutilized. As the demand of water in Southwest cities is going to exceed the supply of water soon, research needs to be undertaken to maximize the use of reclaimed wastewater. Technologies must be developed to improve the quality of reclaimed water.

Modern analytical instruments and techniques can detect organic contaminants at trace levels. However, there are still uncertainties regarding the accuracy of the measurements, which is constantly challenging researcher and engineers. As a result, an increasing number of studies has focused on the presence and fate of trace organics in surface water and wastewater effluent.

The presence of trace organic contaminants in wastewater has become the motivation for the development of tertiary wastewater treatment technology such as advanced oxidation processes (AOPs). Besides, AOPs, activated carbon, ozone, ultraviolent light, filtration and membrane bioreactors have all exhibited high efficiency for removal of trace organics (Carballa et al., 2008; Khanal et al., 2006).

The hydroxyl radical is one of the most effective oxidants in nature. In general, an oxidation reaction is characterized by transfer of electrons from electron donor known as the reductant to the electron acceptor known as the oxidant. During the transfer of electrons between reductants and oxidants, chemical species with an odd number of valence electrons may be produced. This type of chemical species is highly reactive due to unpaired electrons. In addition, radical species

produced in oxidation reaction likely induce additional reactions until thermodynamically stable compounds are formed.

In UV/H_2O_2 AOPs, organic contaminants are destructed through reactions with hydroxyl radical (•OH) that is generated by hydrogen peroxide under ultraviolent (UV) (Dorfman and Adams, 1973). AOPs have been extensively studied in past decades, and research have been developed to commercialize some of the processes nowadays due to their strong ability to degrade biologically toxic or non-biodegradable materials (i.e. aromatics, pharmaceutical, endocrine disrupters, pesticides) in wastewater.

This study particularly focuses on studying the fate of alkylphenols such as p-nonylphenol produced in bioreactors that are used in wastewater treatment processes. Due to the health concerns caused by the presence of these compounds in surface waters, ground water, industrial water and marine shellfish as result of wastewater effluent discharge, it is essential to know their fate and transformation mechanism in wastewater treatment processes. p-Cresol has been selected as a surrogate in this work because of its unique structure that allows similar reactivity with hydroxyl radical compared with p-nonylphenol.

Various models have been developed to understand the kinetics of phenolic compounds in UV/H_2O_2 AOPs. These models consider radical production from a variety of sources (i.e., UV photolysis of hydrogen peroxide, radical scavenging by hydrogen peroxide and other radicals), reaction of target compounds with the hydroxyl radical and radical scavenging by intermediate compounds. Model results indicate that the reaction mechanism began with addition of OH on unique position of the ring, followed by abstraction of a hydrogen atom and finally aliphatic acids are produced as a result of ring cleavage.

Most recently, more complicated models have been developed to study the dynamics of hydroxyl radicals; however, the reaction between the hydroxyl radical and intermediates are rarely studied. The objective of this work is to propose a more comprehensive model that not only considers reactions between hydroxyl radical and by-products, but also counts for ionic strength and pH change. The model was validated using empirical data. The validated model was expected to be used as a tool to predict the concentration of p-cresol and its byproducts produced in UV/H_2O_2 AOPs.

1.5.2. Analytical techniques

A Thermo Scientific Genesys 10s UV–Vis spectrophotometer was used to obtain absorption spectra of samples for mathematical correction of inner filter effect (IIFE) (MacDonald et al., 1997) (Figure 1.5-1). The absorption scan was set from 200 nm to 600 nm.

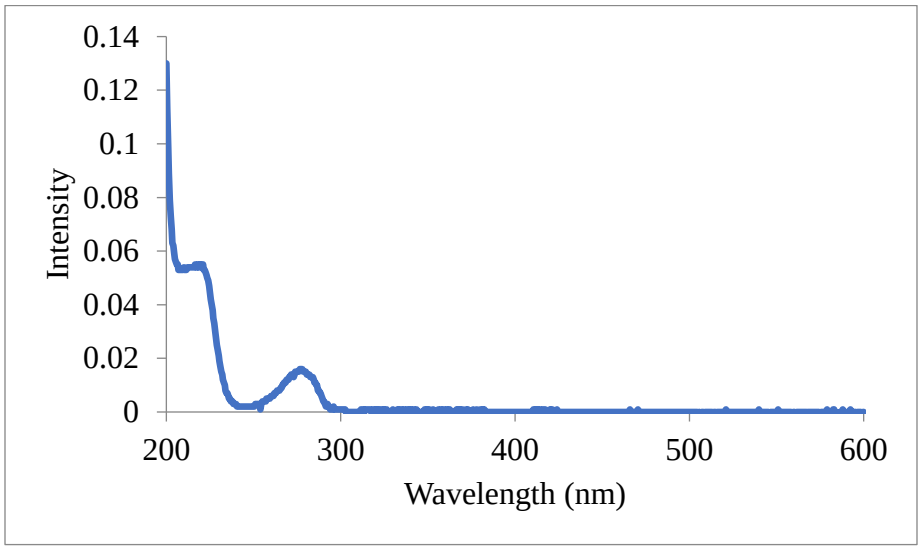

Figure 1.5-1 UV Spectrum of P-Cresol measured in deionized water

Excitation-emission matrices (EEM) Florescence Spectroscopy has been widely used to characterize dissolved organic matter (DOM) (Chen et al., 2003). EEM can be used to quantify

concentrations of DOM. In this research, Perkin Elmer Model LS-55B Luminescence Spectrometer was used to obtain fluorescein concentration of target compound. The excitation range was set from 200 to 450 nm and the emission range was from 250 to 600 nm. Both excitation and emission slits were set at 5 nm. The scan speed used to generate fluorescence contour maps was 600 nm/min. Below is an EEM spectrum of 1000 µM p-Cresol constructed in deionized water (Figure 1.5-2). Region under excitation wavelength from 250 nm to 285 nm and emission wavelength from 275 nm to 340 nm was integrated by trapezoid rule for p-Cresol.

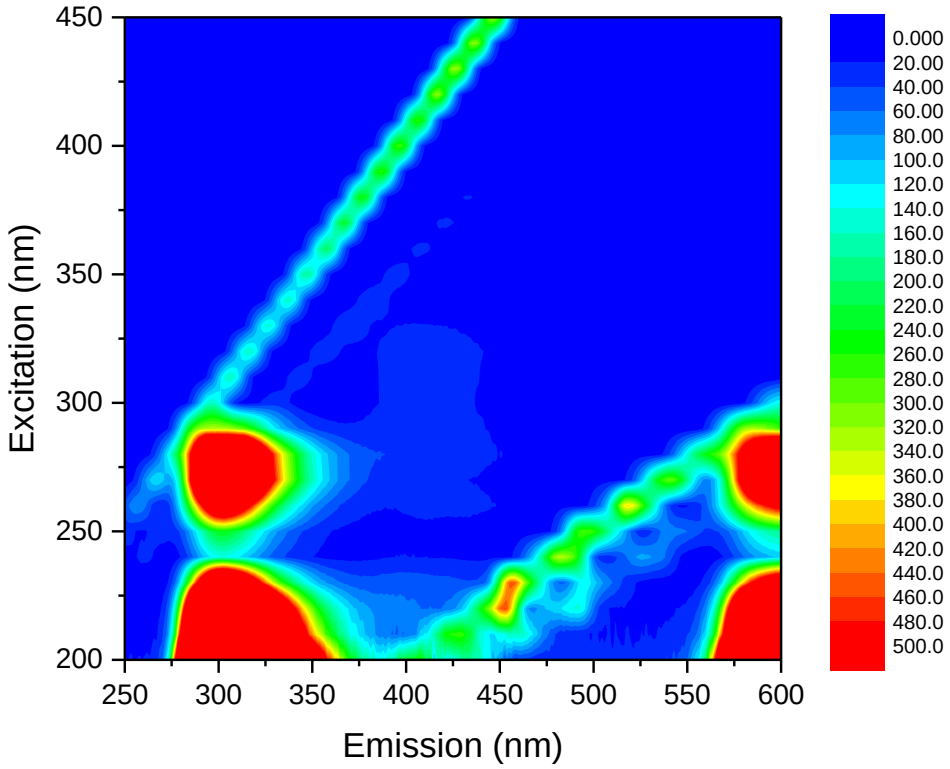

Figure 1.5-2 IFE corrected EEM Spectrum of 1000µM p-Cresol in deionized water

H_2O_2 concentration in this work was effectively determined by a colorimetric method (Boltz et al., 1978) using titanium (IV) sulfate. H_2O_2 concentration measured by this method is reliable when

H_2O_2 concentration is in the range of 10^{-6} to 10^{-1} M. Peroxotitanium is a complex formed by the reaction between the H_2O_2 in the test sample and titanium sulfate solution. It is yellowish color and has molar extinction coefficient of $\varepsilon_{407} = 760\ M^{-1}cm^{-1}$. H_2O_2 concentration can be determined by measuring peroxotitanium concentration by the Thermo Scientific Genesys 10s UV-Vis spectrophotometer at the wavelength of 407 nm.

Total Organic Carbon (TOC) samples were spiked with 60 µL 37% hydrochloric acid before measurements. All TOC samples were accurately measured by a Shimadzu, TOC-v CSH TOC analyzer, which was calibrated by TOC standards before sample measurements.

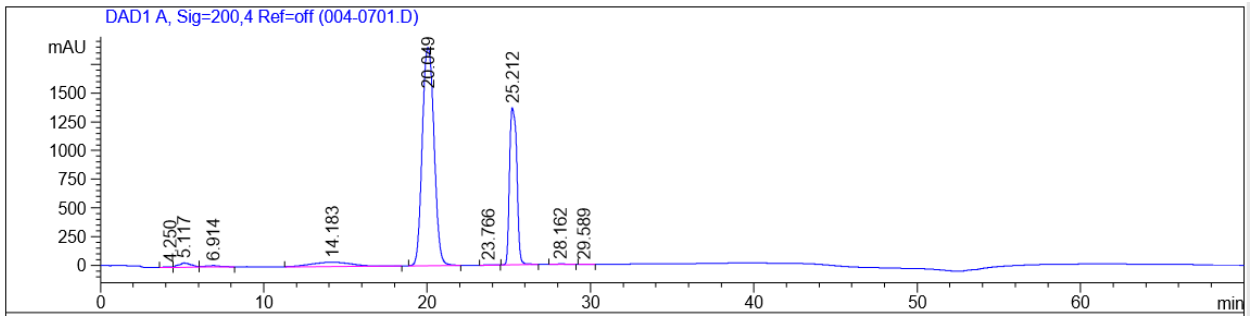

Figure 1.5-3 HPLC chromatograph of p-Cresol (20.049 minute) and its by-product 4-methalcatehol (25.212 minute)

The primary reaction by-product of p-Cresol in H_2O_2/AOP experiment is 4-methalcatehol. Due to overlapping on EEM spectrum, 4-methalcatehol concentration cannot be accurately quantified by EEM technique at present of p-Cresol. Therefore, High Performance Liquid Chromatograph (HPLC) was utilized to measure p-cresol and 4-methalcatehole concentrations in H_2O_2/AOP experiment (Figure 1.5-3). P-cresol and 4-methalcatehole were measured using high performance liquid chromatography (HPLC) with a Phenomenex Synergi Polar Reverse Phase column (15 cm x 4.6 mm x 4 µm). Eluent solvents were 10% methanol in HPLC water (A) and 100% acetonitrile

(B) at constant flow rate 0.4 ml/min. A gradient method was developed as following: initially solvent composition was set at 95% (volume) A and 5% (volume) B. The volume percent of A was gradually decrease to 0% with volume percent of B gradually increased to 100% from 0 to 40 minutes. After 40 minutes, column was equilibrated with initial solvent composition for 30 minutes. Concentrations of p-Cresol and 4-methalcatehol were obtained by comparing integrated areas with those corresponding to standards.

1.5.3. Singlet oxygen

Dissolved organic matter (DOM) is a complex mixture of aromatic and aliphatic organic compounds that have attached functional groups, such as carboxyl, phenol, enol, alcohol, carbonyl, amine, and thiol (Chen et al., 2003). Dissolved organic matter in natural waters has been reported to increase photochemical transformation rates of a variety of organic contaminants. Studies have shown that DOM can generate reactive oxygen species (ROS) upon light absorption. ROS mainly consist of singlet oxygen ($^1O_2$), superoxide radical ($\bullet O_2^-$), and hydroxyl radical (•OH). In addition, light absorption may produce excited triplet states of DOM (^{3}DOM*). These highly reactive species are candidates for initiating light-induced transformation of organic contaminants (Wenk et al., 2011). Compounds that produce ROS have a general name "photosensitizer" (PS). Photosensitizers in DOM absorb energy of photons to become excited singlet state photosensitizer (^{1}PS*). Due to transient nature of ^{1}PS*, it is rapidly converted to excited triplet state photosensitizer (^{3}PS*) in aqueous solution. The lifetime of ^{1}PS* is typically nanoseconds, while the lifetime of ^{3}PS* is typically microseconds (Kochevar et al., 2000). Since the lifetime of ^{3}PS* is three order of magnitude longer than that of ^{1}PS*, with presence of sufficient dissolved oxygen in aqueous solution, ^{3}PS* react with dissolved oxygen molecule to form singlet oxygen ($^1O_2$). At the end of the cycle, ^{3}PS* molecules lose excitation energy. They may be converted back to ground state PS, which

makes PS available again to start another cycle. Common synthetic photosensitizers used for generating singlet oxygen suggested by Irene et al. (Kochevar et al., 2000) are rose bengal, methylene blue, phenalenone, and meso-tetraphenyl porphyrin. Typically, 103-105 singlet oxygen molecules can be generated by a single PS molecule before it becomes extinct in the process. However, the production rate and steady state concentration of ROS are quantum yield and absorption coefficient dependent. The correlations among wavelength dependent energy absorption behavior of photosensitizer, the efficiency of ROS production in aqueous medium, and the removal rate of total organic compounds (TOrCs) mediated by ROS are not well understood. Mathematical models need to be developed to explore the nature of ROS-mediated indirect photolysis of TOrCs.

Light-induced degradation of TOrCs follows two main pathways: direct photolysis and indirect photolysis. In direct photolysis, TOrCs are excited by absorbing photons, which results in decomposition of the molecule. In indirect photolysis, degradation of TOrCs is achieved by forming reactive intermediates in solution, such as hydroxyl radical (•OH), singlet oxygen ($^1O_2$), triplet-state dissolved organic matter (^{3}DOM*), peroxyl radicals, and hydrogen peroxide (H_2O_2). These reactive species can react with TOrCs and initiate the degradation process. It has been reported that hydroxyl radical (•OH) is considered one of the most important reactive intermediate in indirect photolysis due to its ability to react with large number of compounds (Lee et al., 2013). Indirect photolysis has found to be more efficient than direct photolysis in degradation of certain antibacterial compounds such as sulfamethoxazole due to hydroxyl radicals (•OH) reaction. Additionally, some compounds have shown higher degradation rates in solutions that contain relatively high concentration of nitrates or humic acids. Nitrates and humic acids are candidate photosensitizers to form hydroxyl radicals in indirect photolysis of TOrCs such as sulfamethoxazole (Ryan et al., 2011). In conclusion,

indirect photolysis is important for photodecomposition of selected groups of TOrCs through reacting with reactive intermediates.

Natural organic matter (NOM) refers to DOM presents in natural aquatic systems. Effluent organic matter (EfOM) refers to DOM present in wastewater effluent. As expected, DOM concentrations are substantially higher in EfOM than in NOM (Quaranta et al., 2012). Effluent from wastewater treatment plants may contribute to even more that 12% total river discharge (Imai et al., 2002). Studies have shown that DOM found in wastewater effluent is similar to DOM found in natural aquatic systems. Degradations of compounds in effluent are comparable to the attenuation of contaminants in natural process, such as photodegradation, biodegradation and infiltration. The observation of natural degradation of organic contaminates in rivers is a motivation behind this research (Dong et al., 2015).

1.6. Struvite prevention using carbon dioxide

1.6.1. Background

Struvite ($MgNH_4PO_4 \cdot 6H_2O$) is a white insoluble mineral comprised of magnesium, ammonia and phosphate. The formation of struvite in wastewater treatment process clogs pipes and coats pump impellers, which reduces system capacity and efficiency. In some extreme situations, struvite precipitation can cause plant shutdown and thus expensive cleaning is needed to return to normal operation (Doyle & Parsons, 2002). Traditional struvite prevention methods used in wastewater treatment processes involve addition of corrosive and expensive chemicals. Therefore, injecting carbon dioxide from digester gas to streams that are affected by struvite formation is an alternative of struvite control by reducing pH of wastewater. The use of carbon dioxide has two major benefits. First, the use of carbon dioxide can be cost free as carbon dioxide is a by-product

from anaerobic digestion in wastewater treatment. Second, carbon dioxide reduces the safety and environmental concerns.

Traditionally, struvite is removed by reducing phosphate concentration in wastewater through formation of phosphate complexes or reducing pH through addition of strong acids (Doyle & Parsons, 2002). Twenty anti-scaling products have been studied and evaluated based on their ability to delay the formation time and reduce the mass of precipitates formed. Then, seven products that inhibited struvite formation were tested in synthesized wastewater and ranked based on cost and risk to human health and environment. Ferric chloride has been identified as one of the anti-scaling products that is at high cost and risk, ranking 6^{th} out of 7 in the list (Buchanan, 1994). Nevertheless, ferric chloride or ferric containing salt has been widely used in wastewater treatment plants for struvite prevention nowadays (Sharp, et al., 2013). Research that searches for alternatives of struvite prevention products has been undertaken. Among several anti-scaling and chelating products tested in the digester centrate, only ethylenediaminetetraacetic acid (EDTA) can prevent struvite formation. However, EDTA may persist in environment and thus needs to be removed before discharge to nature (Doyle et al, 2003).

The addition of ferric chloride to wastewater has several disadvantages include high cost, health concerns, equipment corrosion and increased sludge production (Sharp et al., 2013). In addition, metals such as iron have been found in minerals recovered from anaerobic digester (Uysal et al., 2010), which is an indication that the addition of ferric chloride may cause problems downstream, where struvite is precipitated at engineered locations for nutrient recovery due to the low bioavailable of ferric containing minerals (Mayer et al., 2016).

In conventional wastewater treatment processes, organic and inorganic matters are treated through anaerobic digestion process. Anaerobic digestion is a biological process where different types of bacteria are supplied in anaerobic digester for the purpose of reducing the amount of organic and inorganic matters without presence of oxygen. After anaerobic digestor, solid and liquid wastes are separated by centrifugation and the liquid that is separated from this process is referred to as centrate. During anaerobic digestion process, biogas is produced as a mixture of methane, carbon dioxide and trace gases. Some wastewater treatment plants recover high purity methane before venting carbon dioxide and trace gases to atmosphere (Sun et al., 2015). Carbon dioxide has been used in wastewater treatment, but rarely studied.

In this study, we are conducting bench and pilot testing to investigate the feasibility of injecting commercialized carbon dioxide as a substitute of carbon dioxide from digester into centrate to reduce pH and prevent struvite formation. First, an equilibrium model was developed to study the equilibrium behavior of centrate by addition of carbon dioxide under atmospheric pressure and elevated pressure. Simulated results were validated by experimental data collected in centrates from Tucson, Phoenix, Portland and Chicago. Second, a pilot plant that is mainly composed of a carbon dioxide tank, a pressurized hydro tank and a plug flow reactor was constructed at Tres Rios wastewater treatment plant to test the hypotheses at a larger scale. Finally, a design protocol was developed based on measurable water quality parameters as a guide for wastewater treatment operators to prevent struvite formation using carbon dioxide. This work demonstrates the feasibility of using carbon dioxide to reduce the pH of centrate, which strongly indicates that struvite formation can be reduced in such a low pH solution. This work also provides design parameters for wastewater treatment plants that are experiencing

struvite formation issues and considering recycling carbon dioxide from biogas for struvite prevention.

1.6.2. Struvite microscopy characterization

Centrate used in this experiment was collected from Tres Rios Water Reclamation Facility in Tucson, Arizona. Centrate samples were filtered through a 0.45μm filter (Pall Corporation, sterilized membrane) after collection and stored at 4°C prior to experiments. All chemicals were purchased from commercial sources and used without further purification, including ammonium chloride (NH_4Cl) (Fisher Scientific, crystalline ACS certified), sodium phosphate monobasic ($NaH_2PO_4 \cdot H_2O$) (Spectrum, crystal ACS reagent), magnesium chloride ($MgCl2 \cdot 6H_2O$) (source unknown), and sodium hydroxide (NaOH) (VWR, 40% w/w). The characterization of precipitated crystals was performed through Hitachi S-4800 scanning electron microscopy (SEM) and energy dispersive X-ray spectroscopy (EDX) in core imaging facility at the University of Arizona.

Struvite was precipitated in deionized water and in centrate (Figure 1.6-1). In the first experiment, Mg^{2+}, NH_4^+ and PO_4^{3-} ions were added at equimolar concentrations of 5mM as NH_4Cl, $NaH_2PO_4 \cdot H_2O$ and $MgCl2 \cdot 6H_2O$ in a 500mL beaker. In the second experiment, filtered centrate was used with concentrations of magnesium, orthophosphate and ammonia at 22.5 mg/L, 110 mg/L and 1260 mg/L, respectively. In both experiments, the pH was initially adjusted to 9 by incremental addition of 1M NaOH. The development of struvite can be observed by measuring the pH; a pH decrease indicates struvite formation, as protons are liberated in the formation reaction (Eq. 1) (Kristell S. Le Corre, 2005).

$$Mg^{2+} + NH_4^+ + H_nPO_4^{n-3} + 6H_2O \rightarrow MgNH_4PO_4 \cdot 6H_2O + nH^+ \quad (1)$$

At the end of the precipitation experiments, solutions were filtered through 0.45µm sterilized membrane filter with the assistance of a dry vacuum pump. The filter and precipitates were air dried and precipitates were analyzed using scanning electron microscopy (SEM) analysis to confirm struvite formation.

SEM Characterization of Precipitated Minerals:

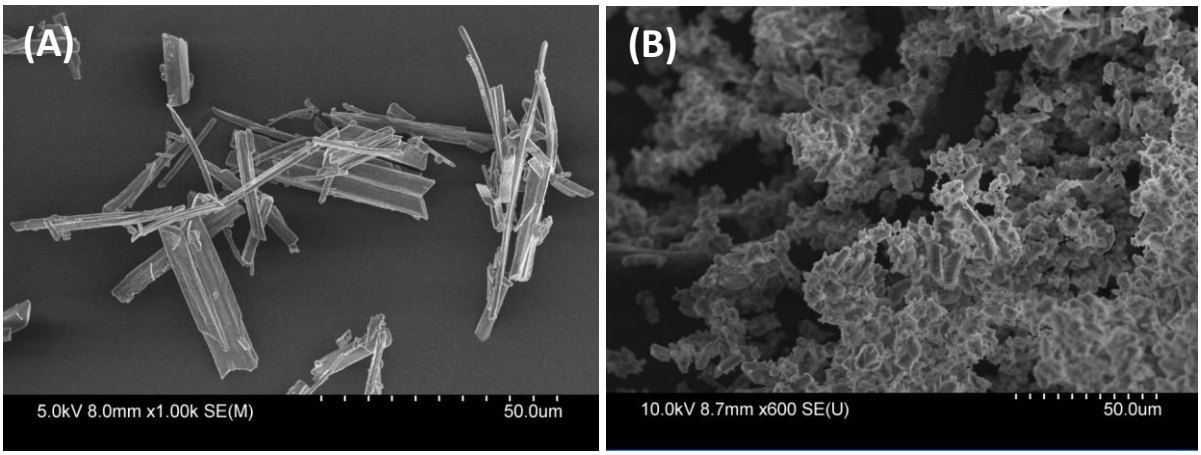

Figure 1.6-1 Images of precipitate grown in deionized water (A) and centrate (B) from Tres Rios water reclamation facility Tucson, Arizona

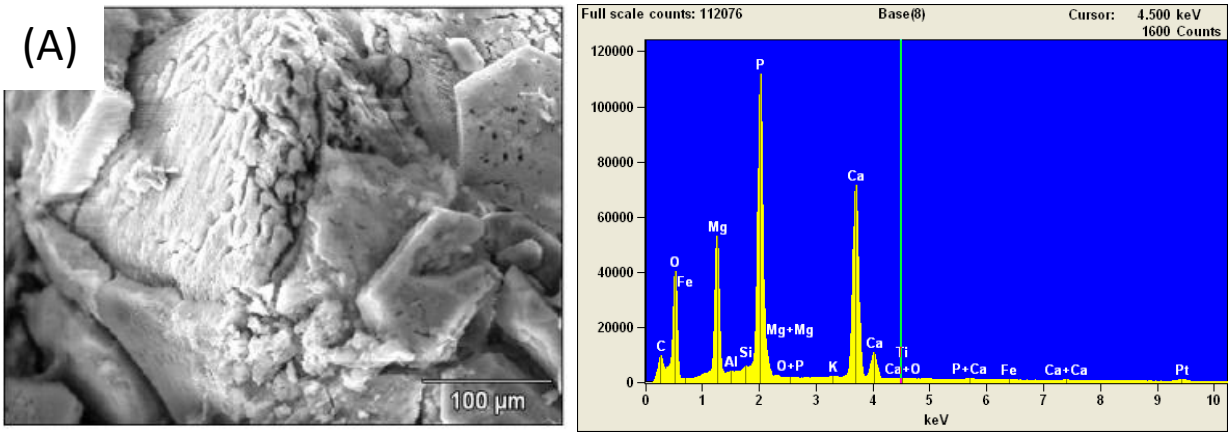

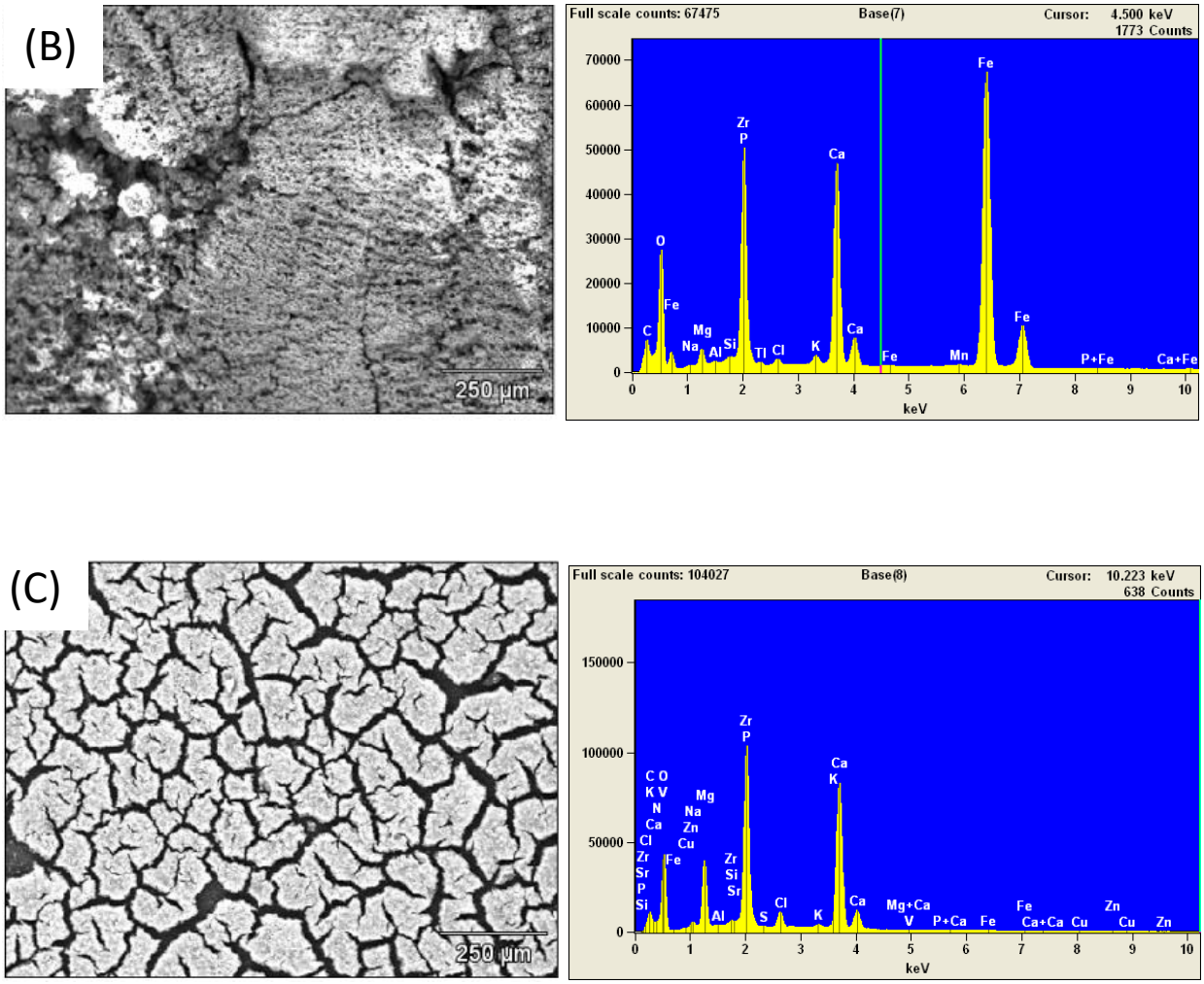

Figure 1.6-2 SEM Images and EDX spectra of naturally occurred precipitates from Tres Rios water reclamation facility Tucson, Arizona before (A) and after (B) ferric chloride addition and precipitate grown in laboratory (C)

Figure 1.6-2(A) is SEM image of naturally occurred mineral in centrate discharge pipe before ferric chloride was added to prevent struvite formation. Molar ratio of magnesium to phosphate in specimen Figure 1.6-2(A) is 1:1.2 as calculated from EDX data. Sharp edges in the image are indications of crystal formation. It was found that calcium is less abundant in the region where magnesium is abundant as shown in Figure 1.6-3, which indicates calcium and magnesium may be competitors in the crystallization process. Figure1.6-2(B) is SEM image of mineral occurred

in centrate discharge pipe after ferric chloride is used in the plant. The molar ratio of magnesium to phosphate is 1:6.0 in specimen Figure 1.6-2(B). The examined surface is relatively flat and uniform in composition. However, in a small region where mineral has foamy texture, calcium is rarely found where iron is abundant in Figure 1.6-4. In the natural process, calcium and iron may be competing to form complex with magnesium so that calcium and iron do not co-exist in the region of interest. Image Figure 1.6-2(C) shows the precipitate formed in laboratory using centrate collected from Tres Rios Water Reclamation Facility with concentrations of magnesium, orthophosphate and ammonia at 0.926 mM, 3.55 mM, and 89.9 mM respectively. Precipitate was recovered by adjusting initial pH of centrate to 9 and no external ions were added. The molar ratio of magnesium to phosphate is 1:1.5 for precipitate formed in laboratory. The iron concentration is low in this specimen and ion composition is relatively uniform in the examined region. Struvite usually precipitates in a 1:1 molar ratio of magnesium to phosphate. The EDX data shows that none of the samples examined is pure struvite. In addition, the formation of mineral is affected by the level of iron in centrate. The results from Figure 1.6-2(B) indicate iron has a potential to form complexes with phosphate, resulting in higher percentage of phosphate in the mineral. More synthesized struvite images using centrate from Tres Rios Water Reclamation Facility are present in Figure 1.6-5.

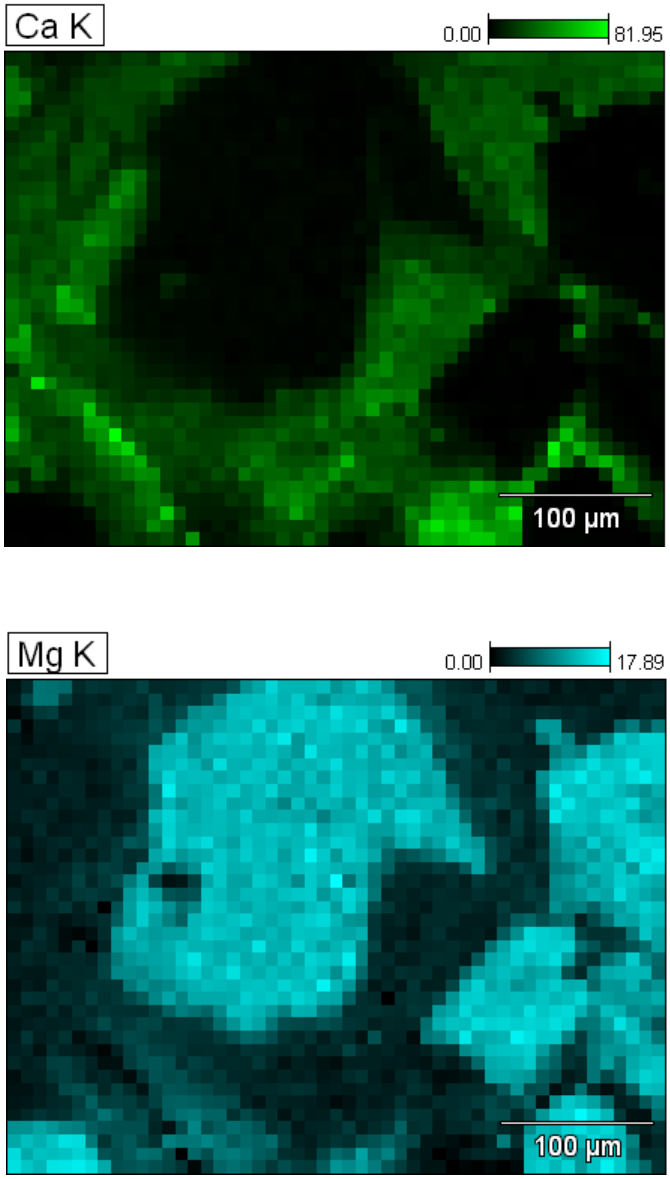

Figure 1.6-3 Spatial distribution of calcium (top) and magnesium (bottom) in naturally occurred mineral from Tres Rios Water Reclamation Facility before ferric chloride addition

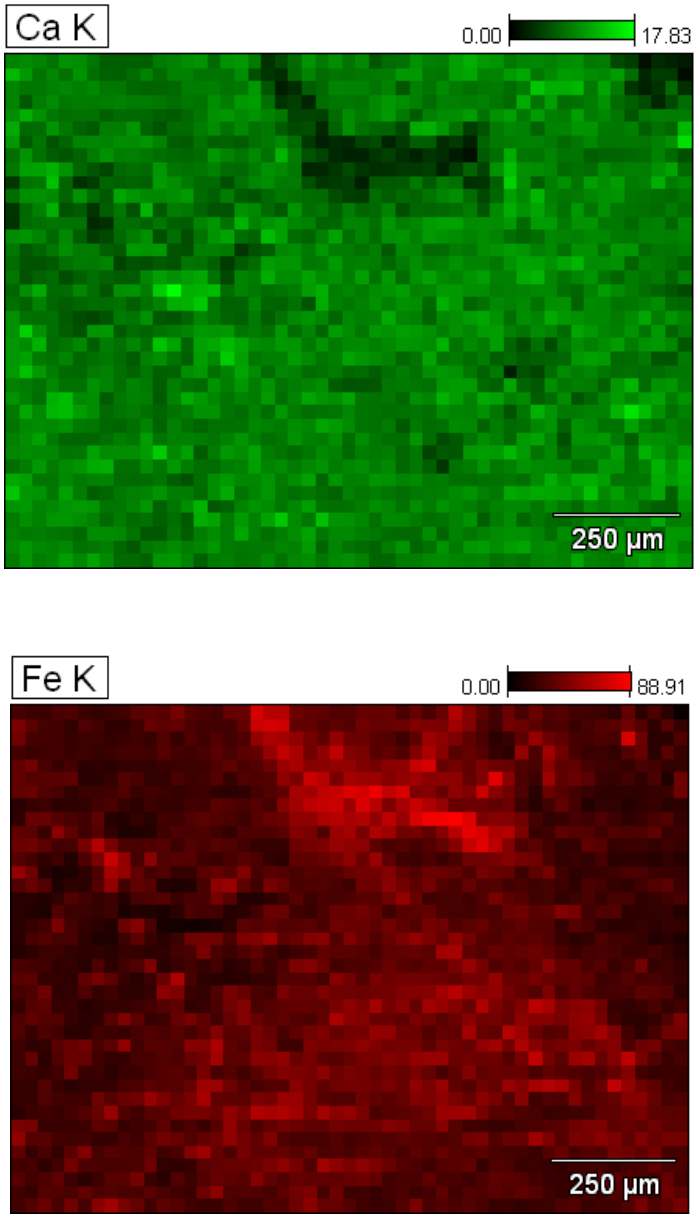

Figure 1.6-4 Spatial distribution of calcium (top) and iron (bottom) in naturally occurred mineral from Tres Rios Water Reclamation Facility after ferric chloride addition

(1)

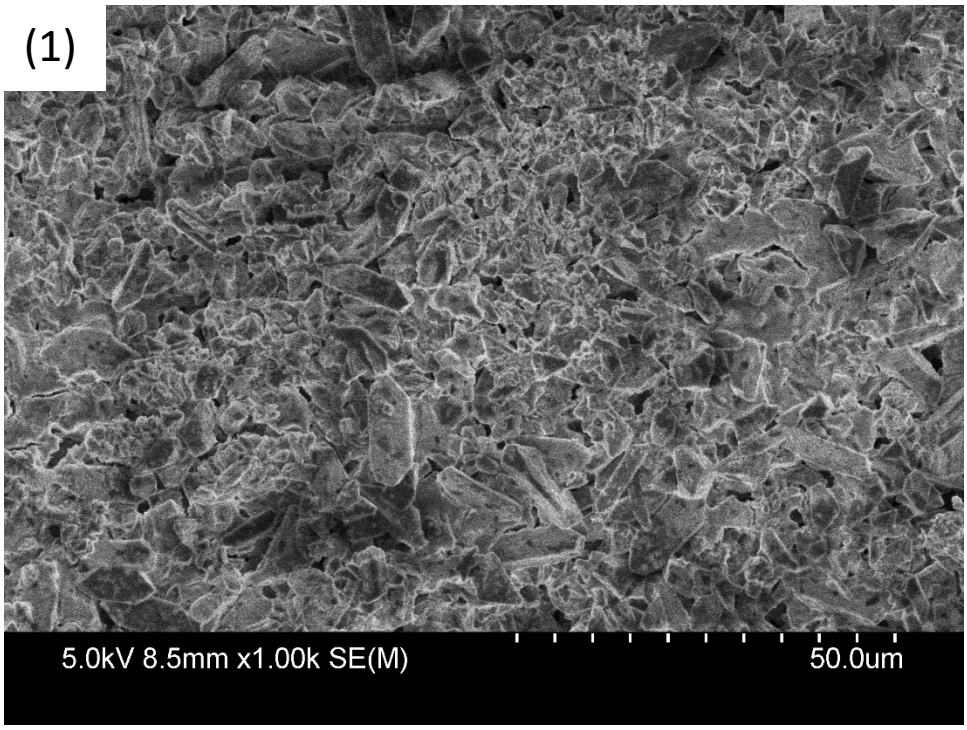

(2)

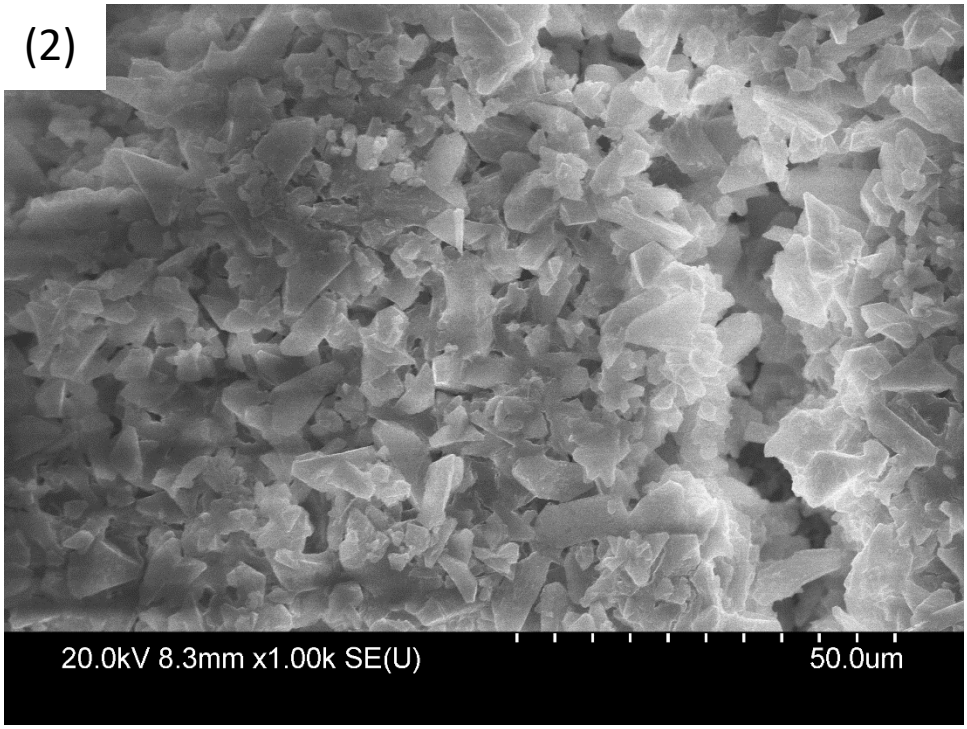

(3)

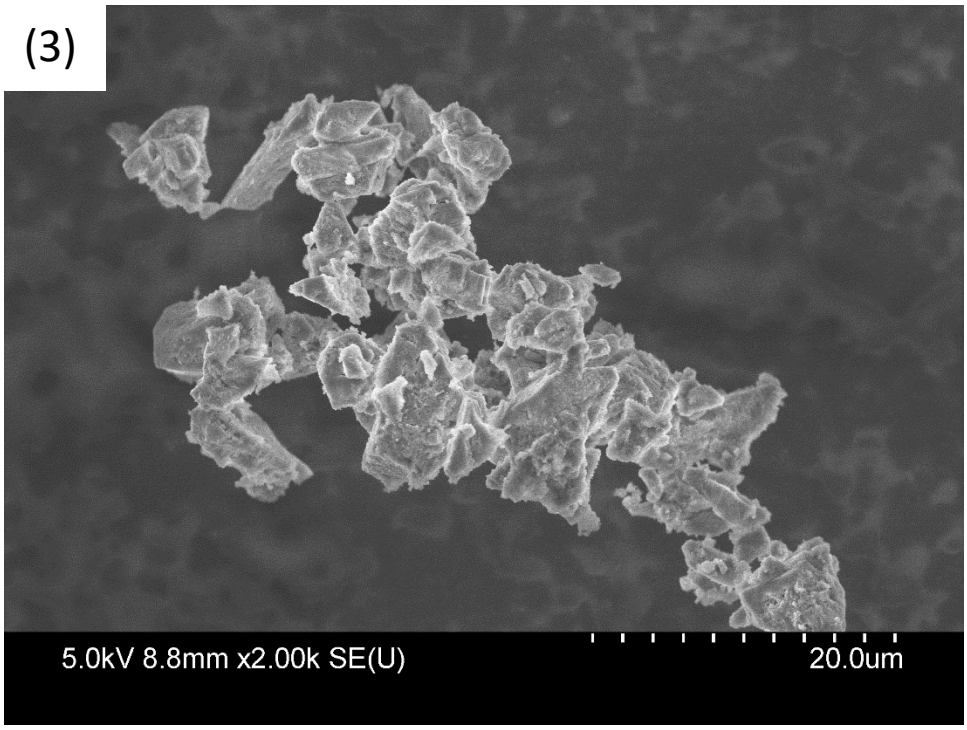

(4)

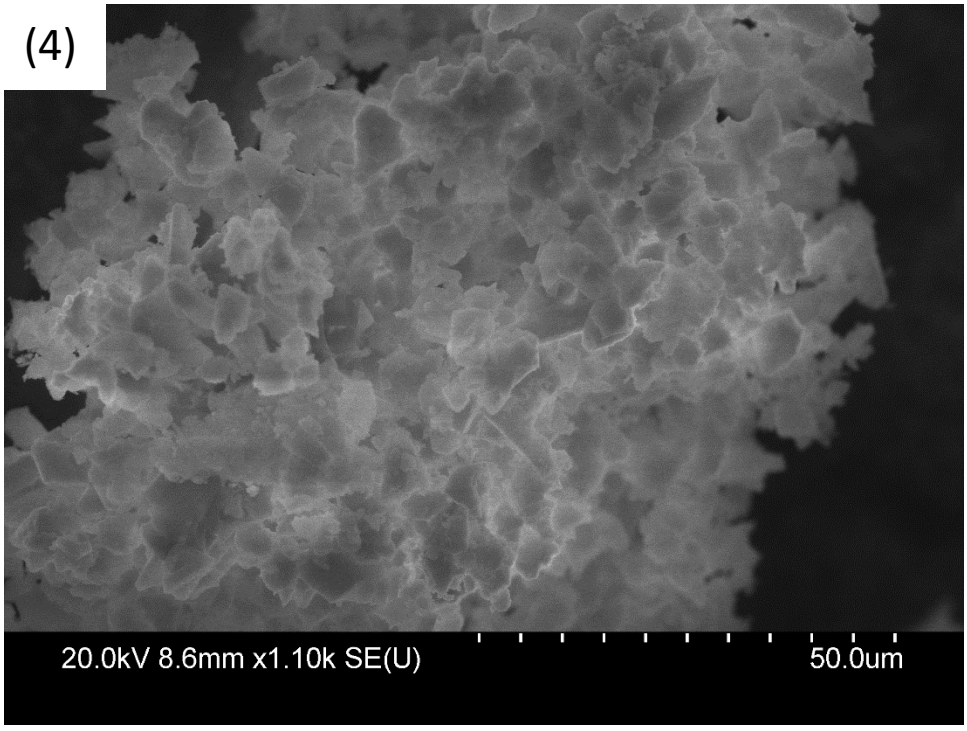

(5)

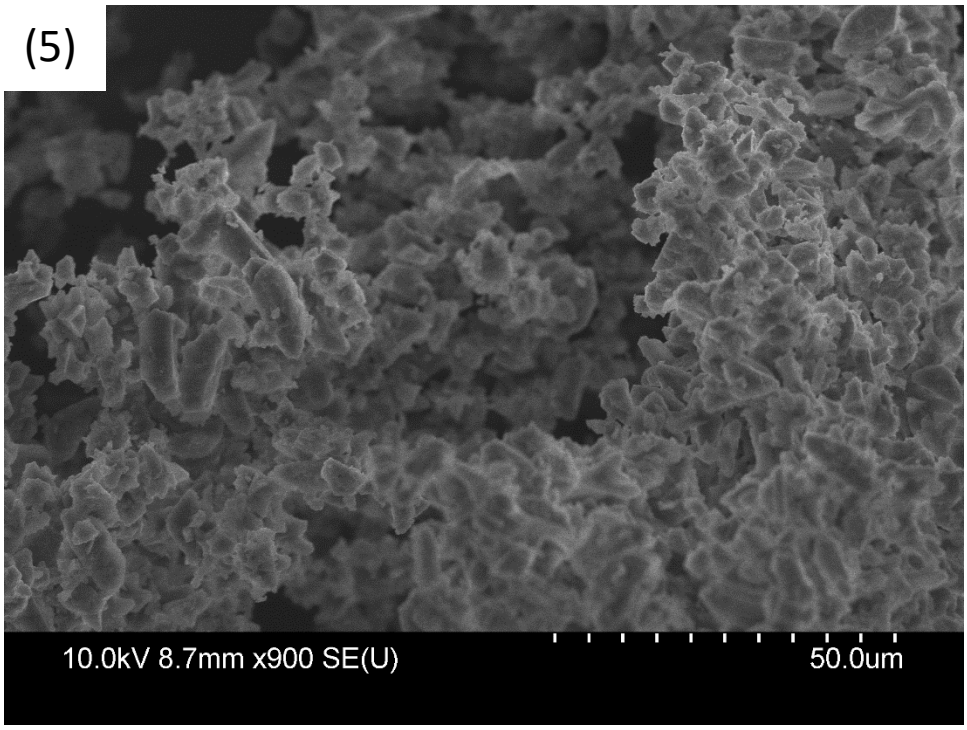

(6)

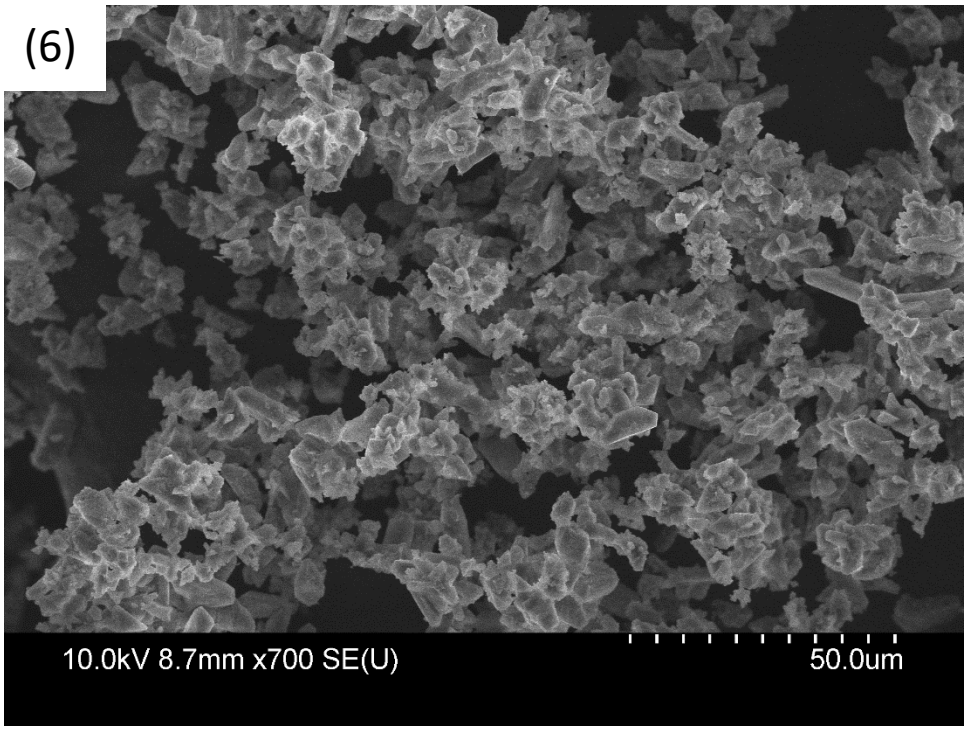

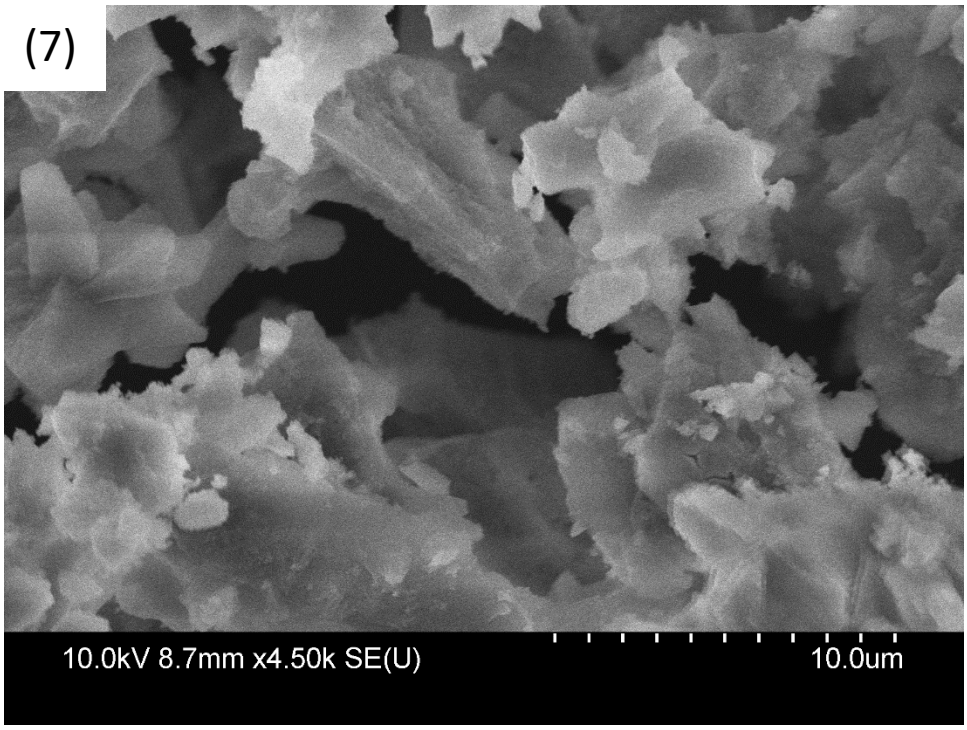

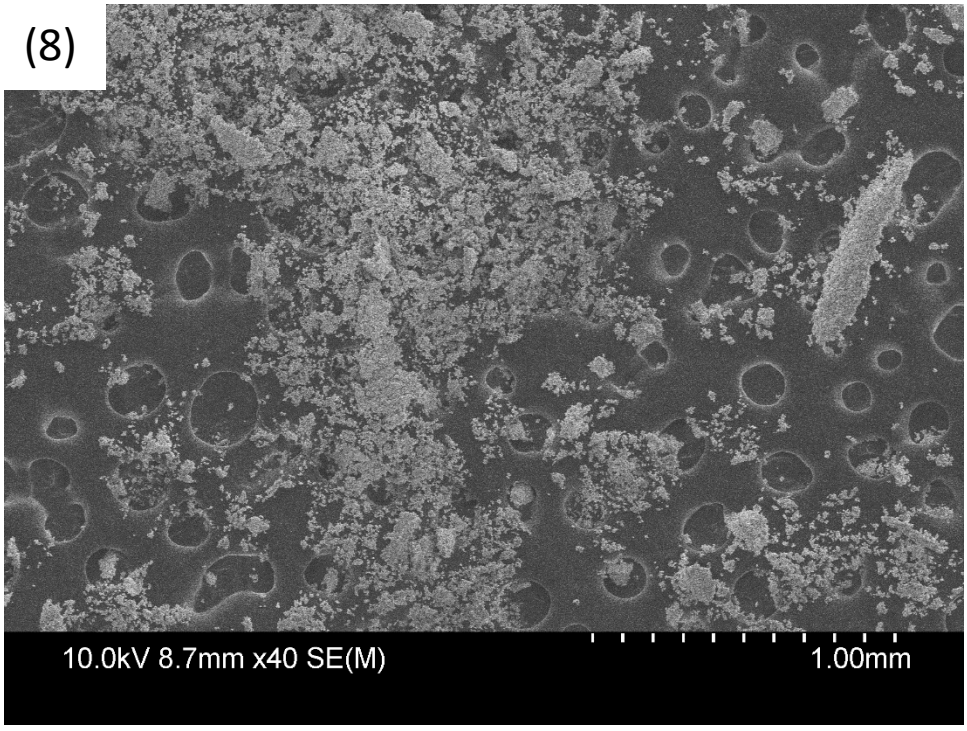

Figure 1.6-5 (1)-(8) are additional SEM images of struvite synthesized in laboratory using centrate from Tres Rios Water Reclamation Facility

1.6.3. Struvite precipitation model

A model was developed to calculate supersaturation index (SI) of struvite as a function of pH in deionized water. Supersaturation index is defined as ratio of K_{so} to K_{sp}, $SI = \frac{K_{so}}{K_{sp}}$,where K_{so} is ion product, and K_{sp} is solubility constant. Struvite formation is possible if ratio of K_{so} and K_{sp} is greater than 1 (log SI > 0). Assume the following species are present in aqueous solution:

$H^+,\ OH^-,\ Cl^-, Na^+$

$NH_4^+,\ NH_3(aq),$

$H_3PO_4(aq), H_2PO_4^-,\ HPO_4^{2-},\ PO_4^{3-},$

$MgH_2PO_4^+,\ MgHPO_4(aq),\ MgPO_4^-,\ Mg^{2+},\ MgOH^+$

Dissociation Equations:

$$H_3PO_4(aq) \xrightarrow{Ka1} H^+ + H_2PO_4^- \quad (1)$$

$$H_2PO_4^- \xrightarrow{Ka2} H^+ + HPO_4^{2-} \quad (2)$$

$$HPO_4^{2-} \xrightarrow{Ka3} H^+ + PO_4^{3-} \quad (3)$$

$$H_2O \xrightarrow{Ka4} H^+ + OH^- \quad (4)$$

$$MgOH^+ \xrightarrow{Ka5} Mg^{2+} + OH^- \quad (5)$$

$$MgPO_4^- \xrightarrow{Ka6} Mg^{2+} + PO_4^{3-} \quad (6)$$

$$MgHPO_4(aq) \xrightarrow{Ka7} Mg^{2+} + HPO_4^{2-} \quad (7)$$

$$MgH_2PO_4^+ \xrightarrow{Ka8} Mg^{2+} + H_2PO_4^- \quad (8)$$

$$NH_4^+ \xrightarrow{Ka9} H^+ + NH_3 \quad (9)$$

Rearrange equation (1) - (9)

$$[HPO_4^{2-}] = \frac{[H^+][PO_4^{3-}]}{Ka3} \quad (10)$$

$$[H_2PO_4^-] = \frac{[H^+][HPO_4^{2-}]}{Ka2} = \frac{[H^+]^2[PO_4^{3-}]}{Ka2Ka3} \quad (11)$$

$$[H_3PO_4]_{(aq)} = \frac{[H^+][H_2PO_4^-]}{Ka1} = \frac{[H^+]^3[PO_4^{3-}]}{Ka1Ka2Ka3} \quad (12)$$

$$[MgOH^+] = \frac{[Mg^+][OH^-]}{Ka5} \quad (13)$$

$$[MgPO_4^-] = \frac{[PO_4^{3-}][Mg^{2+}]}{Ka6} \quad (14)$$

$$[MgHPO_4]_{(aq)} = \frac{[H^+][PO_4^{3-}][Mg^{2+}]}{Ka7} \quad (15)$$

$$[MgH_2PO_4^+] = \frac{[Mg^{2+}][H^+][HPO_4^{2-}]}{Ka8Ka2} = \frac{[Mg^{2+}][H^+]^2[PO_4^{3-}]}{Ka8Ka2Ka3} \quad (16)$$

$$[NH_3]_{(aq)} = \frac{Ka9[NH_4^+]}{[H^+]} \quad (17)$$

$$[OH^-] = \frac{Ka4}{H^+} \quad (18)$$

Mass balance of phosphate, magnesium and ammonia

$$C_{total\_Phosphate} = [PO_4^{3-}] + [HPO_4^{2-}] + [H_2PO_4^-] + [H_3PO_4]_{(aq)} \quad (19)$$

$$C_{total\_Magnesium} = [Mg^{2+}] + [MgOH^+] + [MgPO_4^-] + [MgHPO_4]_{(aq)} + [MgH_2PO_4^+] \quad (20)$$

$$C_{total\_Ammonia} = [NH_4^+] + [NH_3]_{(aq)} \quad (21)$$

Rearrange equation (10) to (18) and substitute in equation (19) to (21)

$$[PO_4^{3-}] = \frac{C_{total\_Phosphate}}{1 + \frac{[H^+]}{Ka3} + \frac{[H^+]^2}{Ka2Ka3} + \frac{[H^+]^3}{Ka1Ka2Ka3}} \quad (22)$$

$$[Mg^{2+}] = \frac{C_{total\_Magnesium}}{1 + \frac{Ka4}{Ka5 \cdot [H^+]} + \frac{[PO_4^{3-}]}{Ka6} + \frac{[H^+][PO_4^{3-}]}{Ka7} + \frac{[H^+]^2[PO_4^{3-}]}{Ka2Ka3Ka8}} \quad (23)$$

$$[NH_4^+] = \frac{C_{total\_Ammonia}}{1 + \frac{Ka9}{[H^+]}} \quad (24)$$

Charge Balance:

$$\sum C_{anion} = \sum C_{cation}$$

$$3[PO_4^{3-}] + 2[HPO_4^{2-}] + [H_2PO_4^-] + [MgPO_4^-] + [Cl^-] + [OH^-] = 2[Mg^{2+}] + [MgOH^+] + [MgH_2PO_4^+] + [NH_4^+] + [Na^+] + [H^+] \quad (25)$$

$$[Na^+] = C_{total\_Phosphate} \quad (26)$$

$$[Cl^-] = 2C_{total\_Magnesium} + C_{total\_Ammonia} \quad (27)$$

$$I = 0.5 \sum Ci \cdot Zi^2 \quad (28)$$

$$I = 0.5\{[H^+](+1)^2 + [OH^-](-1)^2 + [PO_4^{3-}](-3)^2 + [HPO_4^{2-}](-2)^2 + [H_2PO_4^-](-1)^2 + [H_3PO_4]_{(aq)}(0)^2$$
$$+ [MgOH^+](+1)^2 + [MgPO_4^-](-1)^2 + [MgHPO_4]_{(aq)}(0)^2 + [MgH_2PO_4^+](+1)^2 + [NH_4^+](+1)^2$$
$$+ [NH_3]_{(aq)}(0)^2 + [Na^+](+1)^2 + [Cl^-](-1)^2\}$$

$$= 0.5\{[H^+] + \frac{Ka4}{[H^+]} + 9[PO_4^{3-}] + 4\frac{[H^+][PO_4^{3-}]}{Ka3} + \frac{[H^+]^2[PO_4^{3-}]}{Ka2Ka3} + \frac{[Mg^{2+}]Ka4}{Ka5\cdot[H^+]} + \frac{[Mg^{2+}][PO_4^{3-}]}{Ka6}$$
$$+ \frac{[H^+]^2[PO_4^{3-}][Mg^{2+}]}{Ka8} + [NH_4^+] + C_{total\_Phosphate} + (2C_{total\_Magnesium} + C_{total\_Ammonia})\}$$

(29)

$$\lg \gamma_{PO_4^{3-}} = -A(-3)^2(\frac{\sqrt{I}}{1+\sqrt{I}} - BI) \quad (30)$$

$$\lg \gamma_{Mg^{2+}} = -A(+2)^2(\frac{\sqrt{I}}{1+\sqrt{I}} - BI) \quad (31)$$

$$\lg \gamma_{NH_4^+} = -A(+1)^2(\frac{\sqrt{I}}{1+\sqrt{I}} - BI) \quad (32)$$

$$K_{so} = \alpha_{PO_4^{3-}}\alpha_{Mg^{2+}}\alpha_{NH_4^+} = \gamma_{PO_4^{3-}}[PO_4^{3-}]\gamma_{Mg^{2+}}[Mg^{2+}]\gamma_{NH_4^+}[NH_4^+] \quad (33)$$

$$SI = \frac{K_{so}}{K_{sp}} \quad (34)$$

$$\log SI = \log(\frac{K_{so}}{K_{sp}}) \quad (35)$$

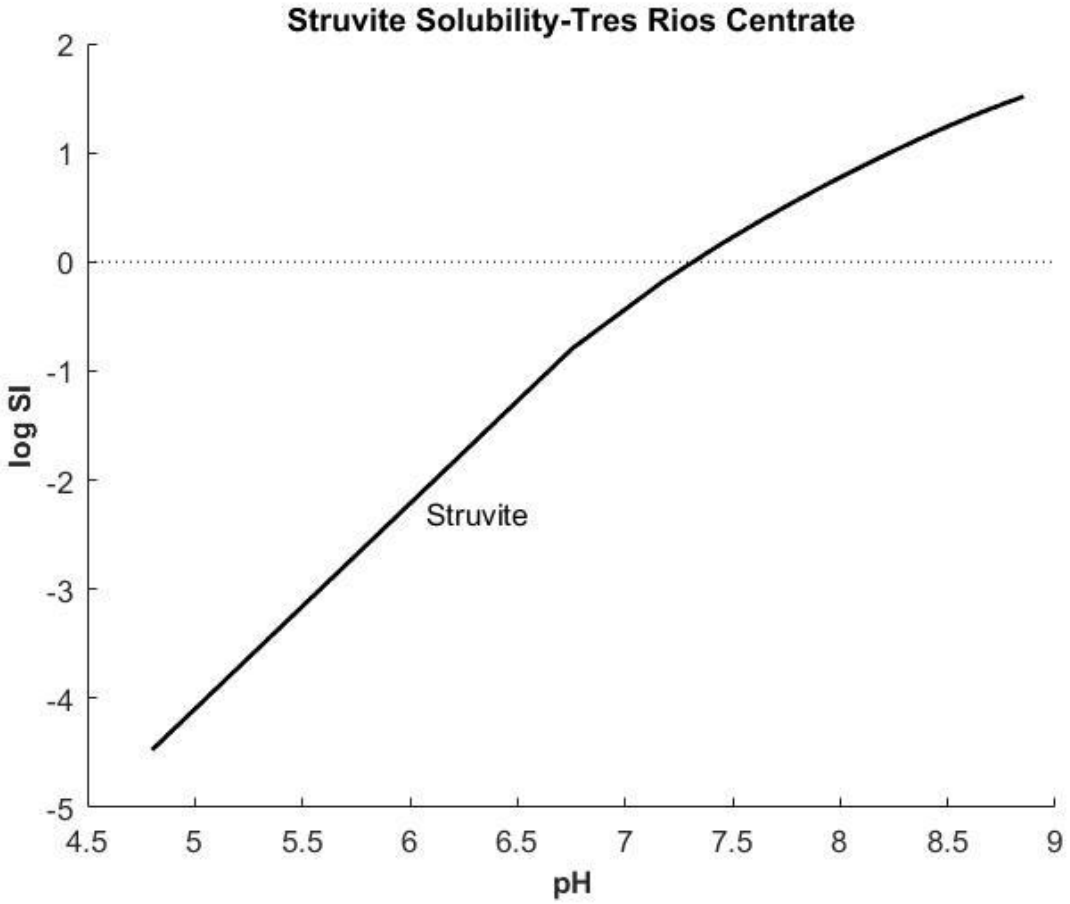

Figure 1.6-6 Model predicted struvite supersaturaion index (SI = K_{so}/K_{sp}) under atmospheric pressure at 25 ℃. Total magnesium, ammonia, and phosphate concentrations were set equal to typical values found in Trest Rios centrate (22.5 mg/L, 1260 mg/L, and 110 mg/L, respectively)

Struvite solubility depends on pH and is more soluble in highly basic or slightly acidic solutions. Figure 1.6-6 shows the solubility (in terms of supersaturation Index, SI = K_{so}/K_{sp}, where K_{so} is the ion product and K_{sp} is the solubility product) as a function of pH in aqueous solution. Concentration of total magnesium 22.5 mg/L, ammonia 1260 mg/L and orthophosphate 110 mg/L are entered to the model for calculations. This curve was generated by equations (1) – (35) described in this section. Values of SI > 1 (log SI > 0) indicate the possibility of struvite precipitation. Figure 1.6-6 suggests that struvite formation can be controlled by the addition of a

strong acid. In the solids handling systems of wastewater treatment plants, pH can then be raised for struvite precipitation and recovery. However, disadvantages of strong acid for pH control such as cost, worker safety, equipment corrosion, and environmental issues associated with the production of industrial chemicals motivate investigation of alternative pH control methods.

1.7. Explanation of dissertation format

Five projects have been included in this dissertation that have either been published or prepared for publication in peer-reviewed journals. The five manuscripts are presented in appendices A-E.

The first and second projects focus on characterization of PM in ambient air to fill knowledge gaps on size-resolved chemical composition, size distribution and source apportionment of pollution in the targeted regions of analysis (Marina, California and Manila, Philippines).

The third project was devoted to analyzing long-term precipitation and aerosol data collected at Pinnacles National Monument (~65 km east of the Pacific Ocean coastline) to examine interrelationships between aerosol and precipitation chemistry. In the three aforementioned projects, a Positive Matrix Factorization (PMF) model was employed to identify pollution sources.

The fourth and fifth projects are focused on providing knowledge to improve wastewater treatment processes. In the fourth project, MATLAB algorithm ODE15s was utilized to model the degradation mechanism of p-cresol in the presence of hydroxy radical and ultraviolet irradiation in deionized water. The model considers scavenging effects between hydroxyl radical and reaction intermediates and predicts concentration of target compounds and reaction by-products as a function of time. Experiments were carried out in a batch reactor and the

concentrations of target compounds were analyzed by high performance liquid chromatography (HPLC) coupled with UV/Vis detector and used to validate the model.

In the fifth project, bench and pilot experiments were conducted to investigate the feasibility of using carbon dioxide to acidify centrate as an indication of increasing struvite solubility in wastewater. A pilot plant was built at Tres Rios Water Reclamation Facility to verify the hypotheses at a pilot plant scale. Mathematical models were developed to calculate parameters that are required to achieve desired pH for struvite prevention. Centrate acquired from Tucson, Phoenix, Portland, and Chicago were tested and the results were used to validate an equilibrium model.

Conclusions and key findings associated with each study are presented in Chapter 2. A detailed description of each study is provided in Appendices A-E.

CHAPTER 2. PRESENT STUDY

The following is summary of key findings. The complete discussion of methods, results and conclusions are provided in papers in appendices A-E.

2.1. Sized-resolved characteristics of water-soluble particulate elements in a coastal area: source identification, influence of wildfires, and diurnal variability

The composition of water-soluble fraction of 29 elements was examined in this study to understand chemical and physical properties of aerosol in atmosphere. Elements were collected by Micro Orifice Uniform Deposition Impactors (MOUDIs) during two separate summer campaigns in 2013 (NiCE) and 2016 (FASE) at a central California coastal site. Characteristic peaks were found in four diameter ranges: 0.1-0.18 μm, 0.32-0.56 μm, 1.0-1.8 μm, and 3.2-5.6 μm. Species that exhibited peaks in the supermicrometer size range (1.8-5.6 μm) include sea salt constitutes (Na, K), crustal matter (Fe, Al, Ti). Size distributions ranged widely among the full suite of elements, indicating the study region was impacted by diverse sources of pollutions. In addition to variations in size distributions, the number of modes varied in different environmental conditions such as with influence of wildfire and without influence of wildfire during NiCE and FASE periods.

Positive Matrix Factorization (PMF) is a receptor model developed many including the Environmental Protection Agency (EPA) to identify pollution sources. By employing PMF, six characteristic sources were identified in the study region: Marine Emissions (45.4%), Secondary Aerosol (24.4%), Biomass Burning (13.1%), Waste Facilities (8.7%), Vehicular Emissions (4.4%) and Crustal Emissions (3.9% of total mass). PMF model also allows investigation of temporally-resolved particulate matters (PM) levels during daytime and nighttime periods. Day

to night ratios for Vehicular Emissions (day/night mass concentration ratio = 31.3), Crustal Emissions (day/night = 20.0), and Secondary Aerosol (day/night = 27.2) were found larger than 1.0, which suggests increased anthropogenic activities, higher diffusion and more frequent photochemical reactions during daytime period. Elements that enhanced in crustal source factor were selected for enrichment factor (EF) analysis. Several species that are commonly associated with crustal matter exhibited values greater than the threshold values, indicating the mixing of non-crustal pollutants such as sea salt (e.g., Na, K), marine biota emissions (I), and anthropogenic emissions (Ni, Zn, As, Cd).

Two separate wildfires occurred during NiCE and FASE campaigns exhibited contrasting behaviors in some degrees. NO_3^-, NH_4^+, I, Zn, V, and Ti were reduced, however Pt was enhanced during FASE wildfire period. The differences of two wildfires indicate they may be characterized by different transport time of fire plumes to sampling sites, fuel type, and flame condition. Despite the differences, the enhancement of MSA, nss SO_4^{2-}, oxalate, K, Cu, As, Rb were observed in both wildfires.

This study suggests that regulations should be implemented for wildfire prevention owing to harmful particles that are emitted during wildfire period are detrimental to human health. The present study has board implications for regions that are impacted by similar pollution sources. My contributions to this project include analyzing acquired data, reviewing literature, conducting data interpretation, and drafting results into a manuscript for publication.

2.2. Size-resolved composition and morphology of particulate matter during the Southwest monsoon in Metro Manila, Philippines

This study characterized chemical composition and morphology of aerosols collected by Micro-Orifice Uniform Deposition Impactors (MOUDIs) during CAMP^{2}Ex campaign in the Southwest monsoon season of 2019 in the Philippines. Several techniques were used in this study include mass spectroscopy for water-soluble chemical composition analysis, gravimetry for quantifying total particulate mass, black carbon spectroscopy for measuring black carbon concentration and electron microscopy analysis for examining the morphology of particles, source apportionment model (PMF) for pollution source identification. Five pollution sources identified by PMF model suggest pollutions in Metro Manila were contributed by the following sources: Aged/Transported (48.0%; NH_4^+, SO_4^{2-}, MSA, oxalate), Sea Salt (22.5%; Cl^-, NO_3^-, Ca^{2+}, Na^+, Mg^{2+}, Ba, Sr), Combustion (18.7%; Ni, As, Co, P, Mo, Cr), Vehicular/Resuspended Dust (5.6%; Al, Ti, Fe), and Waste Processing (5.1%; Zn, Cd, Pb, Mn, Cu). Total mass concentrations were measured twice in two separate sampling events with mass at 18.6 μg m^{-3} and 53.0 μg m^{-3}. Water-soluble mass concentrations were measured 12 times separately and the mass was ranging 2.7–16.6 μg m^{-3} with average at 8.53 ± 4.48 μm m^{-3}. Black carbon mass concentration was 14.3 μg m^{-3} and only measured once. Size distribution analysis revealed that bulk mass of particulate was between 0.18–1.0 μm with a dominant mode between 0.32–0.56 μm. Most of the black carbon (BC) mass was accumulated between 0.10–1.0 μm. Due to peaking between 0.18–0.32 μm, black carbon is less impacted by wet scavenging. Wet scavenging is a complex process as it is governed by several parameters such as atmospheric pressure, rain intensity, and collision efficiency. Microscopy analysis provided evidence non-spherical particles in submicrometer range (< 1μm) where particles are usually considered to be sphere, which is significant in

calculations of parameters such as single scattering albedo, asymmetry parameter, and extinction efficiency.

Results of this work have broad implications for aerosol impacts on public health, visibility, and regional climate, atmospheric circulation. Results obtained from this study provide contextual data for the airborne component of the Cloud, Aerosol, and Monsoon Processes Philippines Experiment ($CAMP^2Ex$) planned for the SWM season in 2019. In this project, I conducted microscopy analysis, assisted in data interpretation and assisting with PMF analysis, prepared tables and figures, and assisted with the drafting of the manuscript.

2.3. Sources of pollution and interrelationships between aerosol and precipitation chemistry at a central California site

This study analyzed aerosol and precipitation data collected between 2010 and 2016 at Pinnacles National Monument. Seven distinct pollution sources were identified by Positive Matrix Factorization (PMF): aged sea salt (25.7% of $PM_{2.5}$), biomass burning (24.2% of $PM_{2.5}$), fresh sea salt (8.2% of $PM_{2.5}$), secondary sulfate (11.7% of $PM_{2.5}$), dust (10.0% of $PM_{2.5}$), vehicular emissions (8.2% of $PM_{2.5}$) and secondary nitrate (5.2% of $PM_{2.5}$). Among these source factors, secondary sulfate exhibited a significant reduction over time. In contrast, PM_{Coarse} increased over time, which may be result of long range transported of dust. SO_4^{2-}, NO_3^-, Cl^- were found to be the most abundant species in monthly profiles of precipitation data. Intercomparison between aerosol and precipitation data revealed that PM_{Coarse} and Dust and Sea Salt source factors exhibited positive correlation with calcium ion in precipitation, which indicates larger particles affect precipitation. In addition, sulfate was significantly correlated with Dust and Sea Salt source factors, suggesting partition of sulfate to dust and sea salt particles. The uptake of HNO_3 was believed responsible for reducing precipitation pH value.

The results of this work provide insights on improving air quality in regions that are impacted by similar pollution sources and demonstrate use of aerosol and precipitation chemistry data to investigate aerosol and precipitation interactions. My contribution to this project was data analysis, assistance with interpretation of data, and editing the manuscript.

2.4. Modeling the oxidation of phenolic compounds by hydrogen peroxide

Tertiary wastewater treatment technology such as advanced oxidation processes (AOPs) has been widely used for the removal of trace organic contaminants from water and wastewater. Numerous models have been developed to predict degradation efficiency of target compounds in H_2O_2 assisted photo-degradation reactions. These models focused on the production and consumption of hydroxyl radicals and the reaction between hydroxyl radical and target compounds. However, the degradation rate of target compound is not only determined by the concentration of hydroxyl radical, but also affected by radical scavenging by reaction intermediates. In this study, p-cresol has been chosen as surrogate for the development of a full kinetic photo-degradation model that considers reaction between radical and reaction intermediate compounds. The model predicted reaction mechanism confirmed previous proposed mechanism that OH addition is the first step of the photo-chemical reaction and followed by abstraction of H to form benzoquinone and finally aliphatic acids are formed via ring cleavage. 4-methylcatechol was determined to be the first reaction intermediate of p-cresol and OH-induced oxidation of p-cresol was determined to be the dominant reaction pathway for the formation of 4-methylcatechol. In the kinetic model, both direct photolysis and reaction with OH radical were considered. Molecular oxygen was found involved in several steps of the reaction especially in the oxidation of 4-methylcatechol to 4-methylbenzoquinone. Even significant pH drop has observed in experiment, total organic carbon (TOC) results suggest no carbon dioxide has evolved from solution. It was found that formic acid, acetic acid and oxalic acid were formed during the experiments. Model also revealed that 4-methylcatechol react with hydroxyl radical and the degradation rate of 4-methylcatechol is a function of initial concentration of hydrogen peroxide.

The degradation mechanism of p-cresol was predicted by a comprehensive kinetic model that considers reaction between hydroxyl radical and reaction intermediates. The development of a full model offers more accurate predictions on evaluation of process such as AOPs. In this project, I collected experiment data, reviewed literature, and provided useful discussions.

2.5. Sustainable struvite control using carbon dioxide

This research uses carbon dioxide to lower pH of centrate for preventing formation of struvite that can coat pipes, clog pumps and create process issues. Both bench and pilot experiments were carried out to evaluate the feasibility of the method. Mathematical models were developed to produce design protocols for wastewater treatment plants that experienced struvite issues and considered implement proposed technology to prevent struvite formation. Design parameters are easy measurable water quality parameters such as alkalinity and concentration of struvite components. First, a struvite solubility model was developed to investigate pH at which struvite formation is infeasible. Several minerals were considered in the model, including $MgNH_4PO_4 \cdot 6H_2O_{(s)}$, $MgOH_{2(s)}$, $MgHPO_{4(s)}$, and $Mg_3(PO_4)_{2(s)}$ and supersaturation index (SI) was calculated as an indicator for precipitation. SI was plotted as a function of pH and SI >1 indicates formation of precipitation. In Tucson centrate, pH > 6.6 is where struvite formation becomes possible. Second, a CO_2 injection model was developed to predict equilibrium pH at various CO_2 partial pressures. Aqueous CO_2 concentration was calculated by Henry's Law. Model results were validated by bench experiments conducted in centrate from Phoenix, Chicago, Portland and Tucson. Due to the amount of acid that required to reduce pH to desired level is a function of mineral alkalinity and concentration of struvite components. Tucson sample has higher concentration of struvite components, even alkalinity of Tucson sample is lower than Chicago sample, it requires more acid to reach target pH. Finally, a pilot plant was built originally to test the feasibility of proposed method in pilot scale, however an alternative CO_2 injection method was investigated during pilot experiments. The pilot system is mainly comprised of a 1,000-gallon hydro tank, a ceramic diffuser placed at the bottom of the tank, and a CO_2 tank that is constantly providing gaseous CO_2 to the system. In-line pH probes and flow

meters were installed to monitor pH and flow rate changes. The function of the tank is to produce CO_2 pre-saturated centrate. Sampling ports were installed 0.9, 1.8, 3.7, 6.7 and 7.3m behind the injection point. Both gaseous CO_2 and CO_2 pre-saturated liquid were injected at the injection point as two separate experiments. It was found that mixing CO_2 pre-saturated centrate with fresh centrate is more effective in reducing pH compared with injecting gaseous CO_2 in centrate flow.

This study highly relies on computer simulation. Model results suggest that carbon dioxide is feasible to reduce pH of centrate to a level that the formation of struvite is inhibited. My contributions to this project included (i) developing a struvite precipitation model, (ii) order high pressure pH probe for bench experiments, (iii) procure pipes, parts, fittings, valves, flow meters, pumps, and order 1,000-gallon hydro-tank and tank modification for pilot experiments, (iv) fabricate pilot plant, (v) conduct bench and pilot experiments, and (vi) prepare meeting agendas and presentations. Mineral characterization results are presented in Appendix E.

APPENDIX A

SIZE-RESOLVED CHARACTERISTICS OF WATER-SOLUBLE PARTICULATE ELEMENTS IN A COASTAL AREA: SOURCE IDENTIFICATION, INFLUENCE OF WILDFIRES, AND DIURNAL VARIABILITY

This article has been published in the Atmospheric Environment (2019).

Lin Ma[1], Hossein Dadashazar[1], Rachel A. Braun[1], Alexander B. MacDonald[1], Mojtaba Azadi Aghdam[1], Lindsay C. Maudlin[2], Armin Sorooshian[1,3*]

[1]Department of Chemical and Environmental Engineering, University of Arizona, Tucson, AZ, USA
[2]Department of Geosciences, Auburn University, Auburn, AL
[3]Department of Hydrology and Atmospheric Sciences, University of Arizona, Tucson, AZ, USA

Size-resolved Characteristics of Water-Soluble Particulate Elements in a Coastal Area: Source Identification, Influence of Wildfires, and Diurnal Variability

Lin Ma[1], Hossein Dadashazar[1], Rachel A. Braun[1], Alexander B. MacDonald[1], Mojtaba Azadi Aghdam[1], Lindsay C. Maudlin[2], Armin Sorooshian[1,3*]

[1]Department of Chemical and Environmental Engineering, University of Arizona, Tucson, AZ, USA

[2]Department of Geosciences, Auburn University, Auburn, AL

[3]Department of Hydrology and Atmospheric Sciences, University of Arizona, Tucson, AZ, USA

[*]Corresponding author: Armin Sorooshian (E-mail: armin@email.arizona.edu; Phone: (520) 626-5858; Fax: (520) 621-6048; Postal Address: PO BOX 210011, Tucson, Arizona, 85721, USA)

Key words: MOUDI; PMF; California; Wildfire; Aerosol; Sea Salt

Abstract

Size-resolved elemental measurements were conducted for the water-soluble fraction of particulate matter at a central California coastal city, Marina, during two separate summertime field campaigns: the Nucleation in California Experiment (NiCE) in 2013 and the Fog and Stratocumulus Evolution (FASE) campaign in 2016. Two Micro-Orifice Uniform Deposit Impactors (MOUDIs) were used to quantify mass size distributions of 29 elements and a Positive Matrix Factorization (PMF) model revealed six characteristic sources during the measurement periods: (i) Crustal Emissions (3.9% of total mass), (ii) Secondary Aerosol (24.4%), (iii) Biomass Burning (13.1%), (iv) Waste Facilities (8.7%), (v) Vehicular Emissions (4.4%), and (vi) Marine Emissions (45.4%). Characteristic elements from each of these sources included the following: (i) Crustal Emissions (Fe, Al, Ti, Pt), (ii) Secondary Aerosol (Zn, As, Rb, K, Cu, V), (iii) Biomass Burning (Rb, K, Cu, Pt), (iv) Waste Facilities (Ag, Cd, Ni, Al), (v) Vehicular Emissions (Zn, Zr, V, Mn), and (vi) Marine Emissions (Na, Sr, V, Mn). Temporally-resolved results revealed higher PM levels associated with Vehicular Emissions (day/night mass concentration ratio = 31.3), Crustal Emissions (day/night = 20.0), and Secondary Aerosol (day/night = 27.2) during the day compared to night due to some combination of more daytime anthropogenic activity, wind speed/directional factors, and photochemistry. The Marine Emissions factor exhibited a day/night concentration ratio of exactly 1.0. Mass size distributions revealed characteristic peaks in four diameter ranges: 0.1-0.18 μm, 0.32-0.56 μm, 1.0-1.8 μm, and 3.2-5.6 μm. The number of modes varied depending on the species and degree of wildfire influence, with additional differences observed between the NiCE and FASE wildfire periods.

1. Introduction

Elements associated with airborne particulate matter (PM) are important for a number of reasons. They serve as tracer species to identify the source of air masses (Blanco et al., 2003; Font et al., 2015), have negative impacts on public health (Baghurst et al., 1992; Mateos et al., 2018), are important agents in the biogeochemical cycling of nutrients and contaminants in ecosystems (Avila et al., 1998; Kersten et al., 1991; Wang et al., 2014; Weiss-Penzias et al., 2018), and affect aqueous-phase chemistry by serving as catalysts that can either promote the formation of species such as sulfate (Alexander et al., 2009) or promote the degradation of other species such as carboxylic acids (Furukawa and Takahashi, 2011; Pehkonen et al., 1993). Elements originate from a variety of natural and anthropogenic emission sources. Natural sources include sea spray, soil and crustal rock, vegetation, and volcanoes (Nriagu, 1979, 1989b). Among the most abundant elements contained in ambient PM globally are constituents of sea salt (e.g., Cl, Na, Mg, Ca, K) and crustal matter (e.g., Si, Al, Fe) (Seinfeld and Pandis, 2016). A host of different elements originate from various anthropogenic sources such as fuel combustion, vehicular and ship emissions, mining, smelting, and power plants (Becagli et al., 2012; Prabhakar et al., 2014; Singh et al., 2002). Identifying the size distribution and sources of elements can help improve understanding of their physical and chemical properties and effects in the atmosphere.

Particulate elements have detrimental health impacts due to their oxidative properties (Pietrogrande et al., 2018) and ability to enter into the bloodstream (Valiulis et al., 2008). Their inhalation by humans can cause oxidative injury to the respiratory tract owing to reactive oxygen species (ROS) that are produced by elements inside the body that elevate the oxidative stress of affected areas (Li et al., 2008). Water-soluble transition elements have been linked to severe

diseases such as DNA damage and mutagenicity (Valavanidis et al., 2008). Size-resolved knowledge of element concentrations is important as fine particles are transported deeper into the respiratory system, as compared to larger ones, where they are transferred directly to the bloodstream (Cena et al., 2014; Youn et al., 2016). Aside from effects on human well-being, elements can also impact environmental health as they are transferred from one ecosystem or medium to another. For example, continental dust emissions can be transported from land to the atmosphere and subsequently become associated with cloud droplets that can deposit into aqueous ecosystems (e.g., ocean, lake) via precipitation. The ocean's geochemistry is sensitive to nutrient inputs (Duce et al., 1991); for example, Fe associated with dust and wildfire emissions can fertilize the ocean and affect the growth of ocean microorganisms (Bruland et al., 2001; Capone and Hutchins, 2013; Ito, 2011; Ito, 2015; Ito and Shi, 2016). Contaminants emitted from sources such as mines can deposit to soils and subsequently impact living beings that consume vegetation grown with the soil (Soltani et al., 2017).

During their lifetime in the aerosol phase, elements can alter aerosol chemical composition and, consequently, hygroscopic and optical properties. When element-containing particles are captured inside cloud droplets, soluble elements can complex with organic species to then undergo in-cloud photochemical oxidation reactions that can change the profile of organics through mechanisms such as depletion reactions (Zuo and Hoigne, 1992). Iron-catalyzed photooxidation reactions are one of the most studied mechanisms among various elements (e.g., Sorooshian et al., 2013); however, other transition elements exhibit photo-catalytic activities (Strlic et al., 2003).

The central coast of California represents a region with a myriad of emissions from both natural and anthropogenic sources resulting in a highly complex soup of PM (Maudlin et al.,

2015). Documented sources based on analysis of long-term United States Environmental Protection Agency (EPA) PM data collected at the Pinnacles National Monument site (~65 km east of the Pacific coast) include marine emissions, shipping, biomass burning, dust, and various anthropogenic sources such as vehicles and agriculture (Dadashazar et al., 2019). A detailed investigation of PM data closer to the central California coastline has yet to be conducted that quantifies the relative importance and diurnal nature of different sources, and that characterizes the size-resolved concentration profile of elements. The water-soluble fraction of elements is specifically of interest for a variety of reasons: nucleation efficiency, atmospheric residence time, particle growth/shrinkage mechanisms, bioavailability, and health effects in epidemiological and toxicological studies (Fang et al., 2015; Heal et al., 2005; Jiang et al., 2014; Knaapen et al., 2002; Lindberg and Harriss, 1983; Sarti et al., 2015).

The goal of this study is to examine the size-resolved nature of water-soluble PM elements in a California coastal environment. A unique aspect of this study is that the influence of two major wildfires is examined relative to background conditions, in addition to contrasting night versus day periods with and without wildfire influence. Total water-soluble mass concentrations are reported for 29 elements, followed by examination of the relative abundance of mass concentration in the submicrometer size range for each species, since this range has the greatest impacts for human health and the cloud condensation nuclei (CCN) number concentration budget. Results from a source apportionment model are discussed in order to identify the relative influence of different sources of elements in the study region. Lastly, mass size distributions are reported with the goal of identifying characteristic mode sizes and variations between fire and non-fire conditions. The results of this work have broad implications for applications requiring size-resolved chemical information and for the general understanding

of water-soluble elemental composition for regions experiencing wildfires, marine emissions, and a variety of point sources of anthropogenic pollution.

2. Experimental Methods

2.1 Sample Measurements

Size-resolved aerosol measurements were conducted during two separate summertime field campaigns in the coastal city of Marina, California (36.7°N, 121.8°W), which is ~5 km to the east of the Pacific Ocean coastline (Figure 1). Ground-based measurements were conducted between 3 July 2013 and 9 August 2013 during the Nucleation in California Experiment (NiCE) and between 15 July 2016 and 12 August 2016 during the Fog and Stratocumulus Evolution (FASE) experiment (Table 1). Diurnal measurements were conducted during NiCE (local times: day= 0600-2100, night = 2100-0600), but not FASE. Measurements were conducted using two Micro-Orifice Uniform Deposit Impactors (MOUDIs, MSP Corporation; Marple et al., 1991) with the following aerodynamic cutpoint diameters: 0.056, 0.1, 0.18, 0.32, 0.56, 1.0, 1.8, 3.2, 5.6, 10.0, and 18.0 μm. Sample sets were collected over a period of multiple days to obtain sufficient signal for the various species of interest across the full size spectrum analyzed.

Teflon substrates (PTFE membrane, 2 μm pore, 46.2 mm, Whatman) were used for particle collection. Collected samples were cut in half, with one half archived in a freezer and the other half placed in glass vials with 10 mL of milli-Q water. While strong acids (e.g., HNO_3, CH_3COOH, HCl, HF) can extract a greater fraction of metals (e.g., Sahuquillo et al., 1999; Jamali et al., 2009; Betha et al., 2013), water is more appropriate for this study that is focused on reporting concentrations, inter-relationships, and sources for the water-soluble fraction of elements (e.g., Mukhtar and Limbeck, 2013). Sonication of individual glass vials was conducted for 20 min at 30 °C prior to analysis with either inductively coupled plasma mass spectrometry

(ICP-MS; Agilent 7700 Series) for NiCE samples or triple quadrupole inductively coupled plasma mass spectrometry (ICP-QQQ; Agilent 8800 Series) for FASE samples. Limits of detection (LOD) of the 29 examined elements (Na, K, I, Zn, Fe, Al, Cu, Sr, V, Ni, Mn, Ti, As, Rb, Zr, Pt, Ag, Cd, Hg, Ba, Mo, Cr, Cs, Y, Sn, Co, Pb, Ag, Rh) were calculated automatically by the ICP instruments and were in the ppt range (Table S1). The sample concentrations represent an average of three separate measurements with a standard deviation of 3% or less. Data are also reported for six selected water-soluble anions and cations (methanesulfonate (MSA), Cl^-, NO_3^-, non-sea salt (nss) SO_4^{2-}, NH_4^+, oxalate) speciated and quantified using ion chromatography (IC; Thermo Scientific Dionex ICS 2100 system). IC species LODs (Table S1) were calculated using their respective calibration curve, where LOD is three times the standard deviation of the residuals (predicted signal minus measured signal) divided by the slope of the calibration curve (Miller and Miller, 2018). All species concentrations for samples have been corrected by subtracting concentrations from background substrate samples. Details associated with the quality assurance and quality control of these measurements are also reported in other work (Braun et al., 2017; Maudlin et al., 2015; Youn et al., 2015).

Average meteorological data values are reported in Table 1 corresponding to each MOUDI set. The meteorological measurements were conducted at the Monterey Peninsula station (KMRY; 36.6°N, 121.8°W), which is part of the Mesowest database (Horel et al., 2002). Details regarding the identification of wildfire influences can be found in Maudlin et al. (2015) and Braun et al. (2017).

2.2 Positive Matrix Factorization (PMF)

To identify emissions sources for the water-soluble fraction of PM, a PMF receptor model (US EPA's PMF version 5) was initialized with data from the NiCE and FASE MOUDI

measurements. This technique has been used extensively for source apportionment of aerosol species (Alleman et al., 2010; Begum et al., 2007; Lestari and Mauliadi, 2009; Paatero and Tapper, 1994). PMF analysis was performed using data for the water-soluble fraction of 19 elements (Na, K, I, Zn, Fe, Al, Cu, Sr, V, Ni, Mn, Ti, As, Rb, Zr, Pt, Ag, Cd, Hg) and six selected ions (MSA, Cl^-, NO_3^-, nss SO_4^{2-}, NH_4^+, oxalate). Note that 10 elements (Ba, Mo, Cr, Cs, Y, Sn, Co, Pb, Ag, Rh) that were found to be unnecessary for improving the PMF results were excluded. Species were classified into "strong", "weak", and "bad" categories based on signal-to-noise (S/N) ratios. In our case, only "strong" species (S/N > 1) (Norris et al., 2014) were used in the modeling. Data points below the detection limit (DL) were replaced by half of the DL and uncertainty was replaced by 5/6 of the DL (Reff et al., 2007). For species without a reportable concentration for a specific size range in a MOUDI set, concentrations were replaced by the median value of existing concentrations for that size range and the uncertainty was replaced by four times the median value (Brown et al., 2015). For species with concentrations that were available in the MOUDI sets, their uncertainties were calculated as follows (Reff et al., 2007):

$$\sigma_{ij} = 0.05 \cdot X_{ij} + DL_{ij} \qquad \text{(Equation 1)}$$

where σ_{ij}, X_{ij}, and DL_{ij} are the uncertainty, concentration, and detection limit, respectively, of the j^{th} species in the i^{th} sample.

3. Study Area Description

The city of Marina had a population of 21,700 as of 2016 (US Census Bureau), with the nearest major city being Salinas just over 10 km to the east of the sampling site, which had a 2016 population of 157,200 (US Census Bureau). The measurement site was influenced by urban

emissions in the form of vehicular traffic and extensive agriculture that occurs around the Marina area, especially in Salinas. Additionally, there are several potential point sources of pollution nearby, including the Dynegy Power Plant to the northeast (~14.5 km), the Las Animas Concrete Plant ~ 3.2 km to the southwest, the Cemex Lapis Sand Plant ~ 5.4 km to the northwest, the Monterey Regional Waste Management District facility ~ 4.5 km to the north, and the Assured Aggregate Recycling facility ~ 0.6 km to the south (Figure 1). Due to proximity to the coast, one obvious PM source is marine emissions, which includes biogenic emissions, sea salt, and shipping emissions owing to shipping lanes just off the coast leading up north to Oakland and San Francisco (Sorooshian et al., 2015b; Wang et al., 2014).

A unique aspect of this work is the ability to examine the superimposition of two separate wildfire events on top of background emissions normally impacting the study site. The fire-impacted air masses sampled during NiCE originated from a cluster of fires (Douglas Complex, Whiskey Complex, and Big Windy fires) located by the border of California and Oregon (Figure 1). As documented by Maudlin et al. (2015), the transport time of the biomass burning plumes from the source of that fire cluster to the measurement site ranged from 34-70 h, with the predominant fuel source categorized as "timber, grass and shrub models" (Braun et al., 2017). In contrast, the source of the fire-impacted air masses during FASE (Soberanes Fire) was much closer to the measurement site (30 km to the southwest) in Garrapta State Park, with biomass burning plumes estimated to reach the sample site in approximately 2.5-4.5 h (Braun et al., 2017). The fuel type during the Soberanes Fire was classified as "chaparral, tall grass, and timber" (Braun et al., 2017).

4. Results and Discussion

4.1 Total Water-Soluble Mass Concentrations

Water-soluble mass concentration data are compared between the following seven categories: (i) NiCE wildfire; (ii) FASE wildfire; (iii) non-wildfire conditions in FASE and NiCE; and (iv-vii) day versus night conditions during NiCE with and without wildfire influence. For the ensuing discussion, non-fire data from NiCE and FASE were combined as similar conditions existed during the different sampling periods, although the results from both campaigns are still shown separately in Figure 2 and Table S2. Mass concentrations of the 29 elements for the seven categories are summarized in tabular format in Tables S2-S4 and visually in Figures 2-3, with averages (± standard deviations) of the total sum of species as follows: 1064 ± 663 ng m^{-3} (NiCE wildfire), 560 ± 154 ng m^{-3} (FASE wildfire), 1037 ± 502 ng m^{-3} (non-wildfire), 1533 ng m^{-3} (day NiCE wildfire), 594 ng m^{-3} (night NiCE wildfire), 1028 ± 271 ng m^{-3} (day NiCE non-wildfire), and 1169 ± 787 ng m^{-3} (night NiCE non-wildfire). The concentrations of species ranged widely over seven orders of magnitude (10^{2} to 10^{-5} ng m^{-3}), with the total concentration results being heavily biased by a few species stemming from marine emissions (i.e., mainly Na).

The highest concentrations among all elements was for Na and K for the seven categories, with the range of concentrations among all MOUDI sets being 456 – 1403 ng m^{-3} and 64 – 98 ng m^{-3}, respectively. These elements are major components of sea salt with the following contributions to pure sea salt on a mass basis (Seinfeld and Pandis, 2016): Na = 30.61%, K = 1.1%. Potassium is also an important component of biofuels (Artaxo et al., 1994; Savoie and Prospero, 1980). Next in terms of mass concentration was the sub-group of elements (average concentrations ~ 0.1 – 10 ng m^{-3}) comprised of the following: Zn, I, Sr, Cu, V, Al, Fe, Ba, Mn, Ni, Ti, Rb, Cr, As. Notably enhanced in fire periods was Fe, which is a component of dust that can be lofted up in biomass burning plumes as has been demonstrated in the western United

States (Kavouras et al., 2012; Schlosser et al., 2017; Sturtz et al., 2014), various parts of Africa (Gaudichet et al., 1995; Maenhaut et al., 1996), and Moscow (Popovicheva et al., 2014). The least abundant elements (average concentrations < 0.1 ng m^{-3}) included Pd, Mo, Zr, Cs, Y, Sn, Co, Pb, Ag, Pt, Cd, Rh, and Hg.

When comparing the ratio of day versus night concentrations during NiCE for species with values above the LOD in all MOUDI sets (Figure 3), the most significant increase in non-fire conditions during the daytime was for the following (day/night mass concentration ratios): Pb (3.66), Zn (2.75), Sr (2.55). The largest reductions, quantified as day/night mass concentration ratios, were for Cr (0.28), Al/Ba (0.54), and As (0.75). During wildfire conditions, the highest day/night ratios were for Zr (36.48), Cd (21.32), Fe (7.25), Mo (5.53), and Mn (5.31); in contrast, the largest reductions were for Hg (0.36), Pd (0.50), and Ti (0.58). Subsequent discussion based on PMF analysis reveals that many of these species enhanced in daytime are associated with anthropogenic activities, especially vehicular traffic (Adachi and Tainosho, 2004; Budai and Clement, 2018; Lin et al., 2015).

4.2 Sub- and Supermicrometer Mass Fractions

The average weight percentage of the combined 29 species in the submicrometer portion (as compared to all particle sizes) for all MOUDI sets was as follows: 41.2% ± 6.0% (NiCE wildfire), 37.8% ± 21.1% (FASE wildfire), 16.8% ± 7.7% (non-wildfire), 37.0% (day NiCE wildfire), 45.5% (night NiCE wildfire), 13.4% ± 7.1% (day NiCE non-wildfire), and 24.0% ± 1.2% (night NiCE non-wildfire). During non-fire conditions in both NiCE and FASE, the species with the highest weight percentage in the submicrometer range (> 80%) were V, As, and Mo. Species exhibiting the majority of their concentration in the supermicrometer range (> 80%) included Na, Co, Hg, Sr, and Mn. Influence from the two wildfires led to disparate size

distribution behavior. For instance, during the NiCE fire period, more species exhibited weight percentages greater than 80% in submicrometer stages (V, Ni, I, As, Y, Sn, Pb, Pt, Cd, Rh). In contrast, only one species exhibited more than 80% of its weight percentage in the supermicrometer stages (Hg). During the FASE fire period, only I exhibited submicrometer weight percentages above 80%, while several species exhibited more than 80% in the supermicrometer stages (Fe, Ba, Mn, Ni, Cr, Co, Pb, Cd).

4.3 Source Apportionment of Water-Soluble Fraction of Elements

Positive matrix factorization (PMF) modeling was conducted to help identify the major sources of the elements examined. Several PMF solutions were evaluated, ranging from two to ten source factors. The six-factor solution (Figure 4) was chosen for further analysis as the calculated ratio of $Q_{robust}/Q_{expected}$ (1.12) was close to the ideal value (1.00). In addition, the scaled residuals were normally distributed and between -3 and 3, suggesting that the model fit the data well. Based on both the characteristic species present in the results and knowledge of the sampling environment, source names were assigned to the six factors as follows with their total weight percentage contribution to total PM from the MOUDI sets (D_p > 0.056 μm) also shown: Crustal Emissions (3.9%), Secondary Aerosol (24.4%), Biomass Burning (13.1%), Waste Facilities (8.7%), Vehicular Emissions (4.4%), and Marine Emissions (45.4%). We note that Vehicular Emissions is a category that includes all aspects of emissions from vehicles including exhaust, tire and brake wear, and resuspended crustal material. Also, Secondary Aerosol is a category with a signature of secondarily produced species, but that does not preclude the contribution of secondary species in the other factors.

Table 2 summarizes how much each PMF factor contributes to the day and night periods during NiCE, for both wildfire periods, and for all non-fire periods. The relative concentrations

associated with each source indicate that Marine Emissions were the most important on a mass basis except for the FASE period with Biomass Burning being most influential. Each of the six PMF source factors is discussed in greater detail in the following section, with interrelationships between all 29 elements summarized in Table S5 in the form of a correlation matrix based on total mass concentrations from each of the 17 MOUDI sets.

4.3.1 Crustal Emissions

The first PMF factor accounted for 3.9% of the total PM mass concentration, and is characteristic of crustal emissions as the species it contributed the most to in terms of mass percentage are typically associated with dust and sand (Behera et al., 2015; Darzi and Winchester, 1982; McKendry et al., 2001; Moyers et al., 1977; Prabhakar et al., 2014): Fe (73.3%), Al (41.9%), Ti (32.9%), Pt (28.9%), and Mn (14.8%). In addition to long-range transport of dust, there are local emissions of dust due to wind-driven emissions and road dust associated with vehicular traffic. In particular, there is blowing sand within a few km of the sample site due to sand dunes by the coastline, in addition to the emissions from the nearby Las Animas Concrete Plant and the Cemex Lapis Sand Plant (Figure 1). The dominant components of sand from the latter facility that were among the 29 elements examined included Al, with trace amounts of Fe, Ti, Na, and K (https://www.cemexusa.com).

The mass concentrations associated with the Crustal Emissions source factor were 20 times larger during daytime as compared to nighttime (Table 2). This may be partly due to favorable daytime meteorological conditions, specifically higher wind speeds and also onshore wind coming from the coastline where there is abundant sand and numerous point sources such as the Cemex Lapis Sand Plant (Table 1). There is also the likely possibility of greater anthropogenic influence during the daytime. Crustal enrichment factor (EF) analysis was

conducted for the elements included in the PMF analysis to determine the degree of influence from non-crustal sources to the concentrations of various elements:

$$EF = \left[C_{n(PMF,crustal)}/C_{ref(PMF,crustal)}\right]/\left[C_{n(baseline)}/C_{ref(baseline)}\right] \qquad \text{(Equation 2)}$$

where C_n and C_{ref} represent, respectively, the concentrations of element *n* and a reference species (Al) assumed to have minimal anthropogenic sources (Chester et al., 2000; Liu et al., 2002; Zhang et al., 2015). The top ratio in Equation 2 employs concentrations for individual elements predicted by the PMF model for the crustal emissions source factor, while the bottom ratio applies values from Earth's crust (Goldschmidt, 1937). Values of EF >10 generally indicate that there is a non-crustal source such as from various anthropogenic activities (Acciai et al., 2017; Liu et al., 2002; Zhang et al., 2015).

Crustal EF results are summarized for all the PMF elements in Table S6. Nine species exhibited EFs < 10, ranging from 8.5 to 0 (Cu > Mn > Fe > Rb > Sr > Ti > Zr > V/Ag), suggestive of a close association with Earth's crust. This list of elements includes most of those pronounced in important for the Crustal Emissions source factor (Figure 4). In contrast, eight species exhibited EFs > 10 (Pt > I > Cd > Na > As > Zn > K > Ni) with the highest values for Cd (264.7), I (9729.3), and Pt (23896.4). The Crustal Emissions factor contributed significantly to Pt, which has previously been linked to dust (Wolbach et al., 2018); however, it is also associated with vehicular engines and catalytic converters (Diong et al., 2016; Moldovan et al., 2002; Palacios et al., 2000; Zhang et al., 2019). Pt did not exhibit many significant correlations with other elements (Table S5), and only had positive associations with MSA (r = 0.62) and Rh (r = 0.79). Therefore, its exact non-crustal sources are not fully clear based on this dataset;

however, it was a prominent species in biomass burning periods as will be discussed subsequently.

4.3.2 Secondary Aerosol

The second PMF factor (24.4% of total mass), referred to as Secondary Aerosol, has the chemical signature of secondary aerosol production owing to its significant contributions to the following species known to be linked with gas-to-particle conversion processes: NO_3^- (37.6%), nss SO_4^{2-} (40.4%), NH_4^+ (52.3%), oxalate (43.7%), and MSA (25.5%). More specifically, SO_2 and NH_3 can produce nss SO_4^{2-} and NH_4^+, respectively (Popovicheva et al., 2014; Reid et al., 1998). Nitrogen oxides (NO_x) can be photochemically oxidized to produce HNO_3, which can undergo acid-base chemistry to produce nitrate salts or partition to coarse particles such as dust and sea salt in the form of NO_3^- (Lee et al., 2008; Pakkanen et al., 1996; Ruellan et al., 1999). MSA is mainly produced by the oxidation of ocean-emitted dimethylsulfide (DMS) (Mihalopoulos et al., 1992), while oxalate can be produced secondarily via aqueous-phase processing, especially in clouds (Sorooshian et al., 2006; Wonaschuetz et al., 2012) As photochemistry is important for secondary aerosol production, the ratio of daytime to nighttime concentrations of this source factor (27.2) was the second highest of the six source factors.

While the water-soluble ions were convenient for the PMF analysis to identify the Secondary Aerosol factor, the elements most enhanced in this factor were not secondarily produced but most likely co-emitted with the precursor gases for the water-soluble IC species. This source factor contributed most to the mass concentrations of the following elements: Zn (59.9%), Rb (54.8%), As (43.4%), V (27.3%), and Cu (27.0%). Many of these species exhibited statistically significant correlations between each other and the secondarily produced IC ions identified above when considering their total mass concentrations between the 17 MOUDI sets

(Table S5). Notably, V and As were significantly correlated with not just each other (r = 0.67), but with NO_3^-, nss SO_4^{2-}, and NH_4^+ ($r \geq 0.49$). These elements stem from a variety of types of sources including shipping, smelting, vehicular emissions, and combustion (Moyers et al., 1977; Nriagu, 1989a; Prabhakar et al., 2014). These results are important in pointing to how a blend of elements, many with anthropogenic origins, can become associated with secondarily produced species in the region.

4.3.3 Biomass Burning

The third PMF factor, Biomass Burning (13.1% of total mass), exhibits enhanced contributions to the following species known to be linked with biofuel combustion emissions (Allen and Miguel, 1995; Artaxo et al., 1993; Currie et al., 1994; Echalar et al., 1995; Fine et al., 2001; Gao et al., 2003; Hays et al., 2002; Li et al., 2003; Meng et al., 2013; Pósfai et al., 2003; Reid et al., 2005; Ryu et al., 2004; Schlosser et al., 2017; Sorooshian et al., 2015a; Wasson et al., 2005; Zhang et al., 2017): nss SO_4^{2-} (18.1%), oxalate (29.9%), MSA (28.1%), K (23.8%), Cu (26.5%), As (15.4%), and Rb (25.8%). Interestingly, the most significant contribution of this factor to any species was for Pt (55.8%). Although Pt was associated with the Crustal Emissions factor and crustal material is known to become entrained in fire plumes in the study region (Maudlin et al., 2015), its high crustal EF (Table S6) and lack of correlation with other major crustal species points to its source being somehow linked to biofuel combustion.

This source factor contributed most strongly to the MOUDI sets collected during the Soberanes Fire overlapping with the FASE campaign (5.78 μg m^{-3}; 53.9% contribution), in contrast to a much lower contribution to the NiCE fire period (0.29 μg m^{-3}; 4.6%). Expectedly, this factor contributed relatively less during non-fire periods (2.41 μg m^{-3}; 5.1%). An explanation for why this source profile was much more prominent for one of the two wildfire periods was

that the FASE fire was much closer to the sample site. It is unclear how influential, if at all, the differences in the burnt level of the soils and length of time since the beginning of the fires (Campos et al., 2016) during FASE and NiCE were in explaining the differences in Table 2.

4.3.4 Waste Facilities

The unique feature of the fourth PMF factor (8.7% of total mass) was the overwhelming influence on the concentrations of Ag (94.7%) and Cd (90.2%). Although not as dramatic as for the latter two species, there were also significant contributions to Al (47.5%) and Ni (55.5%). Silver was highly correlated (r) with these species (Cd = 0.98, Ni = 0.84, Al = 0.58) and others not included in the PMF analysis (Pb = 0.80). These species have been linked to electronics and waste (Fujimori et al., 2012). For example, Ni, Cd, and silver oxide are materials used for manufacturing batteries (Eckelman and Graedel, 2007; Vaisanen et al., 2002), Pb is used for circuit board production (Leung et al., 2008), and Al is a key constituent of beverage containers such as soda cans that end up in waste facilities. The sampling site is surrounded by at least two major waste and recycling facilities (Figure 1), which presumably contributed to the emissions of these elements. For example, a variety of waste products are accepted for recycling at the Monterey Regional Waste Management District including appliances, cardboard, bottles, electronic waste (e-waste; e.g., cellular phones, televisions), household batteries, vehicular batteries, and mercury-containing items (www.mrwmd.org).

Mass concentrations from this source factor during the day amounted to 70% of those at nighttime (Table 2), reflective of fairly similar contributions between the two periods as compared to most of the other PMF source factors. Although Marine Emissions and Secondary Aerosol factors dominated total PM mass concentrations during non-fire periods (combined 85.2%), the Waste Facilities factor accounted for (3.28 μg m^{-3}; 6.9%), suggestive of a fairly

important role as compared to other sources in the study region during background conditions without fires.

4.3.5 Vehicular Emissions

The fifth PMF source factor (4.4% of total mass) was a significant contributor to Zr (73.5%) and Zn (26.1%), both of which have previously been linked to Vehicular Emissions (Adachi and Tainosho, 2004; Behera et al., 2015; Birmili et al., 2006). Other components influenced by this source profile included Fe, Sr, V, and Mn. Zirconium was best correlated with Zn ($r = 0.71$), V ($r = 0.69$), Mn ($r = 0.79$), and Y ($r = 0.83$); Zn was also best related to Y ($r = 0.78$), V ($r = 0.72$), and Mn ($r = 0.63$). The strong connection of Zr and Zn to these other elements provides additional support for attributing this source factor to Vehicular Emissions; V is associated with fossil fuel combustion (e.g., Nriagu, 1989), Y is a component in street dust (Adachi and Tainosho, 2004; de Miguel et al., 1997), and Mn is associated with tires, brakes, vehicle catalysts, and fuel combustion (Rocha and Corrêa, 2018; Sanderson et al., 2014). Iron and Sr were also influenced by this PMF factor, consistent with their presence in gasoline, lubricant oil, vehicular catalysts, brakes, and street dust (Sanderson et al., 2014). Of note is the use of a portion of the Marina Municipal Airport runway as a site for vehicle training (such as with the police force), with the marks of the tires visually obvious from aerial imagery as shown in Figure S1.

This source factor was responsible for the highest ratio of daytime versus nighttime concentrations (31.3) owing to more vehicular activity during the daytime. However, it was a relatively minor contributor to total PM mass concentrations during the entire study period and during non-fire periods (0.81 $\mu g\ m^{-3}$; 1.7%)

4.3.6 Marine Emissions

The final and most influential source profile on a mass basis, accounting for 45.4% of total mass, was linked to Marine Emissions. This factor contributed the most to the following major components of sea salt: Na (56.5%) and Cl^- (73.6%). Although a more minor contributor to sea salt, I was strongly influenced by this source factor (79.7%) most likely owing to its documented source from marine biogenic emissions (O'Dowd et al., 2002). A number of water-soluble IC species used in the PMF analysis have known contributions from marine sources and help support this source assignment: NO_3^- (45.0%), is linked to HNO_3 partitioning to the coarse salt particles (Pakkanen et al., 1996); MSA (12.7%) stems largely from ocean-emitted DMS; nss SO_4^{2-} (26.0%) is linked to secondary production from DMS and also SO_2 emitted from shipping along the coastline (e.g., Coggon et al., 2012); and NH_4^+ is linked to some combination of marine biota emissions and shipping (Johnson et al., 2007; Matthias et al., 2010).

As Cl^- and Na were the more dominant components of this PMF source profile based on their mass concentration contributions to sea salt, it was expected that they were best correlated with each other among the 29 elements studied (r = 0.80) (Table S5). Other species they were correlated with, including those not in the PMF analysis, had the following correlation coefficients with Na: I (r = 0.73), Co (r = 0.78), Cs (r = 0.66), Sr (r = 0.66), Cu (r = 0.56), Hg (r = 0.52), and Mn (r = 0.51). All of these species have diverse sources in the marine environment, including marine sediments (McLaren et al., 1981), marine organisms, and sea water (Burton and Price, 1990; Fitzgerald et al., 2007; Weiss-Penzias et al., 2018). Aside from direct marine sources, these species have continental and anthropogenic sources (Malm and Sisler, 2000; Nriagu, 1989b) and could presumably have mixed with sea salt during transport to the sampling site. The concentration ratio of Marine Emissions between daytime versus nighttime periods was

exactly 1.0. This source contributed 52.4% to the total mass concentration during non-fire periods, 41.7% during the NiCE fire, and 16.0% during the FASE fire.

4.4 Mass Size Distributions

The mass size distributions of the 29 elements provide insight into the mixing state of aerosol particles and emissions sources to validate PMF source assignments. Furthermore, the size distributions highlight how influential each element can be to various effects (e.g., respiratory deposition, CCN activity, interaction with solar radiation) that are sensitive to particle size. The size distribution profiles for 12 selected elements are shown in Figure 5, while the results for the other 17 elements are summarized in Figure S2. Distributions are reported separately for non-fire conditions (NiCE and FASE combined), the NiCE fire period, and the FASE fire period. Major differences were not observed when comparing day and night conditions during NiCE. In general, elements exhibited concentration peaks in the following four diameter ranges: 0.1-0.18 μm, 0.32-0.56 μm, 1.0-1.8 μm, and 3.2-5.6 μm.

The characteristic size for the dominant Marine Emissions constituents (Na, K) was between 1.8-5.6 μm, with peaks either in the range of 1.8-3.2 μm or 3.2-5.6 μm depending on which of the three conditions existed (i.e., non-fire, NiCE fire, FASE fire). Two other constituents in the Marine Emissions PMF source profile with lower concentrations, Sr and Mn, also exhibited concentration peaks between 1.8-5.6 μm. Of these four species, K exhibited a second concentration peak between 0.32-0.56 μm that was either comparable or even larger than the supermicrometer mode, with the dominant source contributing to the smaller peak being biomass burning regardless of the fire period examined. Depending on the fire, other species exhibited an enhanced concentration peak in the submicrometer mode, such as Na (0.32-0.56 μm) during NiCE and Rb (0.18-0.32 μm) during FASE. This is presumably due to the

differences in either the fire conditions (e.g., fuel type) or inclusion of other aerosol types, such as soil, with the fire plumes.

The dominant constituents of the Crustal Emissions PMF source profile (Fe, Al, Ti) exhibited concentration peaks between 1.8-5.6 μm, which is similar to the Marine Emissions constituents. Differences existed depending on the air type category examined, with peaks shifted to slightly smaller sizes during the FASE fire (1.8-3.2 μm) as compared to the NiCE fire (3.2-5.6 μm) for Al and Ti. Iron exhibited two significant concentration peaks between 1-1.8 μm and 5.6-10 μm during the FASE fire, while during the NiCE fire its concentration peaked between 0.32-0.56 μm and 3.2-5.6 μm. All three of these crustal species exhibited concentration peaks in the submicrometer mode, although usually the more dominant mode by mass was in the supermicrometer range. Interestingly, Pt exhibited a prominent concentration peak between 1.8-3.2 μm during the FASE fire, which matches the peaks of Al and Ti; however, its high crustal EF value points to influence from a non-crustal source, which was already suggested to be biofuel combustion. In support of this, Pt exhibited a submicrometer peak between 0.18-0.32 μm, which overlaps with the common biomass burning tracer species K.

Most of the elements prominent in the Secondary Aerosol factor (Rb, As, V, Cu) exhibited concentration peaks between 0.32-0.56 μm, which is consistent with the typical size range of secondarily produced species in the study region (Maudlin et al., 2015).

During the FASE fire, several species similarly exhibited a pronounced concentration between 1.8-3.2 μm including Al, Mn, Ti, and Pt. These species are associated with crustal matter, confirming that there was influence from soil during the FASE fire. Lead was also enhanced in this size range during the FASE fire, which is consistent with past work attributing Pb to biomass combustion for some specific fuel types, such as softwood (Sommersacher et al.,

2016) in the study region. Some elements exhibited clear differences in their mass size distributions between the two fires, including either different concentration peak size ranges (Zn, Zr, Pt), or similar concentration peak size ranges but significant differences in mass concentrations at the peak (V: 0.32-0.56 μm). Vanadium's profile indicates how influential the source of the wildfire was as its concentration in the NiCE fire period was significantly higher than that during the FASE fire (0.65 ± 0.24 ng m^{-3} versus 0.04 ± 0.02 ng m^{-3}). This difference is possibly linked to the enrichment of V in the NiCE biofuels compared to those in the Soberanes Fire during FASE; any variations in the soils around the two fire sources is an unlikely explanation, as this would have influenced concentrations in the supermicrometer range.

The key tracer elements linked to the Waste Facilities PMF source factor (Ag, Cd, Ni, Al) similarly had pronounced concentration peaks between 3.2-5.6 μm, which were only obvious during non-fire periods. A number of other anthropogenic pollutants that were included in the PMF analysis (Pt, Ti, Rb, Na, K, Cu, Mn, Ni) and some that were not included in the PMF analysis (Co, Pb, Y, Sn, Cs) exhibited similar concentration modes in non-fire conditions.

The Vehicular Emissions source factor contributed the most to Zr (69.2%) among all elements examined. During the NiCE fire, Zr had an enhanced concentration peak between 3.2-5.6 μm, whereas during the FASE fire and non-fire conditions it exhibited a bimodal concentration profile with peaks between 1.8-3.2 μm and 0.18-0.56 μm. The mass size distributions of other species correlated with Zr (Y, Mn, Zn, V) varied to some extent, but mostly exhibited bimodal concentration profiles with peaks between 0.18-1 μm and 1-10 μm.

5. Conclusions

The present study investigated sized-resolved composition measurements for the water-soluble fraction of 29 particulate elements collected during two summertime campaigns in 2013

(NiCE) and 2016 (FASE) at a central California coastal site. Element concentrations were examined in different environmental conditions including during daytime and nighttime, and with and without the influence of wildfires. The most dominant element measured was Na, owing to the importance of sea salt in the study region. The mass size distributions of Na and other constituents of sea salt (K) and crustal matter (Fe, Al, Ti) revealed major concentration peaks in the supermicrometer size range (1.8-5.6 μm). The full suite of elements exhibited widely ranging mass size distributions, highlighting the complexity of sources and sinks in a fixed region with diverse sources.

To aid in the complexity of the mass size distributions of a large set of elements, PMF modeling was used to isolate six characteristic PM sources: (i) Crustal Emissions (3.9% of total mass), (ii) Secondary Aerosol (24.4%), (iii) Biomass Burning (13.1%), (iv) Waste Facilities (8.7%), (v) Vehicular Emissions (4.4%), and (vi) Marine Emissions (45.4%). Diurnal measurements during the NiCE campaign revealed that three of these sources were especially more dominant during the daytime as compared to nighttime: Crustal Emissions, Secondary Aerosol, and Vehicular Emissions. The Marine Emissions factor exhibited nearly identical concentrations between daytime and nighttime.

When comparing two separate wildfires, several similarities existed in terms of species that were enhanced (MSA, nss SO_4^{2-}, oxalate, K, Cu, As, Rb), but there were key differences. During FASE, Pt exhibited significantly higher levels in contrast to reduced influence from NO_3^-, NH_4^+, I, Zn, V, and Ti. These differences point to the importance of the transport time of fire plumes to sampling sites, fuel type, and flame condition.

Crustal enrichment factor (EF) analysis was used to identify what species were better traced to Earth's crust versus having non-crustal sources. Species commonly associated with

crustal matter (Ti, Fe, Mn) expectedly had low EFs (≤ 2.5) in contrast to several that had values exceeding 10, indicating non-crustal sources such as sea salt (e.g., Na, K), marine biota emissions (I), and anthropogenic emissions (Ni, Zn, As, Cd).

As crustal and marine emissions stem from the natural environment of the study region, the main area of focus for improving air quality and public health should center on mitigation of the impacts of wildfires. Several point sources of pollution exist in addition to vehicles that influence the ambient PM budget of the region, but the PMF results suggest that they contributed less than wildfires for the periods of time that were investigated. Results of this study have broad implications for other regions impacted by similar sources and by wildfires as particle size impacts the effects of particles on public health. For example, As was highly concentrated in the submicrometer size range, particles within which can penetrate deeper into the respiratory system and produce harmful health effects. Differences in fuel type impacted the amount of harmful species such as Pb in the submicrometer stages. More specifically, Pb exhibited a weight percentage of 97% in the submicrometer range during the NiCE fire period versus 13% during the FASE fire period. While species associated with marine emissions dominated the mass concentration profile of the study region, the less abundant elements still have important effects and uses as tracers of sources, some of which were highlighted in this study.

Acknowledgements

This work was funded by Office of Naval Research grants N00014-10-1-0811 and N00014-16-1-2567. We gratefully acknowledge the support of Dr. Shane Snyder's Laboratory at the University of Arizona, who is supported in part by Agilent Technologies. A. B. MacDonald acknowledges support from the Mexican National Council for Science and Technology (CONACyT). R.A. Braun acknowledges support from the ARCS Foundation.

References

Acciai, C., Zhang, Z., Wang, F., Zhong, Z., Lonati, G., 2017. Characteristics and source Analysis of trace Elements in PM2. 5 in the Urban Atmosphere of Wuhan in Spring. Aerosol and Air Quality Research 17, 2224-2234.

Adachi, K., Tainosho, Y., 2004. Characterization of heavy metal particles embedded in tire dust. Environ Int 30, 1009-1017.

Alexander, B., Park, R.J., Jacob, D.J., Gong, S., 2009. Transition metal-catalyzed oxidation of atmospheric sulfur: Global implications for the sulfur budget. Journal of Geophysical Research: Atmospheres 114.

Alleman, L.Y., Lamaison, L., Perdrix, E., Robache, A., Galloo, J.-C., 2010. PM10 metal concentrations and source identification using positive matrix factorization and wind sectoring in a French industrial zone. Atmospheric Research 96, 612-625.

Allen, A.G., Miguel, A.H., 1995. Biomass burning in the Amazon: Characterization of the ionic component of aerosols generated from flaming and smoldering rainforest and savannah. Environ Sci Technol 29, 486-493.

Artaxo, P., Gerab, F., Rabello, M.L., 1993. Elemental composition of aerosol particles from two atmospheric monitoring stations in the Amazon Basin. Nuclear Instruments and Methods in Physics Research Section B: Beam Interactions with Materials and Atoms 75, 277-281.

Artaxo, P., Gerab, F., Yamasoe, M.A., Martins, J.V., 1994. Fine mode aerosol composition at three long-term atmospheric monitoring sites in the Amazon Basin. Journal of Geophysical Research: Atmospheres 99, 22857-22868.

Avila, A., Alarcon, M., Queralt, I., 1998. The chemical composition of dust transported in red rains—its contribution to the biogeochemical cycle of a holm oak forest in Catalonia (Spain). Atmos Environ 32, 179-191.

Baghurst, P.A., McMichael, A.J., Wigg, N.R., Vimpani, G.V., Robertson, E.F., Roberts, R.J., Tong, S.-L., 1992. Environmental exposure to lead and children's intelligence at the age of seven years: the Port Pirie Cohort Study. New Engl J Med 327, 1279-1284.

Becagli, S., Sferlazzo, D.M., Pace, G., di Sarra, A., Bommarito, C., Calzolai, G., Ghedini, C., Lucarelli, F., Meloni, D., Monteleone, F., Severi, M., Traversi, R., Udisti, R., 2012. Evidence for heavy fuel oil combustion aerosols from chemical analyses at the island of Lampedusa: a possible large role of ships emissions in the Mediterranean. Atmos Chem Phys 12, 3479-3492.

Begum, B.A., Biswas, S.K., Hopke, P.K., 2007. Source apportionment of air particulate matter by chemical mass balance (CMB) and comparison with positive matrix factorization (PMF) model. Aerosol and Air Quality Research 7, 446-468.

Behera, S.N., Betha, R., Huang, X., Balasubramanian, R., 2015. Characterization and estimation of human airway deposition of size-resolved particulate-bound trace elements during a recent haze episode in Southeast Asia. Environ Sci Pollut R 22, 4265-4280.

Betha, R., Pradani, M., Lestari, P., Joshi, U.M., Reid, J.S., Balasubramanian, R., 2013. Chemical speciation of trace metals emitted from Indonesian peat fires for health risk assessment. Atmos Res 122, 571-578.

Birmili, W., Allen, A.G., Bary, F., Harrison, R.M., 2006. Trace metal concentrations and water solubility in size-fractionated atmospheric particles and influence of road traffic. Environ Sci Technol 40, 1144-1153.

Blanco, A., De Tomasi, F., Filippo, E., Manno, D., Perrone, M.R., Serra, A., Tafuro, A.M., Tepore, A., 2003. Characterization of African dust over southern Italy. Atmos Chem Phys 3, 2147-2159.

Braun, R.A., Dadashazar, H., MacDonald, A.B., Aldhaif, A.M., Maudlin, L.C., Crosbie, E., Aghdam, M.A., Hossein Mardi, A., Sorooshian, A., 2017. Impact of wildfire emissions on chloride and bromide depletion in marine aerosol particles. Environ Sci Technol 51, 9013-9021.

Brown, S.G., Eberly, S., Paatero, P., Norris, G.A., 2015. Methods for estimating uncertainty in PMF solutions: Examples with ambient air and water quality data and guidance on reporting PMF results. Sci Total Environ 518, 626-635.

Bruland, K.W., Rue, E.L., Smith, G.J., 2001. Iron and macronutrients in California coastal upwelling regimes: Implications for diatom blooms. Limnol Oceanogr 46, 1661-1674.

Budai, P., Clement, A., 2018. Spatial distribution patterns of four traffic-emitted heavy metals in urban road dust and the resuspension of brake-emitted particles: Findings of a field study. Transportation Research Part D: Transport and Environment 62, 179-185.

Burton, J.H., Price, T.D., 1990. The ratio of barium to strontium as a paleodietary indicator of consumption of marine resources. Journal of Archaeological Science 17, 547-557.

Campos, I., Abrantes, N., Keizer, J.J., Vale, C., Pereira, P., 2016. Major and trace elements in soils and ashes of eucalypt and pine forest plantations in Portugal following a wildfire. Sci Total Environ 572, 1363-1376.

Capone, D.G., Hutchins, D.A., 2013. Microbial biogeochemistry of coastal upwelling regimes in a changing ocean. Nat Geosci 6, 711-717.

Cena, L.G., Chisholm, W.P., Keane, M.J., Cumpston, A., Chen, B.T., 2014. Size Distribution and Estimated Respiratory Deposition of Total Chromium, Hexavalent Chromium, Manganese, and Nickel in Gas Metal Arc Welding Fume Aerosols. Aerosol Sci Tech 48, 1254-1263.

Chester, R., Nimmo, M., Fones, G., Keyse, S., Zhang, Z., 2000. Trace metal chemistry of particulate aerosols from the UK mainland coastal rim of the NE Irish sea. Atmos Environ 34, 949-958.

Currie, L., Klouda, G., Klinedinst, D., Sheffield, A., Jull, A., Donahue, D., Connolly, M., 1994. Fossil-and bio-mass combustion: C-14 for source identification, chemical tracer development, and model validation. Nuclear Instruments and Methods in Physics Research Section B: Beam Interactions with Materials and Atoms 92, 404-409.

Dadashazar, H., Ma, L., Sorooshian, A., 2019. Sources of pollution and interrelationships between aerosol and precipitation chemistry at a central California site. Sci Total Environ 651, Part 2, 2019, 1776-1787. https://doi.org/10.1016/j.scitotenv.2018.10.086.

Darzi, M., Winchester, J.W., 1982. Aerosol characteristics at Mauna Loa Observatory, Hawaii, after east Asian dust storm episodes. Journal of Geophysical Research: Oceans 87, 1251-1258.

de Miguel, E., Llamas, J.F., Chacón, E., Berg, T., Larssen, S., Røyset, O., Vadset, M., 1997. Origin and patterns of distribution of trace elements in street dust: unleaded petrol and urban lead. Atmos Environ 31, 2733-2740.

Diong, H.T., Das, R., Khezri, B., Srivastava, B., Wang, X., Sikdar, P.K., Webster, R.D., 2016. Anthropogenic platinum group element (Pt, Pd, Rh) concentrations in PM 10 and PM 2.5 from Kolkata, India. SpringerPlus 5, 1242.

Duce, R., Liss, P., Merrill, J., Atlas, E., Buat-Menard, P., Hicks, B., Miller, J., Prospero, J., Arimoto, R., Church, T., 1991. The atmospheric input of trace species to the world ocean. Global biogeochemical cycles 5, 193-259.

Echalar, F., Gaudichet, A., Cachier, H., Artaxo, P., 1995. Aerosol emissions by tropical forest and savanna biomass burning: characteristic trace elements and fluxes. Geophys Res Lett 22, 3039-3042.

Eckelman, M.J., Graedel, T., 2007. Silver emissions and their environmental impacts: a multilevel assessment. Environ Sci Technol 41, 6283-6289.

Fang, T., Guo, H., Verma, V., Peltier, R., Weber, R., 2015. PM 2.5 water-soluble elements in the southeastern United States: automated analytical method development, spatiotemporal distributions, source apportionment, and implications for heath studies. Atmos Chem Phys 15, 11667-11682.

Fine, P.M., Cass, G.R., Simoneit, B.R., 2001. Chemical characterization of fine particle emissions from fireplace combustion of woods grown in the northeastern United States. Environ Sci Technol 35, 2665-2675.

Fitzgerald, W.F., Lamborg, C.H., Hammerschmidt, C.R., 2007. Marine biogeochemical cycling of mercury. Chem Rev 107, 641-662.

Font, A., de Hoogh, K., Leal-Sanchez, M., Ashworth, D.C., Brown, R.J.C., Hansell, A.L., Fuller, G.W., 2015. Using metal ratios to detect emissions from municipal waste incinerators in ambient air pollution data. Atmos Environ 113, 177-186.

Fujimori, T., Takigami, H., Agusa, T., Eguchi, A., Bekki, K., Yoshida, A., Terazono, A., Ballesteros Jr, F.C., 2012. Impact of metals in surface matrices from formal and informal electronic-waste recycling around Metro Manila, the Philippines, and intra-Asian comparison. Journal of hazardous materials 221, 139-146.

Furukawa, T., Takahashi, Y., 2011. Oxalate metal complexes in aerosol particles: implications for the hygroscopicity of oxalate-containing particles. Atmos Chem Phys 11, 4289-4301.

Gao, S., Hegg, D.A., Hobbs, P.V., Kirchstetter, T.W., Magi, B.I., Sadilek, M., 2003. Water-soluble organic components in aerosols associated with savanna fires in southern Africa: Identification, evolution, and distribution. Journal of Geophysical Research: Atmospheres 108.

Gaudichet, A., Echalar, F., Chatenet, B., Quisefit, J., Malingre, G., Cachier, H., Buat-Menard, P., Artaxo, P., Maenhaut, W., 1995. Trace elements in tropical African savanna biomass burning aerosols. Journal of Atmospheric Chemistry 22, 19-39.

Goldschmidt, V.M., 1937. The principles of distribution of chemical elements in minerals and rocks. The seventh Hugo Müller Lecture, delivered before the Chemical Society on March 17th, 1937. Journal of the Chemical Society (Resumed), 655-673.

Hays, M.D., Geron, C.D., Linna, K.J., Smith, N.D., Schauer, J.J., 2002. Speciation of gas-phase and fine particle emissions from burning of foliar fuels. Environ Sci Technol 36, 2281-2295.

Heal, M.R., Hibbs, L.R., Agius, R.M., Beverland, I.J., 2005. Total and water-soluble trace metal content of urban background PM10, PM2. 5 and black smoke in Edinburgh, UK. Atmos Environ 39, 1417-1430.

Horel, J., Splitt, M., Dunn, L., Pechmann, J., White, B., Ciliberti, C., Lazarus, S., Slemmer, J., Zaff, D., Burks, J., 2002. Mesowest: Cooperative mesonets in the western United States. Bulletin of the American Meteorological Society 83, 211-226.

Ito, A., 2011. Mega fire emissions in Siberia: potential supply of bioavailable iron from forests to the ocean. Biogeosciences 8.

Ito, A., 2015. Atmospheric processing of combustion aerosols as a source of bioavailable iron. Environmental Science & Technology Letters 2, 70-75.

Ito, A., Shi, Z., 2016. Delivery of anthropogenic bioavailable iron from mineral dust and combustion aerosols to the ocean. Atmos Chem Phys 16, 85-99.

Jamali, M.K., Kazi, T.G., Arain, M.B., Affidi, H.I., Jalbani, N., Kandhro, G.A., Shah, A.Q., Baig, J.A., 2009. Speciation of heavy metals in untreated sewage sludge by using microwave assisted sequential extraction procedure. J Hazard Mater 163, 1157-1164.

Jiang, S.Y., Yang, F., Chan, K.L., Ning, Z., 2014. Water solubility of metals in coarse PM and PM2. 5 in typical urban environment in Hong Kong. Atmospheric pollution research 5, 236-244.

Johnson, M., Sanders, R., Avgoustidi, V., Lucas, M., Brown, L., Hansell, D., Moore, M., Gibb, S., Liss, P., Jickells, T., 2007. Ammonium accumulation during a silicate-limited diatom bloom indicates the potential for ammonia emission events. Marine Chemistry 106, 63-75.

Kavouras, I.G., Nikolich, G., Etyemezian, V., DuBois, D.W., King, J., Shafer, D., 2012. In situ observations of soil minerals and organic matter in the early phases of prescribed fires. Journal of Geophysical Research: Atmospheres 117.

Kersten, M., Kriews, M., Förstner, U., 1991. Partitioning of trace metals released from polluted marine aerosols in coastal seawater. Marine Chemistry 36, 165-182.

Knaapen, A.M., Shi, T., Borm, P.J., Schins, R.P., 2002. Soluble metals as well as the insoluble particle fraction are involved in cellular DNA damage induced by particulate matter, Oxygen/Nitrogen Radicals: Cell Injury and Disease. Springer, pp. 317-326.

Lee, T., Yu, X.-Y., Ayres, B., Kreidenweis, S.M., Malm, W.C., Collett Jr, J.L., 2008. Observations of fine and coarse particle nitrate at several rural locations in the United States. Atmos Environ 42, 2720-2732.

Lestari, P., Mauliadi, Y.D., 2009. Source apportionment of particulate matter at urban mixed site in Indonesia using PMF. Atmos Environ 43, 1760-1770.

Leung, A.O., Duzgoren-Aydin, N.S., Cheung, K., Wong, M.H., 2008. Heavy metals concentrations of surface dust from e-waste recycling and its human health implications in southeast China. Environ Sci Technol 42, 2674-2680.

Li, J., Pósfai, M., Hobbs, P.V., Buseck, P.R., 2003. Individual aerosol particles from biomass burning in southern Africa: 2, Compositions and aging of inorganic particles. Journal of Geophysical Research: Atmospheres 108.

Li, N., Xia, T., Nel, A.E., 2008. The role of oxidative stress in ambient particulate matter-induced lung diseases and its implications in the toxicity of engineered nanoparticles. Free Radical Bio Med 44, 1689-1699.

Lin, Y.-C., Tsai, C.-J., Wu, Y.-C., Zhang, R., Chi, K.-H., Huang, Y.-T., Lin, S.-H., Hsu, S.-C., 2015. Characteristics of trace metals in traffic-derived particles in Hsuehshan Tunnel, Taiwan:

size distribution, potential source, and fingerprinting metal ratio. Atmos Chem Phys 15, 4117-4130.

Lindberg, S., Harriss, R., 1983. Water and acid soluble trace metals in atmospheric particles. Journal of Geophysical Research: Oceans 88, 5091-5100.

Liu, C., Zhang, J., Shen, Z., 2002. Spatial and temporal variability of trace metals in aerosol from the desert region of China and the Yellow Sea. Journal of Geophysical Research: Atmospheres 107, ACH 17-11-ACH 17-17.

Maenhaut, W., Salma, I., Cafmeyer, J., Annegarn, H.J., Andreae, M.O., 1996. Regional atmospheric aerosol composition and sources in the eastern Transvaal, South Africa, and impact of biomass burning. Journal of Geophysical Research: Atmospheres 101, 23631-23650.

Malm, W.C., Sisler, J.F., 2000. Spatial patterns of major aerosol species and selected heavy metals in the United States. Fuel processing technology 65, 473-501.

Mateos, A.C., Amarillo, A.C., Carreras, H.A., Gonzalez, C.M., 2018. Land use and air quality in urban environments: Human health risk assessment due to inhalation of airborne particles. Environ Res 161, 370-380.

Matthias, V., Bewersdorff, I., Aulinger, A., Quante, M., 2010. The contribution of ship emissions to air pollution in the North Sea regions. Environmental Pollution 158, 2241-2250.

Maudlin, L., Wang, Z., Jonsson, H., Sorooshian, A., 2015. Impact of wildfires on size-resolved aerosol composition at a coastal California site. Atmos Environ 119, 59-68.

McKendry, I., Hacker, J., Stull, R., Sakiyama, S., Mignacca, D., Reid, K., 2001. Long-range transport of Asian dust to the lower Fraser Valley, British Columbia, Canada. Journal of Geophysical Research: Atmospheres 106, 18361-18370.

McLaren, J., Berman, S., Boyko, V., Russell, D., 1981. Simultaneous determination of major, minor, and trace elements in marine sediments by inductively coupled plasma atomic emission spectrometry. Analytical Chemistry 53, 1802-1806.

Meng, J., Wang, G., Li, J., Cheng, C., Cao, J., 2013. Atmospheric oxalic acid and related secondary organic aerosols in Qinghai Lake, a continental background site in Tibet Plateau. Atmos Environ 79, 582-589.

Mihalopoulos, N., Nguyen, B., Boissard, C., Campin, J., Putaud, J., Belviso, S., Barnes, I., Becker, K., 1992. Field study of dimethylsulfide oxibation in the boundary layer: Variations of dimethylsulfide, methanesulfonic acid, sulfur dioxide, non-sea-salt sulfate and aitken nuclei at a coastal site. Journal of Atmospheric Chemistry 14, 459-477.

Miller, J., Miller, J.C., 2018. Statistics and chemometrics for analytical chemistry. Pearson Education.

Moldovan, M., Palacios, M., Gomez, M., Morrison, G., Rauch, S., McLeod, C., Ma, R., Caroli, S., Alimonti, A., Petrucci, F., 2002. Environmental risk of particulate and soluble platinum group elements released from gasoline and diesel engine catalytic converters. Sci Total Environ 296, 199-208.

Moyers, J., Ranweiler, L., Hopf, S., Korte, N., 1977. Evaluation of particulate trace species in southwest desert atmosphere. Environ Sci Technol 11, 789-795.

Mukhtar, A., Limbeck, A., 2013. Recent developments in assessment of bio-accessible trace metal fractions in airborne particulate matter: A review. Anal Chim Acta 774, 11-25.

Norris, G., Duvall, R., Brown, S., Bai, S., 2014. EPA Positive Matrix Factorization (PMF) 5.0 fundamentals and User Guide Prepared for the US Environmental Protection Agency Office of Research and Development, Washington, DC. Inc., Petaluma.

Nriagu, J.O., 1979. Global inventory of natural and anthropogenic emissions of trace metals to the atmosphere. Nature 279, 409.

Nriagu, J.O., 1989a. A Global Assessment of Natural Sources of Atmospheric Trace-Metals. Nature 338, 47-49.

Nriagu, J.O., 1989b. A global assessment of natural sources of atmospheric trace metals. Nature 338, 47.

O'Dowd, C.D., Jimenez, J.L., Bahreini, R., Flagan, R.C., Seinfeld, J.H., Hämeri, K., Pirjola, L., Kulmala, M., Jennings, S.G., Hoffmann, T., 2002. Marine aerosol formation from biogenic iodine emissions. Nature 417, 632.

Paatero, P., Tapper, U., 1994. Positive matrix factorization: A non-negative factor model with optimal utilization of error estimates of data values. Environmetrics 5, 111-126.

Pakkanen, T.A., Kerminen, V.-M., Hillamo, R.E., Màkinen, M., Màkelà, T., Virkkula, A., 1996. Distribution of nitrate over sea-salt and soil derived particles—Implications from a field study. Journal of Atmospheric Chemistry 24, 189-205.

Palacios, M., Gomez, M., Moldovan, M., Morrison, G., Rauch, S., McLeod, C., Ma, R., Laserna, J., Lucena, P., Caroli, S., 2000. Platinum-group elements: quantification in collected exhaust fumes and studies of catalyst surfaces. Sci Total Environ 257, 1-15.

Pehkonen, S.O., Siefert, R., Erel, Y., Webb, S., Hoffmann, M.R., 1993. Photoreduction of iron oxyhydroxides in the presence of important atmospheric organic compounds. Environ Sci Technol 27, 2056-2062.

Pietrogrande, M.C., Perrone, M.R., Manarini, F., Romano, S., Udisti, R., Becagli, S., 2018. PM 10 oxidative potential at a Central Mediterranean Site: Association with chemical composition and meteorological parameters. Atmos Environ.

Popovicheva, O., Kistler, M., Kireeva, E., Persiantseva, N., Timofeev, M., Kopeikin, V., Kasper-Giebl, A., 2014. Physicochemical characterization of smoke aerosol during large-scale wildfires: Extreme event of August 2010 in Moscow. Atmos Environ 96, 405-414.

Pósfai, M., Simonics, R., Li, J., Hobbs, P.V., Buseck, P.R., 2003. Individual aerosol particles from biomass burning in southern Africa: 1. Compositions and size distributions of carbonaceous particles. Journal of Geophysical Research: Atmospheres 108.

Prabhakar, G., Sorooshian, A., Toffol, E., Arellano, A.F., Betterton, E.A., 2014. Spatiotemporal distribution of airborne particulate metals and metalloids in a populated arid region. Atmos Environ 92, 339-347.

Reff, A., Eberly, S.I., Bhave, P.V., 2007. Receptor modeling of ambient particulate matter data using positive matrix factorization: Review of existing methods. J Air Waste Manage 57, 146-154.

Reid, J., Koppmann, R., Eck, T., Eleuterio, D., 2005. A review of biomass burning emissions part II: intensive physical properties of biomass burning particles. Atmos Chem Phys 5, 799-825.

Reid, J.S., Hobbs, P.V., Ferek, R.J., Blake, D.R., Martins, J.V., Dunlap, M.R., Liousse, C., 1998. Physical, chemical, and optical properties of regional hazes dominated by smoke in Brazil. Journal of Geophysical Research: Atmospheres 103, 32059-32080.

Rocha, L.D.S., Corrêa, S.M., 2018. Determination of size-segregated elements in diesel-biodiesel blend exhaust emissions. Environ Sci Pollut R, 1-9.

Ruellan, S., Cachier, H., Gaudichet, A., Masclet, P., Lacaux, J.P., 1999. Airborne aerosols over central Africa during the Experiment for Regional Sources and Sinks of Oxidants (EXPRESSO). Journal of Geophysical Research: Atmospheres 104, 30673-30690.

Ryu, S.Y., Kim, J.E., Zhuanshi, H., Kim, Y.J., Kang, G.U., 2004. Chemical composition of post-harvest biomass burning aerosols in Gwangju, Korea. J Air Waste Manage 54, 1124-1137.

Sahuquillo, A., Lopez-Sanchez, J.F., Rubio, R., Rauret, G., Thomas, R.P., Davidson, C.M., Ure, A.M., 1999. Use of a certified reference material for extractable trace metals to assess sources of uncertainty in the BCR three-stage sequential extraction procedure. Anal Chim Acta 382, 317-327.

Sanderson, P., Delgado-Saborit, J.M., Harrison, R.M., 2014. A review of chemical and physical characterisation of atmospheric metallic nanoparticles. Atmos Environ 94, 353-365.

Sarti, E., Pasti, L., Rossi, M., Ascanelli, M., Pagnoni, A., Trombini, M., Remelli, M., 2015. The composition of PM1 and PM2. 5 samples, metals and their water soluble fractions in the Bologna area (Italy). Atmospheric Pollution Research 6, 708-718.

Savoie, D., Prospero, J., 1980. Water-soluble potassium, calcium, and magnesium in the aerosols over the tropical North Atlantic. Journal of Geophysical Research: Oceans 85, 385-392.

Schlosser, J.S., Braun, R.A., Bradley, T., Dadashazar, H., MacDonald, A.B., Aldhaif, A.A., Aghdam, M.A., Mardi, A.H., Xian, P., Sorooshian, A., 2017. Analysis of aerosol composition data for western United States wildfires between 2005 and 2015: Dust emissions, chloride depletion, and most enhanced aerosol constituents. J Geophys Res-Atmos 122, 8951-8966.

Seinfeld, J.H., Pandis, S.N., 2016. Atmospheric chemistry and physics: from air pollution to climate change. John Wiley & Sons.

Singh, M., Jaques, P.A., Sioutas, C., 2002. Size distribution and diurnal characteristics of particle-bound metals in source and receptor sites of the Los Angeles Basin. Atmos Environ 36, 1675-1689.

Soltani, N., Keshavarzi, B., Moore, F., Sorooshian, A., Ahmadi, M.R., 2017. Distribution of potentially toxic elements (PTEs) in tailings, soils, and plants around Gol-E-Gohar iron mine, a case study in Iran. Environ Sci Pollut R 24, 18798-18816.

Sommersacher, P., Kienzl, N., Brunner, T., Obernberger, I., 2016. Simultaneous online determination of S, Cl, K, Na, Zn, and Pb release from a single particle during biomass combustion. Part 2: results from test runs with spruce and straw pellets. Energy & Fuels 30, 3428-3440.

Sorooshian, A., Crosbie, E., Maudlin, L.C., Youn, J.S., Wang, Z., Shingler, T., Ortega, A.M., Hersey, S., Woods, R.K., 2015a. Surface and airborne measurements of organosulfur and methanesulfonate over the western United States and coastal areas. Journal of Geophysical Research: Atmospheres 120, 8535-8548.

Sorooshian, A., Prabhakar, G., Jonsson, H., Woods, R.K., Flagan, R.C., Seinfeld, J.H., 2015b. On the presence of giant particles downwind of ships in the marine boundary layer. Geophys Res Lett 42, 2024-2030.

Sorooshian, A., Varutbangkul, V., Brechtel, F.J., Ervens, B., Feingold, G., Bahreini, R., Murphy, S.M., Holloway, J.S., Atlas, E.L., Buzorius, G., 2006. Oxalic acid in clear and cloudy atmospheres: Analysis of data from International Consortium for Atmospheric Research on Transport and Transformation 2004. Journal of Geophysical Research: Atmospheres 111.

Sorooshian, A., Wang, Z., Coggon, M.M., Jonsson, H.H., Ervens, B., 2013. Observations of sharp oxalate reductions in stratocumulus clouds at variable altitudes: Organic acid and metal measurements during the 2011 E-PEACE campaign. Environ Sci Technol 47, 7747-7756.

Strlic, M., Kolar, J., Selih, V.S., Kocar, D., Pihlar, B., 2003. A comparative study of several transition metals in Fenton-like reaction systems at circum-neutral pH. Acta Chim Slov 50, 619-632.

Sturtz, T.M., Schichtel, B.A., Larson, T.V., 2014. Coupling chemical transport model source attributions with positive matrix factorization: Application to two IMPROVE sites impacted by wildfires. Environ Sci Technol 48, 11389-11396.

Vaisanen, A., Suontamo, R., Silvonen, J., Rintala, J., 2002. Ultrasound-assisted extraction in the determination of arsenic, cadmium, copper, lead, and silver in contaminated soil samples by inductively coupled plasma atomic emission spectrometry. Anal Bioanal Chem 373, 93-97.

Valavanidis, A., Fiotakis, K., Vlachogianni, T., 2008. Airborne Particulate Matter and Human Health: Toxicological Assessment and Importance of Size and Composition of Particles for Oxidative Damage and Carcinogenic Mechanisms. J Environ Sci Heal C 26, 339-362.

Valiulis, D., Šakalys, J., Plauškaitė, K., 2008. Heavy metal penetration into the human respiratory tract in Vilnius. Lithuanian Journal of Physics 48.

Wang, Z., Sorooshian, A., Prabhakar, G., Coggon, M., Jonsson, H., 2014. Impact of emissions from shipping, land, and the ocean on stratocumulus cloud water elemental composition during the 2011 E-PEACE field campaign. Atmos Environ 89, 570-580.

Wasson, S.J., Linak, W.P., Gullett, B.K., King, C.J., Touati, A., Huggins, F.E., Chen, Y., Shah, N., Huffman, G.P., 2005. Emissions of chromium, copper, arsenic, and PCDDs/Fs from open burning of CCA-treated wood. Environ Sci Technol 39, 8865-8876.

Weiss-Penzias, P., Sorooshian, A., Coale, K., Heim, W., Crosbie, E., Dadashazar, H., MacDonald, A.B., Wang, Z., Jonsson, H., 2018. Aircraft Measurements of Total Mercury and Monomethyl Mercury in Summertime Marine Stratus Cloudwater from Coastal California, USA. Environ Sci Technol 52, 2527-2537.

Wolbach, W.S., Ballard, J.P., Mayewski, P.A., Parnell, A.C., Cahill, N., Adedeji, V., Bunch, T.E., Domínguez-Vázquez, G., Erlandson, J.M., Firestone, R.B., 2018. Extraordinary biomass-burning episode and impact winter triggered by the Younger Dryas cosmic impact~ 12,800 years ago. 2. Lake, marine, and terrestrial sediments. The Journal of Geology 126, 185-205.

Wonaschuetz, A., Sorooshian, A., Ervens, B., Chuang, P.Y., Feingold, G., Murphy, S.M., Gouw, J., Warneke, C., Jonsson, H.H., 2012. Aerosol and gas re-distribution by shallow cumulus clouds: An investigation using airborne measurements. Journal of Geophysical Research: Atmospheres 117.

Youn, J.-S., Crosbie, E., Maudlin, L., Wang, Z., Sorooshian, A., 2015. Dimethylamine as a major alkyl amine species in particles and cloud water: Observations in semi-arid and coastal regions. Atmos Environ 122, 250-258.

Youn, J.S., Csavina, J., Rine, K.P., Shingler, T., Taylor, M.P., Saez, A.E., Betterton, E.A., Sorooshian, A., 2016. Hygroscopic Properties and Respiratory System Deposition Behavior of Particulate Matter Emitted By Mining and Smelting Operations. Environ Sci Technol 50, 11706-11713.

Zhang, G., Lin, Q., Peng, L., Yang, Y., Fu, Y., Bi, X., Li, M., Chen, D., Chen, J., Cai, Z., 2017. Insight into the in-cloud formation of oxalate based on in situ measurement by single particle mass spectrometry. Atmos Chem Phys 17, 13891-13901.

Zhang, L., Wang, Y., Liu, Y., Li, Z., Li, X., 2019. Variation of platinum group elements (PGE) in airborne particulate matter (PM2. 5) in the Beijing urban area, China: A case study of the 2014 APEC summit. Atmos Environ.

Zhang, Y., Zhang, H.-H., Yang, G.-P., Liu, Q.-L., 2015. Chemical characteristics and source analysis of aerosol composition over the Bohai Sea and the Yellow Sea in Spring and Autumn. Journal of the Atmospheric Sciences 72, 3563-3573.

Zuo, Y., Hoigne, J., 1992. Formation of hydrogen peroxide and depletion of oxalic acid in atmospheric water by photolysis of iron (III)-oxalato complexes. Environ Sci Technol 26, 1014-1022.

Table 1. Summary of MOUDI sample set measurement details and associated average meteorological conditions during the NiCE (2013) and FASE (2016) campaigns. Sample sets are denoted by the campaign name (N for NiCE, F for FASE) and MOUDI set number; in addition, for NiCE sets, an extension is provided for whether the sample set was collected during daytime (D: 0600-2100 local time) or night time (N: 2100-0600 local time). RH = relative humidity; WS = wind speed; WD = wind direction; T = temperature.

Sample Set	Start Date	End Date	Fire/Non-Fire	Total Hours	Flow Rate (LPM)	RH (%)	WS ($m\ s^{-1}$)	WD (°)	T (°C)
N1-D	03-Jul-13	09-Jul-13	NF	93.8	27.6	75	3	244	16
N2-N	03-Jul-13	10-Jul-13	NF	63.0	26.4	87	1	176	14
N3-D	10-Jul-13	16-Jul-13	NF	104.5	27.6	78	3	253	15
N4-N	10-Jul-13	17-Jul-13	NF	63.0	26.4	88	1	210	13
N5-D	17-Jul-13	24-Jul-13	NF	102.5	27.6	82	3	259	15
N6-N	17-Jul-13	24-Jul-13	NF	63.0	26.4	93	1	226	13
N7-D	24-Jul-13	31-Jul-13	F	94.3	27.6	77	3	258	16
N8-N	24-Jul-13	31-Jul-13	F	63.0	26.4	89	1	211	14
N9-D	31-Jul-13	09-Aug-13	NF	131.0	27.6	79	3	253	15
N10-N	31-Jul-13	09-Aug-13	NF	81.0	26.4	89	2	219	14
F1	15-Jul-16	19-Jul-16	NF	94.0	28.6	82	3	213	14
F2	19-Jul-16	25-Jul-16	NF	138.9	28.6	76	3	225	15
F3	25-Jul-16	28-Jul-16	F	69.0	29.0	93	2	152	12
F4	28-Jul-16	01-Aug-16	F	96.7	28.9	81	3	312	15
F5	01-Aug-16	05-Aug-16	F	94.6	29.3	83	3	234	16
F6	05-Aug-16	09-Aug-16	F	95.5	29.1	83	3	235	14
F7	09-Aug-16	12-Aug-16	F	77.8	28.6	84	3	185	15

Table 2. Mass concentrations (μg m^{-3}) associated with each of the six PMF source factors for different subsets of time periods examined in this study: daytime, nighttime, NiCE and FASE wildfires, and all non-fire periods including day and night. The "Day/Night" column corresponds to the mass concentration ratio of day versus night periods. Values in parentheses signify the percentage contribution of each source factor to the time period referenced by the column header. These results are based on the water-soluble fraction of PM.

PMF Source Factor	Day	Night	Day/Night	NiCE Fire	FASE Fire	Non-Fire
Crustal Emissions	1.99 (9.6%)	0.10 (0.6%)	20.0	1.71 (27.3%)	0.38 (3.6%)	0.52 (1.1%)
Secondary Aerosol	2.53 (12.1%)	0.09 (0.5%)	27.2	0.00 (0.0%)	0.17 (1.6%)	15.57 (32.8%)
Biomass Burning	0.16 (0.8%)	1.53 (8.5%)	0.1	0.29 (4.6%)	5.78 (53.9%)	2.41 (5.1%)
Waste Facilities	2.07 (9.9%)	2.80 (15.7%)	0.7	1.66 (26.4%)	0.60 (5.6%)	3.28 (6.9%)
Vehicular Emissions	0.54 (2.6%)	0.02 (0.1%)	31.3	0.00 (0.0%)	2.08 (19.4%)	0.81 (1.7%)
Marine Emissions	13.52 (65.0%)	13.34 (74.6%)	1.0	2.62 (41.7%)	1.71 (16.0%)	24.91 (52.4%)

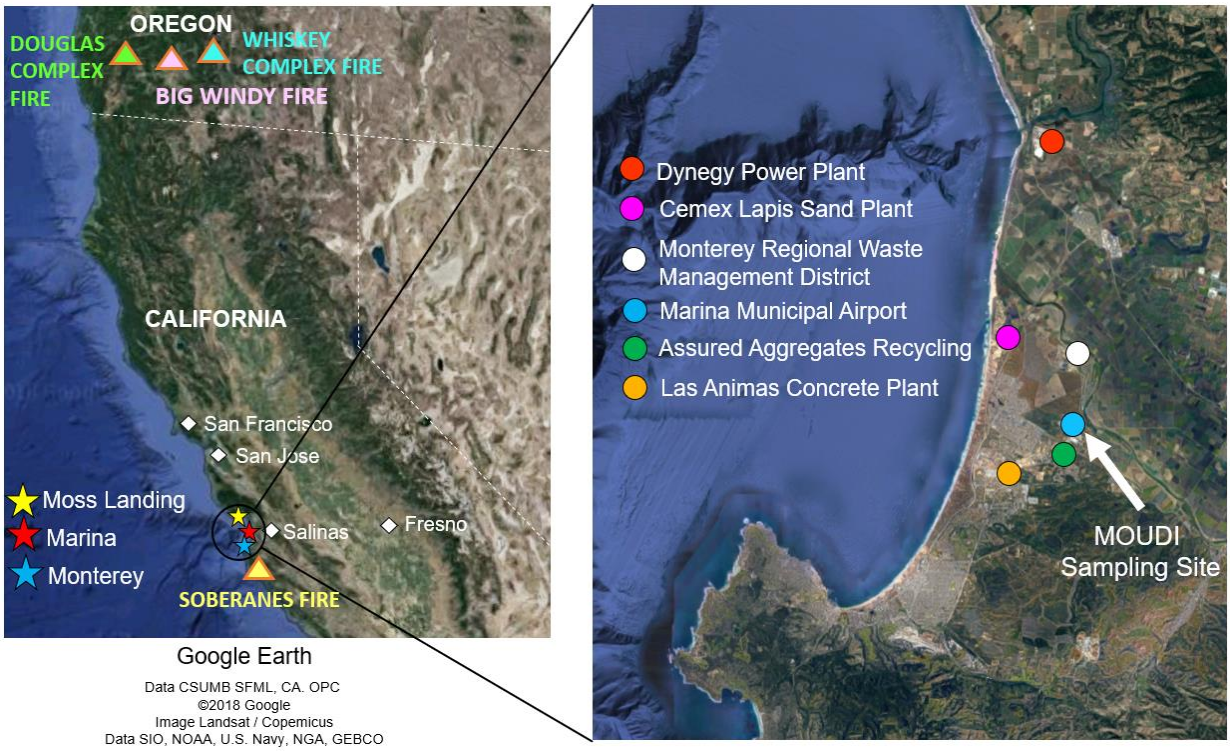

Figure 1. Map showing the Marina sampling station relative to other nearby emission sources and location of wildfires in 2013 during the NiCE campaign (Douglas Complex, Big Windy, and Whiskey Complex Fires) and 2016 during the FASE campaign (Soberanes Fire).

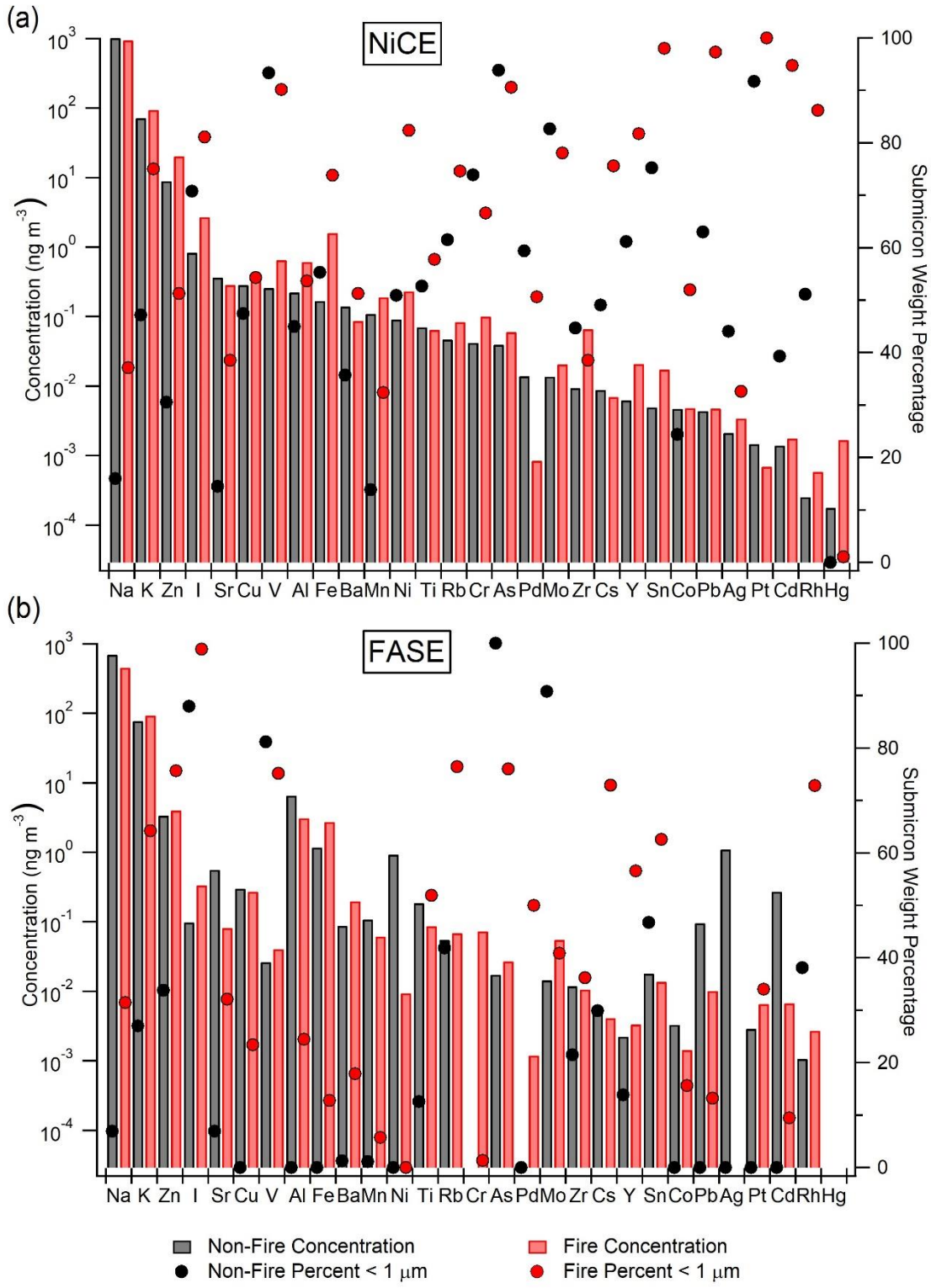

Figure 2. Submicrometer and supermicrometer water-soluble concentrations of elements collected in non-wildfire and wildfire conditions during the (a) NiCE and (b) FASE campaigns.

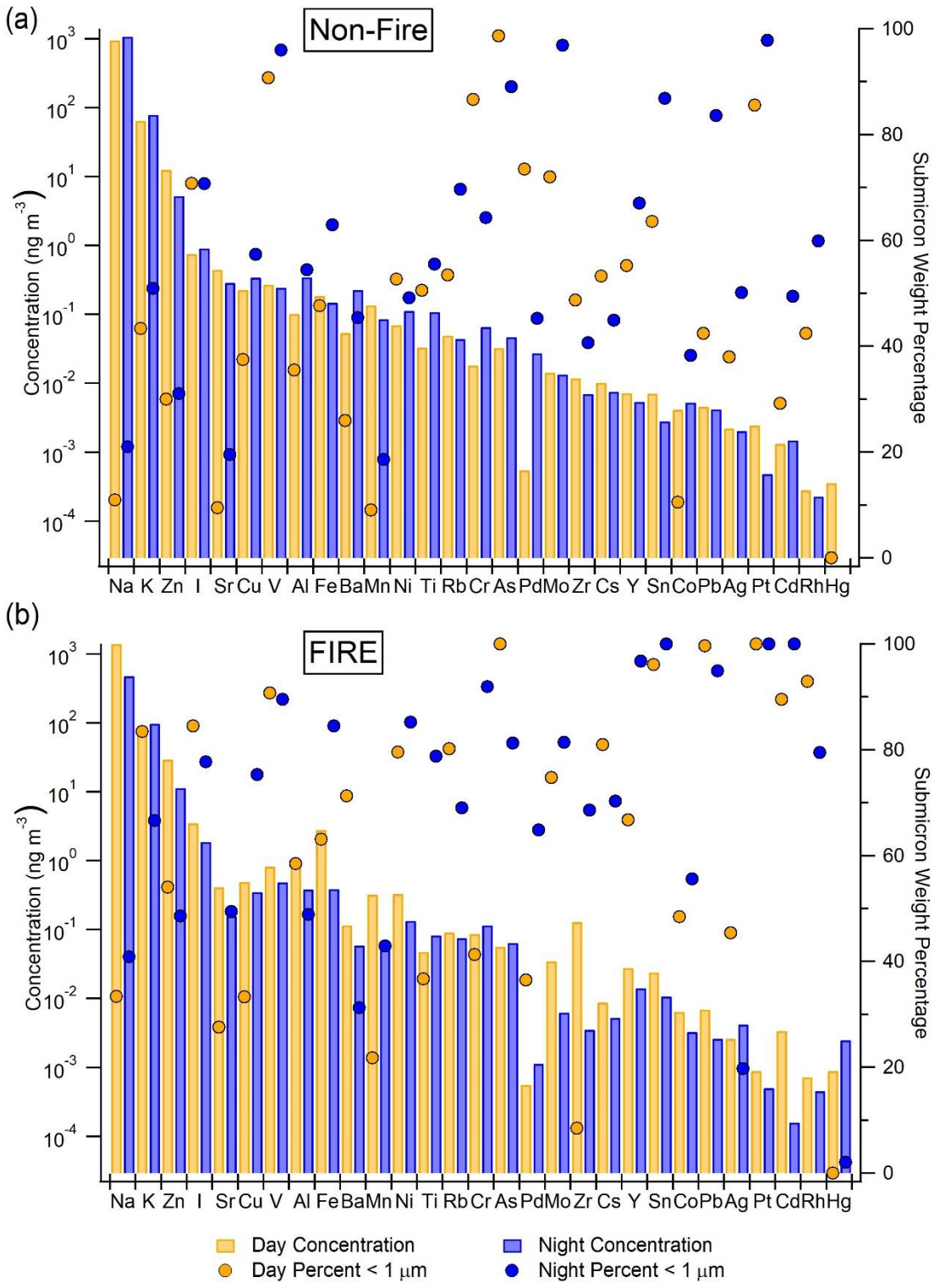

Figure 3. Diurnal variations of water-soluble element concentrations in submicrometer and supermicrometer size ranges during the NiCE campaign for (a) non-wildfire and (b) wildfire conditions.

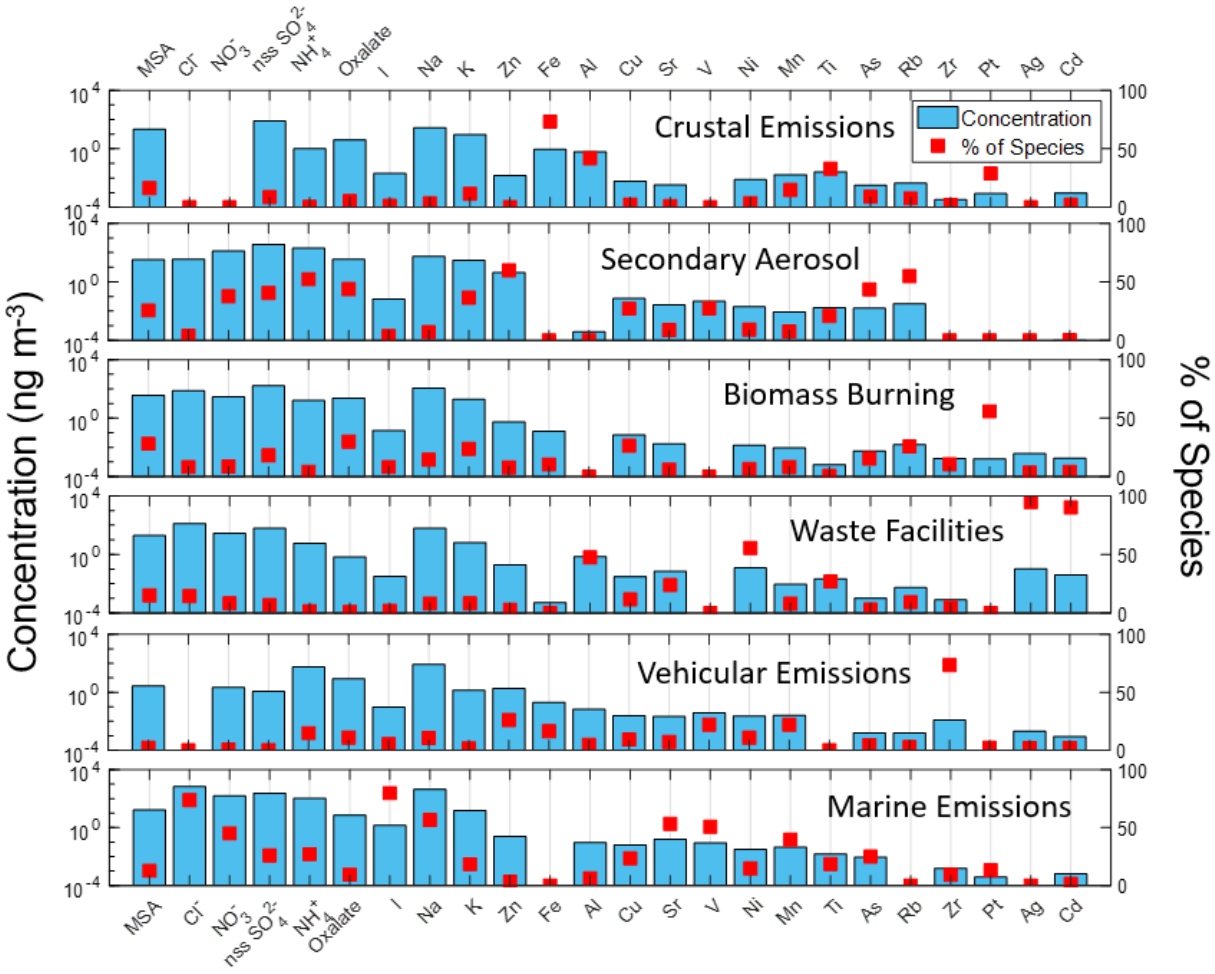

Figure 4. Summary of the six PMF source factor profiles based on water-soluble data of selected ions and elements collected during the NiCE and FASE campaigns. Blue bars represent mass concentrations and red squares represent the percentage of mass concentration contributed to constituents by each source factor. For example, the Crustal Emissions factor accounted for 73.3% of the total measured Fe concentration.

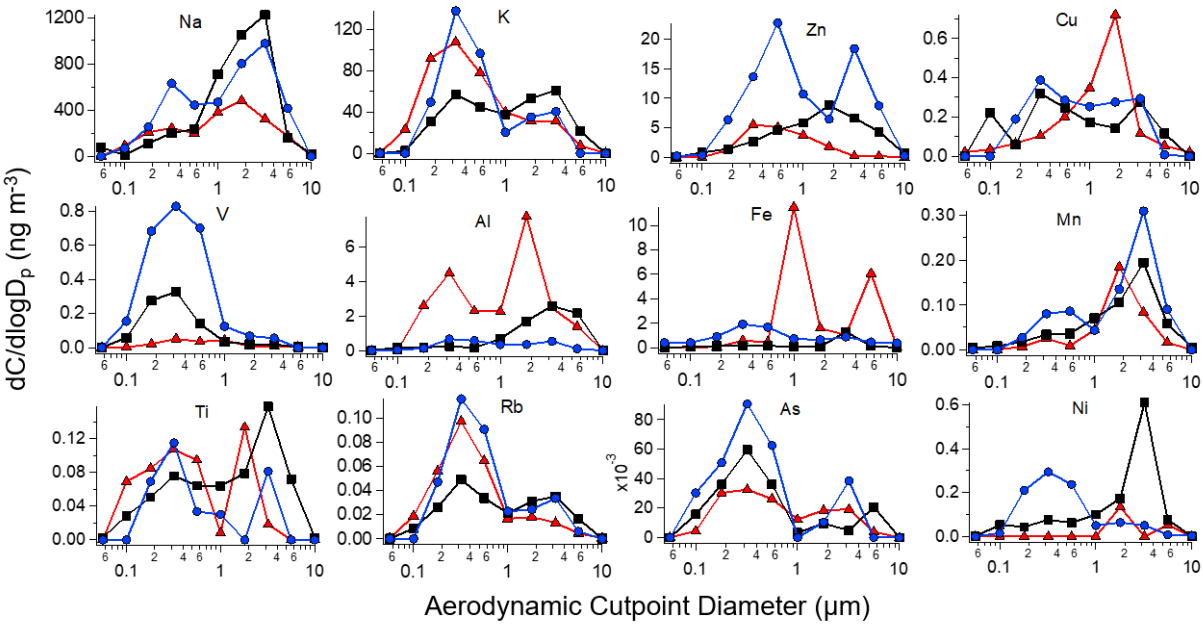

Figure 5. Mass size distributions of selected species from NiCE and FASE campaigns with and without wildfire influence. Black squares represent average non-fire conditions. Blue circles (red triangles) show measurements influenced by wildfire emissions during NiCE (FASE). The remaining 17 elements measured are shown in Figure S2.

Size-resolved Characteristics of Water-Soluble Particulate Elements in a Coastal Area: Source Identification, Influence of Wildfires, and Diurnal Variability

Lin Ma[1], Hossein Dadashazar[1], Rachel A. Braun[1], Alexander B. MacDonald[1], Mojtaba Azadi Aghdam[1], Lindsay C. Maudlin[2], Armin Sorooshian[1,3*]

[1]Department of Chemical and Environmental Engineering, University of Arizona, Tucson, AZ, USA

[2]Department of Geosciences, Auburn University, Auburn, AL

[3]Department of Hydrology and Atmospheric Sciences, University of Arizona, Tucson, AZ, USA

[*]Corresponding author: Armin Sorooshian (E-mail: armin@email.arizona.edu; Phone: (520) 626-5858; Fax: (520) 621-6048; Postal Address: PO BOX 210011, Tucson, Arizona, 85721, USA)

Supplementary Information

(9 pages including cover page; 6 tables and 2 figures are included)

Table S1. Limits of detection (LOD) for the 29 elements speciated by ICP and six water-soluble ions speciated by IC.

ICP	ppt
Na	7.74
K	10.48
Zn	5.88
I	3.00
Sr	1.10
Cu	1.13
V	1.35
Al	29.47
Fe	1.19
Ba	3.70
Mn	1.62
Ni	2.84
Ti	39.05
Rb	1.57
Cr	1.15
As	7.95
Pd	1.68
Mo	2.26
Zr	1.01
Cs	0.73
Y	0.52
Sn	1.77
Co	0.72
Pb	0.50
Ag	0.74
Pt	1.07
Cd	4.19
Rh	0.30
Hg	2.74

IC	ppm
MSA	0.012
Chloride	0.002
Nitrate	0.009
Sulfate	0.012
Ammonium	0.042
Oxalate	0.012

Table S2. Average water-soluble mass concentrations (ng m^{-3}) of selected elements during NiCE and FASE non-fire periods. The percent contribution of the submicrometer mass concentration to the total mass concentration is shown in the "Weight Percentage" columns.

	NiCE Non-Fire			FASE Non-Fire		
Elements	< 1 μm	> 1 μm	Weight Percentage	< 1 μm	> 1 μm	Weight Percentage
Na	1.69E+02	8.47E+02	15.99	5.08E+01	6.50E+02	6.94
K	3.40E+01	3.78E+01	47.14	2.11E+01	5.62E+01	27.02
Zn	2.22E+00	6.64E+00	30.53	9.12E-01	2.46E+00	33.78
I	5.89E-01	2.43E-01	70.77	8.58E-02	1.17E-02	88.01
Sr	4.18E-02	3.25E-01	14.50	3.79E-02	5.22E-01	6.96
Cu	1.67E-01	1.19E-01	47.44	0.00E+00	3.00E-01	0.00
V	2.41E-01	1.63E-02	93.36	2.10E-02	5.22E-03	81.18
Al	1.19E-01	1.05E-01	44.98	0.00E+00	6.56E+00	0.00
Fe	9.49E-02	7.25E-02	55.32	0.00E+00	1.17E+00	0.00
Ba	8.49E-02	5.51E-02	35.68	6.59E-04	8.72E-02	1.30
Mn	1.62E-02	9.39E-02	13.85	1.10E-03	1.07E-01	1.10
Ni	4.50E-02	4.63E-02	50.95	0.00E+00	9.25E-01	0.00
Ti	3.73E-02	3.35E-02	52.70	2.41E-02	1.63E-01	12.59
Rb	2.72E-02	1.95E-02	61.55	2.31E-02	3.18E-02	41.83
Cr	2.92E-02	1.28E-02	73.88	0.00E+00	0.00E+00	N/A
As	3.71E-02	2.52E-03	93.84	1.73E-02	0.00E+00	100.00
Pd	7.81E-04	1.31E-02	59.38	0.00E+00	2.92E-05	0.00
Mo	1.16E-02	2.27E-03	82.68	1.30E-02	1.31E-03	90.84
Zr	4.19E-03	5.21E-03	44.72	3.35E-03	8.48E-03	21.48
Cs	3.74E-03	5.12E-03	49.09	1.70E-03	3.66E-03	29.93
Y	4.15E-03	2.12E-03	61.15	1.01E-04	2.13E-03	13.90
Sn	3.30E-03	1.64E-03	75.24	8.35E-03	9.56E-03	46.75
Co	1.17E-03	3.54E-03	24.42	0.00E+00	3.32E-03	0.00
Pb	1.91E-03	2.46E-03	63.02	0.00E+00	9.57E-02	0.00
Ag	6.38E-04	1.48E-03	44.05	0.00E+00	1.10E+00	0.00
Pt	1.20E-03	2.63E-04	91.70	0.00E+00	2.88E-03	0.00
Cd	3.83E-04	1.02E-03	39.32	0.00E+00	2.72E-01	0.00
Rh	1.63E-04	9.09E-05	51.15	3.21E-04	7.42E-04	38.15
Hg	0.00E+00	1.77E-04	0.00	0.00E+00	0.00E+00	N/A

Table S3. Same as Table S2 but for NiCE and FASE fire periods.

	NiCE Fire			FASE Fire		
Elements	< 1 μm	> 1 μm	Weight Percentage	< 1 μm	> 1 μm	Weight Percentage
Na	3.32E+02	6.09E+02	37.12	1.33E+02	3.23E+02	31.50
K	7.02E+01	2.38E+01	75.03	6.89E+01	2.40E+01	64.20
Zn	1.07E+01	9.68E+00	51.31	2.70E+00	1.28E+00	75.64
I	2.21E+00	4.80E-01	81.13	3.29E-01	7.56E-03	98.86
Sr	9.60E-02	1.89E-01	38.51	2.58E-02	5.60E-02	32.13
Cu	2.14E-01	2.07E-01	54.34	5.13E-02	2.21E-01	23.42
V	5.88E-01	6.32E-02	90.14	2.76E-02	1.30E-02	75.15
Al	3.40E-01	2.73E-01	53.69	7.98E-01	2.28E+00	24.48
Fe	1.05E+00	5.47E-01	73.80	1.11E-01	2.63E+00	12.83
Ba	5.01E-02	3.66E-02	51.28	3.82E-02	1.59E-01	17.88
Mn	4.80E-02	1.43E-01	32.36	2.45E-03	5.90E-02	5.71
Ni	1.88E-01	4.35E-02	82.39	0.00E+00	9.40E-03	0.00
Ti	4.10E-02	2.36E-02	57.75	5.53E-02	3.12E-02	51.90
Rb	6.26E-02	2.07E-02	74.61	5.67E-02	1.20E-02	76.42
Cr	7.09E-02	3.02E-02	66.62	1.59E-04	7.27E-02	1.32
As	5.43E-02	5.98E-03	90.63	1.95E-02	7.55E-03	76.04
Pd	4.69E-04	3.77E-04	50.67	5.08E-05	1.15E-03	50.00
Mo	1.55E-02	4.97E-03	78.07	1.60E-02	3.87E-02	40.87
Zr	6.64E-03	5.94E-02	38.53	6.46E-03	4.15E-03	36.21
Cs	5.39E-03	1.61E-03	75.63	2.96E-03	1.16E-03	72.88
Y	1.61E-02	4.83E-03	81.76	1.92E-03	1.43E-03	56.54
Sn	1.69E-02	4.66E-04	98.05	6.62E-03	7.12E-03	62.60
Co	2.46E-03	2.38E-03	52.00	3.81E-04	1.05E-03	15.60
Pb	4.68E-03	7.83E-05	97.29	1.25E-03	8.83E-03	13.23
Ag	1.01E-03	2.40E-03	32.59	0.00E+00	0.00E+00	N/A
Pt	6.96E-04	0.00E+00	100.00	2.18E-03	4.42E-03	34.01
Cd	1.59E-03	1.77E-04	94.75	1.04E-03	5.67E-03	9.49
Rh	5.11E-04	7.15E-05	86.22	1.99E-03	7.30E-04	72.82
Hg	2.54E-05	1.65E-03	1.03	0.00E+00	0.00E+00	N/A

Table S4. Same as Table S2 but for day and night periods for NiCE sample sets, divided into fire and non-fire periods.

Elements	NiCE Fire						NiCE Non-Fire					
	Day		Night		Day/Night	Day/Night	Day		Night		Day/Night	Day/Night
	< 1 µm	> 1 µm	< 1 µm	> 1 µm	< 1 µm	> 1 µm	< 1 µm	> 1 µm	< 1 µm	> 1 µm	< 1 µm	> 1 µm
Na	4.68E+02	9.34E+02	1.97E+02	2.85E+02	2.38	3.28	1.00E+02	8.49E+02	2.37E+02	8.45E+02	0.68	1.22
K	7.54E+01	1.50E+01	6.50E+01	3.26E+01	1.16	0.46	2.77E+01	3.67E+01	4.04E+01	3.89E+01	0.69	0.96
Zn	1.59E+01	1.35E+01	5.53E+00	5.86E+00	2.87	2.30	2.82E+00	9.70E+00	1.62E+00	3.59E+00	3.47	2.55
I	2.96E+00	5.43E-01	1.46E+00	4.17E-01	2.03	1.30	5.36E-01	2.21E-01	6.41E-01	2.66E-01	0.84	0.83
Sr	1.14E-01	2.98E-01	7.83E-02	8.01E-02	1.45	3.73	4.36E-02	4.00E-01	4.00E-02	2.49E-01	1.92	2.81
Cu	1.64E-01	3.28E-01	2.63E-01	8.63E-02	0.62	3.80	8.70E-02	1.40E-01	2.46E-01	9.77E-02	0.99	1.86
V	7.43E-01	7.59E-02	4.33E-01	5.05E-02	1.72	1.50	2.45E-01	2.37E-02	2.37E-01	8.81E-03	1.05	1.94
Al	4.94E-01	3.51E-01	1.86E-01	1.95E-01	2.65	1.80	2.93E-02	7.26E-02	2.08E-01	1.37E-01	0.36	0.87
Fe	1.77E+00	1.03E+00	3.27E-01	5.98E-02	5.41	17.32	9.66E-02	8.94E-02	9.32E-02	5.56E-02	1.57	12.72
Ba	8.20E-02	3.31E-02	1.83E-02	4.01E-02	4.49	0.82	1.19E-02	4.19E-02	1.58E-01	6.83E-02	0.27	0.82
Mn	7.00E-02	2.51E-01	2.60E-02	3.45E-02	2.70	7.27	1.59E-02	1.19E-01	1.65E-02	6.86E-02	3.34	2.06
Ni	2.62E-01	6.72E-02	1.14E-01	1.98E-02	2.29	3.39	3.80E-02	3.19E-02	5.19E-02	6.07E-02	0.74	0.75
Ti	1.73E-02	2.99E-02	6.46E-02	1.74E-02	0.27	1.72	1.55E-02	1.73E-02	5.91E-02	4.97E-02	0.12	0.38
Rb	7.31E-02	1.80E-02	5.20E-02	2.34E-02	1.41	0.77	2.74E-02	2.19E-02	2.70E-02	1.71E-02	1.25	1.21
Cr	3.59E-02	5.10E-02	1.06E-01	9.30E-03	0.34	5.49	1.38E-02	4.26E-03	4.46E-02	2.13E-02	0.34	12.30
As	5.67E-02	0.00E+00	5.19E-02	1.20E-02	1.09	0.00	3.20E-02	3.74E-04	4.21E-02	4.66E-03	0.84	0.08
Pd	2.05E-04	3.56E-04	7.33E-04	3.98E-04	0.28	0.89	2.53E-04	2.92E-04	1.31E-03	2.60E-02	0.33	0.00
Mo	2.60E-02	8.77E-03	5.11E-03	1.17E-03	5.08	7.51	1.04E-02	3.82E-03	1.27E-02	7.13E-04	0.89	1.84
Zr	1.09E-02	1.18E-01	2.42E-03	1.11E-03	4.50	106.35	5.06E-03	6.77E-03	3.32E-03	3.64E-03	1.19	1.77
Cs	7.10E-03	1.67E-03	3.68E-03	1.56E-03	1.93	1.07	4.70E-03	5.45E-03	2.79E-03	4.79E-03	1.84	1.13
Y	1.85E-02	9.20E-03	1.36E-02	4.59E-04	1.36	20.07	4.14E-03	3.01E-03	4.16E-03	1.22E-03	1.76	2.86
Sn	2.30E-02	9.32E-04	1.08E-02	0.00E+00	2.13	N/A	4.27E-03	2.80E-03	2.32E-03	4.83E-04	0.73	1.37
Co	3.11E-03	3.31E-03	1.81E-03	1.45E-03	1.72	2.29	3.65E-04	3.78E-03	1.97E-03	3.30E-03	0.14	2.26
Pb	6.88E-03	2.47E-05	2.47E-03	1.32E-04	2.78	0.19	1.50E-03	3.06E-03	2.32E-03	1.86E-03	1.91	14.02
Ag	1.19E-03	1.43E-03	8.30E-04	3.37E-03	1.43	0.42	6.25E-04	1.58E-03	6.51E-04	1.39E-03	1.00	0.43
Pt	8.91E-04	0.00E+00	5.02E-04	0.00E+00	1.78	N/A	1.93E-03	5.12E-04	4.68E-04	1.43E-05	0.75	0.00
Cd	3.03E-03	3.55E-04	1.59E-04	0.00E+00	19.08	N/A	3.41E-04	9.80E-04	4.25E-04	1.06E-03	1.08	10.62
Rh	6.64E-04	5.05E-05	3.59E-04	9.25E-05	1.85	0.55	1.53E-04	1.28E-04	1.72E-04	5.38E-05	1.04	4.69
Hg	0.00E+00	8.87E-04	5.08E-05	2.42E-03	0.00	0.37	0.00E+00	3.54E-04	0.00E+00	0.00E+00	N/A	N/A

Table S6. Crustal enrichment factors (EFs) based on element concentrations predicted by the PMF model for the Crustal Emissions PMF source factor relative to concentrations from Earth's crust. Aluminum was used as the reference element in the EF calculation (Equation 2).

Elements	Enrichment Factor
Pt	23896.4
I	9729.3
Cd	264.7
Na	136.3
As	90.0
Zn	51.1
K	49.8
Ni	10.9
Cu	8.5
Mn	2.5
Fe	2.5
Rb	2.0
Sr	1.1
Ti	0.6
Zr	0.2
V	0.0
Ag	0.0

Table S5: Mass concentration correlation matrix for 29 elements and six water-soluble ions. Results are based on total water-soluble mass concentrations for each MOUDI set (n = 17). Displayed correlation coefficients (r) are statistically significant at 95% confidence with a two-tailed Student's t-Test.

	MSA	Cl^-	NO_3^-	nss SO_4^{2-}	NH_4^+	Oxalate	Na	K	Zn	I	Fe	Al	Cu	Cr	Sr	V	Ni	Mn	Mo	Ti	As	Rb	Ba	Sn	Zr	Pt	Cs	Co	Pb	Y	Pd	Ag	Cd	Hg	Rh
MSA	1.00																																		
Cl^-		1.00																																	
NO_3^-		0.63	1.00																																
nss SO_4^{2-}			0.70	1.00																															
NH_4^+			0.69	0.61	1.00																														
Oxalate						1.00																													
Na		0.80	0.51				1.00																												
K	0.65					0.75		1.00																											
Zn					0.65				1.00																										
I			0.80		0.87	0.53	0.73		0.95	1.00																									
Fe			-0.57								1.00																								
Al	0.59			-0.50	-0.60							1.00																							
Cu						0.54	0.56	0.48					1.00																							
Cr										0.68	0.81			1.00																						
Sr		0.78	0.53				0.66								1.00																					
V			0.66	0.61	0.83				0.72	0.95						1.00																				
Ni												0.74			0.53		1.00																		
Mn							0.51		0.63	0.76					0.50	0.66		1.00																		
Mo											0.82			0.80					1.00																	
Ti												0.57					0.50			1.00															
As			0.49	0.55	0.78					0.71		-0.54				0.67					1.00															
Rb	0.54					0.81		0.82														1.00														
Ba																							1.00													
Sn																								1.00												
Zr										0.78						0.69		0.79							1.00											
Pt	0.62				-0.48																					1.00									
Cs		0.75	0.55				0.66			0.79					0.54												1.00								
Co		0.65					0.78			0.75			0.55		0.57												0.54	1.00							
Pb																													1.00						
Y					0.74				0.78	0.96						0.88		0.62			0.54				0.83					1.00					
Pd																							0.60								1.00				
Ag												0.58					0.84			0.53									0.80			1.00			
Cd												0.68					0.91			0.54									0.68			0.98	1.00		
Hg		0.70	0.80	0.80	0.57		0.52					-0.54				0.51					0.53						0.51						1.00	
Rh	0.72					0.60		0.66														0.61				0.79							-0.48	1.00

Figure S1: Map of an area within the Marina municipal airport property showing tire marks from extensive vehicular use, including police car training. The measurement site was in the building with the white roof immediately to the left of the areas with the number labels.

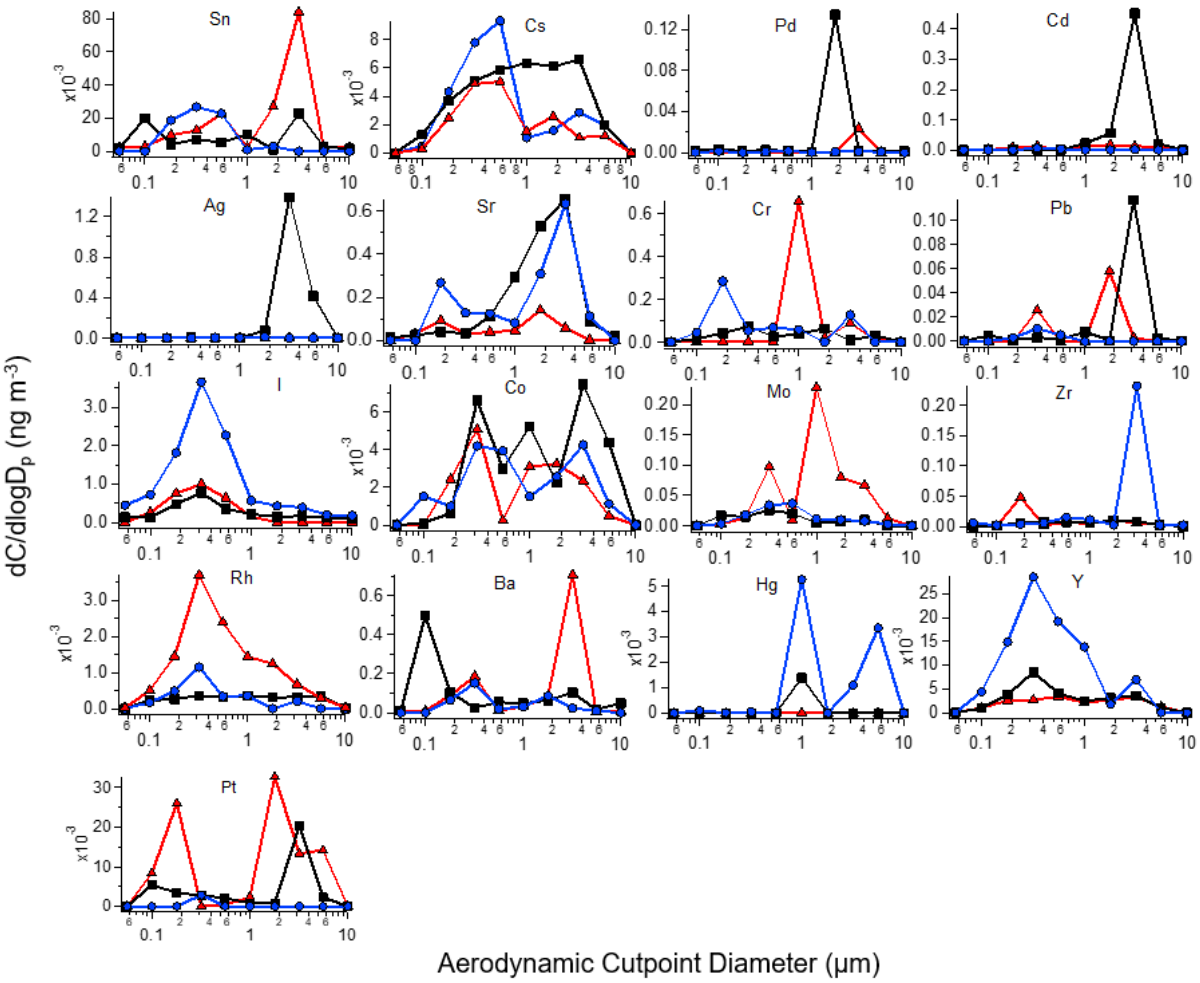

Figure S2: Mass size distributions of elemental species that are not included in Figure 5. Black squares represent average non-fire data. Blue circles and red triangles represent data collected during NiCE and FASE wildfire periods, respectively.

APPENDIX B

SIZE-RESOLVED COMPOSITION AND MORPHOLOGY OF PARTICULATE MATTER DURING THE SOUTHWEST MONSOON IN METRO MANILA, PHILIPPINES

This article has been submitted for publication.

Melliza Templonuevo Cruz[1,2], Paola Angela Bañaga[1,3], Grace Betito[3], Rachel A. Braun[4], Connor Stahl[4], Mojtaba Azadi Aghdam[4], Maria Obiminda Cambaliza[1,3], Hossein Dadashazar[4], Miguel Ricardo Hilario[3], Genevieve Rose Lorenzo[1], Lin Ma[4], Alexander B. MacDonald[4], Preciosa Corazon Pabroa[5], John Robin Yee[5], James Bernard Simpas[1,3], Armin Sorooshian[4,6]

[1]Manila Observatory, Quezon City 1101, Philippines
[2]Institute of Environmental Science and Meteorology, University of the Philippines, Diliman, Quezon City 1101, Philippines
[3]Department of Physics, School of Science and Engineering, Ateneo de Manila University, Quezon City 1101, Philippines
[4]Department of Chemical and Environmental Engineering, University of Arizona, Tucson, AZ, USA
[5]Philippine Nuclear Research Institute, Commonwealth Avenue, Diliman, Quezon City 1101, Philippines
[6]Department of Hydrology and Atmospheric Sciences, University of Arizona, Tucson, AZ, USA

Size-resolved Composition and Morphology of Particulate Matter During the Southwest Monsoon in Metro Manila, Philippines

Melliza Templonuevo Cruz[1,2], Paola Angela Bañaga[1,3], Grace Betito[3], Rachel A. Braun[4], Connor Stahl[4], Mojtaba Azadi Aghdam[4], Maria Obiminda Cambaliza[1,3], Hossein Dadashazar[4], Miguel Ricardo Hilario[3], Genevieve Rose Lorenzo[1], Lin Ma[4], Alexander B. MacDonald[4], Preciosa Corazon Pabroa[5], John Robin Yee[5], James Bernard Simpas[1,3], Armin Sorooshian[4,6]

[1]Manila Observatory, Quezon City 1101, Philippines

[2]Institute of Environmental Science and Meteorology, University of the Philippines, Diliman, Quezon City 1101, Philippines

[3]Department of Physics, School of Science and Engineering, Ateneo de Manila University, Quezon City 1101, Philippines

[4]Department of Chemical and Environmental Engineering, University of Arizona, Tucson, AZ, USA

[5]Philippine Nuclear Research Institute, Commonwealth Avenue, Diliman, Quezon City 1101, Philippines

[6]Department of Hydrology and Atmospheric Sciences, University of Arizona, Tucson, AZ, USA

Abstract

This paper presents novel results from size-resolved particulate matter (PM) mass, composition, and morphology measurements conducted during the 2018 Southwest Monsoon (SWM) season in Metro Manila, Philippines. Micro-Orifice Uniform Deposit Impactors (MOUDIs) were used to collect PM sample sets that were analyzed for mass, morphology, black carbon (BC), and composition of the water-soluble fraction. The bulk of the PM mass was between 0.18–1.0 μm with a dominant mode between 0.32–0.56 μm. Similarly, most of the black carbon (BC) mass was found between 0.10–1.0 μm (the so-called Greenfield gap), peaking between 0.18–0.32 μm, where wet scavenging by rain is inefficient. In the range of 0.10 – 0.18 μm, BC constituted 78.1% of the measured mass. Comparable contributions of BC (26.9%) and the water-soluble fraction (31.3%) to total PM were observed and most of the unresolved mass, which in total amounted to 41.8%, was for diameters exceeding 0.32 μm. The water-soluble ions and elements exhibited an average combined concentration of 8.53 μg m^{-3}, with SO_4^{2-}, NH_4^+, NO_3^-, Na^+, and Cl^- as the major contributors. Positive Matrix Factorization (PMF) was applied to identify the possible aerosol sources and estimate their contribution to the water-soluble fraction of collected PM. The factor with the highest contribution was attributed to "Aged/Transported" aerosol (48.0%) while "Sea Salt" (22.5%) and "Combustion" emissions (18.7%) had comparable contributions. "Vehicular/Resuspended Dust" (5.6%) as well as "Waste Processing" emissions (5.1%) were also identified. Microscopy analysis highlighted the ubiquity of non-spherical particles regardless of size, which is significant when considering calculations of parameters such as single scattering albedo, asymmetry parameter, and extinction efficiency.

Results of this work have implications for aerosol impacts on public health, visibility, and regional climate as each of these depend on physicochemical properties of particles as a function of size. The significant influence from Aged/Transported aerosol to Metro Manila during the SWM season indicates that local sources in this megacity do not fully govern this coastal area's aerosol properties and that PM in Southeast Asia can travel long distances regardless of the significant precipitation and potential wet scavenging that could occur. That the majority of the regional aerosol mass burden is accounted for by BC and other insoluble components has important downstream effects on the aerosol hygroscopic properties, which depend on composition. The results are relevant for understanding the impacts of monsoonal features on size-resolved aerosol

properties, notably aqueous processing and wet scavenging. Finally, the results of this work provide contextual data for future sampling campaigns in Southeast Asia such as the airborne component of the Cloud, Aerosol, and Monsoon Processes Philippines Experiment ($CAMP^2Ex$) planned for the SWM season in 2019. Aerosol characterization via remote-sensing is notoriously difficult in Southeast Asia, which elevates the importance of datasets such as the one presented here.

Introduction

Ambient atmospheric aerosol particles impact human health, visibility, climate, and the hydrological cycle. Major factors governing these behaviors, such as deposition fraction in the respiratory system and activation into cloud condensation nuclei (CCN), include size and chemical composition. Therefore, size-resolved measurements of ambient aerosol particles can lend additional insights to the behaviors and implications of particulate matter (PM) in the atmosphere. One region of interest for characterization of aerosols is Southeast Asia due to increasing urbanization and the exposure of the population to a variety of aerosol sources, both natural and anthropogenic (Hopke et al., 2008). However, use of space-borne remote-sensing instrumentation presents a challenge for characterization of aerosol in this region, due to issues such as varying terrain and cloud cover (Reid et al., 2013).

The Philippines represents a country in Southeast Asia with a developing economy, rapid urbanization, old vehicular technology, and less stringent air quality regulations (e.g., Alas et al., 2017). It is also highly sensitive to the effects of climate change including prolonged dry periods and reductions in southwest monsoon (SWM) rainfall in recent decades (e.g., Cruz et al., 2013). Metro Manila is the country's capital and center of political and economic activities. Also referred to as the National Capital Region, Metro Manila is composed of 16 cities and a municipality that collectively occupy a land area of ~619 km^2. As of 2015, Metro Manila had a population of approximately 12.88 million (Philippine Statistics Authority, 2015). Of the cities comprising the Metro Manila area, the one that is the focus of this study, Quezon City, is the most populated (2.94 million people) with a population density of ~17,000 km^{-2} as of 2015 (Philippine Statistics Authority, 2015).

The rainfall pattern in Southeast Asia is governed by topographic effects and the prevailing surface winds brought by the monsoons. Mountain ranges in the Philippines are generally oriented north to south in the eastern and western coasts. As such, northeasterly winds during the East Asian winter monsoon that starts in November brings wetness (dryness) on the eastern (western) coasts of the country. In contrast, the rainy season starts in May when the Western North Pacific subtropical high moves northeast and the Asian summer monsoon enables the propagation of southwesterly wind through the Philippines (Villafuerte et al., 2014). Metro Manila, located on the western side of the Philippines, therefore experiences wet (May-October) and dry (November-

April) seasons. The large seasonal shift in prevailing wind directions can cause changes in the source locations of aerosol transported to the Philippines and the subsequent direction in which emissions from the Philippines are transported, such as to the northwest (e.g., Chuang et al., 2013) or southwest (e.g., Farren et al., 2019). However, one interesting feature of Metro Manila is the consistency of $PM_{2.5}/PM_{10}$ mass concentrations during both the dry (44/54 μg m^{-3}) and wet seasons (43/55 μg m^{-3}) (Kim Oanh et al., 2006), which stands in contrast to typical assumptions that increased wet scavenging during rainy seasons would lead to decreases in measured PM (e.g., Liao et al., 2006). While similar results are observed in Chennai, India, this behavior is different than other cities in Asia, including Bandung City (Indonesia), Bangkok (Thailand), Beijing (China), and Hanoi City (Vietnam), that exhibit reduced $PM_{2.5}$ levels during the wet season as compared to the dry season (Kim Oanh et al., 2006). While the total PM levels may stay constant across the wet and dry seasons, seasonally-resolved analyses will provide additional insights into how the composition, morphology, and sources (transported vs. local emissions) change on a seasonal basis.

Metro Manila has been drawing growing interest for PM research owing to the significant levels of black carbon (BC). A large fraction of PM in Metro Manila can be attributed to BC (e.g., ~50% of $PM_{2.5}$; Kim Oanh et al., 2006), with previously measured average values of BC at MO reaching ~10 μg m^{-3} for $PM_{2.5}$ (Simpas et al., 2014). The impacts of the high levels of BC present on human health have also received attention (Kecorius et al., 2019). Identified major sources of BC include vehicular, industrial, and cooking emissions (Bautista et al., 2014; Kecorius et al., 2017). Vehicular emissions, especially along roadways where personal cars and motorcycles, commercial trucks, and motorized public transportation, including powered tricycles and *jeepneys*, are plentiful. For instance, measurements of $PM_{2.5}$ at the National Printing Office (NPO) located alongside the major thoroughfare Epifanio de los Santos Avenue (EDSA) were on average 72 μg m^{-3}; this value is twice the average concentration at the Manila Observatory (MO), an urban mixed site located approximately 5 km from NPO (Simpas et al., 2014). In addition to local emissions, long-range transport of pollution, such as biomass burning, can also impact the study region (e.g., Xian et al., 2013; Reid et al., 2016a/b). However, most past work referenced above has focused on either total $PM_{2.5}$ or PM_{10} composition, and therefore, detailed size-resolved composition information has been lacking in this region. Like other monsoonal regions (Crosbie et al., 2015; Qu et al., 2015), it is of interest for instance to know if products of aqueous processing (e.g., sulfate,

organic acids) during the monsoonal period, promoted by the high humidity, become more prominent in certain size ranges to ultimately enhance hygroscopicity, which is otherwise suppressed with higher BC influence.

A year-long sampling campaign (Cloud, Aerosol, and Monsoon Processes Philippines Experiment ($CAMP^2Ex$) weatHEr and CompoSition Monitoring (CHECSM) study) was established in July 2018 to collect size-resolved aerosol measurements in Metro Manila. The aim of this study is to report size-resolved PM measurements taken over the course of the SWM (July-October) of 2018 in Quezon City, Metro Manila, Philippines as part of CHECSM. The results of this study are important for the following reasons: (i) they provide size-resolved analysis of BC in an area previously characterized as having one of the highest BC mass percentages in the whole world; (ii) they provide a basis for better understanding the unusual phenomenon of having similar PM levels during a wet and dry season; (iii) they provide contextual data for contrasting with both other coastal megacities and also other monsoonal regions; and (iv) they can lend insights into the characteristics of aerosol transported both into and out of Metro Manila and how important local sources are in Metro Manila relative to transported pollution. Outcomes of this study include (i) the first size-resolved characterization of both aerosol composition and morphology in Metro Manila for the SWM, with implications in terms of PM effects on climate, visibility, the hydrological cycle, and public health owing to the dependence of these impacts on particle size; (ii) archival data that contributes to the timeline of aerosol research in Metro Manila, and more broadly Southeast Asia, where there is considerable concern over air pollution; and (iii) baseline data for aerosol composition to be used to inform and assist research to be conducted during future field campaigns in Southeast Asia including the same seasonal period (i.e., SWM) in 2019 as part of *$CAMP^2Ex$*, which will involve both surface and airborne measurements.

2. Experimental Methods

2.1 Sample Site

Sampling was performed at MO in Quezon City, Philippines (14.64° N, 121.08° E). The sampling instrumentation was located on the 3rd floor of the MO office building (~85 m above sea level). Figure 1 visually shows the sampling location and potential surrounding sources. Past work focused on $PM_{2.5}$ suggested that the study location is impacted locally mostly by traffic, various forms of industrial activity, meat cooking from local eateries, and, based on the season,

biomass burning (Cohen et al., 2009). Fourteen sample sets were collected during the SWM season (July-October 2018), with details about the operational and meteorological conditions during each sample set shown in Table 1. Meteorological data were collected using a Davis Vantage Pro 2 Plus weather station co-located with the aerosol measurements at MO. Except for precipitation, which is reported here as accumulated rainfall, reported values for each meteorological parameter represent averages for the sampling duration of each aerosol measurement.

The mean temperature during the periods of MOUDI sample collection ranged from 24.9 to 28.1° C, with accumulated rainfall ranging widely from no rain to up to 78.4 mm. To identify sources impacting PM via long-range transport to the Metro Manila region, Figure 1a summarizes the five-day back-trajectories for air masses arriving at MO on the days when samples were being collected, calculated using the NOAA Hybrid Single-Particle Lagrangian Integrated Trajectory (HYSPLIT) model (Stein et al., 2015; Rolph, 2016). Trajectory calculations were started at 00, 06, 12, and 18 hours in MO at the height of the MOUDI inlet using meteorological files from the NCEP/NCAR Reanalysis dataset. Trajectory cluster analysis was conducted using TrajStat (Wang et al., 2009). The back-trajectories in Figure 1a show that indeed 66% of the wind came from the southwest during the sampling periods.

2.2 MOUDI Sample Sets

Particulate matter was collected on Teflon substrates (PTFE membrane, 2 μm pore, 46.2 mm, Whatman) in Micro-Orifice Uniform Deposit Impactors (MOUDI, MSP Corporation, Marple et al., 2014). Size-resolved measurements were taken at the following aerodynamic cutpoint diameters (D_p): 18, 10, 5.6, 3.2, 1.8, 1.0, 0.56, 0.32, 0.18, 0.10, 0.056 μm. For a subset of the sampling periods, two pairs of MOUDI sets were collected simultaneously such that both sets in each pair could undergo different types of analyses. One set in each pair underwent gravimetric analysis using a Sartorius ME5-F microbalance. MOUDI set 13 was additionally examined with a Multi-wavelength Absorption Black Carbon Instrument (MABI; Australian Nuclear Science and Technology Organisation). This optically-based instrument quantifies absorption and mass concentrations at seven wavelengths between 405 and 1050 nm; however, results are reported only for 870 nm to be consistent with other studies as BC is the predominant absorber at that wavelength (e.g., Ramachandran and Rajesh, 2007; Ran et al., 2016). One additional sample set for microscopy analysis was collected for one hour on August 1 using aluminum substrates.

2.3 Chemical Composition Analysis

In order to preserve samples for additional analysis, each Teflon substrate was cut in half. A half of each substrate was extracted in 8 mL of Milli-Q water (18.2 MΩ-cm) through sonication for 30 min in a sealed polypropylene vial. A blank substrate was processed in the same method to serve as a background control sample. Subsequent chemical analysis of the water-soluble components in the aqueous extracts were performed using ion chromatography (IC; Thermo Scientific Dionex ICS - 2100 system) for the following species: cations = Na^+, NH_4^+, Mg^{2+}, Ca^{2+}, dimethylamine (DMA), trimethylamine (TMA), diethylamine (DEA); anions =, methanesulfonate (MSA), pyruvate, adipate, succinate, maleate, oxalate, phthalate, Cl^-, NO_3^-, SO_4^{2-}. Owing to co-elution of TMA and DEA in the IC system, a cumulative sum of the two is reported here, which represents an underestimate of their total mass concentration owing to overlap in parts of their peaks. Limits of detection (LOD) were calculated for each species based on their respective calibration curve (Table S1), with LOD being three times the standard deviation of the residuals (predicted signal minus measured signal) divided by the slope of the calibration curve (Miller and Miller, 2018).

The aqueous extracts were simultaneously characterized for elemental composition using triple quadrupole inductively coupled plasma mass spectrometry (ICP-QQQ; Agilent 8800 Series) for the following species: K, Al, Fe, Mn, Ti, Ba, Zn, Cu, V, Ni, P, Cr, Co, As, Se, Rb, Sr, Y, Zr, Nb, Mo, Ag, Cd, Sn, Cs, Hf, Tl, Pb. Limits of detection of the examined elements were calculated automatically by the ICP-QQQ instrument and were in the ppt range (Table S1). The sample concentrations represent an average of three separate measurements with a standard deviation of 3% or less.

Note that some species were detected by both IC and ICP-QQQ (i.e., Na^+, K^+, Mg^{2+}, Ca^{2+}), and that the IC concentrations are used here for all repeated species with the exception of K^+ owing to better data quality from ICP-QQQ. All IC and ICP-QQQ species concentrations for samples have been corrected by subtracting concentrations from background control samples.

2.4 Microscopy Analysis

As already noted, one MOUDI set on August 1 was devoted to microscopy analysis. Morphology and additional elemental composition analysis was carried out on this set of aluminum

substrates using scanning electron microscopy equipped with energy dispersive X-ray spectroscopy (SEM-EDX) in the Kuiper Imaging cores at the University of Arizona. Secondary electron (SE) imaging and EDX elemental analysis were performed using a Hitachi S-4800 high resolution SEM coupled to a Noran system Six X-ray Microanalysis System by Thermo Fisher Scientific. EDX analysis on individual particles was performed with 30 kV accelerating voltage to obtain weight percentages of individual elements. SEM-EDX results showed that the background control aluminum substrate was dominated by Al (88.27%), with minor contributions from Ag (5.34%), C (4.87%), O (0.79%), Fe (0.67%), and Co (0.05%). Such contributions were manually subtracted from spectra of individual particles on sample substrates, with the remaining elements scaled up to hundred percent. Image processing was conducted with Image J software to measure particle dimensions and adjust the contrast and brightness of images to provide better visualization.

2.5 Computational Analysis

This study reports basic descriptive statistics for chemical concentrations and correlations between different variables. Statistical significance hereafter corresponds to 95% significance based on a two-tailed Student's t-test. To complement correlative analysis for identifying sources of species, positive matrix factorization (PMF) modeling was carried out using the United States Environmental Protection Agency's (US EPA) PMF version 5. Species considered as "strong" based on high signal-to-noise ratios (S/N > 1) and those with at least 50% of the concentrations above the detection limit were used in the PMF modeling (Norris et al., 2014). Data points with concentrations exceeding the LOD had uncertainty quantified as follows:

$$\sigma_{ij} = 0.05 \cdot X_{ij} + LOD_{ij} \qquad \text{(Equation 1)}$$

where σ_{ij}, X_{ij}, and LOD_{ij} are the uncertainty, concentration, and LOD, respectively, of the j^{th} species in the i^{th} sample (Reff et al., 2007). When concentration data were not available for a particular stage of a MOUDI set for a species, the geometric mean of the concentrations for that MOUDI stage and species was applied with uncertainty counted as four times the geometric mean value (Polissar et al., 1998; Huang et al., 1999). A 25% extra modeling uncertainty was applied to account for other sources of errors such as changes in the source profiles and chemical

transformations (Dumanoglu et al., 2014; Norris et al., 2014). The model was run 20 times with a randomly chosen starting point for each run.

3. Results

3.1 Total Mass Concentrations and Charge Balance

The average total mass concentration (± standard deviation) of water-soluble species across all MOUDI stages (Table 1) during the study period was 8.53 ± 4.48 μg m^{-3} (range = 2.7–16.6 μg m^{-3}). The species contributing the most to the total water-soluble mass concentration during the SWM included SO_4^{2-} (44% ± 6%), NH_4^+ (18% ± 5%), NO_3^- (10 ± 3%), Na^+ (8 ± 3%), and Cl^- (6% ± 3%). The meteorological parameters from Table 1 best correlated to total water-soluble mass concentrations were temperature (r = 0.64) and rainfall (r = -0.49). The highest total mass concentration (set MO13/14 = 16.6 μg m^{-3}) occurred during the period with one of the highest average temperatures (27.8 °C) and second least total rainfall (0.8 mm). Other sampling periods with high mass concentrations (sets MO7, MO8, and MO12) coincided with the highest temperature and lowest rainfall observations. High temperatures, and thus more incident solar radiation, presumably enhanced production of secondary aerosol species via photochemical reactions as has also been observed in other regions for their respective monsoon season (Youn et al., 2013). Low rainfall is thought to have been coincident with reduced wet scavenging of aerosol at the study site as has been demonstrated for other regions such as North America (Tai et al., 2010) and megacities such as Tehran (Crosbie et al., 2014). However, set MO11 exhibited a very low concentration even with high temperature and lack of rainfall, which may be due to changes in the source and transport of aerosol since this sample set coincided with a significant change in average wind direction (290.2° for MO11 vs. 90.1° – 127.5° for all other MOUDI sets). While the reported rainfall measurements were taken at MO, inhomogeneous rainfall patterns in the regions surrounding the Philippines could also contribute to the wet scavenging of PM, thereby lowering the quantity of transported particles reaching the sample site. Future work will address the influence of spatiotemporal patterns of precipitation on PM loadings in the Philippines as a point measurement at an aerosol observing site may be misleading.

On two occasions, two simultaneous MOUDI sets (Sets MO3/MO4 and MO13/MO14) were collected for the potential to compare different properties that require separate substrates. The total mass concentrations based on gravimetric analysis of sets MO3 and MO13 were 18.6 μg

m^{-3} and 53.0 μg m^{-3}, respectively (Figure 2). Both sets exhibited a dominant concentration mode between 0.32–0.56 μm and the MO3 set was different in that it exhibited bimodal behavior with a second peak between 1.8–3.2 μm. The sum of speciated water-soluble species accounted for only 27.8% and 31.3% of the total gravimetric mass of sets MO3 and MO13, respectively, indicative of significant amounts of water-insoluble species undetected by IC and ICP-QQQ. When adding the total mass of BC (14.3 μg m^{-3}) to the other resolved species from set MO13 (the one time BC was measured), there was still 22.1 μg m^{-3} of unresolved mass (41.8% of total PM). Most of the unaccounted mass was for $D_p > 0.32$ μm. The observation of BC accounting for 26.9% of total PM (14.3 μg m^{-3}) is consistent with past work highlighting the significant fraction of BC in the ambient aerosol of Manila (Kim Oanh et al., 2006; Bautista et al., 2014; Simpas et al., 2014; Kecorius et al., 2017). However, this fraction of BC is very high compared to measurements during the monsoon season in other parts of the world. The mass fraction of BC in total suspended PM (TSPM) was 1.6%/2.2% for the monsoon season in 2013/2014 in Kadapa in southern India, even though the TSPM measured was comparable to that in Manila (64.9 and 49.9 μg m^{-3}, for 2013 and 2014 in Kadapa, respectively) (Begam et al., 2017). Multiple studies during the monsoon season in a coastal region in southwest India showed BC mass contributions of 1.9 – 5% (Aswini et al., 2019 and references therein). Airborne measurements around North America and in Asian outflow revealed that BC accounted for only ~1-2% of $PM_{1.0}$ (Shingler et al., 2016) and ~5-15% of accumulation mode aerosol mass (Clarke et al., 2004), respectively.

To investigate further about the missing species, a charge balance was carried out for all MOUDI sets (Table 2) to compare the sum of charges for cations versus anions based on IC analysis including K from ICP-QQQ analysis (species listed in Section 2.3). The slope of the charge balances (cations on y-axis) for the cumulative dataset was 1.33 and ranged from 0.89 to 1.41 for the 12 individual MOUDI sets that had IC and ICP-QQQ analysis conducted on them. Eleven of the 12 sets exhibited slopes above unity indicating that there was a deficit in the amount of anions detected, which presumably included species such as carbonate and various organics. To further determine if there were especially large anion or cation deficits in specific size ranges, slopes are also reported for 0.056–1 μm and > 1 μm. There were no obvious differences other than two MOUDI sets exhibited slopes below 1.0 for the smaller diameter range (0.056–1 μm) while all slopes exceeded unity for > 1 μm.

3.2 Mass Size Distributions and Morphology

3.2.1 Black Carbon

The size-resolved nature of BC has not been characterized in Manila and MOUDI set MO13 offered a view into its mass size distribution (Figure 3a). There was a pronounced peak between 0.18–0.32 μm (5.0 μg m^{-3}), which is evident visually in the substrate's color when compared to all other stages of that MOUDI set (Figure 3b). This observed peak in the mass size distribution of BC is similar to previous studies of the outflow of East Asian countries (Shiraiwa et al., 2008), biomass burning and urban emissions in Texas (Schwarz et al., 2008), measurements in the Finnish Arctic (Raatikainen et al., 2015), and airborne measurements over Europe (Reddington et al., 2013). In contrast, measurements in Uji, Japan showed a bimodal size distribution for the mass concentration of BC in the submicrometer range (Hitzenberger and Tohno, 2001). In the present study, there were significant amounts of BC extending to as low as the 0.056-0.1 μm MOUDI stage (0.28 μg m^{-3}) and extending up in the supermicrometer range with up to 0.25 μg m^{-3} measured between 1.8–3.2 μm. Remarkably, BC accounted for approximately 78.1% (51.8%) by mass of the total PM in the range of 0.10 – 0.18 μm (0.18 – 0.32 μm). For comparison, the mass percent contribution of BC measured in the megacity of Nanjing, China was 3.3% (1.6%) at 0.12 (0.08) μm (Ma et al., 2017). Based on visual inspection of color on all MOUDI sets, MO13 appears to be representative of the other sets based on the relative intensity of the color black on substrates with different cutpoint diameters (Figure 3b); the 0.18–0.32 μm substrate always was the most black, with varying degrees of blackness extending consistently into the supermicrometer stages.

Microscopy analysis revealed evidence of non-spherical particles in each MOUDI stage below 1 μm (Figure 4), which is significant as the common assumption theoretically is that submicrometer particles are typically spherical (e.g., Mielonen et al., 2011). Errors in this assumption impact numerical modeling results and interpretation of remote sensing data for aerosols (e.g., Kahnert et al., 2005) owing to incorrect calculations of parameters such as single scattering albedo, asymmetry parameter, and extinction efficiency (e.g., Mishra et al., 2015). Some studies have noted that submicrometer particles could be composed of an agglomeration of small spherical particles originally formed through gas-to-particle conversion processes (Almeida et al., 2019), which could potentially explain the appearance for some of the observed particles in Figure

4. Since only single particles were examined that may not be fully representative of all particles on a particular MOUDI substrate, it is noteworthy that all five particles shown between 0.056 – 1 μm were irregularly shaped with signs of both multi-layering and constituents adhered to one another. The images show that a potentially important source of BC in the area could be soot aggregates, which are formed by a vaporization-condensation process during combustion often associated with vehicular exhaust (e.g., Chen et al., 2006; Chithra and Nagendra, 2013; Wu et al., 2017). Kecorius et al. (2017) projected that 94% of total roadside refractory PM in the same study region was linked to *jeepneys*, with number concentration modes at 20 and 80 nm. They associated the larger mode with soot agglomerates, which is consistent with the smallest MOUDI size range examined here (0.056-0.1 μm; Figure 4b) exhibiting signs of agglomeration.

The total BC mass concentration integrated across all stages of MOUDI set MO13 (14.3 μg m^{-3}) was remarkably high in contrast to BC levels measured via either filters, aethalometers, or single particle soot photometers in most other urban regions of the world (Metcalf et al., 2012 and references therein): Los Angeles Basin (airborne: 0.002–0.53 μg m^{-3}), Atlanta, Georgia (ground: 0.5–3.0 μg m^{-3}), Mexico City (airborne: 0.276–1.1 μg m^{-3}), Sapporo, Japan (ground: 2.3–8.0 μg m^{-3}), Beijing, China (ground: 6.3–11.1 μg m^{-3}), Bangalor, India (ground: 0.4–10.2 μg m^{-3}), Paris, France (ground: 7.9 μg m^{-3}), Dushanbe, Russia (ground: 4–20 μg m^{-3}), Po Valley, Italy (ground: 0.5–1.5 μg m^{-3}), Thessaloniki, Greece (ground: 3.3–8.9 μg m^{-3}). This is intriguing in light of extensive precipitation, and thus wet scavenging of PM, during the study period, which is offset by enormous anthropogenic emissions in the region such as by powered vehicles like the *jeepneys* that are notorious for BC exhaust (Kecorius et al., 2017).

A possible explanation for the large contribution of BC to PM, and the persistence of PM after rain events (Kim Oanh et al., 2006), is that the BC is not efficiently scavenged by precipitating rain drops. Small particles enter rain drops via diffusion whereas large particles enter via impaction. However, particles with a diameter in the range of 0.1–1 μm (known as the Greenfield gap) are too large to diffuse efficiently and too small to impact, and are therefore not efficiently scavenged (Seinfeld and Pandis, 2016). Absorption spectroscopy of set MO13 (Figure 2b) reveals that 95% of the BC mass is concentrated in the Greenfield gap, and thus the removal of BC due to precipitation is inefficient. The Greenfield gap contains 62 ± 11% of the total mass (calculated for MO3/MO13) and 65 ± 10% of the water-soluble mass (calculated for the other 12 MO sets).

3.2.2 Water-Soluble Ions

There were two characteristic mass size distribution profiles for the water-soluble ions speciated by IC depending on whether the species were secondarily produced via gas-to-particle conversion or associated with primarily emitted supermicrometer particles. The average IC species mass concentration profile across all MOUDI sets is shown in Figure 5. Secondarily produced species exhibited a mass concentration mode between 0.32–0.56 μm, including common inorganic species (SO_4^{2-}, NH_4^+), MSA, amines (DMA, TMA+DEA), and a suite of organic acids, such as oxalate, phthalate, succinate, and adipate, produced via precursor volatile organic compounds (VOCs). Two organic acids with peaks in other size ranges included maleate (0.56–1 μm) and pyruvate (0.1–0.18 μm). Sources of the inorganics are well documented with SO_4^{2-} and NH_4^+ produced by precursor vapors SO_2 and NH_3, respectively, with ocean-emitted dimethylsulfide (DMS) as an additional precursor to SO_4^{2-} and the primary precursor to MSA.

Precursors leading to secondarily produced alkyl amines such as DMA, TMA, and DEA likely originated from a combination of industrial activity, marine emissions, biomass burning, vehicular activity, sewage treatment, waste incineration, and the food industry (e.g., Facchini et al., 2008; Sorooshian et al., 2009; Ge et al., 2011; VandenBoer et al., 2011); another key source of these species, animal husbandry (Mosier et al., 1973; Schade and Crutzen, 1995; Sorooshian et al., 2008), was ruled out owing to a scarcity of such activity in the study region. Secondarily produced amine salts likely were formed with SO_4^{2-} as the chief anion owing to its much higher concentrations relative to NO_3^- or organic acids. Dimethylamine was the most abundant amine similar to other marine (Muller et al., 2009) and urban regions (Youn et al., 2015); the average concentration of DMA integrated over all MOUDI stages for all sample sets was 62.2 ng m^{-3} in contrast to 29.8 ng m^{-3} for TMA+DEA. For reference, the other key cation (NH_4^+) participating in salt formation with acids such as H_2SO_4 and HNO_3 was expectedly much more abundant (1.64 μg m^{-3}). With regard to the competitive uptake of DMA versus NH_3 in particles, the molar ratio of DMA:NH_4^+ exhibited a unimodal profile between 0.1–1.8 μm with a peak of 0.022 between 0.32–0.56 μm and the lowest values at the tails (0.004 between 0.1–0.18 and 1–1.8 μm); DMA was not above detection limits for either D_p < 0.1 μm or D_p > 1.8 μm. The molar ratios observed were consistent with values measured in urban air of Tucson, Arizona and coastal air in Marina,

California (0–0.04; Youn et al., 2015) and near the lower end of the range measured in rural and urban air masses sampled near Toronto (0.005–0.2: VandenBoer et al., 2011).

The most abundant organic acid was oxalate (195 ± 144 ng m^{-3}), followed by succinate (21 ± 41 ng m^{-3}), phthalate (19 ± 25 ng m^{-3}), maleate (17 ± 15 ng m^{-3}), and adipate (5 ± 8 ng m^{-3}). The observation of mass concentrations increasing with decreasing carbon number for dicarboxylic acids (i.e., oxalate > succinate > adipate) is consistent with many past studies for other regions as larger chain acids undergo oxidative decay to eventually form oxalate (e.g., Kawamura and Ikushima, 1993; Kawamura and Sakaguchi, 1999; Sorooshian et al., 2007). Maleate is an unsaturated dicarboxylic acid emitted from gas and diesel engines (Rogge et al., 1993) and a product from the photo-oxidation of benzene (Kawamura and Ikushima, 1993). The aromatic dicarboxylic acid phthalate is a known photo-oxidation product of naphthalene and stems largely from plastic processing and fuel combustion (Fraser et al., 2003; Kautzman et al., 2010; Fu et al., 2012; Kleindienst et al., 2012). The oxidation product (MSA) of ocean-derived DMS exhibited an overall average concentration of 11 ± 7 ng m^{-3}, which is near the lower end of the range of levels reported in other coastal and marine environments (from undetected up to ~200 ng m^{-3}) (e.g., Saltzman et al., 1983, 1986; Berresheim 1987; Watts et al., 1987; Burgermeister and Georgii, 1991; Sorooshian et al., 2015; Xu and Gao, 2015).

Water-soluble species exhibiting a peak in the supermicrometer range, usually between 1.8–5.6 µm, include those with known affiliations with sea salt (Na^+, Cl^-, K+, Mg^{2+}) and crustal materials such as dust (Ca^{2+}). Nitrate peaked between 1.8-3.2 µm, and was best correlated with Na^+ and Mg^{2+}, suggestive of HNO_3 partitioning to sea salt as has been observed in other coastal regions (e.g., Prabhakar et al., 2014a). There was very little NO_3^- in the submicrometer range (0.05 ± 0.04 µg m^{-3}) in contrast to supermicrometer sizes (0.78 ± 0.47 µg m^{-3}). More submicrometer NO_3^- in the form of NH_4NO_3 would be expected if there was an excess of NH_3 after neutralizing SO_4^{2-}. The mean ammonium-to-sulfate molar ratio for submicrometer sizes was 2.32 ± 0.52 (range: 1.11 – 2.78), with full neutralization of SO_4^{2-} in 10 of 12 MOUDI sets. Thus, there was a non-negligible excess in NH_3 that presumably participated in salt formation with HNO_3 and organic species. The significant levels of NO_3^- in the same mode as Na^+ and Cl^- contributed to the significant Cl^- depletion observed, as the mean Cl^-:Na^+ mass ratio between 1-10 µm (i.e., range of peak sea salt influence) was 0.81 ± 0.28, which is much lower than the ratio for pure sea salt (1.81)

(Martens et al., 1973). The subject of Cl^- depletion in this region will be investigated more thoroughly in subsequent work.

Figure 6 shows SEM images of representative single particles in each supermicrometer stage. As would be expected for sea salt and crustal material, most of the particles shown are not spherical. Interestingly, only the particle shown between 1–1.8 μm was close to being spherical. Its composition based on EDX analysis was accounted for mostly by carbon (93.7%) with lower amounts of oxygen (5.8%) and Fe (0.5%). Sea salt particles were found in the next two stages owing to the highest combined weight percentages of Na^+ and Cl^- based on EDX analysis: 1.8–3.2 μm = 36.9%; 3.2–5.6 μm = 46.9%. The salt particles are not necessarily cubical but more rounded with signs of agglomeration. These two particles were the only ones among the 11 MOUDI stages exhibiting an EDX signal for S, with contributions amounting to ~2% in each particle. This may be linked to natural SO_4^{2-} existing in sea salt particles. Also, the particle between 3.2–5.6 μm contained a trace amount of Sc (1%). The largest three particles (≥ 5.6 μm) were expectedly irregularly shaped with both sharp and rounded edges, comprised mostly of oxygen, Al, Fe, and Ca based on EDX analysis.

3.2.3 Water-Soluble Elements

Averaged data across all MOUDI sets reveal that ICP-QQQ elements exhibited a variety of mass concentration profiles ranging from a distinct mode in either the sub- or supermicrometer range to having multiple modes below and above 1 μm (averages across all MOUDI sets shown in Figure 7). There were several elements with only one distinct peak, being in one of the two stages between 0.18-0.56 μm, including As, Cd, Co, Cr, Cs, Cu, Hf, Mn, Mo, Ni, Rb, Se, Sn, Tl, V, and Zn. In contrast, the following elements exhibited only one distinct peak in the supermicrometer range: Al, Ba, P, Pd, Sr, Ti, Y, and Zr. The rest of the elements exhibited more complex behavior with two distinct peaks in the sub- and supermicrometer range (Ag, Fe, Nb). The following section discusses relationships between all of the ions and elements with a view towards identifying characteristic sources.

3.3 Characteristic Sources and Species Relationships

A combination of PMF and correlation analysis helped identify clusters of closely related species stemming from distinct sources. The final PMF solution, based on five groups of species

(Figure 8), passed criteria associated with being physically valid and the close proximity of the calculated ratio of Q_{true}:$Q_{expected}$ (1.2) to 1.0. There was a high coefficient of variation between measured and predicted mass concentration when summing up all species for each MOUDI stage (r^2 = 0.79; sample size, n = 132), which added confidence in relying on the PMF model for source apportionment of PM. The five distinct clusters were named for their most plausible sources based on the species included in the groupings, with their overall contributions to the total mass based on PMF analysis shown in parenthesis (Table 3): Aged/Transported (48.0%), Sea Salt (22.5%), Combustion (18.7%), Vehicular/Resuspended Dust (5.6%), and Waste Processing (5.1%). For reference, a previous study near the northwestern edge of the Philippines identified six source factors for $PM_{2.5}$ that are fairly similar to those here (Bagtasa et al., 2018): sea salt, resuspended fine dust, local solid waste burning, and long range transport of (i) industrial emissions, (ii) solid waste burning, and (iii) secondary sulfate. Each of our five groupings will be discussed in detail below in decreasing order of contribution to total measured mass concentrations.

3.3.1 Aged/Transported Aerosol

Although not due to one individual source, there was a distinct PMF factor that included species commonly produced via gas-to-particle conversion processes (NH_4^+, SO_4^{2-}, MSA, oxalate). Correlation analysis (Table 4) also pointed to a large cluster of species significantly related to each other, including the aforementioned ions and a suite of other organic acids (phthalate, succinate, adipate), MSA, and DMA. The latter three inorganic and organic acid ions exhibited significant correlations with each other ($r \geqslant 0.68$), but also with several elements ($r \geqslant 0.36$: K, V, Rb, Cs, Sn), which were likely co-emitted with the precursor vapors of the secondarily produced ions. Although BC concentrations were quantified from set MO13, their interrelationships with water-soluble ions from simultaneously collected set MO14 are representative for other sets. The results showed that BC was significantly correlated (r: 0.61-0.92) with 15 species, including those mentioned above (owing to co-emission) and also a few elements that were found via PMF to be stronger contributors to the Combustion source discussed in Section 3.3.3 (Ni, Cu, As, Se, Cd, Tl, Pb).

This PMF source factor is referred to as Aged/Transported owing to it characteristic species being linked to sources distant from the sample site. Examples include MSA and DMA being secondarily produced from ocean-derived gaseous emissions (e.g., Sorooshian et al., 2009), and K

stemming from biomass burning emissions from upwind regions such as Sumatra and Borneo (Xian et al., 2013). Previous studies (Reid et al., 2012; Wang et al., 2013) have shown that phenomena such as SWM and El-Nino events not only influence biomass burning activities in the Malay Peninsula but also impact the transport and distribution of emissions in the study region. For instance, Reid et al. (2016b) showed that enhancement in monsoonal flow facilitates the advection of biomass burning and anthropogenic emissions to the Philippines from Sumatra and Borneo. Subsequent work will investigate more deeply the impact of biomass burning from those upwind regions on the sample site during the SWM.

While NH_4^+ and SO_4^{2-} require time for production owing to being secondarily produced from precursor vapors (i.e., SO_2, NH_3), oxalate is the smallest dicarboxylic acid and requires lengthier chemistry pathways for its production and thus is more likely produced in instances of aerosol transport and aging (e.g., Wonaschuetz et al., 2012; Ervens et al., 2018). The various elements associated with this cluster are co-emitted with the precursors to the aforementioned ions and are linked to a variety of sources: metallurgical processes (Anderson et al., 1988; Csavina et al., 2011; Youn et al., 2016), fuel combustion (Nriagu, 1989; Allen et al., 2001; Shafer et al., 2012; Rocha and Correa, 2018), residual oil combustion (Watson et al., 2004), biomass burning (Maudlin et al., 2015), marine and terrestrial biogenic emissions (Sorooshian et al., 2015), and plastics processing (Fraser et al., 2003). In addition, there is extensive ship traffic in the general study region, which is a major source of species in this cluster of species, particularly V and SO_4^{2-} (e.g., Murphy et al., 2009; Coggon et al., 2012).

PMF analysis suggested that the Aged/Transported factor contributed 48.0% to the total water-soluble mass budget during the study period. Most of the contribution resided in the submicrometer range (68.9%) unlike the supermicrometer range (18.6%), which is consistent with the overall mass size distribution of total PM peaking in the submicrometer range (Figure 2). The reconstructed mass size distribution for this PMF source factor shows the dominance of the mass in the submicrometer range with a peak between 0.32–0.56 μm (Figure 9). The correlation matrices for the sub- and supermicrometer size ranges also show that the correlations between the species most prominent in the Aged/Transported category are stronger for the former size range (Tables S2-S3). The contribution of this PMF factor to the supermicrometer range is likely associated with species secondarily produced on coarse aerosol such as dust and sea salt. This is evident in the

individual species mass size distributions where there is a dominant submicrometer mode but also non-negligible mass above 1 μm.

Even though the PM in a heavily populated urban region, such as Metro Manila, is typically thought to be dominated by local sources of aerosols, the current PMF results show that the largest contributions to water-soluble aerosol mass are from Aged/Transported pollution. This finding is contrary to the expectation that (a) the signal of transported aerosols would be lost in the noise of locally-produced aerosols, and (b) the removal of aerosols over the ocean surrounding the Philippines by processes such as wet scavenging would significantly reduce the contribution of transported aerosols. Even though other cities may have different pollution signatures, varying in pollutant type and amount, this phenomenon of Aged/Transported pollution forming a significant portion of the water-soluble mass may be applicable to other cities, especially those in Southeast Asia.

3.3.2 Sea Salt

As the MO sampling site is approximately 13 km from the nearest shoreline (Figure 1a) and downwind of Manila Bay in the SWM season, there was a great potential for marine emissions to impact the samples. There were several species with similar mass size distributions (mode: 1.8–5.6 μm) and highly correlated total mass concentrations ($r \geqslant 0.51$) that are linked to sea salt: Cl^-, Na^+, Ca^{2+}, Mg^{2+}, Ba, and Sr. The correlations between these species were stronger when examining just the supermicrometer range as compared to the submicrometer range (Tables S2-S3). The majority of these species was used in PMF analysis and formed a distinct cluster amounting to 22.0% of the total study period's mass budget. This source contributed only 0.6% to the submicrometer mass concentration but 53.5% for the supermicrometer size range. The reconstructed mass size distribution for this source factor is shifted farthest to the larger diameters as compared to the other four sources with a peak between 1.8-3.2 μm (Figure 9).

It is noteworthy that this factor has the highest share of NO_3^- among all identified sources. This result is consistent with mass size distributions shown in Figure 5 in which NO_3^- peaks in the supermicrometer range similar to sea salt constituents (e.g., Na^+ and Cl^-). Although sea salt particles naturally contain NO_3^- (Seinfeld and Pandis, 2016) (mass ratio of NO_3^-:Na^+ = 9.8×10^{-8} – 6.5×10^{-5}), the extremely high ratio of NO_3^-:Na^+ (mass ratio ~1.8) suggests that only a negligible portion of NO_3^- in this factor originated from primary sea salt particles. Thus, the majority of NO_3^-

is most likely due to HNO_3 partitioning to existing sea salt particles (e.g., Fitzgerald, 1991; Allen et al., 1996; Dasgupta et al., 2007; Maudlin et al., 2015). In addition, the Cl^-:Na^+ mass ratio in this profile (0.65) is smaller than that in sea salt particles (1.81), indicating high Cl^- depletion mainly due to reactions of HNO_3 with NaCl (Ro et al., 2001; Yao et al., 2003; Braun et al., 2017). Moreover, elevated loadings of trace elements (e.g., Ba, Cu, Zn, and Co) could be linked to mixing of marine emissions with urban sources (e.g., vehicle and industrial emissions) during their transport inland to the sampling site (Roth and Okada, 1998). This process of aging is consistent with the observed morphology of the sea salt particles in this study, revealing non-cubical shapes that are rounded owing to the likely addition of acidic species such as HNO_3 (Figure 6).

3.3.3 Combustion

There are numerous sources of combustion in the study region including a variety of mobile sources (e.g., cars, utility vehicles, trucks, buses, motorcycles) and stationary sources (e.g., power stations, cement works, oil refineries, boiler stations, utility boilers). Consequently, the next highest contributor to total mass during the study period according to PMF (18.7%) was the cluster of species including Ni, As, Co, P, Mo, and Cr, which is defined as the Combustion factor. These species have been reported to be rich in particles emitted from combustion of fossil fuel and residual oil (Linak and Miller, 2000; Allen et al., 2001; Wasson et al., 2005; Mahowald et al., 2008; Mooibroek et al., 2011; Prabhakar et al., 2014b). Although not included in PMF analysis, other species significantly correlated with the previous ones include maleate and Ag, which also stem from fuel combustion (Kawamura and Kaplan, 1987; Lin et al., 2005; Sorooshian et al., 2007). Ag specifically is an element in waste incinerator fly ash (Buchholz and Landsberger, 1993; Tsakalou et al., 2018) and its strong correlation with Co ($r = 0.85$) and Mo ($r = 0.64$) provides support for this source factor being linked to combustion processes. Maleate is commonly found in engine exhaust (Kawamura and Kaplan, 1987), while Cr is a tracer for power plant emissions (Singh et al., 2002; Behera et al., 2015). Of all species examined in this study, BC was best correlated with As ($r = 0.92$), while its correlation with Ni ($r = 0.85$) was among the highest.

As the elements in this cluster peaked in concentration in the submicrometer mode, the weight percentage of this factor is more than double below 1 μm (23.9%) as compared to above 1 μm (11.3%). The reconstructed mass size distribution for this source factor peaks between 0.18–0.32 μm, which is smaller than the modal diameter range for the Aged/Transported source factor

(0.32–0.56 μm) likely owing to closer sources and thus less time for growth to occur via condensation and coagulation.

3.3.4 Vehicular/Resuspended Dust

The next PMF source factor contains chemical signatures of dust because of high contributions to Al, Ti, Ca, and Fe. These crustal elements are strongly related to resuspension of dust by traffic and construction activities (Singh et al., 2002; Harrison et al., 2011). Other elements that were prominent in this factor included Zr, Y, Mn, Cr, and Ba, which are associated with tire and brake wear (Adachi and Tainosho, 2004; Gietl et al., 2010; Song and Gao, 2011; Harrison et al., 2012; Vossler et al., 2016), although some of them can be linked to the exhaust as well (e.g., Lin et al., 2005; Song and Gao, 2011). This source is named Vehicular/Resuspended Dust and contributed 5.6% to the total study period's mass concentrations.

The weight percentage contribution of this factor was much higher for the supermicrometer range (11.3%) as compared to the submicrometer range (1.5%), which is consistent with the Sea Salt source factor owing to similar mass size distributions of the individual species associated with the two source categories (Figures 5 and 7). Additional species correlated significantly with the crustal species included Hf and Nb, which also exhibited mass peaks between 1.8–3.2 μm. The reconstructed mass size distribution for this source factor is similar to that of Sea Salt in that there is a peak between 1.8–3.2 μm, but there is less of a unimodal profile owing to what appears to be a secondary mode between 0.56–1.0 μm (Figure 9), which could be linked to some of the non-dust components of vehicular emissions.

3.3.5 Waste Processing

The final PMF source factor, contributing the least overall to total mass (5.1%), featured Zn, Cd, Pb, Mn, and Cu as its main components. These species are linked to waste processing, including especially electronic waste (e-waste) and battery burning and recycling (Gullett et al., 2007; Iijima et al., 2007), which was previously reported for Manila (Pabroa et al., 2011). The latter study reported that although there are a few licensed operations for battery recycling, there are numerous unregulated cottage melters across Manila that regularly melt metal from batteries and discard the waste freely. Fujimori et al. (2012) additionally showed that e-waste recycling led

to emissions of the following elements (in agreement with this PMF cluster) around Metro Manila: Ni, Cu, Pb, Zn, Cd, Ag, in, As, Co, Fe, and Mn.

This was the only PMF factor exhibiting comparable weight percentages both below (5.1%) and above 1 μm (5.3%). This is reflected in the mass size distributions of the species included in this cluster being fairly uniformly distributed below and above 1 μm. This is also demonstrated in the reconstructed mass size distribution of this source factor as it clearly exhibits a mode between the other four sources (0.56–1.0 μm) and is the broadest mode (Figure 9). The explanation for this is likely rooted in the diversity of sources contained within this source profile that lead to different sizes of particles. Examples of such sources include processing of different types of waste at varying temperatures and through various processes (e.g., burning, melting, grinding) (Keshtkar and Ashbaugh, 2007),

4. Conclusions

This study used various analytical techniques (gravimetry, IC, ICP-QQQ, black carbon spectroscopy, and microscopy), meteorological data, and a source apportionment model (PMF) to characterize the sources, chemical composition, and morphology of size-resolved ambient PM in Metro Manila, Philippines during the SWM season of 2018. The main results of this study include the following:

- The total mass concentrations were measured on two occasions and were 18.6 μg m^{-3} and 53.0 μg m^{-3}. Water-soluble mass concentrations were measured on 12 occasions and were on average 8.53 ± 4.48 μg m^{-3} (range = 2.7–16.6 μg m^{-3}). Simultaneous measurements of total, water-soluble, and BC mass revealed a composition of 26.9% BC, 31.3% water-soluble components, and 41.8% unaccounted mass.
- Size-resolved BC mass concentration was measured on one occasion, with the mass sum of all MOUDI stages reaching 14.3 μg m^{-3}. Most of the BC mass (95%) was contained in the 0.1–1 μm range (i.e., the Greenfield gap) where wet scavenging by rain is inefficient. The measured BC peaked in the size range of 0.18 – 0.32 μm and accounted for 51.8% of the measured PM for that stage. In the range of 0.10 – 0.18 μm, the mass percent contribution of BC to the measured PM was 78.1%.

- Most of the total mass resided in the submicrometer mode (0.32–0.56 μm); however, one MOUDI set revealed an additional supermicrometer mode (1.8–3.2 μm). Water-soluble species that peaked in the submicrometer mode were associated with secondarily produced species, including inorganic acids, amines, MSA, and organic acids. Water-soluble species that peaked in the supermicrometer mode were associated with sea salt and crustal material. Most of the unaccounted mass was for $D_p > 0.32$ μm.
- The most abundant water-soluble species was SO_4^{2-} (44% ± 6%), followed by NH_4^+ (18% ± 5%), NO_3^- (10 ± 3%), Na^+ (8 ± 3%), and Cl^- (6% ± 3%). Correlation analysis revealed that total water-soluble mass was most correlated with temperature (r = 0.64) and rainfall accumulation (r = -0.49) among meteorological factors considered, although other factors were likely influential such as wind direction and speed.
- Regardless of particle size, the majority of single particles examined with SEM-EDX were non-spherical with evidence of agglomeration.
- PMF analysis suggested that there were five factors influencing the water-soluble fraction of PM collected at the sampling site. These factors, their contribution to total water-soluble mass, and the main species that permit them to be linked to a physical source are as follows: Aged/Transported (48.0%; NH_4^+, SO_4^{2-}, MSA, oxalate), Sea Salt (22.5%; Cl^-, NO_3^-, Ca^{2+}, Na^+, Mg^{2+}, Ba, Sr), Combustion (18.7%; Ni, As, Co, P, Mo, Cr), Vehicular/Resuspended Dust (5.6%; Al, Ti, Fe), and Waste Processing (5.1%; Zn, Cd, Pb, Mn, Cu). The dominant contribution of Aged/Transported aerosols to water-soluble mass contradicts two expectations: (i) locally-produced sources in polluted cities should drown out the signal of transported aerosols, and (ii) the signal of transported aerosols should be significantly reduced due to scavenging processes upwind of the measurement site.

Although the current study focuses exclusively on the SWM season in Metro Manila, results of this study are applicable to the study of aerosol impacts on Southeast Asia and other regions. First, the significant presence of Aged/Transported aerosols in Metro Manila indicates that PM in the region has the ability to travel long distances during the SWM season, despite the typical assumption that wet scavenging effectively removes most of the particles. Characterization of aerosols in Metro Manila is therefore important for better understanding the impacts that local emissions will have on locations downwind of Metro Manila, including other populated cities in

Southeast and East Asia. Transport of pollution and decreased wet scavenging during the SWM season may become increasingly important as studies have shown a decrease in SWM rainfall and increase in the number of no-rain days during the SWM season in the western Philippines in recent decades (e.g., Cruz et al., 2013).

Second, Southeast Asia has been named "one of the most hostile environments on the planet for aerosol remote sensing" (Reid et al., 2013). Therefore, space-based remote sensing of aerosol characteristics, such as retrievals of aerosol optical depth (AOD), in this region are difficult. In situ measurements are critical for characterization of PM in this region, especially during seasons such as the SWM when clouds are especially prevalent and remote-sensing retrievals dependent on clear-sky conditions are lacking.

Third, this study provides a valuable dataset to compare to other regions impacted by monsoons where the impacts of enhanced moisture and rainfall on size-resolved composition are not well understood. As aqueous processing results in enhanced production of water-soluble species (e.g., sulfate, organic acids), it is noteworthy for this monsoonal region that the water-soluble fraction remains low relative to BC and other insoluble components. This has major implications for the hygroscopicity of the regional PM.

Finally, the results of this study will be used to inform future sampling campaigns in this region, including CAMP^{2}Ex planned for the SWM season of 2019 based in the Philippines. As the current MOUDI sampling campaign at MO is expected to extend for a full year, future work will focus on changes in aerosol characteristics and sources on a seasonal basis.

Data availability: All data used in this work are available upon request.

Author Contribution: MTC, MOC, JBS, ABM, CS, and AS designed the experiments and all co-authors carried out some aspect of the data collection. MTC, RAB, CS, LM, HD, and AS conducted data analysis and interpretation. MTC and AS prepared the manuscript with contributions from all co-authors.

Competing interests: The authors declare that they have no conflict of interest.

Acknowledgements: This research was funded by NASA grant 80NSSC18K0148. M. T. Cruz acknowledges support from the Philippine Department of Science and Technology's ASTHRD Program. R. A. Braun acknowledges support from the ARCS Foundation. A. B. MacDonald acknowledges support from the Mexican National Council for Science and Technology (CONACYT). We acknowledge Agilent Technologies for their support and Shane Snyder's laboratories for ICP-QQQ data.

References

Adachi, K., and Tainosho, Y.: Characterization of heavy metal particles embedded in tire dust, Environ Int, 30, 1009-1017, 10.1016/j.envint.2004.04.004, 2004.

Alas, H. D., Müller, T., Birmili, W., Kecorius, S., Cambaliza, M.O., Simpas, J. B., Cayetano, M., Weinhold, K., Vallar, E., Galvez, M.C., and Wiedensohler, A.: Spatial Characterization of Black Carbon Mass Concentration in the Atmosphere of a Southeast Asian Megacity: An Air Quality Case Study for Metro Manila, Philippines. Aerosol Air Qual Res. doi.org/10.4209/aaqr.2017.08.0281, 2017.

Allen, H. C., Laux, J. M., Vogt, R., FinlaysonPitts, B. J., and Hemminger, J. C.: Water-induced reorganization of ultrathin nitrate films on NaCl: Implications for the tropospheric chemistry of sea salt particles, J Phys Chem-Us, 100, 6371-6375, DOI 10.1021/jp953675a, 1996.

Allen, A. G., Nemitz, E., Shi, J. P., Harrison, R. M., and Greenwood, J. C.: Size distributions of trace metals in atmospheric aerosols in the United Kingdom, Atmos Environ, 35, 4581-4591, Doi 10.1016/S1352-2310(01)00190-X, 2001.

Almeida, G. P., Bittencourt, A. T., Evangelista, M. S., Vieira-Filho, M. S., and Fornaro, A.: Characterization of aerosol chemical composition from urban pollution in Brazil and its possible impacts on the aerosol hygroscopicity and size distribution, Atmos Environ, 202, 149-159, 10.1016/j.atmosenv.2019.01.024, 2019.

Anderson, J. R., Aggett, F. J., Buseck, P. R., Germani, M. S., and Shattuck, T. W.: Chemistry of Individual Aerosol-Particles from Chandler, Arizona, an Arid Urban-Environment, Environ Sci Technol, 22, 811-818, DOI 10.1021/es00172a011, 1988.

Aswini, A. R., Hegde, P., Nair, P. R., and Aryasree, S.: Seasonal changes in carbonaceous aerosols over a tropical coastal location in response to meteorological processes, Science of The Total Environment, 656, 1261-1279, https://doi.org/10.1016/j.scitotenv.2018.11.366, 2019.

Bagtasa, G., Cayetano, M. G., and Yuan, C. S.: Seasonal variation and chemical characterization of $PM_{2.5}$ in northwestern Philippines, Atmos Chem Phys, 18, 4965-4980, 10.5194/acp-18-4965-2018, 2018.

Bautista, A. T., Pabroa, P. C. B., Santos, F. L., Racho, J. M. D., and Quirit, L. L.: Carbonaceous particulate matter characterization in an urban and a rural site in the Philippines, Atmos Pollut Res, 5, 245-252, 10.5094/Apr.2014.030, 2014.

Begam, G. R., Vachaspati, C. V., Ahammed, Y. N., Kumar, K. R., Reddy, R. R., Sharma, S. K., Saxena, M., and Mandal, T. K.: Seasonal characteristics of water-soluble inorganic ions and carbonaceous aerosols in total suspended particulate matter at a rural semi-arid site, Kadapa (India), Environmental Science and Pollution Research, 24, 1719-1734, 10.1007/s11356-016-7917-1, 2017.

Behera, S. N., Betha, R., Huang, X., and Balasubramanian, R.: Characterization and estimation of human airway deposition of size-resolved particulate-bound trace elements during a recent haze episode in Southeast Asia, Environ Sci Pollut R, 22, 4265-4280, 10.1007/s11356-014-3645-6, 2015.

Berresheim, H.: Biogenic Sulfur Emissions from the Sub-Antarctic and Antarctic Oceans, J Geophys Res-Atmos, 92, 13245-13262, 10.1029/JD092iD11p13245, 1987.

Braun, R. A., Dadashazar, H., MacDonald, A. B., Aldhaif, A. M., Maudlin, L. C., Crosbie, E., Aghdam, M. A., Mardi, A. H., and Sorooshian, A.: Impact of Wildfire Emissions on Chloride and Bromide Depletion in Marine Aerosol Particles, Environ Sci Technol, 51, 9013-9021, 10.1021/acs.est.7b02039, 2017.

Buchholz, B. A., and Landsberger, S.: Trace-Metal Analysis of Size-Fractioned Municipal Solid-Waste Incinerator Fly-Ash and Its Leachates, J Environ Sci Heal A, 28, 423-441, Doi 10.1080/10934529309375887, 1993.

Burgermeister, S., and Georgii, H. W.: Distribution of Methanesulfonate, Nss Sulfate and Dimethylsulfide over the Atlantic and the North-Sea, Atmos Environ a-Gen, 25, 587-595, Doi 10.1016/0960-1686(91)90056-D, 1991.

Chen, Y. Z., Shah, N., Huggins, F. E., and Huffman, G. P.: Microanalysis of ambient particles from Lexington, KY, by electron microscopy, Atmos Environ, 40, 651-663, 10.1016/j.atmosenv.2005.09.036, 2006.

Chithra, V. S., and Nagendra, S. M. S.: Chemical and morphological characteristics of indoor and outdoor particulate matter in an urban environment, Atmos Environ, 77, 579-587, 10.1016/j.atmosenv.2013.05.044, 2013.

Chuang, M.-T., Chang, S.-C., Lin, N.-H., Wang, J.-L., Sheu, G.-R., Chang, Y.-J., and Lee, C.-T.: Aerosol chemical properties and related pollutants measured in Dongsha Island in the northern South China Sea during 7-SEAS/Dongsha Experiment, Atmospheric Environment, 78, 82-92, https://doi.org/10.1016/j.atmosenv.2012.05.014, 2013.

Clarke, A. D., Shinozuka, Y., Kapustin, V. N., Howell, S., Huebert, B., Doherty, S., Anderson, T., Covert, D., Anderson, J., Hua, X., Moore, K. G., McNaughton, C., Carmichael, G., and Weber, R.: Size distributions and mixtures of dust and black carbon aerosol in Asian outflow: Physiochemistry and optical properties, J Geophys Res-Atmos, 109, Artn D15s09

10.1029/2003jd004378, 2004.

Coggon, M. M., Sorooshian, A., Wang, Z., Metcalf, A. R., Frossard, A. A., Lin, J. J., Craven, J. S., Nenes, A., Jonsson, H. H., Russell, L. M., Flagan, R. C., and Seinfeld, J. H.: Ship impacts on the marine atmosphere: insights into the contribution of shipping emissions to the properties of marine aerosol and clouds, Atmos Chem Phys, 12, 8439-8458, 10.5194/acp-12-8439-2012, 2012.

Cohen, D. D., Stelcer, E., Santos, F. L., Prior, M., Thompson, C., and Pabroa, P. C. B.: Fingerprinting and source apportionment of fine particle pollution in Manila by IBA and PMF techniques: A 7-year study, X-Ray Spectrom, 38, 18-25, 10.1002/xrs.1112, 2009.

Crosbie, E., Sorooshian, A., Monfared, N. A., Shingler, T., and Esmaili, O.: A Multi-Year Aerosol Characterization for the Greater Tehran Area Using Satellite, Surface, and Modeling Data, Atmosphere-Basel, 5, 178-197, 10.3390/atmos5020178, 2014.

Crosbie, E., Youn, J. S., Balch, B., Wonaschutz, A., Shingler, T., Wang, Z., Conant, W. C., Betterton, E. A., and Sorooshian, A.: On the competition among aerosol number, size and composition in predicting CCN variability: a multi-annual field study in an urbanized desert, Atmos Chem Phys, 15, 6943-6958, 10.5194/acp-15-6943-2015, 2015.

Cruz, F. T., Narisma, G. T., Villafuerte, M. Q., Chua, K. U. C., and Olaguera, L. M.: A climatological analysis of the southwest monsoon rainfall in the Philippines, Atmos Res, 122, 609-616, 10.1016/j.atmosres.2012.06.010, 2013.

Csavina, J., Landazuri, A., Wonaschutz, A., Rine, K., Rheinheimer, P., Barbaris, B., Conant, W., Saez, A. E., and Betterton, E. A.: Metal and Metalloid Contaminants in Atmospheric Aerosols from Mining Operations, Water Air Soil Poll, 221, 145-157, 10.1007/s11270-011-0777-x, 2011.

Dasgupta, P. K., Campbell, S. W., Al-Horr, R. S., Ullah, S. M. R., Li, J. Z., Amalfitano, C., and Poor, N. D.: Conversion of sea salt aerosol to NaNO(3) and the production of HCl: Analysis of temporal behavior of aerosol chloride/nitrate and gaseous HCl/HNO(3) concentrations with AIM, Atmos Environ, 41, 4242-4257, 10.1016/j.atmosenv.2006.09.054, 2007.

Dumanoglu, Y., Kara, M., Altiok, H., Odabasi, M., Elbir, T., and Bayram, A.: Spatial and seasonal variation and source apportionment of volatile organic compounds (VOCs) in a heavily industrialized region, Atmos Environ, 98, 168-178, 10.1016/j.atmosenv.2014.08.048, 2014.

Ervens, B., Sorooshian, A., Aldhaif, A. M., Shingler, T., Crosbie, E., Ziemba, L., Campuzano-Jost, P., Jimenez, J. L., and Wisthaler, A.: Is there an aerosol signature of chemical cloud processing?, Atmos Chem Phys, 18, 16099-16119, 10.5194/acp-18-16099-2018, 2018.

Facchini, M. C., Decesari, S., Rinaldi, M., Carbone, C., Finessi, E., Mircea, M., Fuzzi, S., Moretti, F., Tagliavini, E., Ceburnis, D., and O'Dowd, C. D.: Important Source of Marine Secondary Organic Aerosol from Biogenic Amines, Environ Sci Technol, 42, 9116-9121, 10.1021/es8018385, 2008.

Farren, N. J., Dunmore, R. E., Mead, M. I., Mohd Nadzir, M. S., Samah, A. A., Phang, S. M., Bandy, B. J., Sturges, W. T., and Hamilton, J. F.: Chemical characterisation of water-soluble ions in atmospheric particulate matter on the east coast of Peninsular Malaysia, Atmos. Chem. Phys., 19, 1537-1553, 10.5194/acp-19-1537-2019, 2019.

Fitzgerald, J. W.: Marine Aerosols - a Review, Atmos Environ a-Gen, 25, 533-545, Doi 10.1016/0960-1686(91)90050-H, 1991.

Fraser, M. P., Cass, G. R., and Simoneit, B. R. T.: Air quality model evaluation data for organics. 6. C-3-C-24 organic acids, Environ Sci Technol, 37, 446-453, 10.1021/es0209262, 2003.

Fu, P. Q., Kawamura, K., Chen, J., Li, J., Sun, Y. L., Liu, Y., Tachibana, E., Aggarwal, S. G., Okuzawa, K., Tanimoto, H., Kanaya, Y., and Wang, Z. F.: Diurnal variations of organic molecular tracers and stable carbon isotopic composition in atmospheric aerosols over Mt. Tai in the North China Plain: an influence of biomass burning, Atmos Chem Phys, 12, 8359-8375, 10.5194/acp-12-8359-2012, 2012.

Fujimori, T., Takigami, H., Agusa, T., Eguchi, A., Bekki, K., Yoshida, A., Terazono, A., and Ballesteros, F. C.: Impact of metals in surface matrices from formal and informal electronic-waste recycling around Metro Manila, the Philippines, and intra-Asian comparison, J Hazard Mater, 221-222, 139-146, https://doi.org/10.1016/j.jhazmat.2012.04.019, 2012.

Ge, X. L., Wexler, A. S., and Clegg, S. L.: Atmospheric amines - Part I. A review, Atmos Environ, 45, 524-546, 10.1016/j.atmosenv.2010.10.012, 2011.

Gietl, J. K., Lawrence, R., Thorpe, A. J., and Harrison, R. M.: Identification of brake wear particles and derivation of a quantitative tracer for brake dust at a major road, Atmos Environ, 44, 141-146, 10.1016/j.atmosenv.2009.10.016, 2010.

Gullett, B. K., Linak, W. P., Touati, A., Wasson, S. J., Gatica, S., and King, C. J.: Characterization of air emissions and residual ash from open burning of electronic wastes during simulated rudimentary recycling operations, J Mater Cycles Waste, 9, 69-79, 10.1007/s10163-006-0161-x, 2007.

Harrison, R. M., Beddows, D. C. S., and Dall'Osto, M.: PMF Analysis of Wide-Range Particle Size Spectra Collected on a Major Highway, Environ Sci Technol, 45, 5522-5528, 10.1021/es2006622, 2011.

Harrison, R. M., Jones, A. M., Gietl, J., Yin, J. X., and Green, D. C.: Estimation of the Contributions of Brake Dust, Tire Wear, and Resuspension to Nonexhaust Traffic Particles Derived from Atmospheric Measurements, Environ Sci Technol, 46, 6523-6529, 10.1021/es300894r, 2012.

Hitzenberger, R., and Tohno, S.: Comparison of black carbon (BC) aerosols in two urban areas – concentrations and size distributions, Atmospheric Environment, 35, 2153-2167, https://doi.org/10.1016/S1352-2310(00)00480-5, 2001.

Hopke, P. K., Cohen, D. D., Begum, B. A., Biswas, S. K., Ni, B., Pandit, G. G., Santoso, M., Chung, Y. S., Davy, P., Markwitz, A., Waheed, S., Siddique, N., Santos, F. L., Pabroa, P. C. B., Seneviratne, M. C. S., Wimolwattanapun, W., Bunprapob, S., Vuong, T. B., Duy Hien, P. and Markowicz, A.: Urban air quality in the Asian region, Sci. Total Environ., 404(1), 103–112, doi:10.1016/j.scitotenv.2008.05.039, 2008.

Huang, S. L., Rahn, K. A., and Arimoto, R.: Testing and optimizing two factor-analysis techniques on aerosol at Narragansett, Rhode Island, Atmos Environ, 33, 2169-2185, Doi 10.1016/S1352-2310(98)00324-0, 1999.

Iijima, A., Sato, K., Yano, K., Tago, H., Kato, M., Kimura, H., and Furuta, N.: Particle size and composition distribution analysis of automotive brake abrasion dusts for the evaluation of antimony sources of airborne particulate matter, Atmos Environ, 41, 4908-4919, 10.1016/j.atmosenv.2007.02.005, 2007.

Kahnert, M., Nousiainen, T., and Veihelmann, B.: Spherical and spheroidal model particles as an error source in aerosol climate forcing and radiance computations: A case study for feldspar aerosols, J Geophys Res-Atmos, 110, Artn D18s13, 10.1029/2004jd005558, 2005.

Kautzman, K. E., Surratt, J. D., Chan, M. N., Chan, A. W. H., Hersey, S. P., Chhabra, P. S., Dalleska, N. F., Wennberg, P. O., Flagan, R. C., and Seinfeld, J. H.: Chemical Composition of

Gas- and Aerosol-Phase Products from the Photooxidation of Naphthalene, J Phys Chem A, 114, 913-934, 10.1021/jp908530s, 2010.

Kawamura, K., and Ikushima, K.: Seasonal-Changes in the Distribution of Dicarboxylic-Acids in the Urban Atmosphere, Environ Sci Technol, 27, 2227-2235, DOI 10.1021/es00047a033, 1993.

Kawamura, K., and Kaplan, I. R.: Motor Exhaust Emissions as a Primary Source for Dicarboxylic-Acids in Los-Angeles Ambient Air, Environ Sci Technol, 21, 105-110, DOI 10.1021/es00155a014, 1987.

Kawamura, K., and Sakaguchi, F.: Molecular distributions of water soluble dicarboxylic acids in marine aerosols over the Pacific Ocean including tropics, J Geophys Res-Atmos, 104, 3501-3509, Doi 10.1029/1998jd100041, 1999.

Kecorius, S., Madueño, L., Löndahl, J., Vallar, E., Galvez, M. C., Idolor, L. F., Gonzaga-Cayetano, M., Müller, T., Birmili, W., and Wiedensohler, A.: Respiratory tract deposition of inhaled roadside ultrafine refractory particles in a polluted megacity of South-East Asia, Science of The Total Environment, 663, 265-274, https://doi.org/10.1016/j.scitotenv.2019.01.338, 2019.

Kecorius, S., Madueno, L., Vallar, E., Alas, H., Betito, G., Birmili, W., Cambaliza, M. O., Catipay, G., Gonzaga-Cayetano, M., Galvez, M. C., Lorenzo, G., Muller, T., Simpas, J. B., Tamayo, E. G., and Wiedensohler, A.: Aerosol particle mixing state, refractory particle number size distributions and emission factors in a polluted urban environment: Case study of Metro Manila, Philippines, Atmos Environ, 170, 169-183, 10.1016/j.atmosenv.2017.09.037, 2017.

Keshtkar, H., and Ashbaugh, L. L.: Size distribution of polycyclic aromatic hydrocarbon particulate emission factors from agricultural burning, Atmos Environ, 41, 2729-2739, 10.1016/j.atmosenv.2006.11.043, 2007.

Kim Oanh, N. T., Upadhyay, N., Zhuang, Y. H., Hao, Z. P., Murthy, D. V. S., Lestari, P., Villarin, J. T., Chengchua, K., Co, H. X., Dung, N. T. and Lindgren, E. S.: Particulate air pollution in six Asian cities: Spatial and temporal distributions, and associated sources, Atmos. Environ., 40(18), 3367–3380, doi:10.1016/j.atmosenv.2006.01.050, 2006.

Kleindienst, T. E., Jaoui, M., Lewandowski, M., Offenberg, J. H., and Docherty, K. S.: The formation of SOA and chemical tracer compounds from the photooxidation of naphthalene and its methyl analogs in the presence and absence of nitrogen oxides, Atmos Chem Phys, 12, 8711-8726, 10.5194/acp-12-8711-2012, 2012.

Liao, H., Chen, W. T., and Seinfeld, J. H.: Role of climate change in global predictions of future tropospheric ozone and aerosols, J Geophys Res-Atmos, 111, Artn D12304, 10.1029/2005jd006852, 2006.

Lin, C. C., Chen, S. J., Huang, K. L., Hwang, W. I., Chang-Chien, G. P., and Lin, W. Y.: Characteristics of metals in nano/ultrafine/fine/coarse particles collected beside a heavily trafficked road, Environ Sci Technol, 39, 8113-8122, 10.1021/es048182a, 2005.

Linak, W. P., and Miller, C. A.: Comparison of particle size distributions and elemental partitioning from the combustion of pulverized coal and residual fuel oil, J Air Waste Manage, 50, 1532-1544, Doi 10.1080/10473289.2000.10464171, 2000.

Ma, Y., Li, S., Zheng, J., Khalizov, A., Wang, X., Wang, Z., and Zhou, Y.: Size-resolved measurements of mixing state and cloud-nucleating ability of aerosols in Nanjing, China, Journal of Geophysical Research: Atmospheres, 122, 9430-9450, 10.1002/2017jd026583, 2017.

Mahowald, N., Jickells, T. D., Baker, A. R., Artaxo, P., Benitez-Nelson, C. R., Bergametti, G., Bond, T. C., Chen, Y., Cohen, D. D., Herut, B., Kubilay, N., Losno, R., Luo, C., Maenhaut, W., McGee, K. A., Okin, G. S., Siefert, R. L., and Tsukuda, S.: Global distribution of atmospheric phosphorus sources, concentrations and deposition rates, and anthropogenic impacts, Global Biogeochem Cy, 22, 10.1029/2008gb003240, 2008.

Marple, V., Olson, B., Romay, F., Hudak, G., Geerts, S. M. and Lundgren, D.: Second generation micro-orifice uniform deposit impactor, 120 MOUDI-II: Design, Evaluation, and application to long-term ambient sampling, Aerosol Sci. Technol., 48(4), 427–433, doi:10.1080/02786826.2014.884274, 2014.

Martens, C. S., Wesolowski, J. J., Harriss, R. C., and Kaifer, R.: Chlorine Loss from Puerto-Rican and San-Francisco-Bay Area Marine Aerosols, J Geophys Res, 78, 8778-8792, DOI 10.1029/JC078i036p08778, 1973.

Maudlin, L. C., Wang, Z., Jonsson, H. H., and Sorooshian, A.: Impact of wildfires on size-resolved aerosol composition at a coastal California site, Atmos Environ, 119, 59-68, 10.1016/j.atmosenv.2015.08.039, 2015.

Metcalf, A. R., Craven, J. S., Ensberg, J. J., Brioude, J., Angevine, W., Sorooshian, A., Duong, H. T., Jonsson, H. H., Flagan, R. C., and Seinfeld, J. H.: Black carbon aerosol over the Los Angeles Basin during CalNex, J Geophys Res-Atmos, 117, 10.1029/2011jd017255, 2012.

Mielonen, T., Levy, R. C., Aaltonen, V., Komppula, M., de Leeuw, G., Huttunen, J., Lihavainen, H., Kolmonen, P., Lehtinen, K. E. J., and Arola, A.: Evaluating the assumptions of surface reflectance and aerosol type selection within the MODIS aerosol retrieval over land: the problem of dust type selection, Atmos Meas Tech, 4, 201-214, 10.5194/amt-4-201-2011, 2011.

Miller, J., and Miller, J.C.: Statistics and chemometrics for analytical chemistry. Pearson Education, 2018.

Mishra, S. K., Agnihotri, R., Yadav, P. K., Singh, S., Prasad, M. V. S. N., Praveen, P. S., Tawale, J. S., Rashmi, Mishra, N. D., Arya, B. C., and Sharma, C.: Morphology of Atmospheric Particles over Semi-Arid Region (Jaipur, Rajasthan) of India: Implications for Optical Properties, Aerosol Air Qual Res, 15, 974-+, 10.4209/aaqr.2014.10.0244, 2015.

Mooibroek, D., Schaap, M., Weijers, E. P., and Hoogerbrugge, R.: Source apportionment and spatial variability of $PM_{2.5}$ using measurements at five sites in the Netherlands, Atmospheric Environment, 45, 4180-4191, 10.1016/j.atmosenv.2011.05.017, 2011.

Mosier, A. R., Andre, C. E., and Viets, F. G.: Identification of Aliphatic-Amines Volatilized from Cattle Feedyard, Environ Sci Technol, 7, 642-644, DOI 10.1021/es60079a009, 1973.

Muller, C., Iinuma, Y., Karstensen, J., van Pinxteren, D., Lehmann, S., Gnauk, T., and Herrmann, H.: Seasonal variation of aliphatic amines in marine sub-micrometer particles at the Cape Verde islands, Atmos Chem Phys, 9, 9587-9597, 2009.

Murphy, S. M., Agrawal, H., Sorooshian, A., Padro, L. T., Gates, H., Hersey, S., Welch, W. A., Jung, H., Miller, J. W., Cocker, D. R., Nenes, A., Jonsson, H. H., Flagan, R. C., and Seinfeld, J. H.: Comprehensive Simultaneous Shipboard and Airborne Characterization of Exhaust from a Modern Container Ship at Sea, Environ Sci Technol, 43, 4626-4640, 10.1021/es802413j, 2009.

Norris, G., Duvall, R., Brown, S., and Bai, S.: EPA Positive Matrix Factorization (PMF) 5.0 fundamentals and User Guide Prepared for the US Environmental Protection Agency Office of Research and Development, Washington, DC. Inc., Petaluma, 2014.

Nriagu, J. O.: A Global Assessment of Natural Sources of Atmospheric Trace-Metals, Nature, 338, 47-49, DOI 10.1038/338047a0, 1989.

Pabroa, P. C. B., Santos, F. L., Morco, R. P., Racho, J. M. D., Bautista, A. T., and Bucal, C. G. D.: Receptor modeling studies for the characterization of air particulate lead pollution sources in Valenzuela sampling site (Philippines), Atmos Pollut Res, 2, 213-218, 10.5094/Apr.2011.027, 2011.

Philippine Statistics Authority: https://psa.gov.ph/, Accessed 28 August 2018.

Polissar, A., Hopke, P., Paatero, P., Malm, W., and Sisler, J.: Atmospheric aerosol over Alaska 2. Elemental composition and sources. Journal of Geophysical Research 103, 19045-19057, 1998.

Prabhakar, G., Ervens, B., Wang, Z., Maudlin, L. C., Coggon, M. M., Jonsson, H. H., Seinfeld, J. H., and Sorooshian, A.: Sources of nitrate in stratocumulus cloud water: Airborne measurements during the 2011 E-PEACE and 2013 NiCE studies, Atmos Environ, 97, 166-173, 10.1016/j.atmosenv.2014.08.019, 2014a.

Prabhakar, G., Sorooshian, A., Toffol, E., Arellano, A. F., and Betterton, E. A.: Spatiotemporal distribution of airborne particulate metals and metalloids in a populated arid region, Atmos Environ, 92, 339-347, 10.1016/j.atmosenv.2014.04.044, 2014b.

Qu, W. J., Wang, J., Zhang, X. Y., Wang, D., and Sheng, L. F.: Influence of relative humidity on aerosol composition: Impacts on light extinction and visibility impairment at two sites in coastal area of China, Atmos Res, 153, 500-511, 10.1016/j.atmosres.2014.10.009, 2015.

Raatikainen, T., Brus, D., Hyvärinen, A. P., Svensson, J., Asmi, E., and Lihavainen, H.: Black carbon concentrations and mixing state in the Finnish Arctic, Atmos. Chem. Phys., 15, 10057-10070, 10.5194/acp-15-10057-2015, 2015.

Ramachandran, S., and Rajesh, T. A.: Black carbon aerosol mass concentrations over Ahmedabad, an urban location in western India: Comparison with urban sites in Asia, Europe, Canada, and the United States, J Geophys Res-Atmos, 112, 10.1029/2006jd007488, 2007.

Ran, L., Deng, Z. Z., Wang, P. C., and Xia, X. A.: Black carbon and wavelength-dependent aerosol absorption in the North China Plain based on two-year aethalometer measurements, Atmos Environ, 142, 132-144, 10.1016/j.atmosenv.2016.07.014, 2016.

Reddington, C. L., McMeeking, G., Mann, G. W., Coe, H., Frontoso, M. G., Liu, D., Flynn, M., Spracklen, D. V., and Carslaw, K. S.: The mass and number size distributions of black carbon aerosol over Europe, Atmos. Chem. Phys., 13, 4917-4939, 10.5194/acp-13-4917-2013, 2013.

Reff, A., Eberly, S.I., and Bhave, P.V.: Receptor modeling of ambient particulate matter data using positive matrix factorization: Review of existing methods. J Air Waste Manage 57, 146-154, 2007.

Reid, J. S., Xian, P., Hyer, E. J., Flatau, M. K., Ramirez, E. M., Turk, F. J., Sampson, C. R., Zhang, C., Fukada, E. M., and Maloney, E. D.: Multi-scale meteorological conceptual analysis of observed active fire hotspot activity and smoke optical depth in the Maritime Continent, Atmos Chem Phys, 12, 2117-2147, 10.5194/acp-12-2117-2012, 2012.

Reid, J. S., Hyer, E. J., Johnson, R. S., Holben, B. N., Yokelson, R. J., Zhang, J. L., Campbell, J. R., Christopher, S. A., Di Girolamo, L., Giglio, L., Holz, R. E., Kearney, C., Miettinen, J., Reid, E. A., Turk, F. J., Wang, J., Xian, P., Zhao, G. Y., Balasubramanian, R., Chew, B. N., Janjai, S., Lagrosas, N., Lestari, P., Lin, N. H., Mahmud, M., Nguyen, A. X., Norris, B., Oanh, N. T. K., Oo, M., Salinas, S. V., Welton, E. J., and Liew, S. C.: Observing and understanding the Southeast Asian aerosol system by remote sensing: An initial review and analysis for the Seven Southeast Asian Studies (7SEAS) program, Atmos Res, 122, 403-468, 10.1016/j.atmosres.2012.06.005, 2013.

Reid, J. S., Xian, P., Holben, B. N., Hyer, E. J., Reid, E. A., Salinas, S. V., Zhang, J. L., Campbell, J. R., Chew, B. N., Holz, R. E., Kuciauskas, A. P., Lagrosas, N., Posselt, D. J., Sampson, C. R., Walker, A. L., Welton, E. J., and Zhang, C. D.: Aerosol meteorology of the Maritime Continent for the 2012 7SEAS southwest monsoon intensive study - Part 1: regional-scale phenomena, Atmos Chem Phys, 16, 14041-14056, 10.5194/acp-16-14041-2016, 2016a.

Reid, J. S., Lagrosas, N. D., Jonsson, H. H., Reid, E. A., Atwood, S. A., Boyd, T. J., Ghate, V. P., Xian, P., Posselt, D. J., Simpas, J. B., Uy, S. N., Zaiger, K., Blake, D. R., Bucholtz, A., Campbell, J. R., Chew, B. N., Cliff, S. S., Holben, B. N., Holz, R. E., Hyer, E. J., Kreidenweis, S. M., Kuciauskas, A. P., Lolli, S., Oo, M., Perry, K. D., Salinas, S. V., Sessions, W. R., Smirnov, A., Walker, A. L., Wang, Q., Yu, L. Y., Zhang, J. L., and Zhao, Y. J.: Aerosol meteorology of Maritime Continent for the 2012 7SEAS southwest monsoon intensive study - Part 2: Philippine receptor observations of fine-scale aerosol behavior, Atmos Chem Phys, 16, 14057-14078, 10.5194/acp-16-14057-2016, 2016b.

Rocha, L. D. S., and Correa, S. M.: Determination of size-segregated elements in diesel-biodiesel blend exhaust emissions, Environ Sci Pollut R, 25, 18121-18129, 10.1007/s11356-018-1980-8, 2018.

Rogge, W. F., Mazurek, M. A., Hildemann, L. M., Cass, G. R., and Simoneit, B. R. T.: Quantification of Urban Organic Aerosols at a Molecular-Level - Identification, Abundance and Seasonal-Variation, Atmos Environ a-Gen, 27, 1309-1330, Doi 10.1016/0960-1686(93)90257-Y, 1993.

Ro, C. U., Oh, K. Y., Kim, H., Kim, Y. P., Lee, C. B., Kim, K. H., Kang, C. H., Osan, J., De Hoog, J., Worobiec, A., and Van Grieken, R.: Single-particle analysis of aerosols at Cheju Island, Korea, using low-Z electron probe X-ray microanalysis: A direct proof of nitrate formation from sea salts, Environ Sci Technol, 35, 4487-4494, 10.1021/es0155231, 2001.

Rolph, G.D.: Real-time Environmental Applications and Display sYstem (READY) website (http://ready.Arl.NOAA.Gov), NOAA Air Resour. Lab., Silver Spring, Md., 2016.

Roth, B., and Okada, K.: On the modification of sea-salt particles in the coastal atmosphere, Atmos Environ, 32, 1555-1569, Doi 10.1016/S1352-2310(97)00378-6, 1998.

Saltzman, E. S., Savoie, D. L., Zika, R. G., and Prospero, J. M.: Methane Sulfonic-Acid in the Marine Atmosphere, J Geophys Res-Oceans, 88, 897-902, DOI 10.1029/JC088iC15p10897, 1983.

Saltzman, E. S., Savoie, D. L., Prospero, J. M., and Zika, R. G.: Methanesulfonic-Acid and Non-Sea-Salt Sulfate in Pacific Air - Regional and Seasonal-Variations, J Atmos Chem, 4, 227-240, Doi 10.1007/Bf00052002, 1986.

Schade, G. W., and Crutzen, P. J.: Emission of Aliphatic-Amines from Animal Husbandry and Their Reactions - Potential Source of N_2O and HCN, J Atmos Chem, 22, 319-346, Doi 10.1007/Bf00696641, 1995.

Schwarz, J. P., Gao, R. S., Spackman, J. R., Watts, L. A., Thomson, D. S., Fahey, D. W., Ryerson, T. B., Peischl, J., Holloway, J. S., Trainer, M., Frost, G. J., Baynard, T., Lack, D. A., de Gouw, J. A., Warneke, C., and Del Negro, L. A.: Measurement of the mixing state, mass, and optical size of individual black carbon particles in urban and biomass burning emissions, Geophysical Research Letters, 35, 10.1029/2008gl033968, 2008.

Seinfeld, J. H., and Pandis, S. N.: Atmospheric chemistry and physics (3rd ed.). New York: Wiley-Interscience, 2016.

Shafer, M. M., Toner, B. M., Oyerdier, J. T., Schauer, J. J., Fakra, S. C., Hu, S. H., Herner, J. D., and Ayala, A.: Chemical Speciation of Vanadium in Particulate Matter Emitted from Diesel Vehicles and Urban Atmospheric Aerosols, Environ Sci Technol, 46, 189-195, 10.1021/es200463c, 2012.

Shingler, T., Sorooshian, A., Ortega, A., Crosbie, E., Wonaschutz, A., Perring, A. E., Beyersdorf, A., Ziemba, L., Jimenez, J. L., Campuzano-Jost, P., Mikoviny, T., Wisthaler, A., and Russell, L. M.: Ambient observations of hygroscopic growth factor and f(RH) below 1: Case studies from surface and airborne measurements, J Geophys Res-Atmos, 121, 13661-13677, 10.1002/2016jd025471, 2016.

Shiraiwa, M., Kondo, Y., Moteki, N., Takegawa, N., Sahu, L. K., Takami, A., Hatakeyama, S., Yonemura, S., and Blake, D. R.: Radiative impact of mixing state of black carbon aerosol in Asian outflow, Journal of Geophysical Research: Atmospheres, 113, 10.1029/2008jd010546, 2008.

Simpas, J., Lorenzo, G., and Cruz, M. T.: Monitoring Particulate Matter Levels and Composition for Source Apportionment Study in Metro Manila, Philippines, in: Improving Air Quality in Asian Developing Countries: Compilation of Research Findings, Kim Oanh, N. T. (Ed.), NARENCA, Vietnam Publishing House of Natural Resources, Environment and Cartography, Vietnam, 239-261, 2014.

Singh, M., Jaques, P. A., and Sioutas, C.: Size distribution and diurnal characteristics of particle-bound metals in source and receptor sites of the Los Angeles Basin, Atmos Environ, 36, 1675-1689, Pii S1352-2310(02)00166-8, Doi 10.1016/S1352-2310(02)00166-8, 2002.

Song, F., and Gao, Y.: Size distributions of trace elements associated with ambient particular matter in the affinity of a major highway in the New Jersey-New York metropolitan area, Atmos Environ, 45, 6714-6723, 10.1016/j.atmosenv.2011.08.031, 2011.

Sorooshian, A., Ng, N. L., Chan, A. W. H., Feingold, G., Flagan, R. C., and Seinfeld, J. H.: Particulate organic acids and overall water-soluble aerosol composition measurements from the 2006 Gulf of Mexico Atmospheric Composition and Climate Study (GoMACCS), J Geophys Res-Atmos, 112, 10.1029/2007jd008537, 2007.

Sorooshian, A., Murphy, S. N., Hersey, S., Gates, H., Padro, L. T., Nenes, A., Brechtel, F. J., Jonsson, H., Flagan, R. C., and Seinfeld, J. H.: Comprehensive airborne characterization of aerosol from a major bovine source, Atmos Chem Phys, 8, 5489-5520, DOI 10.5194/acp-8-5489-2008, 2008.

Sorooshian, A., Padro, L. T., Nenes, A., Feingold, G., McComiskey, A., Hersey, S. P., Gates, H., Jonsson, H. H., Miller, S. D., Stephens, G. L., Flagan, R. C., and Seinfeld, J. H.: On the link between ocean biota emissions, aerosol, and maritime clouds: Airborne, ground, and satellite measurements off the coast of California, Global Biogeochem Cy, 23,

10.1029/2009gb003464, 2009.

Sorooshian, A., Crosbie, E., Maudlin, L. C., Youn, J. S., Wang, Z., Shingler, T., Ortega, A. M., Hersey, S., and Woods, R. K.: Surface and airborne measurements of organosulfur and methanesulfonate over the western United States and coastal areas, J Geophys Res-Atmos, 120, 8535-8548, 10.1002/2015jd023822, 2015.

Stein, A. F., Draxler, R. R., Rolph, G. D., Stunder, B. J. B., Cohen, M. D., and Ngan, F.: NOAA's Hysplit Atmospheric Transport and Dispersion Modeling System, B Am Meteorol Soc, 96, 2059-2077, 10.1175/Bams-D-14-00110.1, 2015.

Tai, A. P. K., Mickley, L. J., and Jacob, D. J.: Correlations between fine particulate matter (PM2.5) and meteorological variables in the United States: Implications for the sensitivity of PM2.5 to climate change, Atmos Environ, 44, 3976-3984, 10.1016/j.atmosenv.2010.06.060, 2010.

Tsakalou, C., Papamarkou, S., Tsakiridis, P. E., Bartzas, G., and Tsakalakis, K.: Characterization and leachability evaluation of medical wastes incineration fly and bottom ashes and their vitrification outgrowths, J Environ Chem Eng, 6, 367-376, 10.1016/j.jece.2017.12.012, 2018.

VandenBoer, T. C., Petroff, A., Markovic, M. Z., and Murphy, J. G.: Size distribution of alkyl amines in continental particulate matter and their online detection in the gas and particle phase, Atmos Chem Phys, 11, 4319-4332, 10.5194/acp-11-4319-2011, 2011.

Villafuerte, M. Q., Matsumoto, J., Akasaka, I., Takahashi, H. G., Kubota, H., and Cinco, T. A.: Long-term trends and variability of rainfall extremes in the Philippines, Atmos Res, 137, 1-13, 10.1016/j.atmosres.2013.09.021, 2014.

Vossler, T., Cernikovsky, L., Novak, J., and Williams, R.: Source apportionment with uncertainty estimates of fine particulate matter in Ostrava, Czech Republic using Positive Matrix Factorization, Atmos Pollut Res, 7, 503-512, 10.1016/j.apr.2015.12.004, 2016.

Wang, J., Ge, C., Yang, Z. F., Hyer, E. J., Reid, J. S., Chew, B. N., Mahmud, M., Zhang, Y. X., and Zhang, M. G.: Mesoscale modeling of smoke transport over the Southeast Asian Maritime Continent: Interplay of sea breeze, trade wind, typhoon, and topography, Atmos Res, 122, 486-503, 10.1016/j.atmosres.2012.05.009, 2013.

Wang, Y. Q., Zhang, X. Y., and Draxler, R. R.: TrajStat: GIS-based software that uses various trajectory statistical analysis methods to identify potential sources from long-term air pollution measurement data, Environ Modell Softw, 24, 938-939, 10.1016/j.envsoft.2009.01.004, 2009.

Wasson, S. J., Linak, W. P., Gullett, B. K., King, C. J., Touati, A., Huggins, F. E., Chen, Y. Z., Shah, N., and Huffman, G. P.: Emissions of chromium, copper, arsenic, and PCDDs/Fs from open burning of CCA-treated wood, Environ Sci Technol, 39, 8865-8876, 10.1021/es050891g, 2005.

Watson, J. G.: *Protocol for Applying and Validating the CMB Model for $PM_{2.5}$ and VOC*. Report No. EPA-451/R-04-001. US Environmental Protection Agency, Research Triangle Park, NC., 2004.

Watts, S. F., Watson, A., and Brimblecombe, P.: Measurements of the Aerosol Concentrations of Methanesulfonic Acid, Dimethyl-Sulfoxide and Dimethyl Sulfone in the Marine Atmosphere of the British-Isles, Atmos Environ, 21, 2667-2672, Doi 10.1016/0004-6981(87)90198-3, 1987.

Wonaschuetz, A., Sorooshian, A., Ervens, B., Chuang, P. Y., Feingold, G., Murphy, S. M., de Gouw, J., Warneke, C., and Jonsson, H. H.: Aerosol and gas re-distribution by shallow cumulus clouds: An investigation using airborne measurements, J Geophys Res-Atmos, 117, 10.1029/2012jd018089, 2012.

Wu, D., Zhang, F., Lou, W. H., Li, D., and Chen, J. M.: Chemical characterization and toxicity assessment of fine particulate matters emitted from the combustion of petrol and diesel fuels, Sci Total Environ, 605, 172-179, 10.1016/j.scitotenv.2017.06.058, 2017.

Xian, P., Reid, J. S., Atwood, S. A., Johnson, R. S., Hyer, E. J., Westphal, D. L., and Sessions, W.: Smoke aerosol transport patterns over the Maritime Continent, Atmos Res, 122, 469-485, 10.1016/j.atmosres.2012.05.006, 2013.

Xu, G. J., and Gao, Y.: Characterization of marine aerosols and precipitation through shipboard observations on the transect between 31 degrees N-32 degrees S in the West Pacific, Atmos Pollut Res, 6, 154-161, 10.5094/Apr.2015.018, 2015.

Yao, X. H., Fang, M., and Chan, C. K.: The size dependence of chloride depletion in fine and coarse sea-salt particles, Atmos Environ, 37, 743-751, 10.1016/S1352-2310(02)00955-X, 2003.

Youn, J. S., Wang, Z., Wonaschutz, A., Arellano, A., Betterton, E. A., and Sorooshian, A.: Evidence of aqueous secondary organic aerosol formation from biogenic emissions in the North American Sonoran Desert, Geophys Res Lett, 40, 3468-3472, 10.1002/grl.50644, 2013.

Youn, J. S., Crosbie, E., Maudlin, L. C., Wang, Z., and Sorooshian, A.: Dimethylamine as a major alkyl amine species in particles and cloud water: Observations in semi-arid and coastal regions, Atmos Environ, 122, 250-258, 10.1016/j.atmosenv.2015.09.061, 2015.

Youn, J. S., Csavina, J., Rine, K. P., Shingler, T., Taylor, M. P., Saez, A. E., Betterton, E. A., and Sorooshian, A.: Hygroscopic Properties and Respiratory System Deposition Behavior of Particulate Matter Emitted By Mining and Smelting Operations, Environ Sci Technol, 50, 11706-11713, 10.1021/acs.est.6b03621, 2016.

Table 1. Summary of average operating parameters, meteorological conditions, and total resolved water-soluble mass concentration for each MOUDI sample set collected at Manila Observatory (MO) during the 2018 Southwest Monsoon period. On two occasions, simultaneous MOUDI sets were collected for one set to undergo gravimetric analysis (MO3 and MO13) to compare with mass resolved from chemical speciation of the water-soluble fraction (MO4 and MO14). One additional MOUDI set devoted to microscopy analysis was collected using aluminum substrates for one hour on August 1 at 30 LPM.

Sample set name	Dates	Duration (hrs)	Flow rate (LPM)	Wind speed (m/s)	Wind direction (°)	T (°C)	Rain (mm)	Water-soluble mass (μg m^{-3})
MO1	Jul 19-20	24	30	3.3	90.1	24.9	47	4.6
MO2	Jul 23-25	54	30	1.3	95.8	26.7	7.8	6.5
MO3/4	Jul 25-30	119	28/30	1.2	111.8	26.7	49.6	5.2
MO5	Jul 30-Aug 1	42	29	2.6	98.1	27.5	52.8	9.2
MO6	Aug 6-8	48	27	0.9	127.5	26.1	30.4	5.1
MO7	Aug 14-16	48	28	3.0	107.8	27.8	2.8	13.7
MO8	Aug 22-24	48	29	3.5	108.7	28.1	1	12.8
MO9	Sep 1-3	48	27	0.7	98.6	26.6	51.6	6.2
MO10	Sep 10–12	48	29	1.0	94.7	26.2	78.4	6.4
MO11	Sep 18–20	48	27	0.5	290.2	27.8	0	2.7
MO12	Sep 26-28	48	27	1.2	96.3	27.8	6.8	13.5
MO13/14	Oct 6-8	48	28/26	0.6	108.2	27.8	0.8	16.6

Table 2. Charge balance slopes (cations on y-axis; anions on x-axis) for the MOUDI sets shown including the averages of all sets (All) for three size ranges: submicrometer stages spanning 0.056 – 1.0 μm; supermicrometer stages (> 1.0 μm); and all stages (> 0.056 μm). The species used in the charge balance analysis include those speciated with the IC (listed in Section 2.3) plus K from ICP-QQQ analysis.

Sample set	0.056 – 1.0 μm	> 1 μm	> 0.056 μm
MO1	0.87	1.37	0.89
MO2	1.46	1.26	1.41
MO4	1.25	1.17	1.21
MO5	1.35	1.43	1.41
MO6	1.29	1.45	1.31
MO7	1.40	1.23	1.36
MO8	1.35	1.33	1.36
MO9	1.28	1.55	1.26
MO10	1.37	1.36	1.35
MO11	0.97	1.60	1.27
MO12	1.37	1.19	1.33
MO14	1.31	1.28	1.29
All	1.35	1.24	1.33

Table 3. Contributions (in weight percentage) of each PMF source factor to the total mass in different diameter ranges.

Diameter Range (μm)	Aged/ Transported	Sea Salt	Combustion	Vehicular/ Resuspended Dust	Waste Processing
> 0.056	48.0%	22.5%	18.7%	5.6%	5.1%
0.056 - 1.0	68.9%	0.6%	23.9%	1.5%	5.1%
> 1.0	18.6%	53.5%	11.3%	11.3%	5.3%

Table 4. Correlation matrix (r values) between water-soluble species based on total MOUDI-integrated mass concentrations (> 0.056 μm). Blank cells represent statistically insignificant values. Results for the sub- and supermicrometer ranges are in Tables S2-S3. Panels A-E represent important species from each of the source profiles identified in Section 3.3: A = Aged/Transported, B = Sea Salt, C = Combustion, D = Vehicular/Resuspended Dust, E = Waste Processing. DMA – Dimethylamine, MSA – Methanesulfonate, PH – Phthalate, OX – Oxalate, MA – Maleate, SU – Succinate, AD – Adipate.

A)

OX	1.00														
SO_4	0.74	1.00													
NH_4	0.68	0.99	1.00												
Sn	0.71	0.87	0.85	1.00											
Rb	0.73	0.74	0.73	0.69	1.00										
K	0.76	0.71	0.69	0.69	0.97	1.00									
Cs	0.72	0.82	0.81	0.74	0.96	0.91	1.00								
V	0.36	0.64	0.63	0.48	0.53	0.51	0.57	1.00							
DMA		0.35		0.38	0.45	0.37	0.45		1.00						
MSA	0.71	0.89	0.89	0.79	0.90	0.85	0.92	0.51	0.47	1.00					
PH	0.68	0.67	0.68	0.73	0.82	0.76	0.80		0.38	0.88	1.00				
SU	0.63	0.56	0.59	0.44	0.87	0.81	0.82		0.68	0.78	0.84	1.00			
AD	0.40	0.66	0.70	0.62	0.70	0.70	0.77		0.84	0.74	0.75	0.90	1.00		
Se	0.75	0.75	0.73	0.66	0.80	0.78	0.79	0.32	0.34	0.78	0.80	0.88	0.88	1.00	
Tl	0.75	0.87	0.86	0.80	0.89	0.85	0.94	0.74	0.65	0.80	0.52	0.70		0.43	1.00
	OX	**SO_4**	**NH_4**	**Sn**	**Rb**	**K**	**Cs**	**V**	**DMA**	**MSA**	**PH**	**SU**	**AD**	**Se**	**Tl**

B)

Cl	1.00							
NO_3	0.76	1.00						
Ba	0.66	0.80	1.00					
Sr	0.78	0.87	0.91	1.00				
Ca	0.58	0.79	0.75	0.78	1.00			
Na	0.93	0.87	0.75	0.85	0.63	1.00		
Mg	0.91	0.87	0.77	0.87	0.66	0.99	1.00	
Hf					0.57			1.00
	Cl	**NO_3**	**Ba**	**Sr**	**Ca**	**Na**	**Mg**	**Hf**

C)

As	1.00							
Ni	0.58	1.00						
Co			1.00					
P		0.33	0.34	1.00				
Mo					1.00			
Cr	0.62	0.49		0.20		1.00		
MA			0.67		-0.42		1.00	
Ag			0.85		0.64			1.00
	As	**Ni**	**Co**	**P**	**Mo**	**Cr**	**Mal**	**Ag**

D)

Zr	1.00					
Y	0.75	1.00				
Al	0.88	0.76	1.00			
Fe	0.33	0.61	0.25	1.00		
Ti	0.84	0.66	0.82	0.41	1.00	
Nb	0.70	0.50	0.59	0.59	0.70	1.00
	Zr	**Y**	**Al**	**Fe**	**Ti**	**Nb**

E)

Cd	1.00				
Zn	0.60	1.00			
Cu	0.21	0.27	1.00		
Mn	0.28	0.61	0.22	1.00	
Pb	0.78	0.58	0.38	0.27	1.00
	Cd	**Zn**	**Cu**	**Mn**	**Pb**

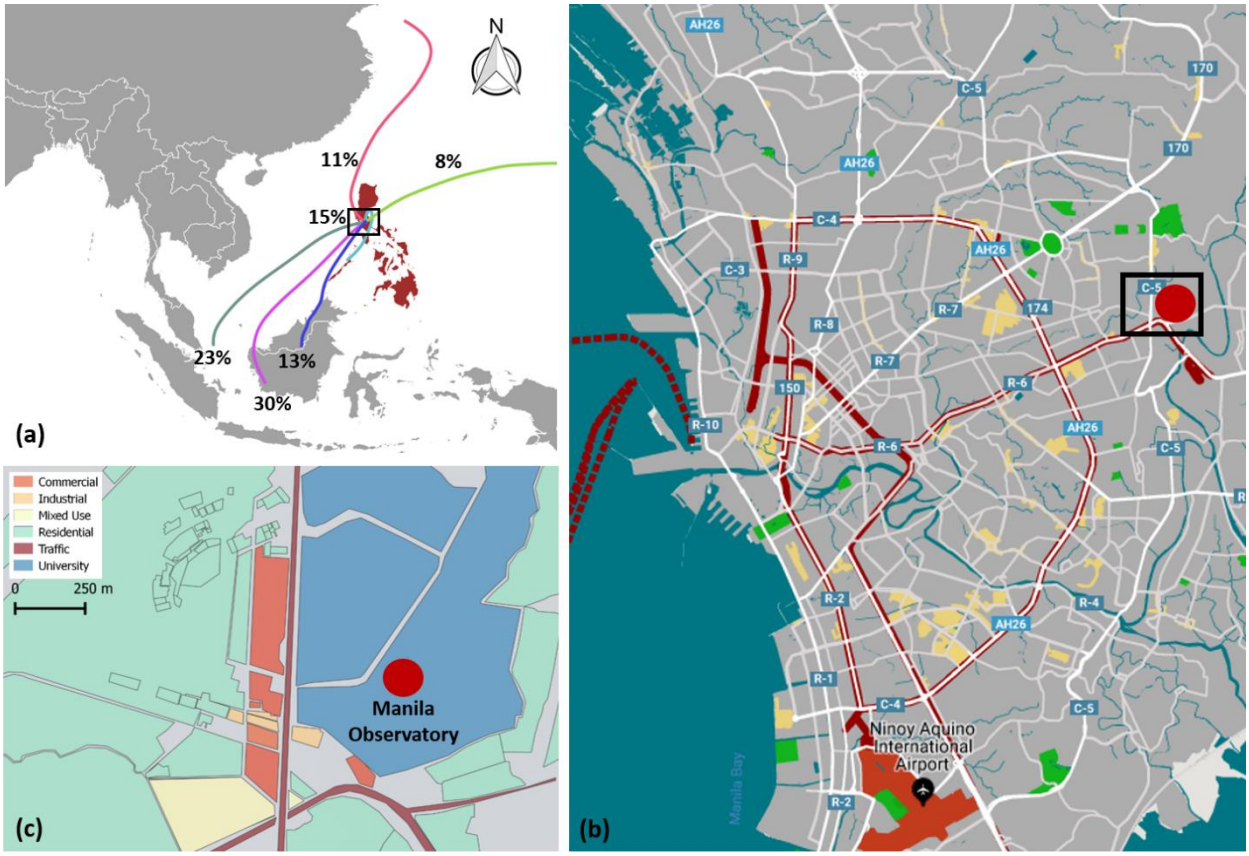

Figure 1. (a) Location of Metro Manila, Philippines relative to Southeast Asia. Also shown are 5-day backward trajectory frequencies during the sampling duration based on HYSPLIT cluster analysis; note that 15% correspond to trajectories within the black square. (b) Close-up view of Metro Manila showing the location of the Manila Observatory sampling site with a black rectangle. The base map shows roads, commercial centers, and major transit lines in the city. (c) Land use classification in the vicinity of the sampling site. (Sources: GADM, Snazzy Maps, OpenStreetMap, NOAA HYSPLIT, & TrajSat)

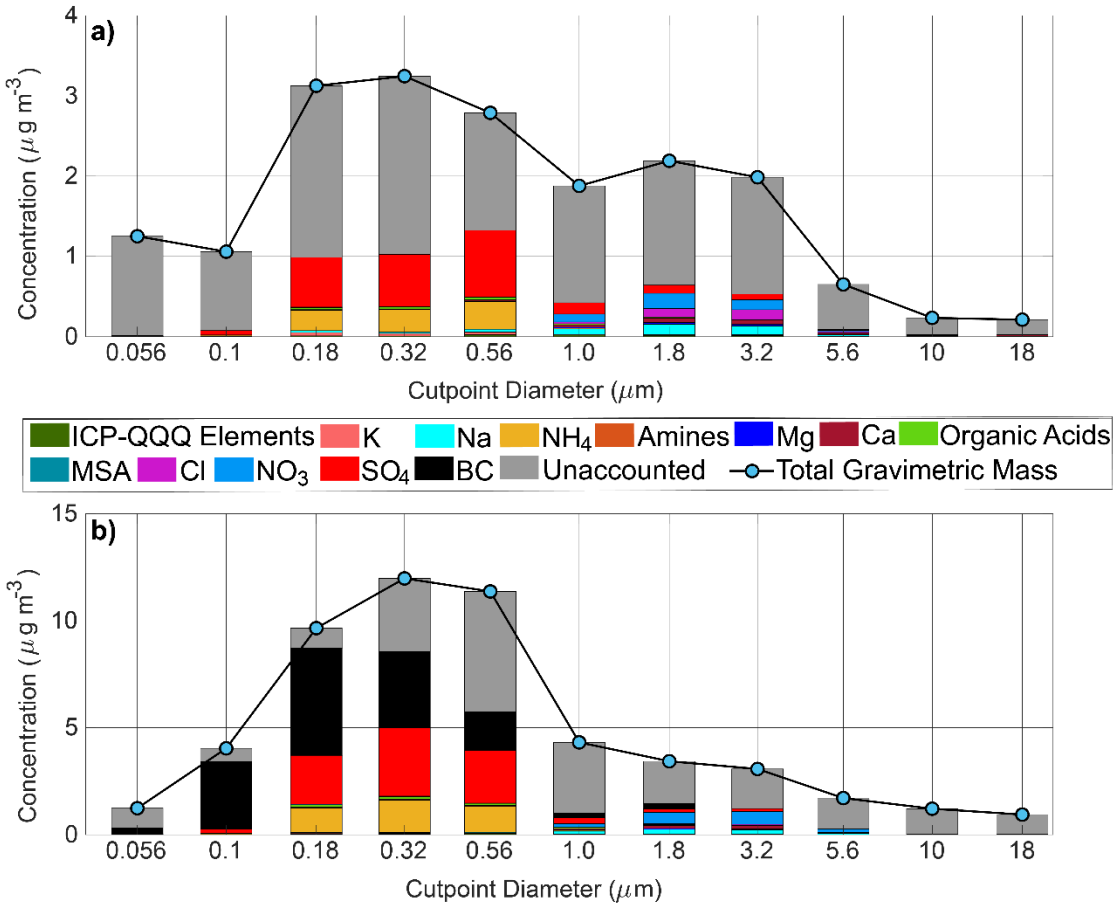

Figure 2. Mass size distributions of total PM (blue markers) and resolved chemical species (colored bars) for MOUDI sets (a) MO3/4 and (b) MO13/14. Note that set MO13 was the single MOUDI set where BC was quantified. ICP-QQQ = sum of water-soluble elements except K; amines = sum of DMA, TMA, DEA; organic acids = sum of oxalate, succinate, adipate, pyruvate, phthalate, maleate.

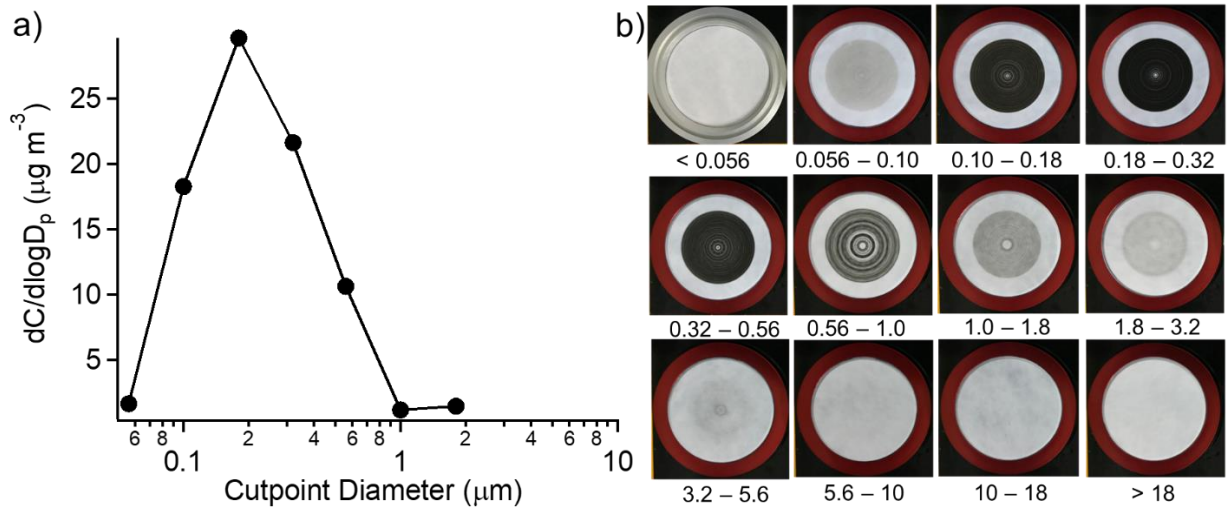

Figure 3. (a) Mass size distribution of BC retrieved from the MABI optical measurement at 870 nm for set MO13. Missing values were below detection limits. (b) Photographs of each stage of set MO13 with numbers below each image representing the aerodynamic diameter ranges in units of μm.

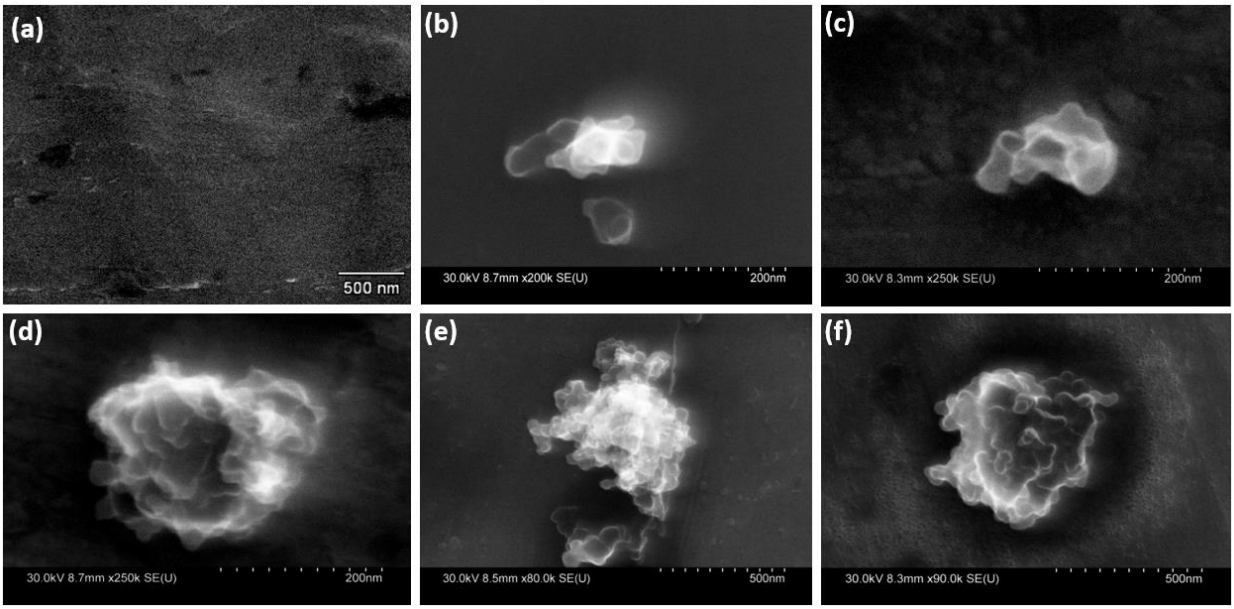

Figure 4. SEM image of a (a) blank filter and (b-f) individual particles in different sub-micrometer aerodynamic diameter ranges sampled by the MOUDI: (b) 0.056–0.1 μm, (c) 0.1–0.18 μm, (d) 0.18–0.32 μm, (e) 0.32–0.56 μm, (f) 0.56–1.0 μm.

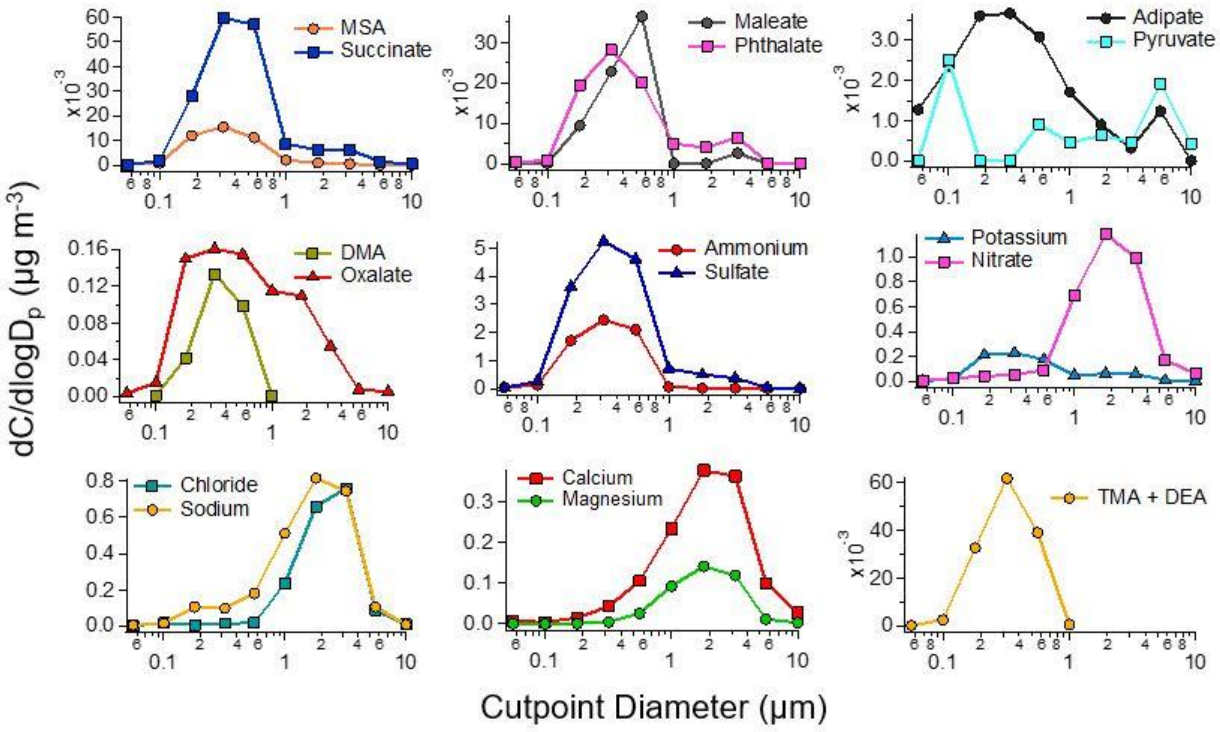

Figure 5. Average mass size distribution of water-soluble ions speciated via IC in addition to potassium from ICP-QQQ analysis.

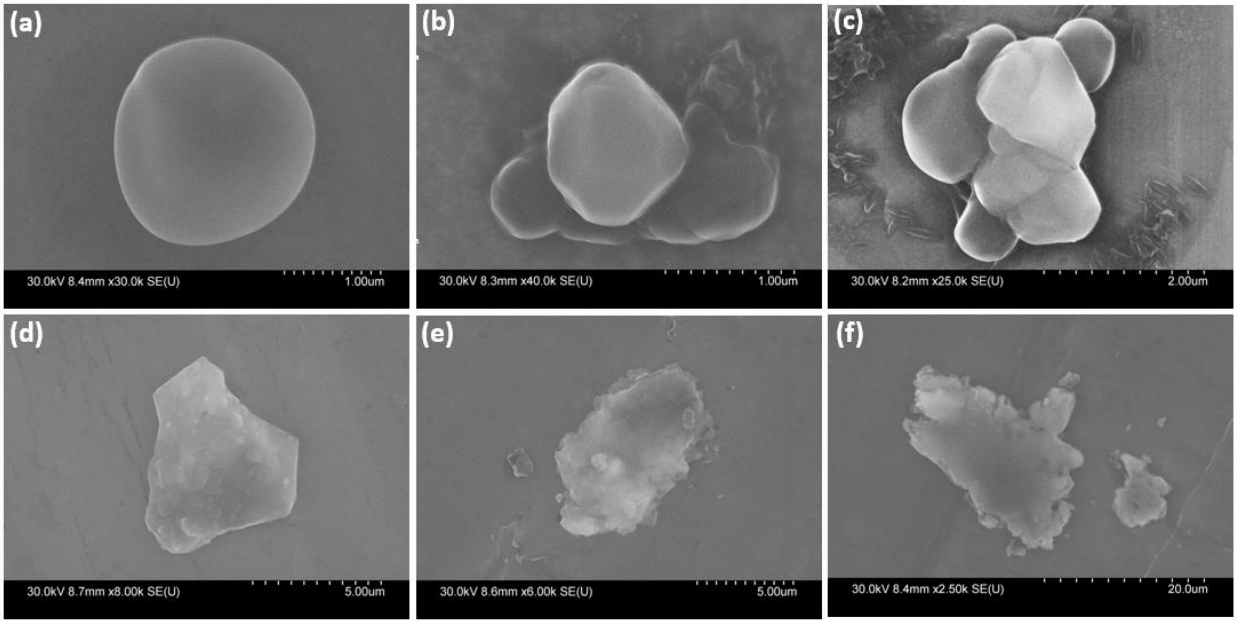

Figure 6. Same as Figure 4, but for different supermicrometer aerodynamic diameter ranges sampled by the MOUDI: (a) 1.0–1.8 μm, (b) 1.8–3.2 μm; (c) 3.2–5.6 μm, (d) 5.6–10 μm, (e) 10-18 μm, (f) > 18 μm.

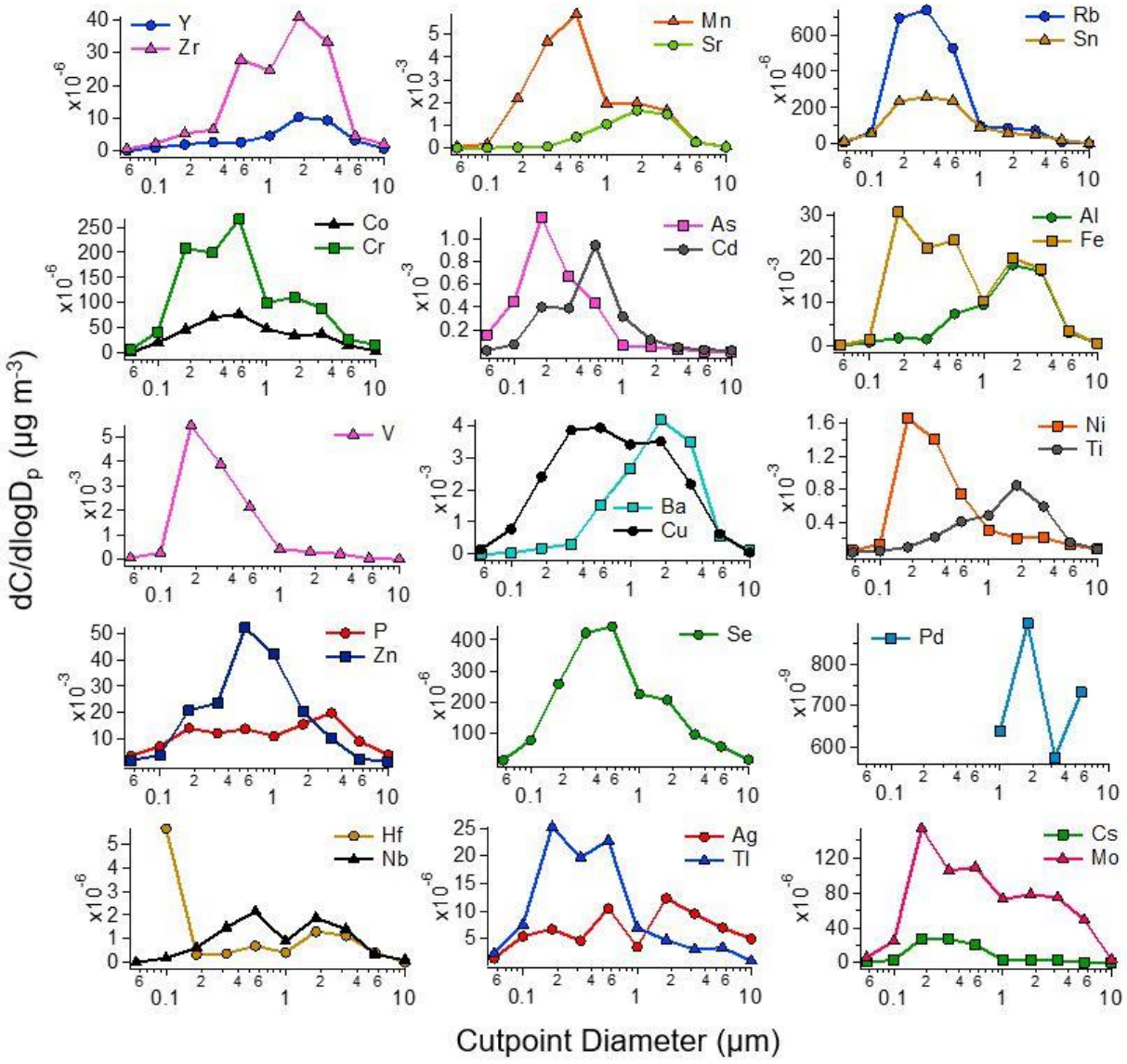

Figure 7. Average mass size distribution of water-soluble elements speciated via ICP-QQQ.

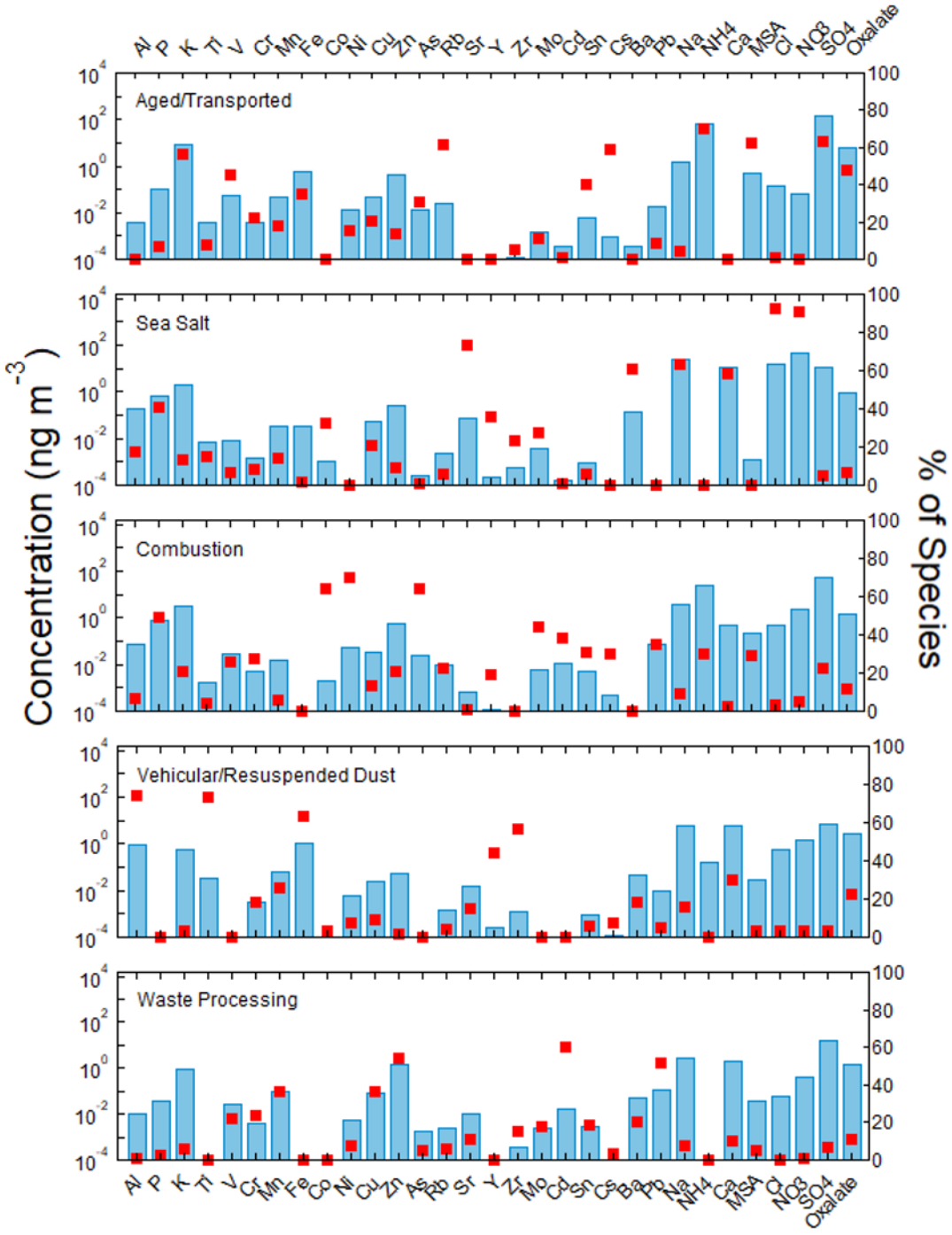

Figure 8. Overview of the PMF five factor solution with blue bars representing mass concentrations and red squares signifying the percentage of mass concentration contributed to constituents by each source factor.

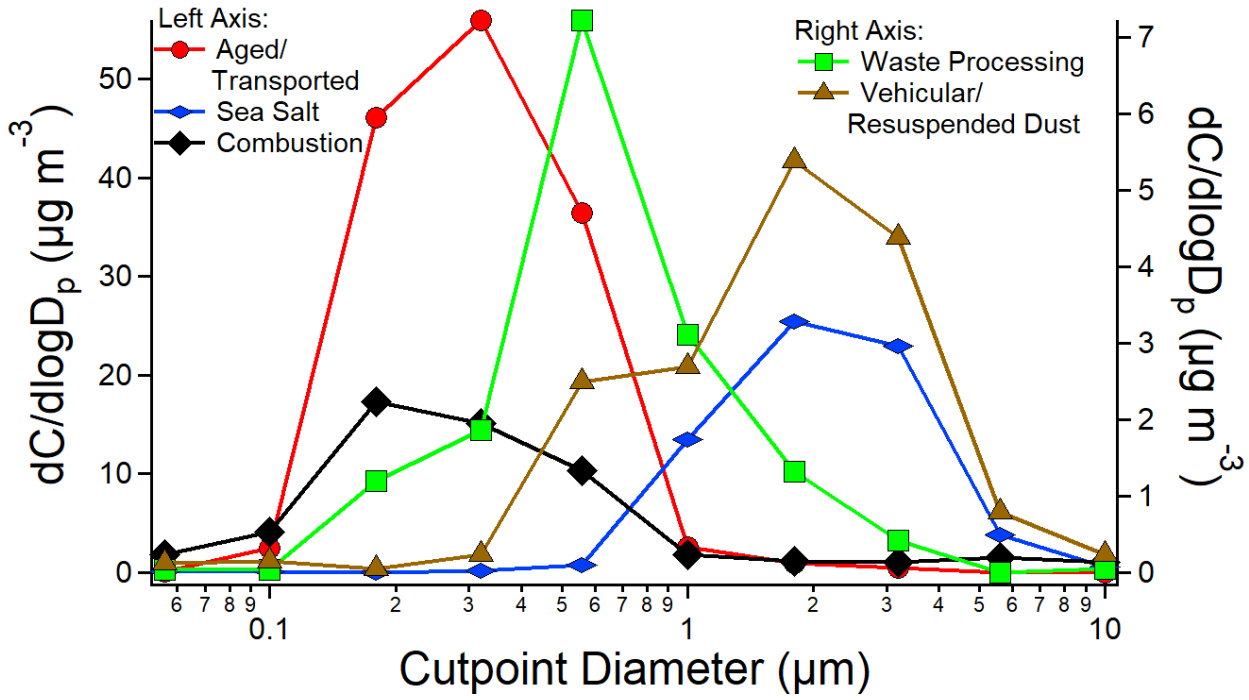

Figure 9. Reconstructed mass size distributions using PMF for the five major source profiles.

Table S1. Aqueous limits of detection (LOD) for the elements speciated by ICP-QQQ and water-soluble ions speciated by IC.

ICP	ppt
Ag	0.74
Al	29.47
As	7.95
Ba	3.70
Cd	4.19
Co	0.72
Cr	1.15
Cs	0.73
Cu	1.13
Fe	1.19
Hf	0.96
K	10.48
Mn	1.62
Mo	2.26
Nb	0.52
Ni	2.84
P	770.73
Pd	1.68
Rb	1.57
Se	82.39
Sn	1.77
Sr	1.10
Ti	39.05
Tl	0.38
V	1.35
Y	0.52
Zn	5.88
Zr	1.01

IC	ppm
Adipate	0.023
Ammonium	0.042
Calcium	0.045
Chloride	0.002
DMA	0.053
Magnesium	0.037
Maleate	0.007
MSA	0.012
Nitrate	0.009
Oxalate	0.012
Phthalate	0.021
Pyruvate	0.064
Sodium	0.043
Succinate	0.011
Sulfate	0.012
TMA & DEA	0.315

Table S2. Submicrometer (0.056 – 1 µm) correlation matrix of all water-soluble species measured by IC and ICP-MS based on total MOUDI-integrated mass concentrations. DMA – Dimethylamine, MSA – Methanesulfonate, PH – Phthalate, OX – Oxalate, MA – Maleate, SU – Succinate, AD – Adipate.

	DMA	MSA	PH	OX	MA	SU	AD	NH_4	NO_3	SO_4	Cl	Na	Mg	K	Ca	Al	Fe	Mn	Ti	Ba	Zn	Cu	V	Ni	P	Cr	Co	As	Se	Rb	Sr	Y	Zr	Nb	Mo	Ag	Cd	Sn	Cs	Hf	Tl	Pb
DMA	1.00																																										
MSA	0.42	1.00																																									
PH	0.37	0.92	1.00																																								
OX		0.92	0.85	1.00																																							
MA					1.00																																						
SU	0.67	0.78	0.82	0.68		1.00																																					
AD	0.81	0.69	0.75	0.66		0.80	1.00																																				
NH_4		0.86	0.67	0.87		0.46	0.64	1.00																																			
NO_3						-0.63			1.00																																			
SO_4		0.86	0.66	0.88			0.63	0.99		1.00																																		
Cl									0.52		1.00																																		
Na		0.42		0.56				0.57		0.62		1.00																																
Mg		0.30		0.32				0.36		0.39		0.73	1.00																															
K		0.84	0.76	0.86		0.81	0.71	0.61		0.63		0.41		1.00																													
Ca					0.47				0.38			0.50	0.52		1.00																													
Al		0.39	0.35	0.46		0.48		0.42		0.47		0.62	0.76	0.37	0.32	1.00																												
Fe				0.42			0.57					0.48		0.46			1.00																											
Mn				0.40						0.29		0.59		0.43	0.61		0.81	1.00																										
Ti		0.41	0.38	0.56		0.46		0.34		0.38		0.56	0.47	0.63	0.48	0.61	0.59	0.73	1.00																								
Ba				0.30				0.37	0.29	0.42		0.69	0.77		0.60	0.65		0.38	0.39	1.00																								
Zn				0.41				0.40	0.32	0.46		0.72	0.49	0.31	0.75	0.41	0.43	0.69	0.49	0.80	1.00																							
Cu	0.80			0.34			0.56			0.34		0.33	0.31	0.34		0.36		0.33	0.32	0.42	0.44	1.00																						
V		0.36		0.37				0.47		0.49				0.35							0.29		1.00																				
Ni		0.36		0.46				0.44		0.50		0.32		0.44							0.37	0.51	0.83	1.00																				
P	0.39																			0.32		0.65	0.37	0.40	1.00																		
Cr		0.38		0.58			0.62	0.45		0.50		0.67	0.36	0.59	0.43	0.36	0.87	0.74	0.59	0.47	0.66	0.48	0.32	0.41		1.00																
Co					0.68																		0.38		0.58		1.00																
As				0.29										0.31			0.52						0.43	0.42		0.56		1.00															
Se		0.82	0.81	0.80		0.90	0.92	0.74		0.73		0.33	0.39	0.75		0.40			0.49							0.31			1.00														
Rb	0.40	0.88	0.84	0.87		0.88	0.72	0.64		0.65		0.33		0.97		0.37	0.30	0.28	0.52			0.34	0.35	0.45		0.47			0.80	1.00													
Sr									0.75		0.65	0.58	0.65		0.53	0.58		0.30	0.39	0.75	0.56					0.34					1.00												
Y						0.81											0.46									0.49						1.00											
Zr		0.35		0.54				0.41		0.44		0.64	0.67	0.47		0.80	0.34	0.44	0.84	0.63	0.50					0.46			0.51	0.40	0.51		1.00									
Nb				0.40								0.61	0.40	0.43	0.53	0.41	0.61	0.85	0.91	0.40	0.59					0.61							0.73	1.00								
Mo		0.41		0.63	-0.45			0.72		0.75		0.61		0.34			0.39	0.35		0.41	0.53	0.77	0.81	0.81	0.80	0.56	0.55	0.49							1.00								
Ag																				0.40							0.44								0.49	1.00						
Cd					0.46	-0.51		0.31		0.35		0.41	0.35		0.35	0.28				0.73	0.65	0.30			0.38	0.31					0.33					0.48		1.00					
Sn	0.34	0.77	0.71	0.87				0.84		0.86		0.50		0.63		0.37	0.35	0.28	0.37		0.30	0.39	0.31	0.38		0.51		0.37	0.59	0.61			0.35		0.74			1.00				
Cs	0.40	0.91	0.83	0.91		0.84	0.73	0.74		0.76		0.38		0.90		0.35			0.42			0.31	0.41	0.50		0.42			0.82	0.95			0.34		0.46			0.70	1.00			
Hf																																								1.00		
Tl	0.65	0.73	0.52	0.87	-0.67			0.82	0.57	0.84		0.74		0.87		0.61	0.79	0.62	0.53	0.52	0.54	0.86	0.65	0.65	0.89	0.84	0.83	0.86	0.73	0.86	0.55	0.57	0.64		0.89	0.53		0.77	0.94		1.00	
Pb		0.32		0.42				0.59		0.65		0.57	0.43			0.40				0.65	0.63	0.56	0.44	0.52	0.58	0.40					0.28				0.78		0.76	0.53	0.35		0.78	1.00

Table S3. Supermicrometer (> 1 µm) correlation matrix of all water-soluble species measured by IC and ICP-MS based on total MOUDI-integrated mass concentrations. DMA – Dimethylamine, MSA – Methanesulfonate, PH – Phthalate, OX – Oxalate, MA – Maleate, SU – Succinate, AD – Adipate.

	DMA	MSA	PH	OX	MA	SU	AD	NH_4	NO_3	SO_4	Cl	Na	Mg	K	Ca	Al	Fe	Mn	Ti	Ba	Zn	Cu	V	Ni	P	Cr	Co	As	Se	Rb	Sr	Y	Zr	Nb	Mo	Ag	Cd	Sn	Cs	Hf	Tl	Pb
DMA	1.00																																									
MSA		1.00																																								
PH	-1.00		1.00																																							
OX		0.60		1.00																																						
MA					1.00																																					
SU		0.62		0.85		1.00																																				
AD	1.00						1.00																																			
NH_4		0.59		0.56		0.48		1.00																																		
NO_3				0.58					1.00																																	
SO_4		0.63		0.86		0.70		0.65	0.72	1.00																																	
Cl				0.55		0.53			0.71	0.57	1.00																																
Na				0.74		0.62		0.27	0.85	0.79	0.93	1.00																															
Mg				0.79		0.68		0.28	0.85	0.83	0.91	0.99	1.00																														
K				0.69	0.96	0.57		0.32	0.71	0.77	0.71	0.79	0.82	1.00																												
Ca				0.37	0.92				0.73	0.52	0.50	0.54	0.57	0.66	1.00																											
Al				0.76	0.91	0.72			0.65	0.65	0.77	0.80	0.82	0.73	0.63	1.00																										
Fe				0.77		0.66			0.65	0.62	0.74	0.76	0.80	0.71	0.58	0.92	1.00																									
Mn				0.59				0.40	0.76	0.82	0.59	0.71	0.74	0.83	0.79	0.69	0.63	1.00																							
Ti				0.82		0.80		0.26	0.57	0.66	0.68	0.73	0.77	0.71	0.52	0.85	0.79	0.59	1.00																						
Ba				0.47					0.77	0.69	0.63	0.71	0.72	0.80	0.69	0.57	0.50	0.83	0.47	1.00																					
Zn								0.41	0.29	0.52				0.33	0.38			0.67		0.48	1.00																					
Cu	0.96					0.56											0.45					1.00																			
V									0.50	0.59		0.39	0.41	0.51	0.39			0.70		0.75	0.67		1.00																		
Ni										0.28		0.30		0.44	0.43			0.31			0.36		0.45	1.00																	
P			0.51											0.45	0.30			0.36		0.52		0.62	0.36		1.00															
Cr				0.62				0.31	0.61	0.72	0.56	0.65	0.69	0.76	0.67	0.72	0.72	0.84	0.62	0.68	0.51		0.52		0.32	1.00														
Co																					0.75	0.61				1.00														
As				0.38				0.30	0.48	0.62	0.30	0.48	0.49	0.31	0.38			0.56		0.54	0.59		0.72			0.63		1.00												
Se		0.41		0.70		0.51		0.39	0.48	0.79	0.47	0.64	0.70	0.66		0.46	0.54	0.58	0.48	0.54	0.34		0.54	0.50		0.72		0.57	1.00											
Rb		0.71		0.80	0.91	0.63		0.52	0.71	0.92	0.58	0.75	0.80	0.91	0.68	0.73	0.68	0.89	0.71	0.76	0.51		0.57	0.32	0.34	0.78		0.44	0.73	1.00									
Sr				0.62					0.84	0.76	0.77	0.85	0.86	0.94	0.72	0.75	0.72	0.87	0.68	0.90	0.32		0.57		0.46	0.75		0.38	0.62	0.85	1.00								
Y				0.47					0.69	0.51	0.66	0.69	0.69	0.67	0.64	0.76	0.69	0.73	0.63	0.67			0.29		0.45	0.59		0.36		0.62	0.76	1.00							
Zr				0.82		0.84		0.28	0.68	0.73	0.77	0.84	0.87	0.75	0.54	0.90	0.87	0.65	0.83	0.59						0.63			0.52	0.78	0.75	0.76	1.00						
Nb				0.75		0.71			0.47	0.53	0.74	0.75	0.77	0.67	0.36	0.86	0.86	0.49	0.76	0.35						0.63			0.51	0.58	0.60	0.60	0.83	1.00					
Mo	-1.00		0.55						0.44																									1.00						
Ag	1.00				1.00																	0.51					0.91							0.73	1.00				
Cd				0.32				0.36		0.46								0.37		0.31	0.70		0.61	0.36		0.39		0.57	0.53	0.40							1.00			
Sn				0.30					0.45	0.51	0.32	0.42	0.43	0.43			0.37	0.51		0.58	0.42		0.82			0.41	0.77	0.57	0.59	0.49	0.47						0.48	1.00		
Cs				0.75	0.92	0.64		0.57	0.63	0.81	0.37	0.59	0.62	0.55	0.56	0.59	0.58	0.64	0.53	0.36						0.52		0.51	0.40	0.76	0.50	0.46	0.63	0.44	0.40				1.00		
Hf					-1.00				0.47						0.59	0.41																0.58	0.37							1.00		
Tl																					0.42							0.57	0.43											1.00	
Pb				0.48				0.43	0.43	0.64		0.37	0.42	0.31	0.31	0.25	0.32	0.47		0.47	0.59	0.37	0.56		0.30	0.47		0.78	0.63	0.50	0.34		0.34				0.65	0.51	0.57			1.00

APPENDIX C

SOURCES OF POLLUTION AND INTERRELATIONSHIPS BETWEEN AEROSOL AND PRECIPITATION CHEMISTRY AT A CENTRAL CALIFORNIA SITE

This article has been published in the Science of The Total Environment (2019).

Hossein Dadashazar[a], Lin Ma[a], Armin Sorooshian[a,b*]

[a]Department of Chemical and Environmental Engineering, University of Arizona, PO BOX 210011, Tucson, AZ 85721, USA
[b]Department of Hydrology and Atmospheric Sciences, University of Arizona, PO BOX 210011, Tucson, AZ 85721, USA

Sources of Pollution and Interrelationships Between Aerosol and Precipitation Chemistry at a Central California Site

Hossein Dadashazar[a], Lin Ma[a], Armin Sorooshian[a,b*]

[a]Department of Chemical and Environmental Engineering, University of Arizona, PO BOX 210011, Tucson, AZ 85721, USA

[b]Department of Hydrology and Atmospheric Sciences, University of Arizona, PO BOX 210011, Tucson, AZ 85721, USA

[*]Corresponding author (phone: 520-626-5858, email: armin@email.arizona.edu, address: PO BOX 210011, Tucson, AZ 85721)

Abstract

This study examines co-located aerosol and precipitation chemistry data between 2010-2016 at Pinnacles National Monument ~65 km east of the coastline in central California. Positive matrix factorization analysis of the aerosol composition data revealed seven distinct pollutant sources: aged sea salt (25.7% of $PM_{2.5}$), biomass burning (24.2% of $PM_{2.5}$), fresh sea salt (15.0% of $PM_{2.5}$), secondary sulfate (11.7% of $PM_{2.5}$), dust (10.0% of $PM_{2.5}$), vehicle emissions (8.2% of $PM_{2.5}$), and secondary nitrate (5.2% of $PM_{2.5}$). The influence of meteorology and transport on monthly patterns of $PM_{2.5}$ composition is discussed. Only secondary sulfate exhibited a statistically significant change (a reduction) over time among the $PM_{2.5}$ source factors. In contrast, PM_{coarse} exhibited a significant increase most likely due to dust influence. Monthly profiles of precipitation chemistry are summarized showing that the most abundant species in each month was either SO_4^{2-}, NO_3^-, or Cl^-. Intercomparisons between the precipitation and aerosol data revealed several features: (i) precipitation pH was inversely related to factors associated with more acidic aerosol constituents such as secondary sulfate and aged sea salt, in addition to being reduced by uptake of HNO_3 in the liquid phase; (ii) two aerosol source factors (dust and aged sea salt) and PM_{coarse} exhibited a positive association with Ca^{2+} in precipitation, suggestive of directly emitted aerosol types with larger sizes promoting precipitation; and (iii) sulfate levels in both the aerosol and precipitation samples analyzed were significantly correlated with dust and aged sea salt PMF factors, pointing to the partitioning of secondary sulfate to dust and sea salt particles. The results of this work have implications for the region's air quality and hydrological cycle, in addition to demonstrating that the use of co-located aerosol and precipitation chemistry data can provide insights relevant to aerosol-precipitation interactions.

Keywords: Pinnacles National Monument, Sea Salt, Biomass Burning, PMF, IMPROVE, NADP

1. Introduction

The largest uncertainty in quantifying global anthropogenic radiative forcing is linked to interactions of aerosol particles with clouds (IPCC, 2013), which is partly driven by the difficulty of conducting the required measurements and separating the influence of meteorology and aerosol pollution on clouds. The impact of aerosol particles on precipitation is challenging to address but is important for reasons extending from improving model representation of clouds and precipitation to identifying the impacts of wet deposition on aquatic and terrestrial ecosystems due to inputs of nutrients and contaminants that may have originated from particles serving as cloud condensation nuclei (CCN) or ice nuclei (IN). Precipitation has important effects on aerosol particles owing to scavenging and removing them from the air, in addition to also removing gases (e.g., MacDonald et al., 2018). In this regard, monitoring the composition of wet deposition is important not just for impacts on ecosystems (e.g., Bobbink et al., 1998; Driscoll et al., 2003; Pardo et al., 2011), but for evaluating chemical tracer transport models (e.g., Rodhe et al., 1995; Liu et al., 2001). As observational studies of aerosol-cloud-precipitation interactions relying on airborne in situ measurements and remote sensing have limitations (e.g., cost, statistics, temporal resolution and coverage), alternative methods of examining this complex system can provide much needed insight. One such method is to rely on long-term records of surface-based aerosol and precipitation chemistry data, as has been demonstrated in just a few studies focused on regions such as the southwestern United States (Sorooshian et al., 2013) and Mexico City (Mora et al., 2017). Examining simultaneously collected aerosol and precipitation chemistry data can provide knowledge about topics with important implications including (i) sources of pollutants, (ii) potential interactions between gases and particles with precipitation drops including uptake processes and wet scavenging, and (iii) aerosol types impacting clouds that produce the precipitation.

Aerosol-cloud-precipitation interactions have been the subject of extensive field projects across California, including for stratiform cloud decks off the coast (e.g., Russell et al., 2013; Sorooshian et al., 2018) and for the more convective clouds inland that provide important rainfall for the state (e.g., Fan et al., 2014; Ralph et al., 2016), including intense precipitation events associated with wintertime atmospheric rivers (e.g., Ralph et al., 2004, 2013). Many of these studies have tried to provide details about sources of pollution impacting the clouds and what the sign of the precipitation response was due to an increase in aerosol concentration. This study aims to fill a gap by examining for the first time long term datasets for aerosol and precipitation chemistry at a central California site, with results that can be contrasted with findings from other works that have relied on aircraft and remote sensing.

This study reports on long-term data collected at Pinnacles National Monument, which is distinguished from most other surface monitoring areas in California because of the co-location of monitoring instruments for both aerosol and precipitation chemistry for a long-term period. Another motivation for studying this site is that it represents an area impacted by a diverse set of sources (e.g., urban, agriculture, marine, shipping, wildfires, dust) due to its geographical position. Focus is first placed on a comprehensive analysis of the aerosol composition data to characterize temporal trends, sources of the pollutants, and the impact of meteorology and transport. Subsequently, the precipitation chemistry data are summarized and then compared with the aerosol composition data.

2. Methods

2.1 Site Description

California is of interest in this study owing to its large population (~36.5 million as of 1 July 2017; US Census Bureau; https://www.census.gov/) that is impacted in various ways by aerosol pollution and precipitation. The Pinnacles National Monument (PNM) site was chosen for this analysis owing to its geographic location as an inland California site impacted by a diversity of sources (Figure 1), and because there are co-located aerosol and precipitation monitoring stations operated by the Environmental Protection Agency (EPA) Interagency Monitoring of Protected Visual Environments (IMPROVE) network and the National Atmospheric Deposition Program (NADP) National Trends Network (NTN), respectively. The PNM site is ~65 km east of the ocean and ~115 km south of San Jose (Figure 1). The California coastal range separates the marine atmosphere from the urban atmosphere over major cities such as San Jose (3rd largest in California), which when combined with Sunnyvale and Santa Clara forms a metropolitan area with an estimated population of ~1.9 million (as of 1 July 2017 according to the US Census Bureau; www.census.gov). To the north is the more populated metropolitan area including San Francisco, Oakland, and Hayward, with a combined population of 4.7 million (as of 1 July 2017; www.census.gov). Aside from anthropogenic and marine sources, the general region containing the PNM site is impacted by wildfires (Westerling et al., 2006) and long-range transport of pollution from distant regions such as Asia (VanCuren and Cahill, 2002), Mexico (Xu et al., 2006), and neighboring states (Xu et al., 2006).

2.2 Long-Term Surface Monitoring Stations

Data were retrieved from the NADP/NTN (36.4819°N, -121.155°W, 300 m above MSL; http://nadp.slh.wisc.edu/data/ntn/) and IMPROVE (36.4833°N, -121.1568°W, 302 m above MSL; http://views.cira.colostate.edu/fed/DataWizard/) sites between 5 January 2010 - 27

December 2016 and 2 January 2010 - 29 December 2016, respectively. At the IMPROVE site, 24 hour filter samples were collected every third day during the study period. The collection system consisted of multiple separate sampling modules to characterize different aspects of either $PM_{2.5}$ or PM_{10}. Of relevance to this study are the measurements of species mass concentrations in the $PM_{2.5}$ fraction, including water soluble ions in the $PM_{2.5}$ fraction measured by ion chromatography (SO_4^{-2}, NO_3^-, Cl^-), elemental mass concentrations in the $PM_{2.5}$ fraction measured by either X-ray fluorescence (Fe and heavier elements) or particle-induced X-ray emission (Na to Mn), elemental carbon (EC) and organic carbon (OC) quantified by thermal optical analysis according to IMPROVE-A protocol (Chow et al., 2007), and total $PM_{2.5}$ and PM_{10} mass concentrations via gravimetric analysis. PM_{coarse} is calculated as the difference between PM_{10} and $PM_{2.5}$ mass concentrations. Additional details of sampling protocols and measurement techniques used in IMPROVE can be found elsewhere (Solomon et al., 2014; Chow et al., 2015).

NADP/NTN was initiated in 1978 to monitor the phenomena of wet deposition and its effects on terrestrial features (e.g., agriculture, forests, and water) (Lamb and Bowersox, 2000). Every NADP/NTN site utilizes two instruments for collection of precipitation. The Belfort B5-780 rain-gauge mechanically measures and records the amount of precipitation each day to the nearest 0.01 inch. The Aerochem Metrics 301 precipitation collector (ACM) automatically collects precipitation samples on a weekly basis (Tuesday to Tuesday) for chemical analysis. Weekly samples obtained via the ACM are sent to the Central Analytical Laboratory (CAL) at the Illinois State Water Survey in Champaign, Illinois to quantify the weekly values of the following parameters: pH, conductance, and water-soluble ion concentrations (NH_4^+, Ca^{2+}, Cl^-,

Mg^{2+}, NO_3^-, K^+, Na^+, SO_4^{2-}) measured by ion chromatography. The NTN has a vigorous quality assurance program described in more detail elsewhere (See et al., 1989; NADP, 2014). Weekly values of the chemical measurements and the precipitation amounts were used for calculation of monthly/annual precipitation-weighted averages of pH, ion concentrations, and ion mass fractions. Moreover, wet deposition amounts were calculated by multiplying the weekly ion concentrations by the weekly amounts of precipitation. For all calculations, values below detection limits were substituted with half of the detection limits (DL). A summary of DL values for species in the NADP/NTN and IMPROVE datasets is provided in the supporting information (Tables S1-S2).

2.3 Meteorological Data

Meteorological data including wind speed and direction, temperature, relative humidity, and solar radiation were obtained from the EPA Air Quality System (AQS) database (https://www.epa.gov/outdoor-air-quality-data) for the PNM IMPROVE site. Precipitation accumulation data were obtained from the NADP/NTN site. Planetary boundary layer height (PBLH) data were obtained from the Modern Era-Retrospective Analysis for Research and Applications (MERRA-2) model with 0.5° × 0.625° spatial resolution. Values of near surface specific humidity and surface soil moisture (0-10 cm) were obtained from the Global Land Data Assimilation System (GLDAS) with 0.25° × 0.25° spatial resolution. Parameters obtained from both MERRA-2 and GLDAS were calculated over 0.5° × 0.625° and 0.5° × 0.5° areas, respectively, extending around the PNM site.

2.4 Calculations

2.4.1 Positive Matrix Factorization (PMF)

A PMF model (US EPA's PMF version 5) was applied to the field data to identify sources and evaluate corresponding contributions impacting a sampling site (Paatero and Tapper, 1994; Paatero, 1997; Hopke, 2016). PMF has been widely implemented as a way to conduct source apportionment of $PM_{2.5}$ (Polissar et al., 2001; Lee et al., 2006; Masiol et al., 2014). Seventeen species (SO_4^{2-}, NO_3^-, OC, EC, Na, Al, Si, Cl^-, K, Ca, V, Mn, Fe, Ni, Cu, Zn, Br) were included in the analysis and categorized as "strong" based on exhibiting a signal to noise ratio (S/N) above one. Summary statistics for $PM_{2.5}$ and speciated concentrations included in PMF analysis are given in Table S2. $PM_{2.5}$ was added to the model as a total variable, categorized as a "weak" species to minimize its effect in driving the model results (Kim et al., 2003). Based on Polissar et al. (1998), concentration values below the DL were substituted with a value equal to half of the DL, with an uncertainty of 5/6 of the associated DL. For missing values, median species concentrations were used, with an uncertainty of four times the median. An additional 10% uncertainty was added to account for unconsidered errors for all species.

The uncertainty associated with the model output was assessed via bootstrapping (BS), displacement (DISP), and bootstrapping with displacement (BS-DISP). For BS, 300 resamples were used with a threshold value of 0.6 for the correlation coefficient (r) to qualify as successful mapping in each run. For DISP and BS-DISP analyses, factor swaps and uncertainty in the model output were assessed for dQ_{max} equal to four.

2.4.2 Concentration Weighted Trajectory (CWT) Analysis

As a way of tracking the trajectory of specific aerosol chemical signatures to the sample site, Concentration Weighted Trajectory (CWT) analysis was employed (e.g., Hsu et al., 2003). This method considers grid cells that are assigned a weighted concentration calculated by taking the mean of sample concentrations that have associated trajectories crossing a particular grid cell. The GIS-based software TrajStat (Wang et al., 2009) was used to obtain the CWT profiles. In order to obtain CWT profiles, 96 h back-trajectories were used from the Hybrid Single-Particle Lagrangian Integrated Trajectory (HYSPLIT) model (Stein et al., 2015; Rolph, 2016) ending 500 m above ground level at PNM. Trajectories were obtained every six hours using the National Centers for Environmental Prediction/National Center for Atmospheric Research (NCEP/NCAR) reanalysis data with the "Model vertical velocity" method. Using a domain of -180° to -100° longitude and 20° to 70° latitude with grid cell size 0.5°×0.5° resulted in an average of ~20 trajectory end points for each cell. A point filter was applied to reduce weight in the effect of the cells with only a small number of end points (Wang et al., 2009). Trajectory frequency maps from 2010 to 2016 are provided in Figure S1, showing that the majority of air masses originated over the Pacific Ocean, especially in the summer, which exhibited a more distant trajectory of air down the coastline of the western United States towards the PNM site.

3. Results and Discussion

3.1 Meteorological Profile

The monthly meteorological profile is summarized in Figure 2 for the study region. Precipitation occurred between October and June without any accumulation in the summer months between July

and September. The peak of precipitation accumulation was between December and March. Soil moisture expectedly followed the same general monthly profile as precipitation, suggestive of a greater likelihood of local soil emissions in summer months, especially when coupled to higher wind speeds in those months. Specific humidity was most enhanced in the summer months (July-August) unlike relative humidity, which is sensitive to temperature and exhibited higher levels in the winter months. The PBLH expectedly followed the same general trend as ambient temperature and solar radiation with higher levels in the summer months.

3.2 Source Apportionment of $PM_{2.5}$

PMF analysis was conducted to identify key sources, and multiple PMF solutions ranging from having three to 10 characteristic pollutant sources were analyzed. The final solution with seven sources was chosen based on the physical validity of the results (described in Supporting Information, Figures S2-S6), which also showed the proximity of the calculated ratio of $Q_{true}/Q_{expected}$ (1.1) to 1.0. The optimal solution also exhibited the following characteristics: i) all factors were mapped in BS runs; ii) during DISP, no factor swap was observed (Table S3) and the decrease in Q values was less than 1%; and iii) there were no factor swaps in BS-DISP (Table S3) where OC, EC, SO_4^{2-}, NO_3^-, Cl^-, K, and Na were actively displaced. In addition, there was a high coefficient of variation between measured and predicted $PM_{2.5}$ ($r^2 = 0.91$), which added confidence in relying on the PMF model for source apportionment of $PM_{2.5}$.

The seven resolved source profiles of $PM_{2.5}$ are shown in Figure 3, with their associated monthly profiles summarized in Figure 4, which were derived from BS resampling (n = 10000). Time

series plots of $PM_{2.5}$ mass concentrations from each source are shown in the supporting information (Figure S7). The smoothed results of CWT analysis associated with each factor for the full study period are shown in Figure 5, with seasonal maps shown in Figure S8.

3.2.1 Biomass Burning

The mass concentration associated with the biomass burning source factor accounted for 24.2% of total $PM_{2.5}$. As compared to other sources, biomass burning contributed the most to the overall mass concentrations of EC (55.7%), OC (52.0%), and K (41.1%) (Figure 3), the cluster of which is known to be associated with biomass burning in the western United States (Cahill et al., 2008; Schlosser et al., 2017) owing mainly to wildfires and wood burning for domestic heating (Wang et al., 2012; Masiol et al., 2017). The temporal profile of biomass burning differs from the other six source factors in that it exhibits its highest concentrations (> 1 μg m^{-3}) for an extended period of the year (November – April), and with a minor concentration peak in the summer months of July-August (Figure 4). The more pronounced and longer concentration peak stems most likely from domestic heating, while the smaller peak in the summertime, coupled with the highest variability in mass concentration, is linked to wildfire activity (Westerling et al., 2006; Dennison et al., 2014) (Figure 4). The CWT plot presented in Figure 5 shows that the strongest sources of this pollutant type are expectedly over the western United States, with strong influence from the neighboring states of Oregon and Nevada.

3.2.2 Dust

The dust source factor accounted for 10.0% of total $PM_{2.5}$. This factor is linked to dust, supported by it contributing the most to the mass concentrations of the following crustal elements (e.g., Malm et al., 1994; Chow et al., 2003; Prabhakar et al., 2014a): Al (81.8%), Si (76.3%), Mn (63.3%), Fe (61.1%), and Ca (50.2%). Dust exhibited a bimodal temporal profile with minimum concentrations between November and February owing to low wind speeds and high soil moisture. Maximum mass concentrations of dust occurred between the spring months of March and May, likely related to dust transport from distant sources including Asia (Tratt et al., 2001; VanCuren and Cahill, 2002; Wells et al., 2007; Kavouras et al., 2009; Creamean et al., 2014; Lopez et al., 2016) and neighboring states such as Nevada (Figure 5). Locally generated dust likely did not contribute significantly in those months as PM_{coarse} did not exhibit its highest levels (Figure 4). Ideal conditions for local dust emissions (low soil moisture, high wind speed) occurred later in the summer months. In contrast to March-May, the second concentration peak for dust between September-October was most likely driven by local sources, supported by PM_{coarse} exhibiting maximum mass concentrations (Figure 4) and its highest correlation with dust during these months (Table 1); furthermore, soil moisture is near its lowest values in these months too.

The CWT map of dust is somewhat similar to that of biomass burning in that major sources are California, Nevada, and Oregon. Dust can be co-emitted with biomass burning emissions due to the buoyancy and turbulence associated with fires near the surface (e.g., Kavouras et al., 2012; Popovicheva et al., 2014; Maudlin et al., 2015). The impact of Asian dust is recognizable from seasonal CWT maps (Figure S8) where spring months showed the greatest dust concentrations for trajectories transported over the Pacific Ocean. As Asian dust has previously been linked to

California orographic precipitation (Ault et al., 2011), the PMF and CWT results emphasize the importance of considering also locally generated dust and plumes from neighboring states with regard to impacts on clouds and precipitation in the study region. At high altitudes, dust has been shown to be an important source of IN (e.g., Heintzenberg et al., 1996; Twohy and Gandrud, 1998; DeMott et al., 2003).

3.2.3 Secondary Sulfate

The secondary sulfate source factor (11.7% of total $PM_{2.5}$) contributed the most of any factor to the mass concentrations of sulfate (51.5%), V (77.0%) and Ni (53.5%), the group of which is linked to fuel oil combustion such as with shipping (Moldanova et al., 2009; Coggon et al., 2012). Aside from secondary production of sulfate stemming from SO_2 emitted by ships and potentially other regional combustion sources, another significant source of sulfate in the region is secondary production from dimethlysulfide (DMS) emissions over the ocean. Sulfur emissions from ships were previously found to be of the same order of magnitude as that of DMS fluxes in a marine environment (Corbett and Fischbeck, 1997). The peak in mass concentration for secondary sulfate in July is consistent with many past studies showing a summertime peak owing to enhanced photochemical activity and reactions facilitated in conditions of high moisture (e.g., Hidy et al., 1978; Baumgardner et al., 1999; Tai et al., 2010; Hand et al., 2012).

The CWT map shows that strong contributions come from marine areas, especially along the southern coast where both the Port of Los Angeles and the Port of Long Beach are situated. These two ports are among the busiest ones in the United States by container volume (US

Department of Transportation, 2017). The high sulfate levels stretch from between those ports to farther north by Oakland and San Francisco where there is major port activity as well.

Analysis using the non-parametric Mann-Kendall test at the 95% significance level revealed that secondary sulfate is the only $PM_{2.5}$ factor showing a significant trend versus time in its mean annual concentration. In agreement with previous studies showing sulfate reductions (e.g., Malm et al., 2002; Sorooshian et al., 2011; Chan et al., 2018), this factor exhibited a decreasing trend (-0.06 $\mu g\ m^{-3}\ yr^{-1}$) over the study period most likely due to the reduction in SO_2 emissions (Hand et al., 2012). This is an important result with regard to impacts on regional aerosol properties as sulfate is a hygroscopic component of ambient particles and its reduced levels can alter overall water-uptake properties; also, less sulfate in ambient particles can allow for more ammonium nitrate production as formation of this latter salt is thermodynamically less favorable than ammonium sulfate (e.g., Seinfeld and Pandis, 2016). Less particulate sulfate also has the important effect of limiting the ability of this species to reduce precipitation acidity, where H_2SO_4 has been shown to be the more significant acidifying agent in wet deposition in contrast to the other major inorganic acid, HNO_3, for some regions (e.g., Tuncer et al., 2001; Naimabadi et al., 2018).

3.2.4 Secondary Nitrate

The secondary nitrate source factor accounted for 5.2% of total $PM_{2.5}$, the lowest of any factor. As expected, this source was the dominant contributor to nitrate (63.2%), which is a result of secondary formation from NO_x, sources of which are diverse in the region including ship exhaust, biomass burning, agricultural activity, and urban emissions (Prabhakar et al., 2014b).

The monthly profile of secondary nitrate mimics what would be expected for a species favoring conditions associated with colder conditions in winter months (December – February), coincident with more wood burning and a shallower PBLH. Thermodynamically, nitrate favors the aerosol phase at lower temperatures (e.g., Johnson et al., 1994). In contrast to the other source factors, the CWT map for secondary nitrate exhibits strong sources both over the ocean and over the western United States spanning the states of California, Nevada, Oregon, and Washington, consistent with precursor sources being over land and the ocean.

3.2.5 Fresh and Aged Sea Salt

The fresh sea salt source factor accounted for 15.0% of total $PM_{2.5}$. This factor contributes the most to the overall mass concentrations of Na (60.6%) and Cl^- (93.9%). The monthly profile reveals that the highest $PM_{2.5}$ concentration of fresh sea salt was in May and June. The CWT map expectedly shows greater mass concentrations associated with trajectories coming from the northwest over the Pacific Ocean.

The aged sea salt factor contributed 25.7% to total $PM_{2.5}$. In contrast to fresh sea salt, this factor contributed more to a wider range of species Na (37.1%), Br (36.3%), nitrate (34.9%), Cu (28.6%), OC (24.7%), sulfate (25.1%), and Ni (24.4%), in addition to having a negligible contribution to Cl^-. The high concentration of sulfate, nitrate, and OC can be attributed to sea salt aging processes. Sea salt aging includes the reaction of sea salt aerosol with acidic gases that replace Cl^- (chloride depletion) by other anions and release hydrochloric acid (Meinert and Winchester, 1977; Eldering et al., 1991). Sulfuric acid and nitric acids are among most abundant inorganic acids causing chloride depletion (Sievering et al., 1991; ten Brink, 1998; Yao et al., 2003). Moreover, organic

acids emitted from various sources (e.g., wildfires) will alter sea salt composition. For instance, in a study at a nearby coastal site, Braun et al. (2017) showed that Cl^- exhibited substantially diminished concentrations during the Soberanes Fire.

The temporal profile of aged sea salt differs from that of fresh sea salt in that the peak concentrations were between June and September rather than May-June. This may be explained by more efficient production of secondary aerosol species in the summertime owing to higher incident solar radiation and photochemical reactivity (Lack et al., 2004; Tai et al., 2010). More specifically, there are enhanced biogenic volatile organic compound emissions during the summer in the study region (Sorooshian et al., 2015), which, when coupled to high concentrations of oxidants (e.g., hydroxyl radicals), can produce high levels of secondary organic aerosol (SOA) species such as organic acids that have been shown to partition to coarse sea salt particles (Laskin et al., 2012; Braun et al., 2017). Also notable during the summertime in the region is efficient aqueous chemistry to produce SOA, especially organic acids, and secondary sulfate (Sorooshian et al., 2007) that can subsequently interact with sea salt particles. Similar to fresh sea salt, the CWT map for aged sea salt shows that the major sources reside over the Pacific Ocean, with the difference being that there is more influence from sources, including ship exhaust, closer to the coastline extending from central California to British Columbia. The spatial pattern of highest concentrations is expectedly close to that of secondary sulfate. The findings associated with sea salt emphasize the importance of distinguishing between aged and fresh sea salt owing to different chemical profiles, and thus varying hygroscopic and radiative properties.

3.2.6 Vehicle Emissions

The vehicle emission source factor contributed 8.2% to total $PM_{2.5}$. This factor contributed the most to EC (27.0%) and OC (13.6%), in addition to metals including Cu (71.4%), Zn (46.0%), Fe (20.6%), and Mn (17.3%). OC and EC are established markers of both diesel and gasoline vehicular exhaust (El Haddad et al., 2009; Zhu et al., 2010; Pant and Harrison, 2013). The presence of metal tracers in this factor is due not only to vehicular exhaust, but also non-exhaust emissions such as brake wear, tire wear, and re-suspension of dust (Wahlin et al., 2006; Fabretti et al., 2009; Pant and Harrison, 2013). There is also a notable contribution from this factor to Br (30%), which has been observed in vehicle exhaust in previous studies (Lim et al., 2010; Peltier et al., 2011). In fact, Br is common additive element used in gasoline and lubricating oil (Huang et al., 1994).

The monthly profile of the vehicle emissions factor differs from all other sources in that it exhibited a dominant peak in October, which is coincidentally the month where dust exhibited a secondary peak and linked earlier to locally generated sources rather than long-range transport. Dust can be emitted via vehicular activity (i.e., road dust), which is the connection between vehicular emissions tracers and dust. The lowest concentrations of this source factor in the summer months may be due to more dilution owing to the highest year-round PBLHs (Figure 2). The CWT map shows that the main source regions coincide with areas containing busy roadways including the Central Valley, southern California, and western Nevada.

3.3 PM_{coarse}

Although not a PMF source factor, PM_{coarse} is relevant to the discussion as it provides insight into the nature of larger aerosol particles, specifically dust and sea salt. Its monthly profile most closely

resembles that of aged sea salt rather than dust or fresh sea salt owing to the proximity to the ocean and because the aerosol has been aged by the time it reaches the PNM site, respectively. Consistent with that result, PM_{coarse} concentrations are best correlated with those of aged sea salt (r = 0.65) followed by dust (r = 0.55) on annual time scales (Table 1). PM_{coarse} is best correlated with aged sea salt for half of the year (MAM, JJA), while it was best correlated with dust for the other half of the year (DJF, SON). The CWT profiles of PM_{coarse} expectedly represent a hybrid of the two sea salt factors and dust.

PM_{coarse} exhibited a statistically significant upward trend in its mean annual concentration during the study period (0.17 μg m^{-3} yr^{-1}), which, as will be shown subsequently, may have been driven to at least some extent by increasing levels of coarse dust particles. This speculation is based on a significant relationship between PM_{coarse} and a dust tracer in wet deposition (Ca^{2+}), whereas PM_{coarse} exhibited insignificant relationships with both major sea salt constituents (Na^{+} and Cl^{-}) (Table 2).

3.4 Cumulative Precipitation Chemistry Profile

The monthly profiles and time series of species concentrations and pH are summarized in Figure 6a and Figure S9, respectively. The non-parametric Kruskal-Wallis test was applied (Table S4) to the NADP/NTN data to determine whether the species concentrations and pH values exhibited significant ($p < 0.05$) monthly differences. Except for Na^{+}, Cl^{-}, and Mg^{2+}, all other species and pH showed significant differences in averaged monthly values. Monthly averaged values of pH ranged from 5.33 to 5.51. Of note are the higher concentrations for all species and lowest pH in May, owing largely to very low precipitation in that month and presumably less dilution in solution as compared to other months. This would have led to higher concentrations of acidic species. For

analagous reasons, the month with the highest precipitation accumulation, December, exhibited among the lowest ion concentrations and the highest pH. The non-parametric Mann-Kendall test was applied to the precipitation species concentrations and pH to see if any significant trends were evident during the study period, and none appeared.

The monthly profile of mass fractions reveals that the most abundant species was either Cl^- (0.18 – 0.39), SO_4^{2-} (0.14 – 0.25), or NO_3^- (0.11 - 0.33). The least abundant species was usually K^+ with the exception of June when it mass fraction reached 0.11 in contrast to being < 0.02 in other months. It is unclear though as to what the source was as the biomass burning factor (a major source of K^+) exhibited its lowest concentration in that month.

Another way to examine the precipitation data is by examining deposition fluxes (Figure 6c), which has similarity to the monthly profile of precipitation accumulation. Among months with precipitation, deposition fluxes of the species examined peaked in February, March, and December, with the lowest fluxes being in June. In most months with precipitation, the major sea salt components (Na^+ and Cl^-) accounted for most of the deposition by mass among the species examined. Sulfate and NO_3^- were the next highest in terms of overall deposition flux among the nine months with recorded data, with especially high levels in June and October, as evident by their high combined mass fractions in those months.

There were strong interrelationships between the various ions measured (Table S5), with the strongest being between sea salt constituents: Na^+ and Cl^- (r = 1.00), Mg^{2+} and Cl^- (r = 0.99), Mg^{2+} and Na^+ (r = 0.99). The significant relationships between species typically associated with

secondary production mechanisms (SO_4^{2-}, NO_3^-, NH_4^+) and the rest which are commonly associated with sea salt and/or crustal particles, is consistent with other regions (Hutchings et al., 2009; Satyanarayana et al., 2010; Sorooshian et al., 2013; Mora et al., 2017). This can be explained by the partitioning of secondarily produced species to the coarser aerosol particle types (sea salt, dust) or by scavenging of the former by hydrometeors (Granat et al., 2002; van der Swaluw et al., 2011). The pH of wet deposition exhibited a significant relationship with only NO_3^- ($r = -0.35$) indicative of how that species, at the minimum, is associated with more acidic precipitation. Liquid water in the form of drops readily takes up HNO_3, which is a likely explanation for the reduction in pH.

3.5 Aerosol-Precipitation Chemical Interrelationships

Mass fractions of the precipitation species were compared to concentrations of the PMF factors, $PM_{2.5}$, and PM_{coarse} (Table 2), with the results essentially resembling those when comparing concentrations of the precipitation species with those of PMF factors. The pH of precipitation was inversely related to factors associated with more acidic elements such as secondary sulfate and aged sea salt. The fact that pH was only correlated with NO_3^- among the precipitation species and not secondary nitrate in the aerosol phase is further supportive of the speculation that there was uptake of HNO_3 in the liquid phase, which would not manifest itself in the surface aerosol measurements.

The mass fraction of Ca^{2+} in precipitation exhibited its highest r value (0.34) with the dust source factor, suggestive of dust seeding precipitation leading to the higher Ca^{2+} levels in precipitation samples. As described in previous studies, dust aerosol can play a role as IN and increase

preciptation in mixed-phase clouds (e.g., Muhlbauer and Lohmann, 2009; Rosenfeld et al., 2011). A similar link between dust and precipitation has been observed in nearby regions such as Arizona and New Mexico (Hutchings et al., 2009; Sorooshian et al., 2013), Texas (Ponette-González et al., 2018), and the Sierra Nevada in California (Ault et al., 2011; Creamean et al., 2013). In contrast to fresh sea salt, the aged sea salt source factor was also correlated with Ca^{2+} in precipitation ($r = 0.25$), suggesting that marine emissions are another contributor to Ca^{2+} in the region's wet deposition.

For the three most abundant components in precipitation based on mass fractions, Cl^- was only correlated with dust, SO_4^{2-} was correlated with dust, secondary sulfate, and aged sea salt, while NO_3^- was correlated with fresh sea salt and vehicle emissions (Table 2). It is noteworthy that there was a significant relationship between SO_4^{2-} in precipitation with both the dust and aged sea salt factors of $PM_{2.5}$, in addition to PM_{coarse}, owing most likely to the partitioning of secondary sulfate to coarse aerosol surfaces (Usher et al., 2002; Manktelow et al., 2010; Wang et al., 2016). In the aerosol phase, the secondary sulfate factor was positively correlated with the dust factor ($r = 0.32$, $p < 0.05$), aged sea salt factor ($r = 0.30$, $p < 0.05$), and PM_{coarse} ($r = 0.38$, $p < 0.05$). Size-resolved aerosol measurements closer to the coast in central California show that SO_4^{2-}, NO_3^-, and organic acids reside in the same size range as where sea salt and dust aerosol exhibit their highest mass concentrations (Maudlin et al., 2015). Lastly, it was of note that the biomass burning source factor did not exhibit a significant relationship with the mass fraction of any precipitation species.

4. Conclusions

This study leveraged a long-term dataset of co-located aerosol and precipitation composition measurements at a central California site (Pinnacles National Monument) that is impacted by

diverse pollutant types including marine emissions, dust, wildfires, and urban emissions. The goal was to critically examine the data to understand pollutant sources and to additionally use interrelationships between aerosol and precipitation species to gain insight into both aerosol types impacting clouds that produce the precipitation and interactions between gases and particles with precipitation drops (e.g., uptake processes and wet scavenging).

A thorough characterization of pollution sources was presented including their relative contributions to total $PM_{2.5}$ and the influence of transport, meteorology, and time of year. Aged sea salt was the most influential source on a mass basis to $PM_{2.5}$, which was shown to exhibit a distinct chemical profile relative to fresh salt in that there was a likely contribution from inorganic and organic acids stemming from precursors emissions from both natural and anthropogenic sources. Interstate transport of pollution was shown to be important with regard to aerosol types linked to dust, wildfire emissions, secondary nitrate, and vehicular emissions, while Asian dust was shown to be impactful in the study region in spring months. Of note was that secondary sulfate represented the only $PM_{2.5}$ pollutant source exhibiting a significant trend during the study period as its levels have decreased, with implications of this phenomenon discussed. In contrast, PM_{coarse} exhibited a significant increase owing most likely to the influence of dust.

Intercomparison of aerosol and precipitation data revealed that the two aerosol source factors (dust and aged sea salt) and PM_{coarse} exhibited a positive association with Ca^{2+} in precipitation, suggestive of directly emitted aerosol types with larger sizes impacting precipitation. Furthermore, sulfate levels in both the aerosol and precipitation samples analyzed were

significantly correlated with dust and aged sea salt PMF factors, pointing to the partitioning of secondary sulfate to dust and sea salt particles. Presumably other acids may partition to these coarse aerosol types as well and impact precipitation, such as organic acids; however, speciated organics were unavailable in the precipitation dataset. Intercomparisons of the aerosol and precipitation datasets reveal that there likely was efficient uptake of HNO_3 to drops, which served to reduce precipitation pH values.

The results of this analysis revealed that simultaneously collected aerosol and precipitation chemistry data at a single site can indeed provide useful insight into processes associated with aerosol effects on clouds (via CCN and IN sources) and also precipitation effects on aerosol (via scavenging and uptake of gases). Further research is warrranted to validate some of the explanations provided in this intercomparison as the current datasets cannot provide unambiguous proof of cause-and-effect relationships. However, a major motivation of the intercomparison is to infer about processes to subsequently validate with more focused measurements and modeling studies.

Acknowledgements

All data used can be obtained from websites and references provided in Section 2. This work was funded by Grant 2 P42 ES04940 from the National Institute of Environmental Health Sciences (NIEHS) Superfund Research Program, NIH and ONR grants N00014-16-1-2567 and N00014-10-1-0811. ***IMPROVE is a collaborative association of state, tribal, and federal agencies, and international partners. US Environmental Protection Agency is the primary funding source, with contracting and research support from the National Park Service. The Air Quality Group at the University of California, Davis is the central analytical laboratory, with ion analysis provided by Research Triangle Institute, and carbon analysis provided by Desert Research Institute.***

References

Ault AP, Williams CR, White AB, Neiman PJ, Creamean JM, Gaston CJ, et al. Detection of Asian dust in California orographic precipitation. Journal of Geophysical Research-Atmospheres 2011; 116.

Baumgardner RE, Isil SS, Bowser JJ, and Fitzgerald KM. Measurements of rural sulfur dioxide and particle sulfate: Analysis of CASTNet data, 1987 through 1996. Journal of Air Waste Management 1999; 49, 1266-1279.

Bobbink R, Hornung M, Roelofs JGM. The effects of air-borne nitrogen pollutants on species diversity in natural and semi-natural European vegetation. Journal of Ecology 1998; 86: 717-738.

Braun RA, Dadashazar H, MacDonald AB, Aldhaif AM, Maudlin LC, Crosbie E, et al. Impact of Wildfire Emissions on Chloride and Bromide Depletion in Marine Aerosol Particles. Environmental Science & Technology 2017; 51: 9013-9021.

Cahill CF, Cahill TA, Perry KD. The size- and time-resolved composition of aerosols from a sub-Arctic boreal forest prescribed burn. Atmospheric Environment 2008; 42: 7553-7559.

Chan EAW, Gantt B, and Mcdow S. The reduction of summer sulfate and switch from summertime to wintertime $PM_{2.5}$ concentration maxima in the United States. Atmospheric Environment 2018; 175: 25-32.

Chow JC, Watson JG, Ashbaugh LL, Magliano KL. Similarities and differences in PM10 chemical source profiles for geological dust from the San Joaquin Valley, California. Atmospheric Environment 2003; 37: 1317-1340.

Chow JC, Watson JG, Chen LWA, Chang MCO, Robinson NF, Trimble D, and Kohl S. The IMPROVE-A temperature protocol for thermal/optical carbon analysis: maintaining consistency with a long-term database, Journal of the Air Waste Management Association 2007; 57: 1014-1023.

Chow JC, Lowenthal DH, Chen LWA, Wang XL, Watson JG. Mass reconstruction methods for $PM_{2.5}$: a review. Air Quality Atmosphere and Health 2015; 8: 243-263.

Coggon MM, Sorooshian A, Wang Z, Metcalf AR, Frossard AA, Lin JJ, et al. Ship impacts on the marine atmosphere: insights into the contribution of shipping emissions to the properties of marine aerosol and clouds. Atmospheric Chemistry and Physics 2012; 12: 8439-8458.

Corbett JJ, Fischbeck P. Emissions from ships. Science 1997; 278: 823-824.

Creamean JM, Suski KJ, Rosenfeld D, Cazorla A, DeMott PJ, Sullivan RC, et al. Dust and Biological Aerosols from the Sahara and Asia Influence Precipitation in the Western U.S. Science 2013; 339: 1572-1578.

Creamean JM, Spackman JR, Davis SM, White AB. Climatology of long-range transported Asian dust along the West Coast of the United States. Journal of Geophysical Research-Atmospheres 2014; 119: 12171-12185.

DeMott PJ, Sassen K, Poellot MR, Baumgardner D, Rogers DC, Brooks SD, et al. African dust aerosols as atmospheric ice nuclei. Geophysical Research Letters 2003; 30.

Dennison PE, Brewer SC, Arnold JD, and Moritz MA: Large wildfire trends in the western United States, 1984-2011, Geophysical Research Letter 2014; 41, 2928-2933.

Driscoll CT, Whitall D, Aber J, Boyer E, Castro M, Cronan C, et al. Nitrogen pollution in the northeastern United States: Sources, effects, and management options. Bioscience 2003; 53: 357-374.

El Haddad I, Marchand N, Dron J, Temime-Roussel B, Quivet E, Wortham H, et al. Comprehensive primary particulate organic characterization of vehicular exhaust emissions in France. Atmospheric Environment 2009; 43: 6190-6198.

Eldering A, Solomon PA, Salmon LG, Fall T, Cass GR. Hydrochloric-Acid - a Regional Perspective on Concentrations and Formation in the Atmosphere of Southern California. Atmospheric Environment Part a-General Topics 1991; 25: 2091-2102.

Fabretti JF, Sauret N, Gal JF, Maria PC, Scharer U. Elemental characterization and source identification of $PM_{2.5}$ using Positive Matrix Factorization: The Malraux road tunnel, Nice, France. Atmospheric Research 2009; 94: 320-329.

Fan J, Leung LR, DeMott PJ, Comstock JM, Singh B, Rosenfeld D, et al. Aerosol impacts on California winter clouds and precipitation during CalWater 2011: local pollution versus long-range transported dust. Atmospheric Chemistry and Physics 2014; 14: 81-101.

Granat L, Norman M, Leck C, Kulshrestha UC, Rodhe H. Wet scavenging of sulfur compounds and other constituents during the Indian Ocean Experiment (INDOEX). Journal of Geophysical Research-Atmospheres 2002; 107.

Hand JL, Schichtel BA, Malm WC, and Pitchford ML. Particulate sulfate ion concentration and SO2 emission trends in the United States from the early 1990s through 2010. Atmospheric Chemistry & Physics 2012; 12: 10353-10365.

Heintzenberg J, Okada K, Strom J. On the composition of non-volatile material in upper tropospheric aerosols and cirrus crystals. Atmospheric Research 1996; 41: 81-88.

Hidy GM, Mueller PK, Tong EY. Spatial and Temporal Distributions of Airborne Sulfate in Parts of United-States. Atmospheric Environment 1978; 12: 735-752.

Hopke PK. Review of receptor modeling methods for source apportionment. Journal of the Air & Waste Management Association 2016; 66: 237-259.

Hsu YK, Holsen TM, Hopke PK. Comparison of hybrid receptor models to locate PCB sources in Chicago. Atmospheric Environment 2003; 37: 545-562.

Huang XD, Olmez I, Aras NK, Gordon GE. Emissions of Trace-Elements from Motor-Vehicles - Potential Marker Elements and Source Composition Profile. Atmospheric Environment 1994; 28: 1385-1391.

Hutchings JW, Robinson MS, McIlwraith H, Kingston JT, Herckes P. The Chemistry of Intercepted Clouds in Northern Arizona during the North American Monsoon Season. Water Air and Soil Pollution 2009; 199: 191-202.

IPCC: Summary for Policymakers. Contribution of Working Group I to the Fifth Assessment Report of the Intergovernmental Panel on Climate Change (eds Stocker, T. F., Qin, D., Plattner,

G. K., Tignor, M., Allen, S. K., Boschung, J., Nauels, A., Xia, Y., Bex, V. & Midgley, P. M.) 2013; Cambridge University Press: Cambridge, United Kingdom and New York, NY, USA.

Johnson BJ, Huang SC, Lecave M, Porterfield M. Seasonal Trends of Nitric-Acid, Particulate Nitrate, and Particulate Sulfate Concentrations at a Southwestern United-States Mountain Site. Atmospheric Environment 1994; 28: 1175-1179.

Kavouras IG, Etyemezian V, DuBois DW, Xu J, Pitchford M. Source reconciliation of atmospheric dust causing visibility impairment in Class I areas of the western United States. Journal of Geophysical Research-Atmospheres 2009; 114.

Kavouras IG, Nikolich G, Etyemezian V, DuBois DW, King J, Shafer D. In situ observations of soil minerals and organic matter in the early phases of prescribed fires. Journal of Geophysical Research-Atmospheres 2012; 117.

Kim E, Hopke PK, Edgerton ES. Source identification of Atlanta aerosol by positive matrix factorization. Journal of the Air & Waste Management Association 2003; 53: 731-739.

Lack DA, Tie XX, Bofinger ND, Wiegand AN, Madronich S. Seasonal variability of secondary organic aerosol: A global modeling study. Journal of Geophysical Research-Atmospheres 2004; 109.

Lamb D, Bowersox V. The national atmospheric deposition program: an overview. Atmospheric Environment 2000; 34: 1661-1663.

Laskin A, Moffet RC, Gilles MK, Fast JD, Zaveri RA, Wang BB, et al. Tropospheric chemistry of internally mixed sea salt and organic particles: Surprising reactivity of NaCl with weak organic acids. Journal of Geophysical Research-Atmospheres 2012; 117.

Lee JH, Hopke PK, Turner JR. Source identification of airborne $PM_{2.5}$ at the St. Louis-Midwest Supersite. Journal of Geophysical Research-Atmospheres 2006; 111.

Lim JM, Lee JH, Moon JH, Chung YS, Kim KH. Source apportionment of PM_{10} at a small industrial area using Positive Matrix Factorization. Atmospheric Research 2010; 95: 88-100.

Liu HY, Jacob DJ, Bey I, Yantosca RM. Constraints from Pb-210 and Be-7 on wet deposition and transport in a global three-dimensional chemical tracer model driven by assimilated meteorological fields. Journal of Geophysical Research-Atmospheres 2001; 106: 12109-12128.

Lopez DH, Rabbani MR, Crosbie E, Raman A, Arellano AF, Sorooshian A. Frequency and Character of Extreme Aerosol Events in the Southwestern United States: A Case Study Analysis in Arizona. Atmosphere 2016; 7.

MacDonald AB, Dadashazar H, Chuang PY, Crosbie E, Wang HL, Wang Z, et al. Characteristic Vertical Profiles of Cloud Water Composition in Marine Stratocumulus Clouds and

Relationships With Precipitation. Journal of Geophysical Research-Atmospheres 2018; 123: 3704-3723.

Malm WC, Sisler JF, Huffman D, Eldred RA, Cahill TA. Spatial and Seasonal Trends in Particle Concentration and Optical Extinction in the United-States. Journal of Geophysical Research-Atmospheres 1994; 99: 1347-1370.

Malm WC, Schichtel BA, Ames RB, and Gebhart KA. A 10-year spatial and temporal trend of sulfate across the United States, Journal of Geophysical Research-Atmosphere 2002; 107: 4627.

Manktelow PT, Carslaw KS, Mann GW, Spracklen DV. The impact of dust on sulfate aerosol, CN and CCN during an East Asian dust storm. Atmospheric Chemistry and Physics 2010; 10: 365-382.

Masiol M, Squizzato S, Rampazzo G, Pavoni B. Source apportionment of PM2.5 at multiple sites in Venice (Italy): Spatial variability and the role of weather. Atmospheric Environment 2014; 98: 78-88.

Masiol M, Hopke PK, Felton HD, Frank BP, Rattigan OV, Wurth MJ, et al. Source apportionment of $PM_{2.5}$ chemically speciated mass and particle number concentrations in New York City. Atmospheric Environment 2017; 148: 215-229.

Maudlin LC, Wang Z, Jonsson HH, Sorooshian A. Impact of wildfires on size-resolved aerosol composition at a coastal California site. Atmospheric Environment 2015; 119: 59-68.

Meinert DL, Winchester JW. Chemical Relationships in North-Atlantic Marine Aerosol. Journal of Geophysical Research-Oceans and Atmospheres 1977; 82: 1778-1782.

Moldanova J, Fridell E, Popovicheva O, Demirdjian B, Tishkova V, Faccinetto A, et al. Characterisation of particulate matter and gaseous emissions from a large ship diesel engine. Atmospheric Environment 2009; 43: 2632-2641.

Mora M, Braun RA, Shingler T, Sorooshian A. Analysis of remotely sensed and surface data of aerosols and meteorology for the Mexico Megalopolis Area between 2003 and 2015. Journal of Geophysical Research-Atmospheres 2017; 122: 8705-8723.

Muhlbauer A, Lohmann U. Sensitivity Studies of Aerosol-Cloud Interactions in Mixed-Phase Orographic Precipitation. Journal of the Atmospheric Sciences 2009; 66: 2517-2538.

NADP, 2014. Quality Assurance Plan - Central Analytical Laboratory, NADP QA Plan 2014-01, Version 7: http://nadp.sws.uiuc.edu/lib/qaPlans/qapCal2014.pdf.

Naimabadi A, Shirmardi M, Maleki H, Teymouri P, Goudarzi G, Shahsavani A, et al. On the chemical nature of precipitation in a populated Middle Eastern Region (Ahvaz, Iran) with diverse sources. Ecotoxicology and Environmental Safety 2018; 163: 558-566.

Paatero P, Tapper U. Positive Matrix Factorization - a Nonnegative Factor Model with Optimal Utilization of Error-Estimates of Data Values. Environmetrics 1994; 5: 111-126.

Paatero P. Least squares formulation of robust non-negative factor analysis. Chemometrics and Intelligent Laboratory Systems 1997; 37: 23-35.

Pant P, Harrison RM. Estimation of the contribution of road traffic emissions to particulate matter concentrations from field measurements: A review. Atmospheric Environment 2013; 77: 78-97.

Pardo LH, Fenn ME, Goodale CL, Geiser LH, Driscoll CT, Allen EB, et al. Effects of nitrogen deposition and empirical nitrogen critical loads for ecoregions of the United States. Ecological Applications 2011; 21: 3049-3082.

Peltier RE, Lippmann M. Spatial and seasonal distribution of aerosol chemical components in New York City: (1) Incineration, coal combustion, and biomass burning. Journal of Exposure Science and Environmental Epidemiology 2011; 21: 473-483.

Polissar AV, Hopke PK, Paatero P. Atmospheric aerosol over Alaska - 2. Elemental composition and sources. Journal of Geophysical Research-Atmospheres 1998; 103: 19045-19057.

Polissar AV, Hopke PK, Poirot RL. Atmospheric aerosol over Vermont: Chemical composition and sources. Environmental Science & Technology 2001; 35: 4604-4621.

Ponette-González, AG, Collins JD, Manuel JE, Byers TA, Glass GA, Weathers KC, Gill TE. Wet dust deposition during the 2012 US drought: An overlooked pathway for elemental flux to ecosystems. Journal of Geophysical Research-Atmospheres 2018, 123: 8238-8254.

Popovicheva O, Kistler M, Kireeva E, Persiantseva N, Timofeev M, Kopeikin V, et al. Physicochemical characterization of smoke aerosol during large-scale wildfires: Extreme event of August 2010 in Moscow. Atmospheric Environment 2014; 96: 405-414.

Prabhakar G, Sorooshian A, Toffol E, Arellano AF, Betterton EA. Spatiotemporal distribution of airborne particulate metals and metalloids in a populated arid region. Atmospheric Environment 2014a; 92: 339-347.

Prabhakar G, Ervens B, Wang Z, Maudlin LC, Coggon MM, Jonsson HH, et al. Sources of nitrate in stratocumulus cloud water: Airborne measurements during the 2011 E-PEACE and 2013 NiCE studies. Atmospheric Environment 2014b; 97: 166-173.

Ralph FM, Neiman PJ, Wick GA. Satellite and CALJET aircraft observations of atmospheric rivers over the eastern north pacific ocean during the winter of 1997/98. Monthly Weather Review 2004; 132: 1721-1745.

Ralph FM, Coleman T, Neiman PJ, Zamora RJ, Dettinger MD. Observed Impacts of Duration and Seasonality of Atmospheric-River Landfalls on Soil Moisture and Runoff in Coastal Northern California. Journal of Hydrometeorology 2013; 14: 443-459.

Ralph FM, Prather KA, Cayan D, Spackman JR, DeMott P, Dettinger M, et al. Calwater Field Studies Designed to Quantify the Roles of Atmospheric Rivers and Aerosols in Modulating Us West Coast Precipitation in a Changing Climate. Bulletin of the American Meteorological Society 2016; 97: 1209-1228.

Rodhe H, Langner J, Gallardo L, Kjellstrom E. Global scale transport of acidifying pollutants. Water Air and Soil Pollution 1995; 85: 37-50.

Rolph, G. D. Real-time environmental applications and display system (ready) 2016. [Available at http://ready.arl.noaa.gov.]

Rosenfeld D, Yu X, Liu GH, Xu XH, Zhu YN, Yue ZG, et al. Glaciation temperatures of convective clouds ingesting desert dust, air pollution and smoke from forest fires. Geophysical Research Letters 2011; 38.

Russell LM, Sorooshian A, Seinfeld JH, Albrecht BA, Nenes A, Ahlm L, et al. Eastern Pacific Emitted Aerosol Cloud Experiment. Bulletin of the American Meteorological Society 2013; 94: 709-729.

Satyanarayana J, Reddy LAK, Kulshrestha MJ, Rao RN, Kulshrestha UC. Chemical composition of rain water and influence of airmass trajectories at a rural site in an ecological sensitive area of Western Ghats (India). Journal of Atmospheric Chemistry 2010; 66: 101-116.

Schlosser JS, Braun RA, Bradley T, Dadashazar H, MacDonald AB, Aldhaif AA, et al. Analysis of aerosol composition data for western United States wildfires between 2005 and 2015: Dust emissions, chloride depletion, and most enhanced aerosol constituents. Journal of Geophysical Research-Atmospheres 2017; 122: 8951-8966.

See RB, Schroder LJ, Willoughby TC. A Quality-Assurance Assessment for Constituents Reported by the National Atmospheric Deposition Program and the National Trends Network. Atmospheric Environment 1989; 23: 1801-1806.

Seinfeld, J. H., Pandis SN. Atmospheric chemistry and physics (3rd ed.) 2016. New York: Wiley-Interscience.

Sievering H, Boatman J, Galloway J, Keene W, Kim Y, Luria M, and Ray J. Heterogeneous Sulfur Conversion in Sea-Salt Aerosol-Particles - the Role of Aerosol Water-Content and Size Distribution. Atmospheric Environment. Part A. Generic Topics 1991; 25: 1479-1487.

Solomon PA, Crumpler D, Flanagan JB, Jayanty RKM, Rickman EE, McDade CE. US National $PM_{2.5}$ Chemical Speciation Monitoring Networks-CSN and IMPROVE: Description of networks. Journal of the Air & Waste Management Association 2014; 64: 1410-1438.

Sorooshian A, Lu ML, Brechtel FJ, Jonsson H, Feingold G, Flagan RC, et al. On the source of organic acid aerosol layers above clouds. Environmental Science & Technology 2007; 41: 4647-4654.

Sorooshian A, Wonaschutz A, Jarjour EG, Hashimoto BI, Schichtel BA, Betterton EA. An aerosol climatology for a rapidly growing arid region (southern Arizona): Major aerosol species and remotely sensed aerosol properties. Journal of Geophysical Research-Atmospheres 2011; 116.

Sorooshian A, Shingler T, Harpold A, Feagles CW, Meixner T, Brooks PD. Aerosol and precipitation chemistry in the southwestern United States: spatiotemporal trends and interrelationships. Atmospheric Chemistry and Physics 2013; 13: 7361-7379.

Sorooshian A, Crosbie E, Maudlin LC, Youn JS, Wang Z, Shingler T, et al. Surface and airborne measurements of organosulfur and methanesulfonate over the western United States and coastal areas. Journal of Geophysical Research-Atmospheres 2015; 120: 8535-8548.

Sorooshian A, MacDonald AB, Dadashazar H, Bates KH, Coggon MM, Craven JS, et al. A multi-year data set on aerosol-cloud-precipitation-meteorology interactions for marine stratocumulus clouds. Scientific Data 2018; 5.

Stein AF, Draxler RR, Rolph GD, Stunder BJB, Cohen MD, Ngan F. Noaa's Hysplit Atmospheric Transport and Dispersion Modeling System. Bulletin of the American Meteorological Society 2015; 96: 2059-2077.

Tai APK, Mickley LJ, Jacob DJ. Correlations between fine particulate matter ($PM_{2.5}$) and meteorological variables in the United States: Implications for the sensitivity of $PM_{2.5}$ to climate change. Atmospheric Environment 2010; 44: 3976-3984.

ten Brink HM. Reactive uptake of HNO_3 and H_2SO_4 in sea-salt (NaCl) particles. Journal of Aerosol Science 1998; 29: 57-64.

Tratt DM, Frouin RJ, Westphal DL. April 1998 Asian dust event: A southern California perspective. Journal of Geophysical Research-Atmospheres 2001; 106: 18371-18379.

Tuncer B, Bayar B, Yesilyurt C, Tuncel G. Ionic composition of precipitation at the Central Anatolia (Turkey). Atmospheric Environment 2001; 35: 5989-6002.

Twohy CH, Gandrud BW. Electron microscope analysis of residual particles from aircraft contrails. Geophysical Research Letters 1998; 25: 1359-1362.

US Department of Transportation, Port Performance Freight Statistics Program, 2017 <https://www.bts.gov>.

Usher CR, Al-Hosney H, Carlos-Cuellar S, Grassian VH. A laboratory study of the heterogeneous uptake and oxidation of sulfur dioxide on mineral dust particles. Journal of Geophysical Research-Atmospheres 2002; 107.

VanCuren RA, Cahill TA. Asian aerosols in North America: Frequency and concentration of fine dust. Journal of Geophysical Research-Atmospheres 2002; 107.

van der Swaluw E, Asman WAH, van Jaarsveld H, Hoogerbrugge R. Wet deposition of ammonium, nitrate and sulfate in the Netherlands over the period 1992-2008. Atmospheric Environment 2011; 45: 3819-3826.

Wahlin P, Berkowicz R, Palmgren F. Characterisation of traffic-generated particulate matter in Copenhagen. Atmospheric Environment 2006; 40: 2151-2159.

Wang YQ, Zhang XY, Draxler RR. TrajStat: GIS-based software that uses various trajectory statistical analysis methods to identify potential sources from long-term air pollution measurement data. Environmental Modelling & Software 2009; 24: 938-939.

Wang YG, Hopke PK, Rattigan OV, Chalupa DC, Utell MJ. Multiple-year black carbon measurements and source apportionment using Delta-C in Rochester, New York. Journal of the Air & Waste Management Association 2012; 62: 880-887.

Wang QZ, Zhuang GS, Huang K, Liu TN, Lin YF, Deng CR, et al. Evolution of particulate sulfate and nitrate along the Asian dust pathway: Secondary transformation and primary pollutants via long-range transport. Atmospheric Research 2016; 169: 86-95.

Wells KC, Witek M, Flatau P, Kreidenwei SM, Westphal DL. An analysis of seasonal surface dust aerosol concentrations in the western US (2001-2004): Observations and model predictions. Atmospheric Environment 2007; 41: 6585-6597.

Westerling AL, Hidalgo HG, Cayan DR, and Swetnam TW. Warming and earlier spring increase western US forest wildfire activity. Science 2006: 313, 940-943.

Yao XH, Fang M, Chan CK. The size dependence of chloride depletion in fine and coarse sea-salt particles. Atmospheric Environment 2003; 37: 743-751.

Xu J, DuBois D, Pitchford M, Green M, and Etyemezian V. Attribution of sulfate aerosols in Federal Class I areas of the western United States based on trajectory regression analysis. Atmospheric Environment 2006; 40, 3433-3447.

Zhu CS, Chen CC, Cao JJ, Tsai CJ, Chou CCK, Liu SC, et al. Characterization of carbon fractions for atmospheric fine particles and nanoparticles in a highway tunnel. Atmospheric Environment 2010; 44: 2668-2673.

Table 1. Correlation coefficients (r) between PM_{coarse} and seven PMF factors corresponding to the $PM_{2.5}$ fraction of sampled aerosol. Values are only shown when statistically significant based on $p < 0.05$.

	PM_{coarse}				
	Annual	DJF	MAM	JJA	SON
Biomass burning	-	-	-	0.22	-
Dust	0.55	0.79	0.46	0.58	0.83
Secondary sulfate	0.38	-	0.34	0.36	0.21
Secondary nitrate	-	-	0.47	0.41	-
Fresh sea salt	0.24	-	0.39	0.26	-
Vehicle emissions	0.18	0.23	0.33	0.33	0.29
Aged sea salt	0.65	0.36	0.55	0.68	0.49

Table 2. Correlation coefficients (r) of both weekly mass cocentrations (values before "/") and mass fractions (values after "/") of precipitation species versus the weekly averaged aerosol mass concetrations for seven PMF factors and also total $PM_{2.5}$ and PM_{coarse}. Values are only shown when statistically significant based on $p < 0.05$.

	Ca^{2+}:Rain	Mg^{2+}:Rain	K^{+}:Rain	Na^{+}:Rain	NH_4^{+}:Rain	NO_3^{-}:Rain	Cl^{-}:Rain	SO_4^{2-}:Rain	pH:Rain
Biomass burning	- / -	- / -	- / -	- / -	- / -	- / -	- / -	- / -	-
Dust	0.36 / 0.34	- / -	- / -	- / -0.25	0.31 / -	0.31 / -	- / -0.24	0.30 / 0.37	-
Secondary sulfate	- / 0.27	- / -	- / -	- / -	- / -	- / -	- / -	- / 0.45	-0.23
Secondary nitrate	- / -	- / -	- / -	- / -	- / -	- / -	- / -	- / -	-
Fresh sea salt	- / -	- / -	- / -	- / -	- / -	- / -0.20	- / -	- / -	-
Vehicle emissions	- / -	- / -	- / -0.19	- / -	- / -	- / 0.25	- / -	- / -	-0.31
Aged sea salt	0.26 / 0.25	- / -	- / -	- / -	- / -	0.23 / -	- / -	- / 0.24	-0.24
$PM_{2.5}$	0.24 / -	- / -	- / -	- / -	- / -	0.19 / -	- / -	0.20 / 0.21	-0.23
PM_{coarse}	0.28 / 0.22	- / -	- / -	- / -	0.19 / -	0.24 / -	- / -	0.23 / 0.34	-

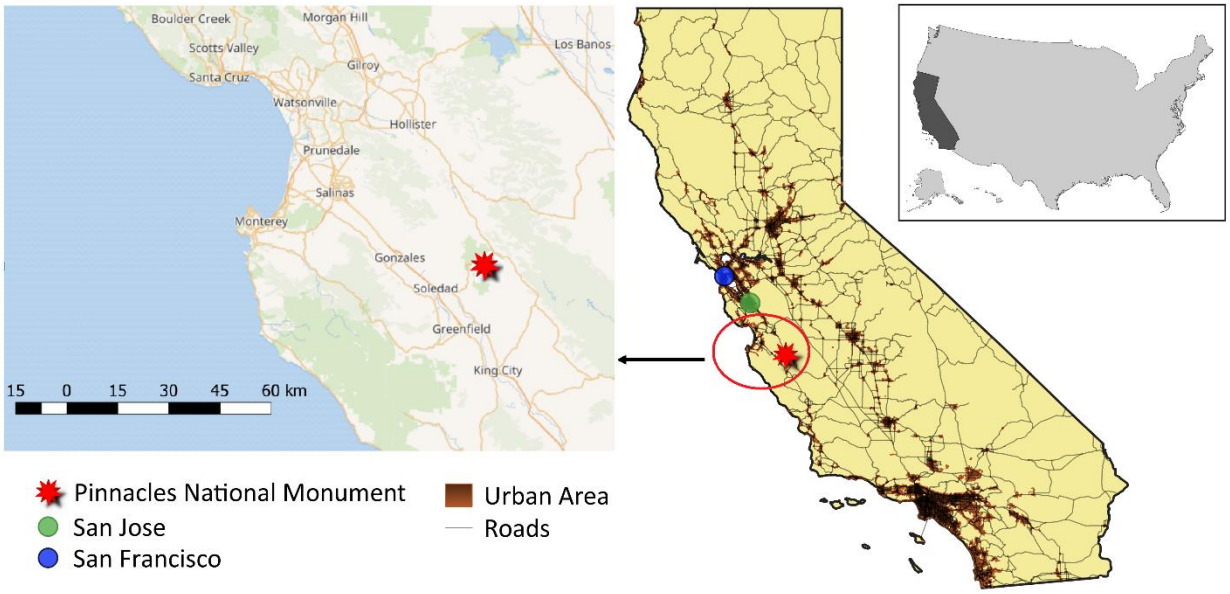

Figure 1. Map showing the study region, including where the collocated IMPROVE and NADP/NTN stations are at Pinnacles National Monument relative to major urban centers and the coastline.

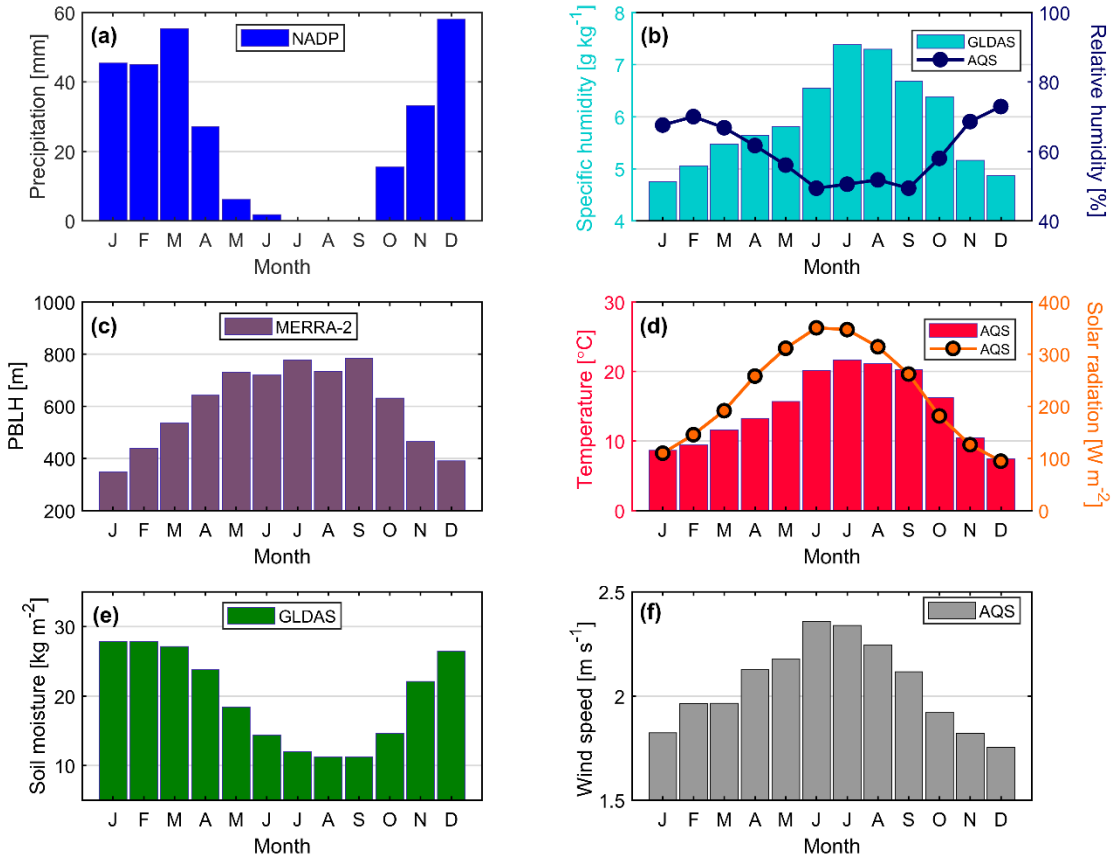

Figure 2. Monthly profiles of (a) precipitation accumulation, (b) specific humidity and relative humidity, (c) planetary boundary layer height (PBLH), (d) temperature and solar radiation, (e) soil moisture, and (f) wind speed based on data between 2010 and 2016. These profiles are obtained from different data sources including EPA AQS monitoring network, MERRA-2, and GLDAS.

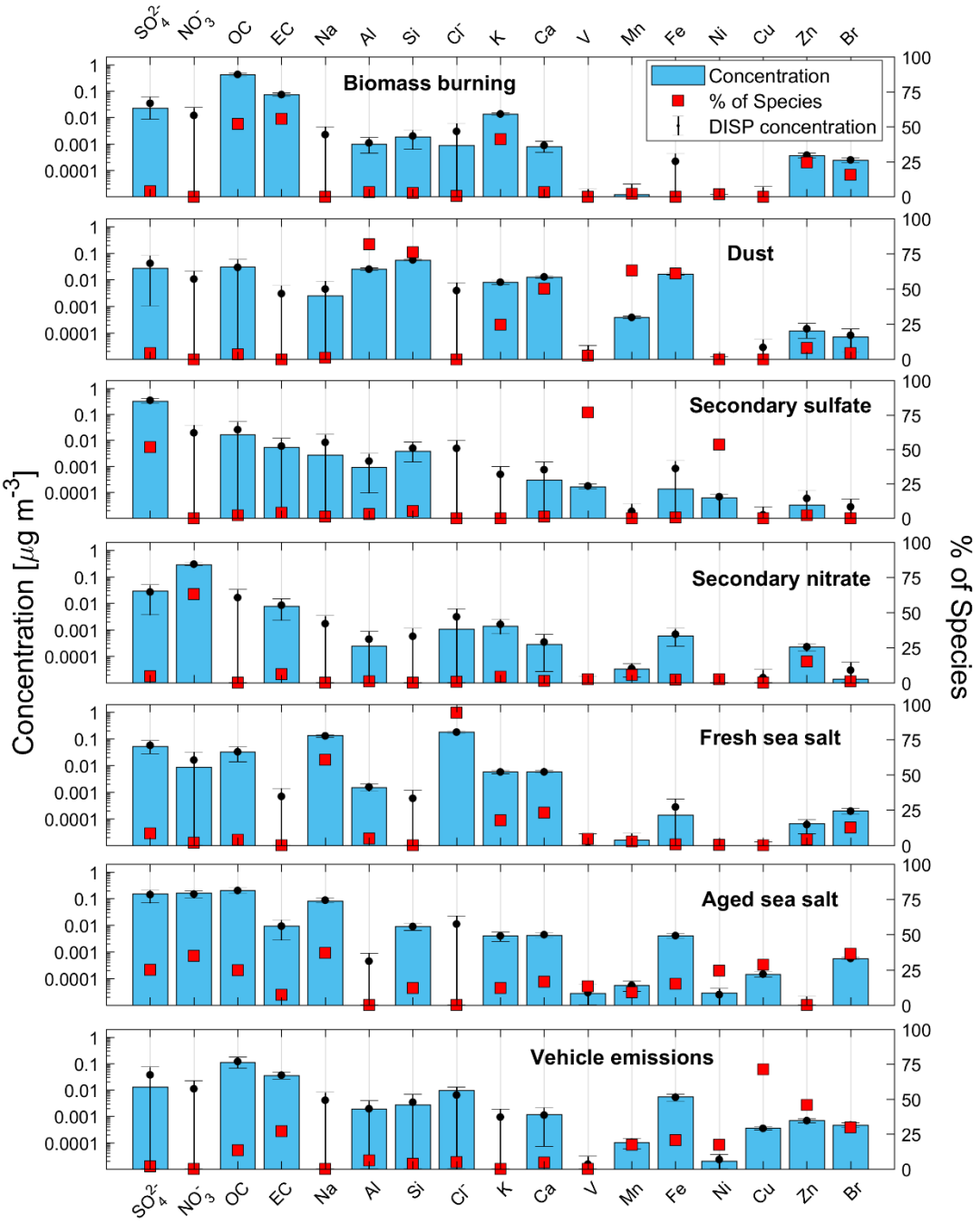

Figure 3. Seven source factor profiles from PMF analysis using chemically-speciated $PM_{2.5}$ data from PNM IMPROVE station. Blue bars represent the mass concentration of the species while red filled markers signify the percent contribution of a particular source factor to the mass sum of a species' overall concentration. Black circles and error bars represent mean and range, respectively, of DISP values of the species mass concentration.

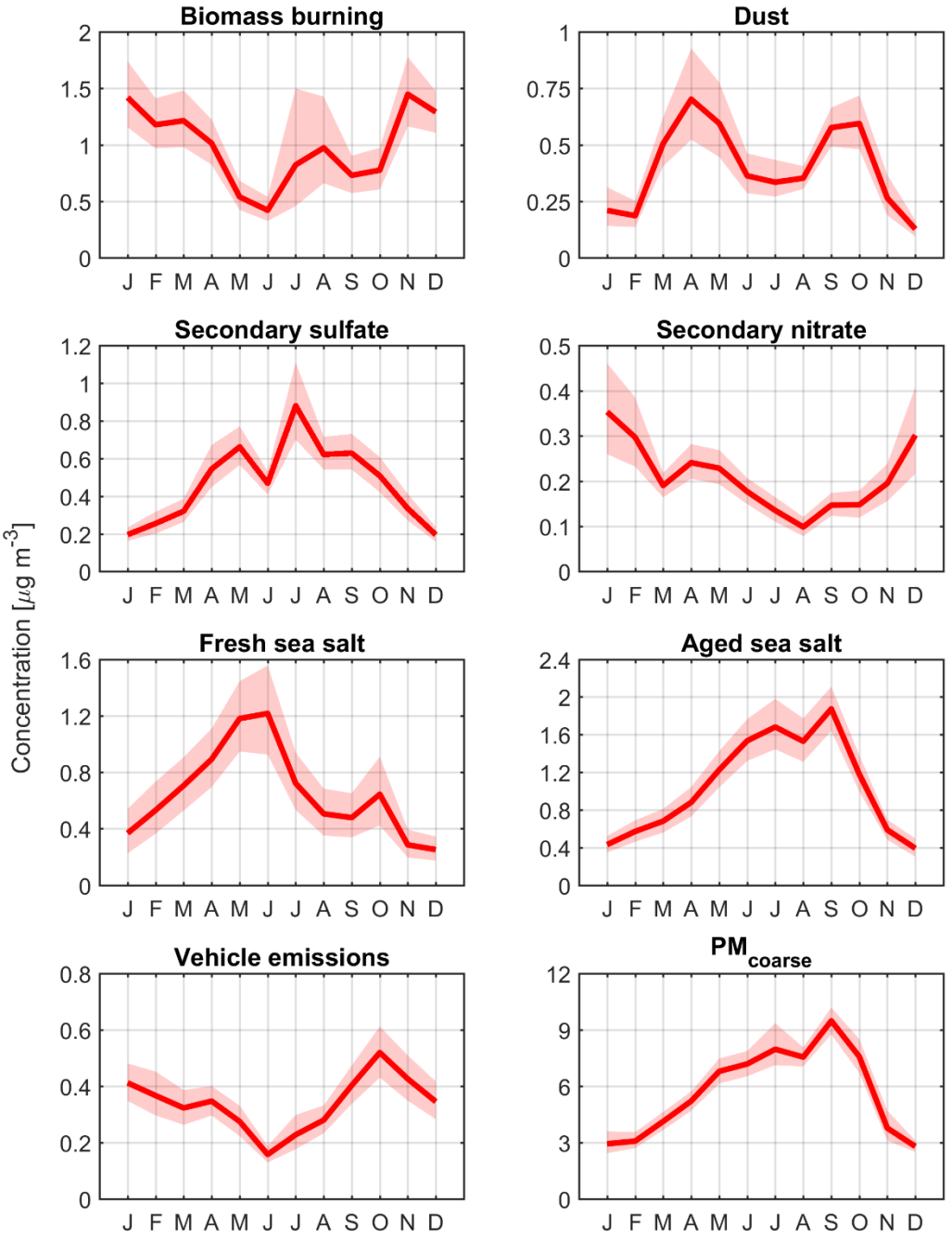

Figure 4. Monthly mean statistics of source factor mass concentrations. Solid lines and shadings represent the mean and 95th confidence intervals, respectively, calculated using bootstrapping (n = 10000).

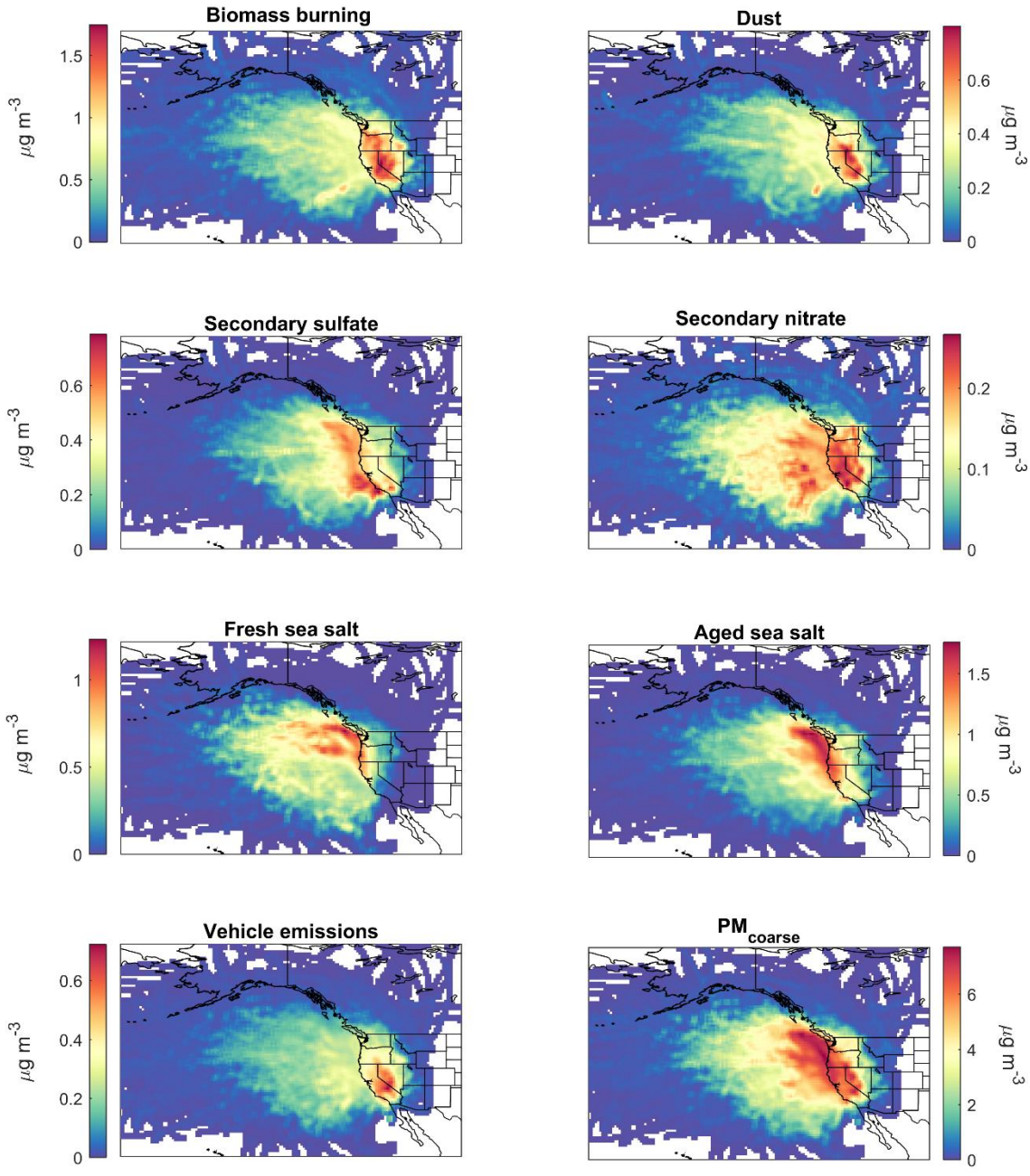

Figure 5. Concentration Weighted Trajectory (CWT) maps of PMF source factors in addition to PM_{coarse}.

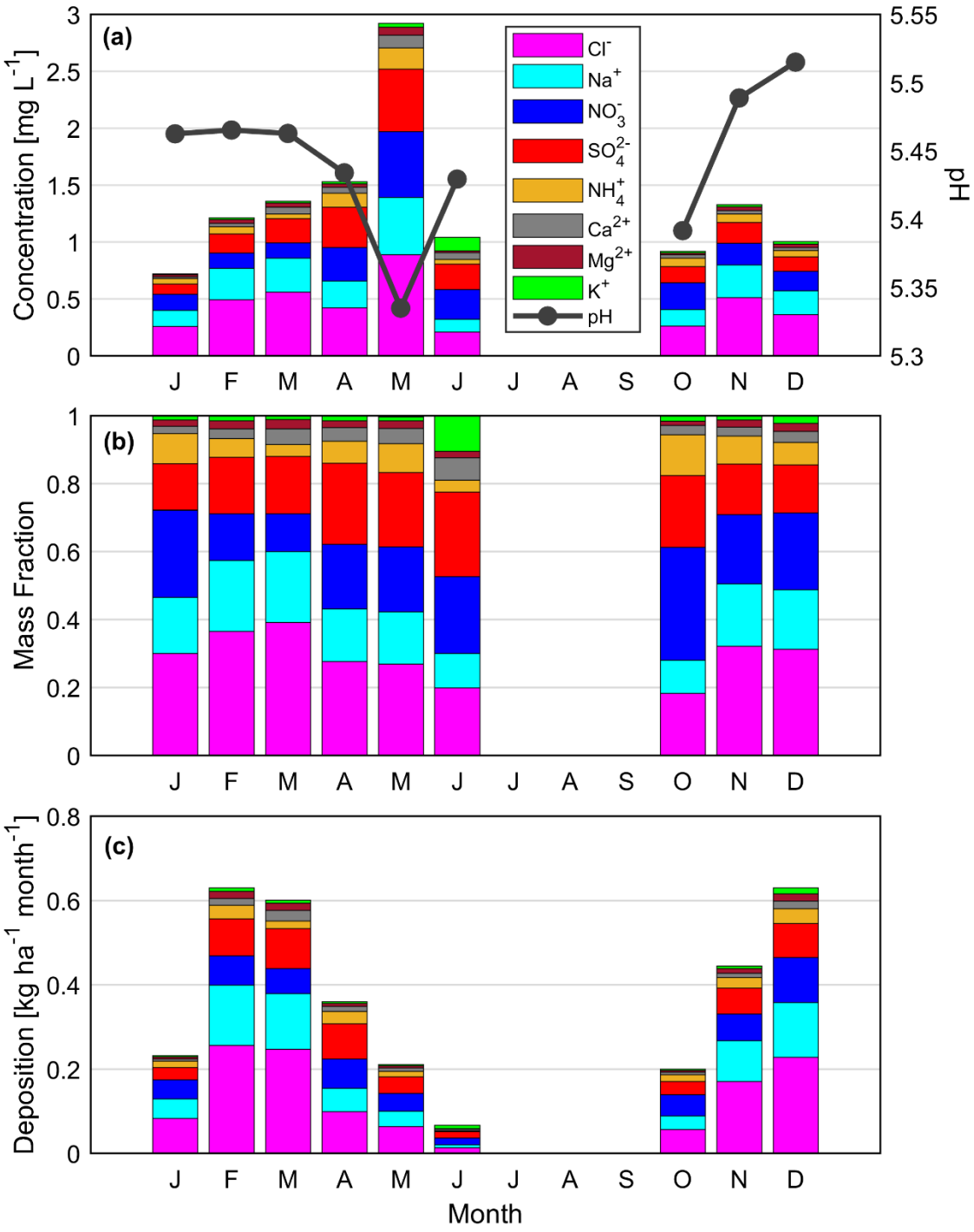

Figure 6. Monthly (a) precipitation-weighted average of weekly species concentrations, (b) precipitation-weighted average of weekly species mass fractions, and (c) wet deposition flux of species from the PNM site between 2010 and 2016. The number of samples in each month ranged from 6-23, except for June (n = 3) and July-September (n = 0).

Sources of Pollution and Interrelationships Between Aerosol and Precipitation Chemistry at a Central California Site

Hossein Dadashazar[a], Lin Ma[a], Armin Sorooshian[a,b*]

[a]Department of Chemical and Environmental Engineering, University of Arizona, PO BOX 210011, Tucson, AZ 85721, USA

[b]Department of Hydrology and Atmospheric Sciences, University of Arizona, PO BOX 210011, Tucson, AZ 85721, USA

[*]Corresponding author (phone: 520-626-5858, email: armin@email.arizona.edu, address: PO BOX 210011, Tucson, AZ 85721)

Supporting Information Summary: 18 Pages including cover page, 5 tables, and 9 figures

PMF runs

PMF solutions ranging from three to 10 sources were analyzed for $PM_{2.5}$ data obtained from PNM IMPROVE station. When considering the three and four factor solutions (Figures S2-S3), the model was not sufficiently successful to separate secondary aerosol into unique sources such as secondary sulfate and secondary nitrate. Secondary sulfate, secondary nitrate, biomass burning, sea salt, and dust were identified in the five factor solution (Figure S4). However, the secondary sulfate factor exhibited characteristics of a mixed source based on the presence of significant concentrations of Na, nitrate, and OC. For the six factor solution (Figure S5), secondary sulfate was described successfully without interference from species stemming from other known sources in the study region. In addition, a new factor including OC, EC, Cu, Br, and Na was identified, exhibiting fingerprints of both aged sea salt and vehicle emissions.

When examining the six and seven factor solutions, aged sea salt and vehicle emissions were successfully separated from one another. Overall, moving from five to seven factors improved the model performance for prediction of the following species: OC (r^2 = 0.79 for 7 factors vs r^2 = 0.65 for 5 factors), nitrate (r^2 = 0.99 for 7 factors vs r^2 = 0.90 for 5 factors), V (r^2 = 0.66 for 7 factors vs r^2 = 0.57 for 5 factors), Br (r^2 = 0.79 for 7 factors vs r^2 = 0.65 for 5 factors), and Zn (r^2 = 0.22 for 7 factors vs r^2 = 0.14 for 5 factors). For the eight factor solution (Figure S6), a new factor was identified, which exhibited a significant contribution to Zn with negligible contribution to other species. Zinc, Cu, Fe, and Mn are the tracers of brake and tire wear (Wahlin et al., 2006). However, the negligible contributions to Cu, Fe, and Mn help to reject the connection of this Zn factor to brake and tire wear. This further can indicate that there may be too many factors being fit in the eight factor solution. To further test the validity of the eight factor solution, error estimation (EE) analysis was performed on solutions ranging from having

five to nine factors (Table S3). There were no swaps in DISP and BS-DISP for five, six, and seven factors. In contrast, 9% and 28% of BS-DISP runs for eight and nine factors, respectively, were rejected due to factor swaps. Therefore, the seven factor solution was recognized as the most physically plausible based on source profiles and EE analysis.

Table S1. Summary ranges of detection limit (DL) for rain species measured by NADP/NTN.

	DL (mg/L)
Ca^{2+}	0.009-0.027
Mg^{2+}	0.001-0.009
K^{+}	0.001-0.004
Na^{+}	<0.006
NH_4^{+}	0.008-0.19
NO_3^{-}	≤0.007
Cl^{-}	<0.014
SO_4^{2-}	<0.03

Table S2. Summary statistics for $PM_{2.5}$ and speciated mass concentrations included in the PMF analysis from the Pinnacles National Monument IMPROVE station between 2010 and 2016. S/N = signal to noise ratio; DL = detection limits; Min/Max = minimum/maximum concentrations; $25^{th}/75^{th}$ = 25^{th} percentile/75^{th} percentile values.

Species	S/N	DL	Min	25th	Median	75th	Max
PM_{10} (μg m^{-3})	10.0	0.39-0.53	2.16E+00	5.76E+00	8.99E+00	1.26E+01	6.32E+01
$PM_{2.5}$ (μg m^{-3})	9.8	0.28-0.39	3.85E-01	2.55E+00	3.57E+00	4.90E+00	2.20E+01
SO_4^{2-} (ng m^{-3})	9.8	3.98-156.92	2.08E+01	3.35E+02	5.40E+02	8.39E+02	5.90E+03
NO_3^- (ng m^{-3})	9.7	5.8-96.5	1.99E+01	2.06E+02	3.82E+02	6.03E+02	3.90E+03
OC (ng m^{-3})	8.5	28.3-152.36	9.31E+01	4.81E+02	7.04E+02	1.02E+03	9.28E+03
EC (ng m^{-3})	2.7	8.3-71.1	5.28E+00	5.75E+01	1.08E+02	1.80E+02	1.60E+03
Na (ng m^{-3})	5.9	3.8-31.12	1.95E+00	6.36E+01	1.55E+02	3.04E+02	1.87E+03
Al (ng m^{-3})	7.1	1.13-13.41	6.35E-01	1.15E+01	2.29E+01	3.92E+01	2.91E+02
Si (ng m^{-3})	7.4	0.73-28.69	4.70E-01	2.59E+01	5.37E+01	9.34E+01	6.50E+02
Cl^- (ng m^{-3})	7.4	2.81-79.3	5.35E+00	2.73E+01	8.10E+01	2.64E+02	2.82E+03
K (ng m^{-3})	9.9	0.16-4.74	3.73E+00	2.01E+01	2.90E+01	4.12E+01	3.80E+02
Ca (ng m^{-3})	8.1	0.06-7.64	1.12E+00	1.19E+01	2.17E+01	3.36E+01	2.21E+02
V (ng m^{-3})	2.0	0.02-0.16	1.00E-02	5.50E-02	1.55E-01	3.10E-01	4.68E+00
Mn (ng m^{-3})	2.7	0.02-0.47	4.00E-02	1.65E-01	5.00E-01	8.30E-01	5.93E+00
Fe (ng m^{-3})	8.7	0.04-9.41	6.30E-01	1.24E+01	2.11E+01	3.39E+01	2.00E+02
Ni (ng m^{-3})	1.0	0.04-0.14	2.00E-02	5.50E-02	5.50E-02	1.60E-01	1.39E+00
Cu (ng m^{-3})	3.2	0.03-2.55	1.50E-02	2.33E-01	4.50E-01	7.60E-01	1.63E+01
Zn (ng m^{-3})	6.0	0.03-1.39	1.05E-01	7.00E-01	1.27E+00	2.17E+00	8.03E+01
Br (ng m^{-3})	7.5	0.03-0.28	6.00E-02	9.83E-01	1.47E+00	2.16E+00	8.78E+00

Table S3. Summary of PMF results for varying number of factors.

	Number of Factors				
Diagnostic	5	6	7	8	9
$Q_{expected}$	9798	8956	8114	7272	6430
Q_{true}	13571	10955	8878	6969	5520
Q_{robust}	13337	10768	8693	6858	5414
$Q_{true}/Q_{expected}$	1.39	1.22	1.09	0.96	0.86
$Q_{robust}/Q_{expected}$	1.36	1.20	1.07	0.94	0.84
BS mapping	100%	100%	100%	100%	100%
DISP swaps	0	0	0	0	0
BS-DISP % cases with swaps	0%	0%	0%	9%	24%

Table S4. Kruskal-Wallis test results for species monthly concentrations and pH for precipitation samples. Species with statistically significant differences ($p < 0.05$) in averaged monthly values are shown in the bold and italic font.

Test	*p* - value
Ca^{2+} monthly concentration	***8.00E-06***
Mg^{2+} *monthly concentration*	1.02E-01
K^{+} monthly concentration	***1.34E-02***
Na^{+} monthly concentration	1.54E-01
NH_4^{+} monthly concentration	***3.39E-02***
NO_3^{-} monthly concentration	***4.20E-02***
Cl^{-} monthly concentration	1.53E-01
SO_4^{2-} monthly concentration	***3.17E-05***
pH monthly value	***3.08E-03***

Table S5. Correlation matrix (r values) between weekly values of species concentrations, pH, and precipitation accumulation ("accumulation"). Values are only shown when statistically significant based on $p < 0.05$.

	Ca^{2+}	Mg^{2+}	K^{+}	Na^{+}	NH_4^{+}	NO_3^{-}	Cl^{-}	SO_4^{2-}	pH	Accumulation
Ca^{2+}	1.00									
Mg^{2+}	0.80	1.00								
K^{+}	0.70	0.79	1.00							
Na^{+}	0.75	0.99	0.78	1.00						
NH_4^{+}	0.64	0.54	0.51	0.48	1.00					
NO_3^{-}	0.69	0.40	0.42	0.34	0.72	1.00				
Cl^{-}	0.75	0.99	0.81	1.00	0.48	0.33	1.00			
SO_4^{2-}	0.86	0.90	0.77	0.85	0.74	0.62	0.86	1.00		
pH						-0.35			1.00	
Accumulation	-0.30		-0.19		-0.24	-0.28		-0.21		1.00

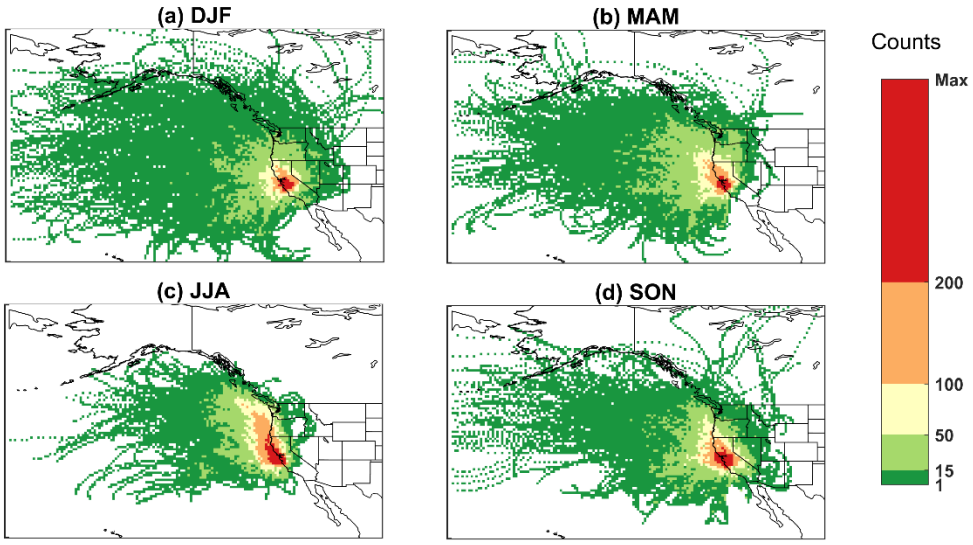

Figure S1. Trajectory frequency maps from 2010 to 2016 for (a) December to February (DJF), (b) March to May (MAM), (c) June to August (JJA), (d) September to November (SON) using 96 h back-trajectories at an ending point of 500 m above ground level at PNM.

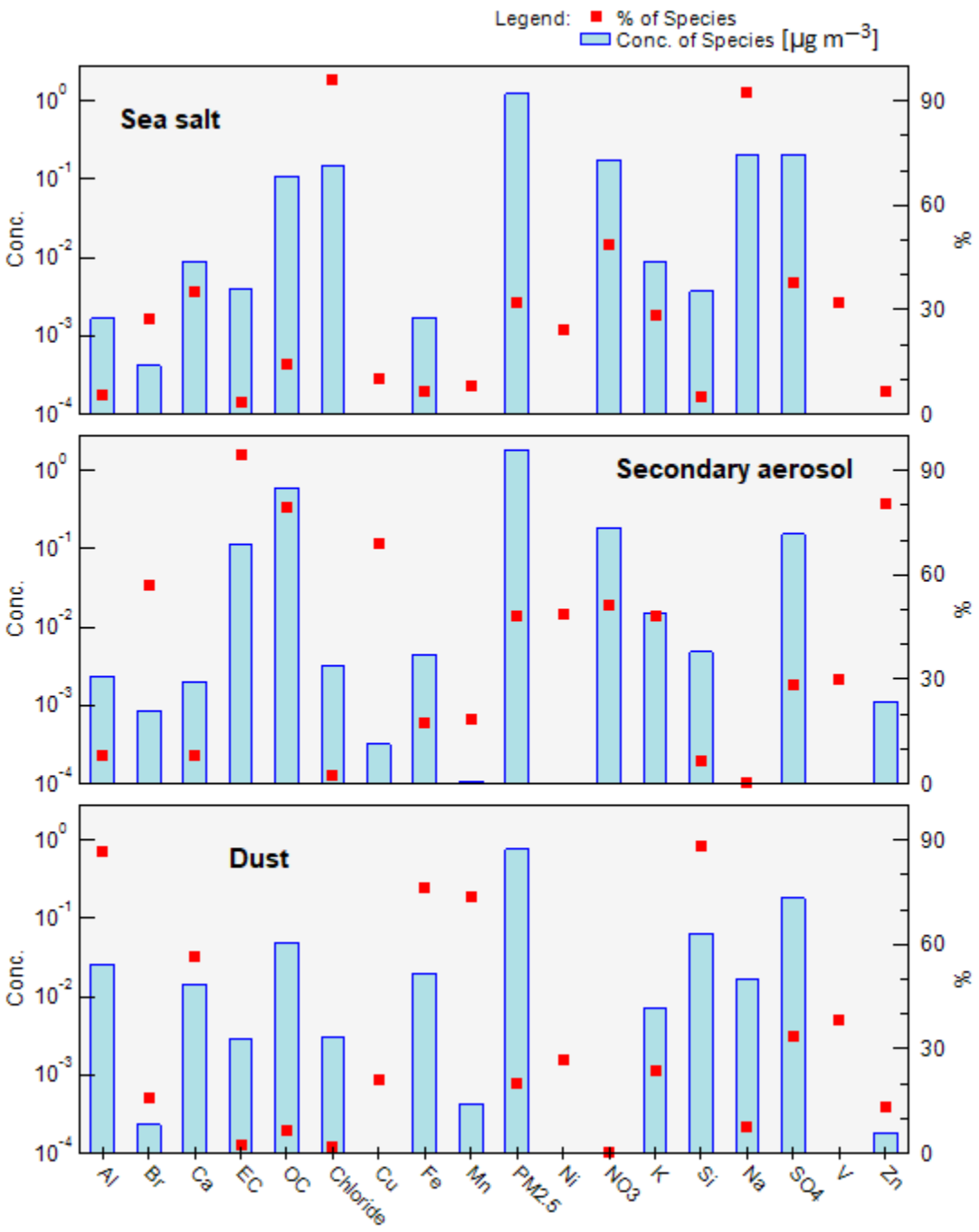

Figure S2. Factor profiles for the three factor PMF solution.

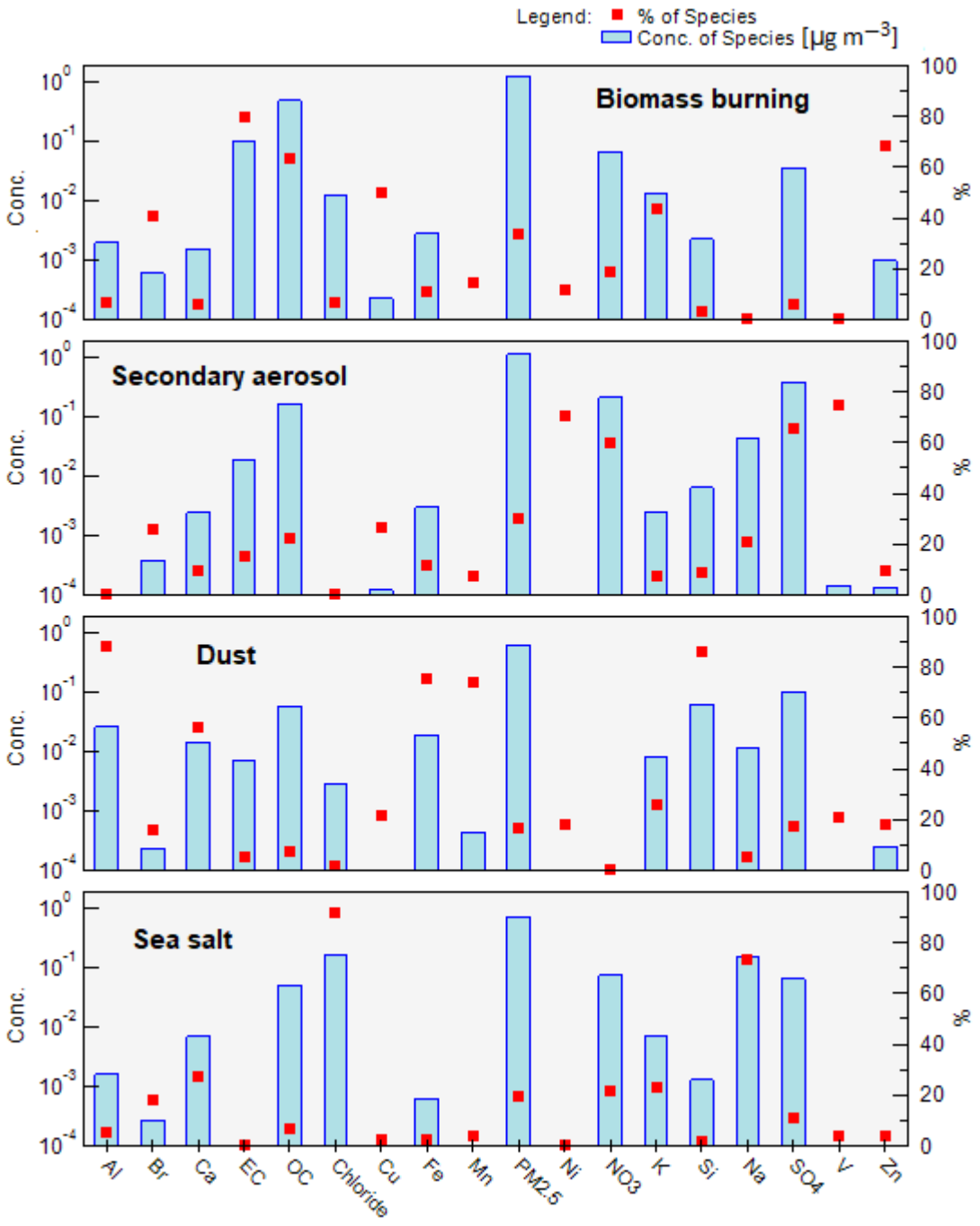

Figure S3. Factor profiles for the four factor PMF solution.

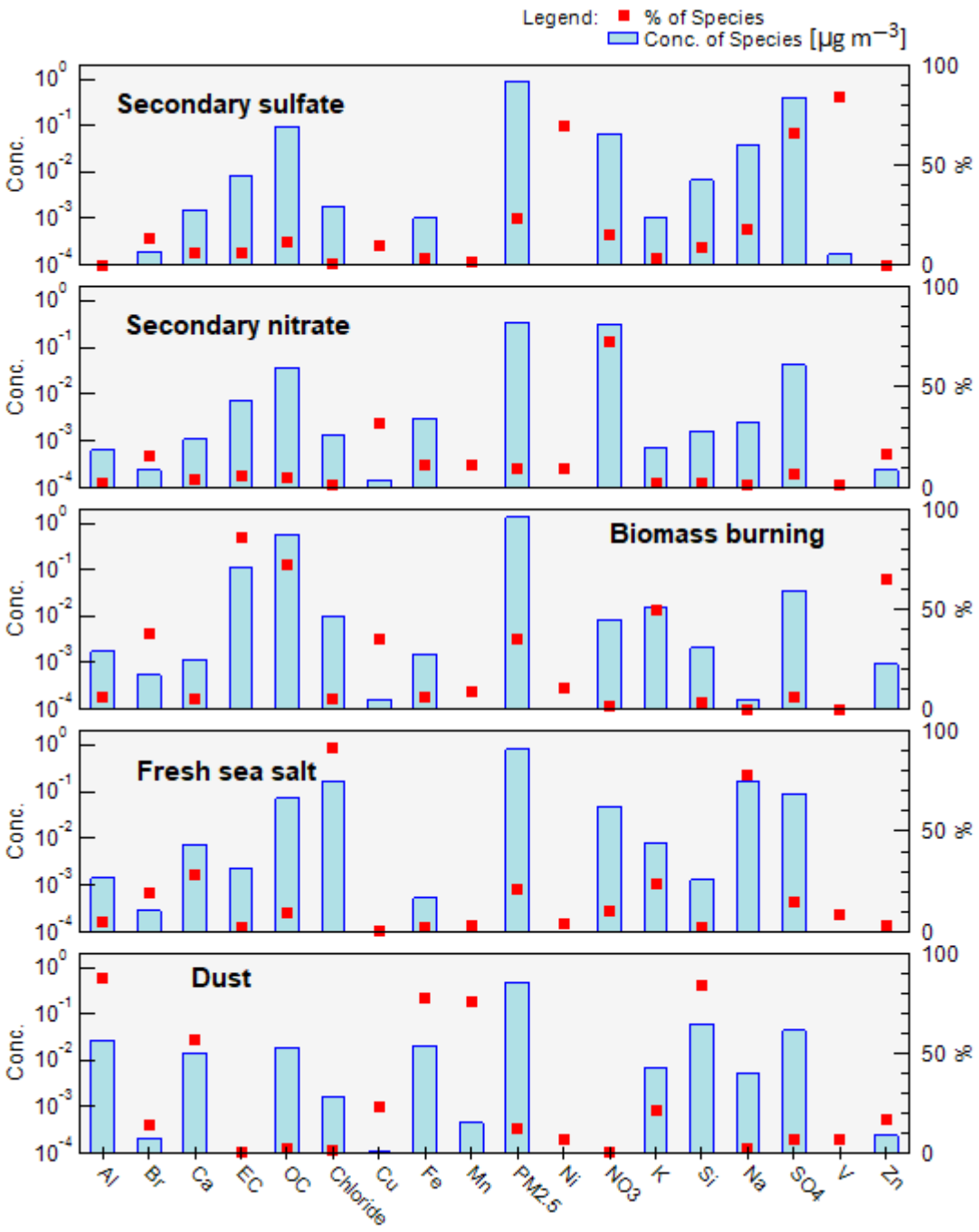

Figure S4. Factor profiles for the five factor PMF solution..

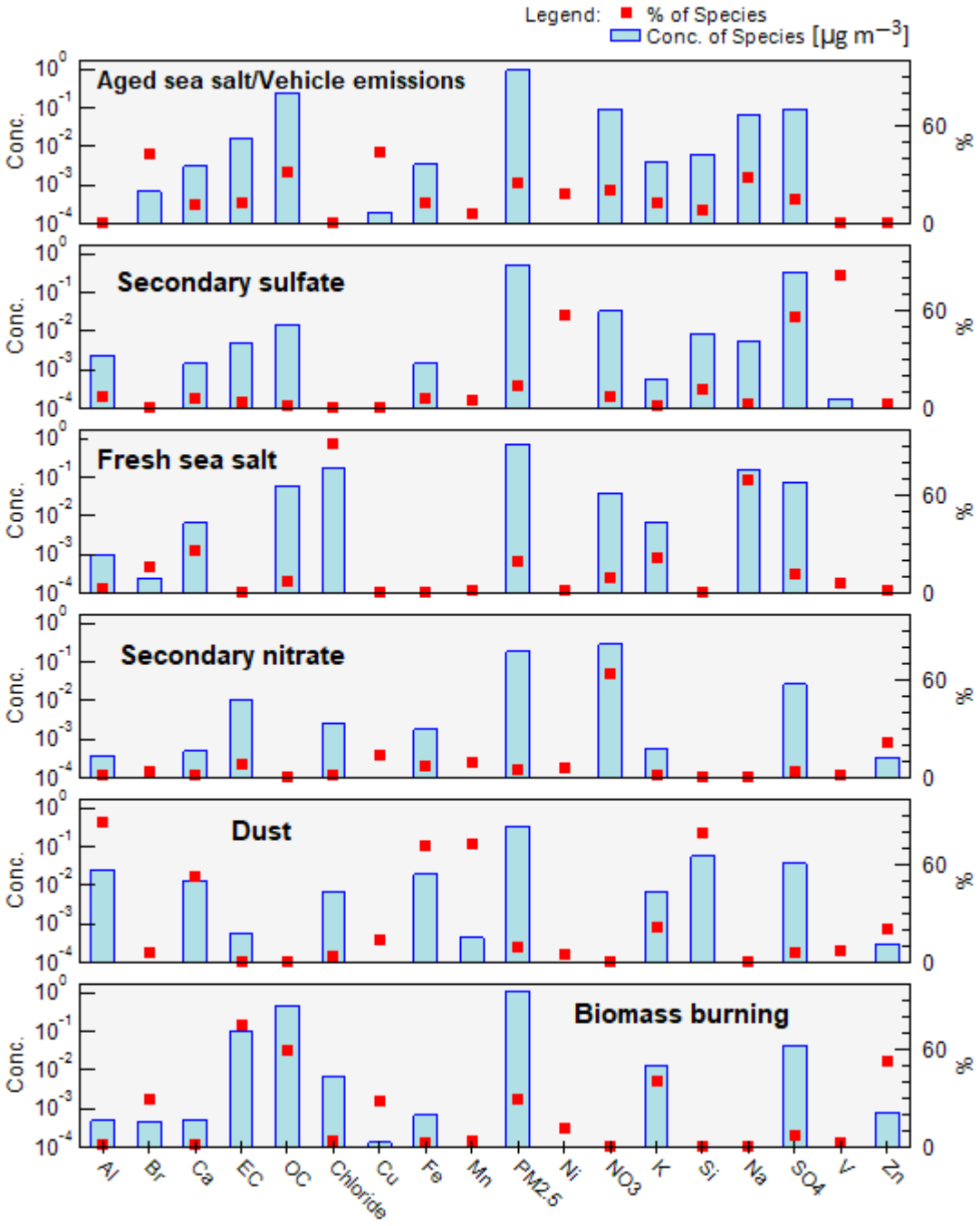

Figure S5. Factor profiles for the six factor PMF solution.

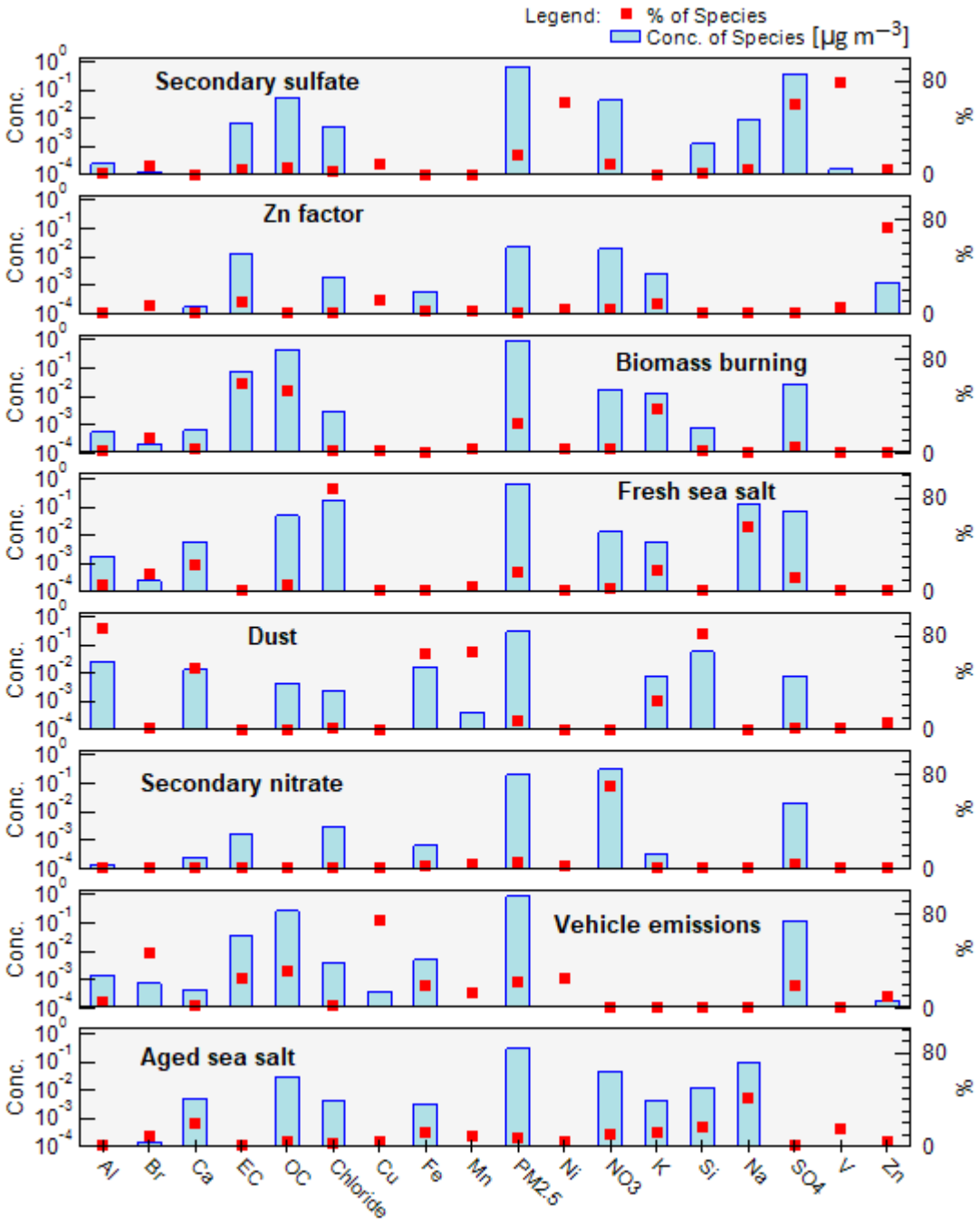

Figure S6. Factor profiles for the eight factor PMF solution.

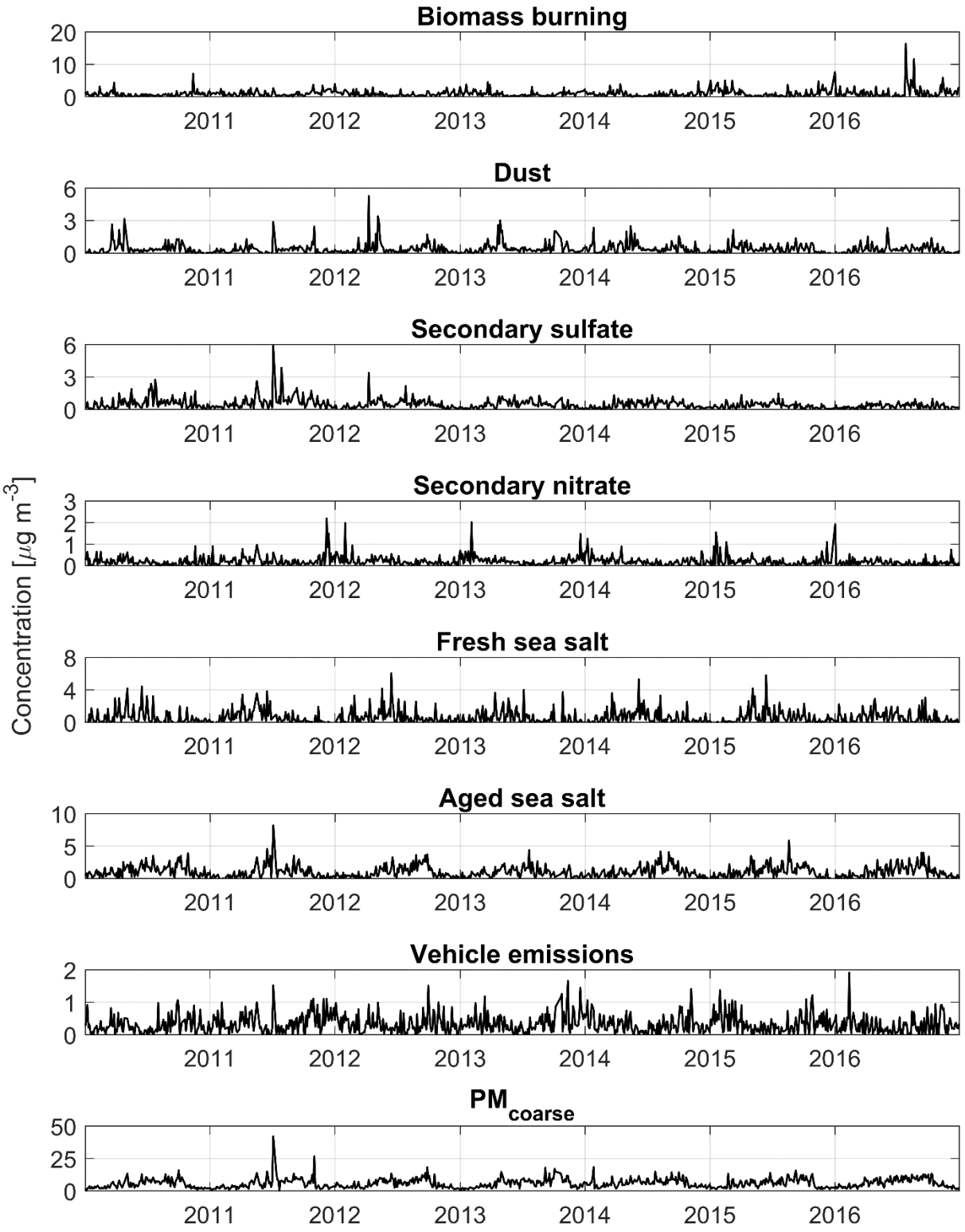

Figure S7. Time series of mass concentration for PM_{coarse} and the seven source factors used to construct $PM_{2.5}$ based on a PMF model.

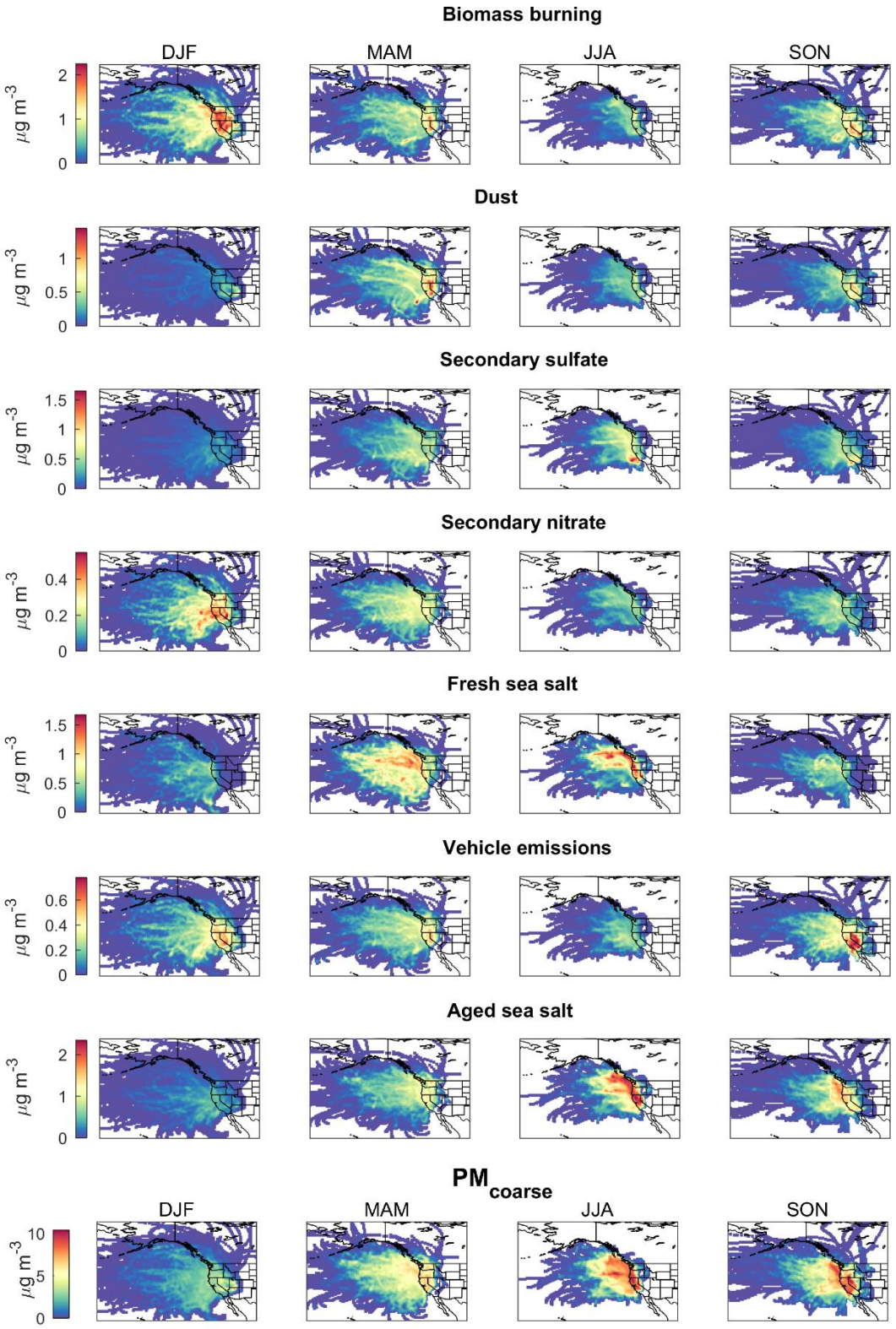

Figure S8. Seasonal Concentration Weighted Trajectory (CWT) maps of PM_{coarse} and PMF source factors for $PM_{2.5}$.

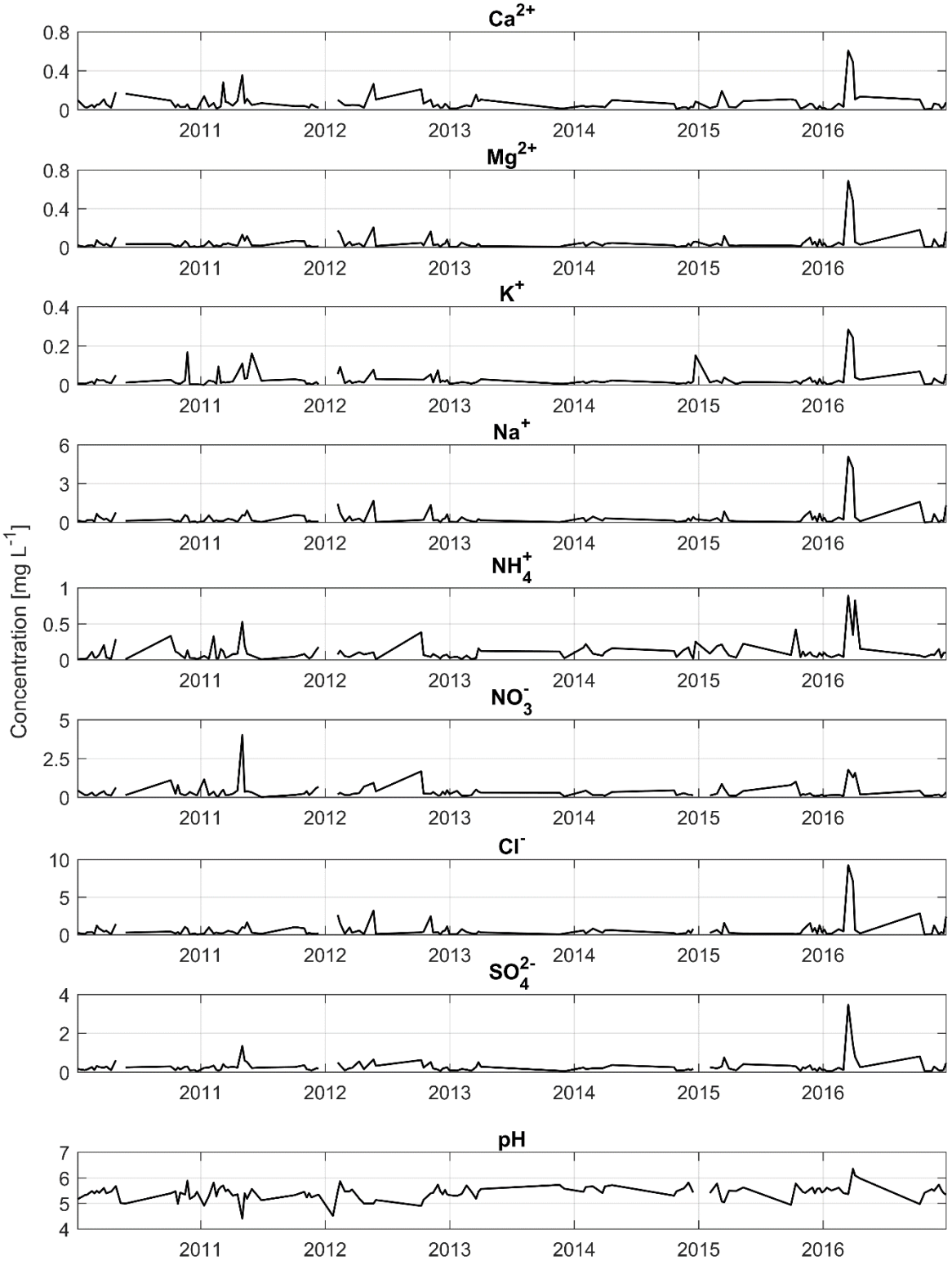

Figure S9. Time series of rain species mass concentrations at PNM measured by NADP/NTN.

References

Wahlin P, Berkowicz R, Palmgren F. Characterisation of traffic-generated particulate matter in Copenhagen. Atmospheric Environment 2006; 40: 2151-2159

APPENDIX D

MODELING THE OXIDATION OF PHENOLIC COMPOUNDS BY HYDROGEN PEROXIDE PHOTOLYSIS

This article has been published in the Chemosphere (2016).

Tianqi Zhang, Long Cheng, Lin Ma, Fanchao Meng, Robert G. Arnold, A. Eduardo Saez
Department of Chemical and Environmental Engineering, University of Arizona, Tucson, AZ, 85721. United States

Chemosphere 161 (2016) 349–357

Contents lists available at ScienceDirect

Chemosphere

journal homepage: www.elsevier.com/locate/chemosphere

Modeling the oxidation of phenolic compounds by hydrogen peroxide photolysis

Tianqi Zhang, Long Cheng, Lin Ma, Fanchao Meng, Robert G. Arnold, A. Eduardo Sáez*

Department of Chemical and Environmental Engineering, University of Arizona, Tucson, AZ, 85721, United States

HIGHLIGHTS

- A mechanism for oxidation of phenolic compounds by hydroxyl radicals is presented.
- Hydroxyl radical scavenging by intermediates reduces effectiveness of process.
- Kinetic model of the full mechanism is necessary for prediction of reactor performance.

ARTICLE INFO

Article history:
Received 7 March 2016
Received in revised form
13 June 2016
Accepted 29 June 2016
Available online 19 July 2016

Handling Editor: I. Cousins

Keywords:
Advanced oxidation processes
Kinetic model
Phenolic compounds
Radical reactions

ABSTRACT

Hydrogen peroxide UV photolysis is among the most widely used advanced oxidation processes (AOPs) for the destruction of trace organics in waters destined for reuse. Previous kinetic models of hydrogen peroxide photolysis focus on the dynamics of hydroxyl radical production and consumption, as well as the reaction of the target organic with hydroxyl radicals. However, the rate of target destruction may also be affected by radical scavenging by reaction products. In this work, we build a predictive kinetic model for the destruction of *p*-cresol by hydrogen peroxide photolysis based on a complete reaction mechanism that includes reactions of intermediates with hydroxyl radicals. The results show that development of a predictive kinetic model to evaluate process performance requires consideration of the complete reaction mechanism, including reactions of intermediates with hydroxyl radicals.

1. Introduction

Alkylphenol ethoxylates are non-ionic surfactants commonly used to formulate products such as detergents, paints, dispersing agents, wetting products, pesticides, and lubricants (Nagarnaik and Boulanger, 2011). These compounds are converted into alkylphenols in bioreactors used in wastewater treatment (Ahel et al., 1996), leading to their presence in surface waters (Scullion et al., 1996; Dong et al., 2015), groundwater (Swartz et al., 2006), municipal and industrial wastewater (Loyo-Rosales et al., 2007), aquatic sediments and marine shellfish (Lye et al., 1999). The most commonly detected metabolite, *p*-nonylphenol, induces breast tumor cell proliferation (Soto et al., 1991) and is a recognized endocrine disrupter (Lee and Lee, 1996). Therefore, the fates of *p*-nonylphenol and other phenolic compounds during wastewater treatment and following the release of treated wastewater into the environment is of practical importance.

Advanced oxidation processes (AOPs) are effective treatments for phenolic compounds due to their high rates of reaction with hydroxyl radicals (second-order rate constants in the range 10^9–10^{10} M^{-1} s^{-1}; Buxton et al., 1988). The UV photolysis of hydrogen peroxide (UV/H_2O_2) is among the most widely used AOPs in water treatment. Various models have been developed to simulate process kinetics. Common elements in these models include: (i) the kinetics of radical production from the direct photolysis of hydrogen peroxide, and hydroxyl radical scavenging by hydrogen peroxide and other radicals; (ii) reaction of hydroxyl radicals with the target compound and, although to a lesser extent, (iii) radical scavenging by reaction byproducts and intermediates (Lay, 1989; Glaze et al., 1995; Liao and Gurol, 1995; Stefan et al., 1996; Crittenden et al., 1999; Murcia et al., 2015; Rojas et al., 2010, 2011).

The first step in the reaction mechanism for radical oxidation of phenolic compounds is OH addition to the ring (Wojnárovits et al.,

* Corresponding author.
E-mail address: esaez@email.arizona.edu (A.E. Sáez).

http://dx.doi.org/10.1016/j.chemosphere.2016.06.110
0045-6535/

2002). The position of OH addition is controlled by substitutions on the ring, but *para*- and *ortho*-hydroxylation normally predominate due to the electrophilic nature of the hydroxyl radical (Omura and Matsuura, 1968; Matsuura and Omura, 1974). Further oxidation of the resulting dihydroxy compound occurs via abstraction of a hydrogen atom to form benzoquinones, after which the ring can be cleaved to yield aliphatic acids (Scheck and Frimmel, 1995).

Previous efforts on the kinetic modeling of the UV/H_2O_2 process generally include a complete description of the chemistry behind radical formation, but rarely consider reaction intermediate and by-products. Glaze et al. (1995) proposed a kinetic model containing the most important elements of UV/H_2O_2 photolysis to predict the time-dependent concentration of a halogenated target. They used a quasi-steady-state assumption (QSSA) to calculate the time-dependent concentrations of free radicals. Their model did not account for CO_2 evolution/pH change and neglected the role of all radical scavenging species except H_2O_2. Stefan et al. (1996) followed a similar approach, but assumed that the target compound (in their case acetone) was transformed to oxalic and formic acids and then to CO_2. Subsequently, Crittenden et al. (1999) modeled UV/H_2O_2 process without reliance on a quasi-steady-state assumption for radical concentrations. Their work showed that the QSSA tends to under-predict hydroxyl radical concentrations in some cases and therefore the rates of target compound decomposition. Furthermore, their model included radical scavenging reactions.

The model of Song et al. (2008) accounted for time-dependent radical concentrations, pH changes due to product formation (CO_2 and low molecular weight acids), and radical scavenging by H_2O_2 and natural organic matter.

More recent modeling efforts of oxidation of phenolic compounds usually include a full formulation of the dynamics of radical formation, but very few or no details of the influence of intermediate compounds and by-products over target compound degradation. De Luis et al. (2011) presented a model of phenol and cresol degradation during the UV/H_2O_2 process that considered possible reactions of the organic compounds with produced radicals, but without considering intermediate compounds and by-products. A similar approach was followed by Rojas et al. (2010, 2011) to model the UV/H_2O_2 and Fenton's reaction processes. Moreira et al. (2012) developed a phenomenological model to simulate the TiO_2 photocatalysis of phenol, which includes specific details about the reaction mechanism.

In this work, *p*-cresol was selected as an example of a substituted phenolic compound. Even though *p*-cresol itself is not a common trace organic in wastewater effluent, it has chemical structure and reactivity with hydroxyl radicals similar to *p*-nonylphenol, which is a common endocrine disrupter compound widely present in wastewater effluent. A mechanism for radical-dependent UV/photolysis was proposed and calibrated based on time-dependent measurements of *p*-cresol and a number of reaction products/intermediates in a batch reactor. The model accounts for changes in ionic strength and pH due to reactant conversions. Reactor fluence rate and the *p*-cresol quantum yield during direct photolysis were considered in the kinetic model. The calibrated model was employed to predict the evolution of concentrations of *p*-cresol and reaction intermediates under various experimental conditions.

2. Materials and methods

2.1. Chemicals

All chemicals were obtained from commercial sources and used without further purification, including *p*-cresol (Acros, 99+%), 4-methylcatechol (Acros, 98%), hydrogen peroxide (Acros, 50 wt%), titanium sulfate (Pfaltz&Bauer, 30%), formate (Fluka, 1000 mg/L ± 4 mg/L), acetate (Fluka, 1000 mg/L ± 4 mg/L), oxalate (Fluka, 1000 mg/L ± 4 mg/L), and TOC standard (Fluka, 50 mg/L ± 2 mg/L). Methanol (Fisher Chemical, HPLC Grade) and acetonitrile (Fisher Chemical, HPLC Grade) were solvents for HPLC analyses. Milli-Q water (resistivity ≥18.0 mΩ cm^{-1}) was obtained from a Barnstead NANOpure II system. Glassware was washed and heated overnight at 550 °C prior to use.

2.2. Experimental procedure

All experiments were conducted in a cylindrical (14-cm diameter, 950-mL) glass batch reactor, equipped with low pressure (LP) UV lamp, UV fluence meter (Hamamatsu, H8025-254) and magnetic stirrer. Stock solutions of *p*-cresol were prepared one day before use. 4-Methylcatechol stock solutions were prepared a half hour before use in amber glass containers. The UV lamp (43-cm long) was turned on two hours before the experiments. The lamp position was 21 cm above the liquid level in the reactor. A quartz sleeve covered the lamp to cut-off wavelengths below 185 nm. Solution volume was 300 mL in all experiments (liquid depth was 1.95 cm). Experiments were initiated by exposing the reactor to UV light. Experiment duration depended on the initial *p*-cresol concentration but ranged from one to three hours. Samples were analyzed immediately after withdrawal. Dilution was frequently necessary to maintain concentrations within the recommended analytical range. Temperature was maintained at T = 24.5 ± 0.5 °C. The trajectory of solution pH was determined in each experiment.

2.3. Analytics

The concentration of *p*-cresol was measured by fluorescence spectrometry (PerkinElmer LS 55). The inner filter effect (IFE) caused by light absorption and reabsorption of light-absorbing compounds was corrected mathematically, accounting for the absorption spectrum of the sample (MacDonald et al., 1997). Solution spectra were measured using a UV–Vis spectrophotometer (Thermo Science, Genesys 10s). Even though the reaction intermediate 4-methylcatechol is produced in concentrations that are comparable in order of magnitude to *p*-cresol, independent measurements showed that its fluorescence intensities were negligible compared to those of *p*-cresol in the relevant range of wavelengths.

Analysis of primary intermediates, particularly 4-methylcatechol, was carried out by HPLC (Agilent Technologies, 1200 Series) with a Polar-RP, 80 A column (15 cm × 4.6 mm × 4 μm) (Phenomenex) and UV/VIS detector at 280 nm. Elution solvents were 10% methanol in water (A) and acetonitrile (B), Q = 0.4 mL/min. The mobile phase initially consisted of 45% vol. B, linearly ramped to 65% vol. B at 15 min and then restored to the initial condition.

Formate, acetate and oxalate were measured via ion chromatography (Dionex, ICS-5000) equipped with an AS18 column (2 × 250 mm) (Dionex IonPac™), an AG18 guard column (2 × 50 mm) (Dionex IonPac™), and an AS-DV (Dionex) autosampler. Ions were detected by suppressed conductivity of the eluent using an ASRS-2mm self-regenerating suppressor (Dionex). The eluent (KOH solution; Q = 0.4 mL/min) was programmed as follows: 1 mM for 8 min, ramped (linearly) to 30 mM in 20 min, then immediately restored to 1 mM.

Hydrogen peroxide was measured using a modified peroxytitanic (colorimetric) method (Boltz and Holwell, 1978). Absorbance was measured spectrophotometrically (Thermo Science, Genesys 10s) at 407 nm. Samples were diluted to maintain absorbance values within linear limits. TOC was monitored using a Total

Organic Carbon analyzer (Shimadzu, TOC-V_{CSH}).

2.4. Proposed mechanism

The proposed mechanism of *p*-cresol oxidation by hydroxyl radicals is shown in Fig. 1. The first step is OH radical addition to the ring to form 4-methylcatechol (Matsuura and Omura, 1974; Olariu et al., 2002). Two possible pathways (Omura and Matsuura, 1968; Scheck and Frimmel, 1995) are used to explain the hydroxylation. One is the attack of OH radical on the phenolic ring, resulting in the formation of a cyclohexadienyl radical, which is subsequently converted into 4-methylcatechol. The other involves abstraction of a hydrogen atom yielding a phenoxyl radical that can combine with a second OH radical. However, the hydrogen abstraction reaction of a methyl H atom (Wang et al., 1998) is at least one order of magnitude slower than the formation of a cyclohexadienyl radical (Sehested et al., 1975; Wojnárovits et al., 2002). Further hydroxylation may convert 4-methylcatechol; however, this reaction has negligible yield (Scheck and Frimmel, 1995). Oxidation of 4-methylcatechol to 4-methylbenzoquinone occurs in two steps: the OH radical attacks the ring forming a 4-methylcatechol semiquinone radical (Gohn and Getoff, 1977), after which the semiquinone radical converts to 4-methylbenzoquinone in the presence of molecular oxygen (Davies et al., 1995). Once 4-methylbenzoquinone is formed, ring tension and oxidizing agents force fission of the ring. The C–C bond in the ring between the carbons attached to oxygen atoms is cleaved, and 3-methyl-muconic acid is one of the fission products (Pospisil et al., 1957; Scheck and Frimmel, 1995). Oxidation of 3-methyl-muconic acid involves the carbon double bonds. Because of the higher acidity of the α-hydrogen adjacent to the double bond, it can be easily abstracted by the OH radical (Jin et al., 2010; Huang et al., 2011). Low molecular weight organic acids such as lactic and oxalic acid are oxidation products. The abstraction of α-hydrogen next to a –COOH group by OH radical forms additional low-molecular -weight acids such as acetic and formic acids (Boonrattanakij et al., 2009). Eventually, oxalic acid, acetic acid and formic acid are oxidized by OH radicals to carbon dioxide (Getoff et al., 1971; Leitner and Dore, 1997; Hart, 1951; Sun and Saeys, 2008).

2.5. Kinetic model

The proposed kinetic model for the oxidation of p-cresol during UV/H_2O_2 photolysis consists of 36 reactions (Table 1). The UV/H_2O_2 photolysis mechanism, including an initiation step that produces hydroxyl radical (·OH) and propagation steps that scavenge ·OH and produce other active radicals ($O_2^{\cdot-}$ and $CO_3^{\cdot-}$), is based on the work of Rojas et al. (2010, 2011) and references therein. Since the reactor was open to the atmosphere, the initial carbon dioxide concentration was assumed to be at equilibrium with atmospheric carbon dioxide. The scavenging effect of inorganic carbon species, bicarbonate and carbonate ions was considered in the model, but calculations showed that their effect was negligible in the range of conditions of the experiments.

The rate of direct photolysis of H_2O_2 is given by

$$R_{R1} = -\Phi_{H_2O_2} f_{H_2O_2} I_0 e^{-2.303 A_z} \quad (1)$$

where $\Phi_{H_2O_2}$ (Table 1) is the quantum yield for the photocatalytic decomposition of H_2O_2, $f_{H_2O_2}$ is the fraction of total light absorbed by H_2O_2, I_0 is the average fluence rate (in Einsteins per unit time and reactor volume) at the reactor surface and A_z is the total absorbance of the solution as function of depth. In the model, H_2O_2, PC, 4 MC and 4 MB are the only important light-absorbing species at 254 nm. Therefore, A_z is given by

$$A_z = (\varepsilon_{H_2O_2}[H_2O_2] + \varepsilon_{PC}[PC] + \varepsilon_{4MC}[4MC] + \varepsilon_{4MB}[4MB])z \quad (2)$$

where $\varepsilon_{H_2O_2}$, ε_{PC}, ε_{4MC} (Table 1) and ε_{4MB} (2100 M^{-1} cm^{-1}; Waite, 1976; Jongberg et al., 2011) are molar extinction coefficients for hydrogen peroxide, *p*-cresol, 4-methylcatechol and 4-methylbenzoquinone at 254 nm, respectively, and z is the distance measured downward within the reactive mixture from the top

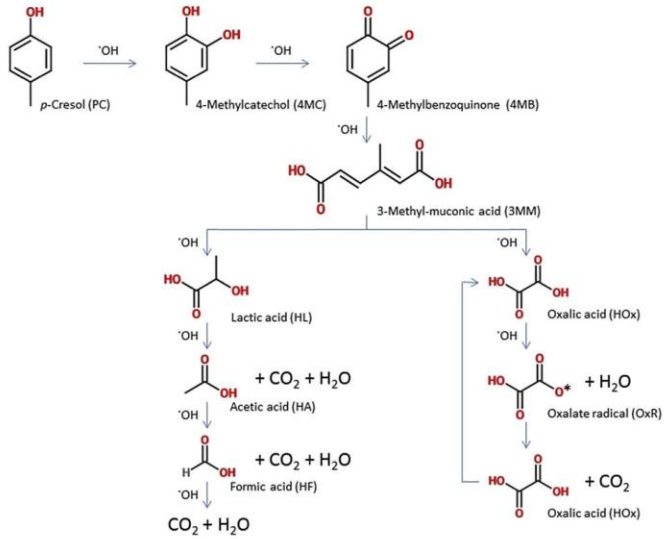

Fig. 1. Proposed mechanism of p-cresol oxidation by hydroxyl radicals (see text for description).

Table 1
Kinetic and equilibrium parameters used in the model. Acronyms are defined in Fig. 1. Quantum yield (Φ) and molar extinction coefficients (ε) are reported for photolysis reactions, kinetic rate constants (k) are reported for relevant reactions, and equilibrium constants (K) are reported for reactions assumed to reach equilibrium instantaneously in the reaction mixture.

	Reaction	Parameters	Reference
R1	$H_2O_2 + h\nu \rightarrow 2\ {}^{\cdot}OH$	$\varepsilon_1 = 18.7\ M^{-1}\ cm^{-1}$ $\Phi_1 = 0.5\ mol/Ein$	Volman and Chen (1959)
R2	${}^{\cdot}OH + H_2O_2 \rightarrow O_2^{\cdot-} + H_2O + H^+$	$k_2 = 2.7 \times 10^7\ M^{-1}\ s^{-1}$	Buxton et al. (1988)
R3	${}^{\cdot}OH + HO_2^{\cdot} \rightarrow O_2^{\cdot-} + H_2O$	$k_3 = 7.5 \times 10^9\ M^{-1}\ s^{-1}$	Buxton et al. (1988)
R4	${}^{\cdot}OH + HCO_3^- \rightarrow CO_3^{\cdot-} + H_2O$	$k_4 = 8.5 \times 10^6\ M^{-1}\ s^{-1}$	Buxton et al. (1988)
R5	${}^{\cdot}OH + CO_3^{2-} \rightarrow CO_3^{\cdot-} + OH$	$k_5 = 3.9 \times 10^8\ M^{-1}\ s^{-1}$	Buxton et al. (1988)
R6	${}^{\cdot}OH + HO_2^{\cdot} \rightarrow O_2 + H_2O$	$k_6 = 6.6 \times 10^9\ M^{-1}\ s^{-1}$	Buxton et al. (1988)
R7	${}^{\cdot}OH + O_2^{\cdot-} \rightarrow O_2 + OH$	$k_7 = 8.0 \times 10^9\ M^{-1}\ s^{-1}$	Buxton et al. (1988)
R8	${}^{\cdot}OH + {}^{\cdot}OH \rightarrow H_2O_2$	$k_8 = 5.5 \times 10^9\ M^{-1}\ s^{-1}$	Buxton et al. (1988)
R9	${}^{\cdot}OH + CO_3^{\cdot-} \rightarrow$ products	$k_9 = 3.0 \times 10^8\ M^{-1}\ s^{-1}$	Holeman et al. (1987)
R10	$O_2^{\cdot-} + H_2O_2 \rightarrow {}^{\cdot}OH + O_2 + OH$	$k_{10} = 0.13\ M^{-1}\ s^{-1}$	Bielski et al. (1985)
R11	$O_2^{\cdot-} + CO_3^{\cdot-} \rightarrow O_2 + CO_3^{2-}$	$k_{11} = 6.5 \times 10^8\ M^{-1}\ s^{-1}$	Eriksen et al. (1985)
R12	$O_2^{\cdot-} + HO_2^{\cdot} \rightarrow HO_2^- + O_2$	$k_{12} = 9.7 \times 10^7\ M^{-1}\ s^{-1}$	Bielski et al. (1985)
R13	$HO_2^{\cdot} + HO_2^{\cdot} \rightarrow H_2O_2 + O_2$	$k_{13} = 8.6 \times 10^5\ M^{-1}\ s^{-1}$	Weinstein and Bielski (1979)
R14	$HO_2^{\cdot} + H_2O_2 \rightarrow {}^{\cdot}OH + O_2 + H_2O$	$k_{14} = 3.7\ M^{-1}\ s^{-1}$	Bielski et al. (1985)
R15	$CO_3^{\cdot-} + H_2O_2 \rightarrow HCO_3^- + O_2^{\cdot-} + H^+$	$k_{15} = 8.0 \times 10^5\ M^{-1}\ s^{-1}$	Neta et al. (1988)
R16	$CO_3^{\cdot-} + HO_2^{\cdot} \rightarrow HCO_3^- + O_2$	$k_{16} = 3.0 \times 10^7\ M^{-1}\ s^{-1}$	Neta et al. (1988)
R17	$CO_3^{\cdot-} + CO_3^{\cdot-} \rightarrow 2CO_3^{2-}$	$k_{17} = 2.0 \times 10^7\ M^{-1}\ s^{-1}$	Neta et al. (1988)
R18	$H_2O_2 \leftrightarrow HO_2^- + H^+$	$k_{18} = 2.51 \times 10^{-2}\ s^{-1}$ $k_{18r} = 1 \times 10^{10}\ M^{-1}\ s^{-1}$	Perry et al. (1981)
R19	$HO_2^{\cdot} \leftrightarrow O_2^{\cdot-} + H^+$	$k_{19} = 1.58 \times 10^5\ s^{-1}$ $k_{19r} = 1 \times 10^{10}\ M^{-1}\ s^{-1}$	Perry et al. (1981)
R20	$CO_2(aq) + H_2O \leftrightarrow H_2CO_3$	$k_{20} = 0.039\ s^{-1}$ $k_{20r} = 23\ s^{-1}$	Housecroft and Sharpe (2005)
R21	$H_2CO_3 \leftrightarrow HCO_3^- + H^+$	$k_{21} = 1.25 \times 10^7\ s^{-1}$ $k_{21r} = 5 \times 10^{10}\ M^{-1}\ s^{-1}$	Greenwood and Earnshaw (1997)
R22	PC + hν → products	$\varepsilon_{22} = 340\ M^{-1}\ cm^{-1}$ $\Phi_{22} = 0.034\ mol/Ein$	This work
R23	PC + ${}^{\cdot}OH \rightarrow 4\ MC$	$k_{23} = 1.2 \times 10^{10}\ M^{-1}\ s^{-1}$	Buxton et al. (1988)
R24	4 MC + hν → products	$\varepsilon_{24} = 310\ M^{-1}\ cm^{-1}$ $\Phi_{24} = 0.007\ mol/Ein$	This work
R25	4 MC + ${}^{\cdot}OH \rightarrow 4\ MB$	$k_{25} = 1.6 \times 10^{10}\ M^{-1}\ s^{-1}$	Gohn and Getoff (1977)
R26	4 MB + ${}^{\cdot}OH \rightarrow 3\ MM$	$k_{26} = 2.0 \times 10^{10}\ M^{-1}\ s^{-1}$	This work
R27	3 MM + ${}^{\cdot}OH \rightarrow$ L + 2 Ox (Ox^{2-})	$k_{27} = 5.0 \times 10^8\ M^{-1}\ s^{-1}$	Kang et al. (2002)
R28	L + ${}^{\cdot}OH \rightarrow$ HA (A$^-$) + CO_2 + H_2O	$k_{28} = 3.0 \times 10^8\ M^{-1}\ s^{-1}$	Buxton et al. (1988)
R29	Ox + ${}^{\cdot}OH \rightarrow Ox^{\cdot}$ + H_2O	$k_{29} = 4.7 \times 10^7\ M^{-1}\ s^{-1}$	Buxton et al. (1988)
R30	Ox^{2-} + ${}^{\cdot}OH \rightarrow Ox^{\cdot}$ + OH	$k_{30} = 7.7 \times 10^6\ M^{-1}\ s^{-1}$	Buxton et al. (1988)
R31	$Ox^{\cdot}$ + $Ox^{\cdot}$ → Ox (Ox^{2-}) + 2 CO_2	$k_{31} = 5.0 \times 10^8\ M^{-1}\ s^{-1}$	Ershov et al. (2008)
R32	HA + ${}^{\cdot}OH \rightarrow$ F + CO_2 + H_2O	$k_{32} = 1.23 \times 10^8\ M^{-1}\ s^{-1}$	Sun and Saeys (2008)
R33	A$^-$ + ${}^{\cdot}OH \rightarrow$ F + CO_2 + OH	$k_{33} = 8.5 \times 10^7\ M^{-1}\ s^{-1}$	Buxton et al. (1988)
R34	F + ${}^{\cdot}OH \rightarrow CO_2 + H_2O$	$k_{34} = 9.77 \times 10^7\ M^{-1}\ s^{-1}$	Sun and Saeys (2008)
E35	Ox ↔ Ox^{2-} + H^+	$K_{35} = 6.31 \times 10^{-5}\ M$	Benjamin (2002)
E36	HA ↔ A$^-$ + H^+	$K_{36} = 1.74 \times 10^{-5}\ M$	Benjamin (2002)
E37	HCO_3^- ↔ CO_3^{2-} + H^+	$K_{37} = 4.48 \times 10^{-11}\ M$	Benjamin (2002)

surface. Note that

$$f_{H_2O_2} = \frac{\varepsilon_{H_2O_2} z [H_2O_2]}{A_z} \tag{3}$$

The volume averaging of equation (1) over the batch reactor is, after manipulations,

$$R_{R1} = -\Phi_{H_2O_2} f_{H_2O_2} I_0 \left(1 - e^{-2.303A}\right) \tag{4}$$

where the angular brackets denote volume average, and $A = A_z$ ($z = l$), where l is the depth of the reacting mixture. Other direct photolysis reactions are treated in the same manner.

Radical reactions are generally second-order reactions. For example, the reaction rate for the consumption of *p*-cresol by OH radical is

$$R_{R23} = -k_{23}[PC]\left[\dot{O}H\right] \tag{5}$$

where k_{23} is the second-order rate constant of *p*-cresol reaction with ${}^{\cdot}OH$ (Table 1).

Acid-base reactions are considered to be at equilibrium. The equilibrium equations are used to relate concentrations of the species involved. For example, for acetic acid,

$$[HA] = \frac{TOT_A\ \gamma_{\pm 1}[H^+]}{K_{36} + \gamma_{\pm 1}[H^+]} \tag{6}$$

$$\gamma_{\pm 1}[A^-] = \frac{TOT_A\ K_{36}}{K_{36} + \gamma_{\pm 1}[H^+]} \tag{7}$$

where $TOT_A = [HA] + [A^-]$, K_{36} is equilibrium constant of acetic acid dissociation and $\gamma_{\pm 1}$ is the activity coefficient, which is calculated from the Davies Equation.

Based on the mechanism proposed, the corresponding mole balances of H_2O_2, *p*-cresol and 4-methylcatechol yield the following system of differential equations:

$$\frac{d[H_2O_2]}{dt} = -\Phi_{H_2O_2} f_{H_2O_2} I_0 \left(1 - e^{-2.303A}\right) - k_2[H_2O_2]\left[\dot{O}H\right] + k_8\left[\dot{O}H\right]^2 - k_{10}[H_2O_2]\gamma_{\pm 1}\left[O_2^{\cdot-}\right] + k_{13}\left[HO_2^{\cdot}\right]^2 - k_{14}[H_2O_2]\left[HO_2^{\cdot}\right] - k_{15}[H_2O_2]\gamma_{\pm 1}\left[CO_3^{\cdot-}\right] - k_{18}[H_2O_2] + k_{18r}\gamma_{\pm 1}\left[HO_2^-\right]\gamma_{\pm 1}\left[H^+\right] \quad (8)$$

$$\frac{d[PC]}{dt} = -\Phi_{PC} f_{PC} I_0 \left(1 - e^{-2.303A}\right) - k_{23}[PC]\left[\dot{O}H\right] \quad (9)$$

$$\frac{d[4MC]}{dt} = -\Phi_{4MC} f_{4MC} I_0 \left(1 - e^{-2.303A}\right) + k_{23}[PC]\left[\dot{O}H\right] - k_{25}[4MC]\left[\dot{O}H\right] \quad (10)$$

$$[TOC] = [TOC]_0 - [CO_2] + [CO_2]_0 \quad (11)$$

where $[TOC]_0$ and $[CO_2]_0$ are initial TOC and CO_2 molar concentrations. More details of the model formulation, including mole balances of radicals ($^{\cdot}OH$, $HO_2^{\cdot}$, $O_2^{\cdot-}$ and $CO_3^{\cdot-}$) and reaction intermediates (4 MB, 3 MM, LA^-, OA^-, OA^{2-}, $OA^{\cdot-}$, AA, AA^- and FA^-), plus algebraic equations ($[H_2CO_3]$ as a function of $[TOTCO_3]$ and charge balance) are provided in the supporting information.

The fact that the reactor is well mixed implies that most species concentrations are uniform in the reactor. However, the relatively high reaction rates of radical species suggest that their concentrations are not necessarily uniform. For example, the OH radical production by reaction R1 (Table 1) is not uniform due to the attenuation of light with depth. In the model equations, radical concentrations are volume-averaged concentrations. The formulation is based on the assumption that kinetics that are not linear on radical concentrations (such as in radical/radical reactions like R8, Table 1) can be expressed in terms of volume-averaged radical concentrations. This approximation was explored in detail by Rojas et al. (2010).

The final system of equations was solved using the stiff-differential-equations solver ODE15s in MATLAB (based on Gear's method). The relative tolerance was 10^{-8}, whereas the absolute tolerances for concentrations of all species were set four orders of magnitude below their respective values.

3. Results and discussion

3.1. Actinometry. Hydrogen peroxide photolysis

The average fluence rate at the surface of the reactor was determined using H_2O_2 actinometry. Hydrogen peroxide direct decomposition experiments were conducted at various initial concentrations. The kinetic model was applied to calculate the reactor surface average fluence rate by fitting experimental data for H_2O_2 decay. Reactions 1–21 (Table 1) were used in the model formulation. A value of $I_0 = 0.85 \times 10^{-6}$ *Ein* $L^{-1}s^{-1}$ was obtained (Fig. 2), which was in agreement with the fluence rate measured by the fluence meter.

3.2. p-Cresol and 4-Methylcatechol direct photolysis

Quantum yields of *p*-cresol and 4-methylcatechol were determined from direct photolysis experiments for each compound separately. In the experiments, *p*-cresol or 4-methylcatechol solutions were exposed to UV light in the absence of H_2O_2. The quantum yield of each compound was calculated by fitting the kinetic model to data representing compound decay. The solution absorbance for all experiments was measured as a function of time to determine A_z (equation (2)). This was necessary in direct photolysis experiments since data showed that the products of direct photolysis reaction also absorb 254-nm light. (*2,2'*-Dihydroxy-*5,5'*-dimethylbiphenyl, 4-methylcatechol and *2*-hydroxy-*4',5*-dimethyldiphenyl ether have been reported as products in the direct photolysis of p-cresol, Joschek and Miller, 1966.) Results are presented in Fig. 3. To generate model predictions, we used the calculated fluence from the actinometry experiments (Fig. 2) and fitted the quantum yields to experimental data.

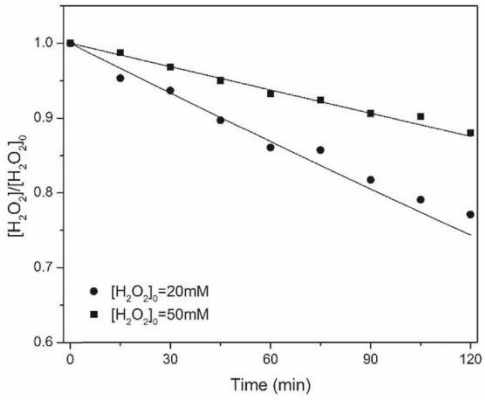

Fig. 2. Decomposition of hydrogen peroxide in Milli-Q water in the batch reactor. Solid lines: model predictions obtained by fitting the model to decay curves using the fluence rate as adjustable parameter.

3.3. Model predictions: p-cresol degradation

Fig. 4 provides predicted and experimental decay curves for *p*-cresol in a series of experiments carried out at different initial concentrations of H_2O_2 and *p*-cresol. Model calculations include the fluence rate determined via actinometry and the quantum yields for *p*-cresol and 4-methylcatechol determined via direct photolysis. In all cases experimental results are accurately predicted by the model. Omitting OH radical scavenging by reaction intermediates significantly overestimates the destruction rate of *p*-cresol in most cases (dashed lines in Fig. 4), which highlights the importance of incorporating the full mechanism in the kinetic model.

Calculations show that intermediates, especially those before ring cleavage (4-methylcatechol and 4-methylbezoquinone) played an important role in hydroxyl radical quenching. There is no reported kinetic rate constant for the reaction of 4-methylbenzoquinone reaction with hydroxyl radical although Scheck and Frimmel (1995) reported that *1,2*-benzoquinone was not detected during oxidation of phenol by the UV/H_2O_2 process because it is easily cleaved into aliphatic compounds. In this study, the rate constant for the reaction of 4-methylbenzoquinone with hydroxyl radical was held to be of the same magnitude as that of 4-methylcatechol, $k_{26} = 2.0 \times 10^{10}\ M^{-1}s^{-1}$, near the diffusion limit. Model results were obtained with no additional fitted parameters; all other rate constants were obtained from preliminary experiments (i.e. actinometry and direct photolysis experiments) or published data (Table 1).

Molecular oxygen participates in several steps of the reaction mechanism—specifically, in the oxidation of 4-methylcatechol to 4-

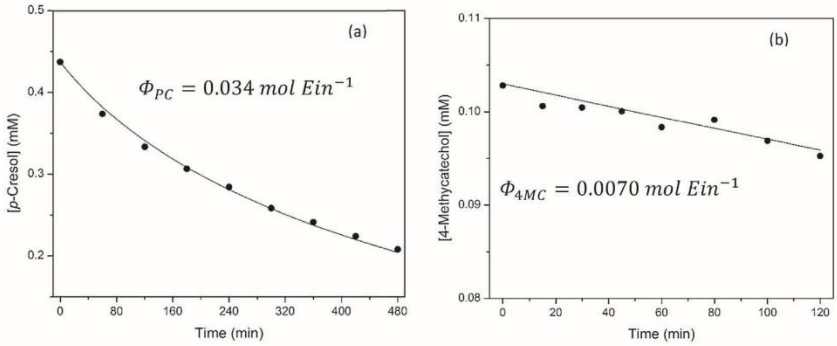

Fig. 3. Decomposition of (a) p-cresol, and (b) 4-mehtylcatechol in aqueous solution by (LP)UV direct photolysis. Solid lines: model predictions obtained from a fit of model results to decay curves using the respective quantum yield as adjustable parameter. (a) $[PC]_0 = 0.438$ mM, (b) $[4\ MC]_0 = 0.103$ mM.

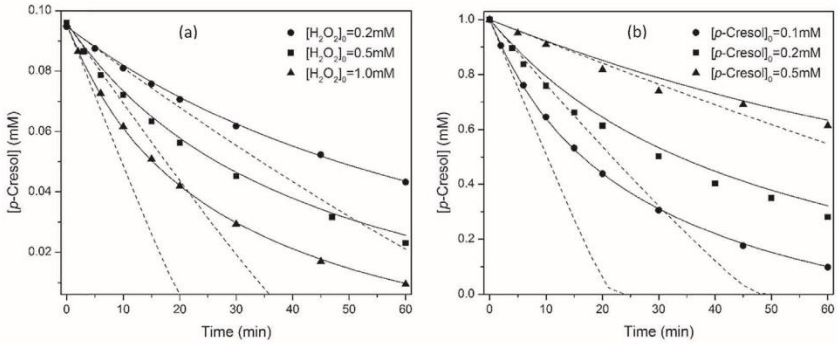

Fig. 4. Degradation of p-cresol in aqueous solution by UV/H_2O_2 advanced oxidation as a function of initial H_2O_2 concentrations (a), and initial p-cresol concentrations (b). Solid lines: full model predictions using the proposed mechanism; dashed lines: model calculations neglecting reactions of intermediates. (a) $[PC]_0 = 0.1$ mM, (b) $[H_2O_2]_0 = 1$ mM.

methylbenzoquinone (Davies et al., 1995) and the oxidation of carbon double bonds (Jin et al., 2010; Huang et al., 2011). To test the potential role of oxygen, we performed experiments with degassed solutions by bubbling argon into the solution before exposure to UV light. During the experiment, an argon atmosphere was maintained over the reactor to prevent oxygen diffusion into the reacting mixture. The results in terms of *p*-cresol concentration vs. time showed no appreciable difference relative to the original experiments, suggesting that dissolved oxygen is not important in *p*-cresol oxidation. Representative results are provided in the supporting information.

There are two possible pathways for the OH-induced oxidation of *p*-cresol to 4-methylcatechol (Omura and Matsuura, 1968; Scheck and Frimmel, 1995): the first involves the cyclohexadienyl radical formed due to OH radical attack that converts the *p*-cresol into dihydroxy compounds. In the second, the phenoxyl radical formed due to the abstraction of hydrogen atom subsequently combines with a second OH radical. However, the second mechanism is dominant only when the OH-radical is present at high concentrations (Waters, 1964). In the kinetic model used here, only one OH radical is involved in the conversion of *p*-cresol to 4-methylcatechol, suggesting that the cyclohexadienyl pathway predominates.

The production of 4-methylcatechol was measured in the experiments (Fig. 5). The reaction of *p*-cresol with OH radical was the only 4-methylcatechol source, but two sinks are considered in the kinetic model: direct photolysis and reaction with OH radical. Even though the rate constant for 4-methylcatechol reaction with OH radical is higher than that of *p*-cresol, 4-methylcatechol accumulates until most of the *p*-cresol is consumed. There was good agreement between data and predictions at low H_2O_2 concentrations (Fig. 5a), but the model tends to underpredict concentrations of 4-methylcatechol at later times and higher measured concentrations (Fig. 5b) while still trending correctly.

The evolutions of formic acid, acetic acid and oxalic acid concentrations are presented in Fig. 6 for a representative experiment. (Results for *p*-cresol degradation in this experiment are in Fig. 5b.) Although the α-hydrogens next to the carbon double bonds and carboxyl groups are more active under oxidizing conditions, there may be several ways in which to break down the aliphatic acid formed by the ring cleavage. Therefore, the final stages of the mechanism proposed (Fig. 1) may lead to formation of other species. Fig. 7 shows the trajectory of total carbon corresponding to measured concentrations of aliphatic acids along with model calculations for a representative experiment. Both model and data indicate that aliphatic acids accumulate throughout the experiment. By the end of the experiment (180 min), essentially all the *p*-cresol is destroyed (Fig. 5b).

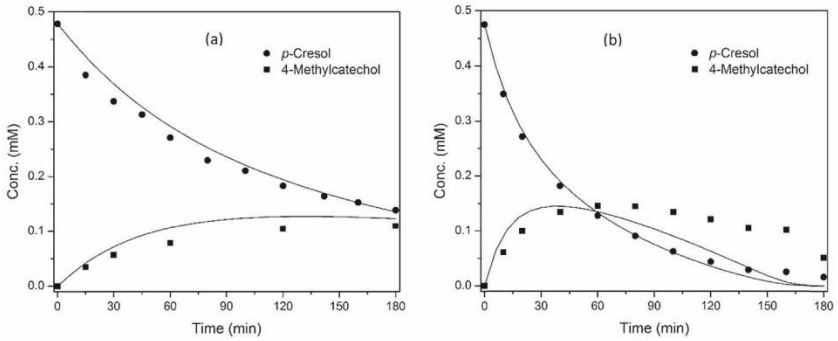

Fig. 5. Degradation of *p*-cresol in aqueous solution by UV/H_2O_2 advanced oxidation. Evolution of 4-methylcatechol concentration with time. Solid lines: model predictions. $[PC]_0 = 0.5$ mM, (a) $[H_2O_2]_0 = 1$ mM, (b) $[H_2O_2]_0 = 5$ mM.

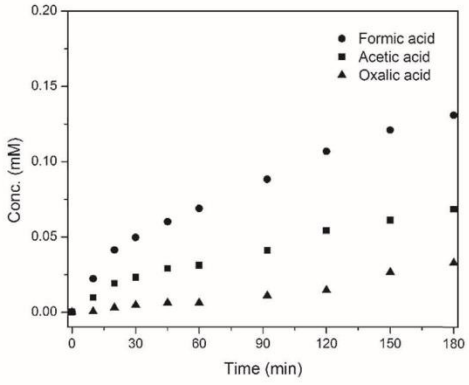

Fig. 6. Evolution of formic acid, acetic acid and oxalic acid concentrations with time. $[PC]_0 = 0.5$ mM, $[H_2O_2]_0 = 5$ mM.

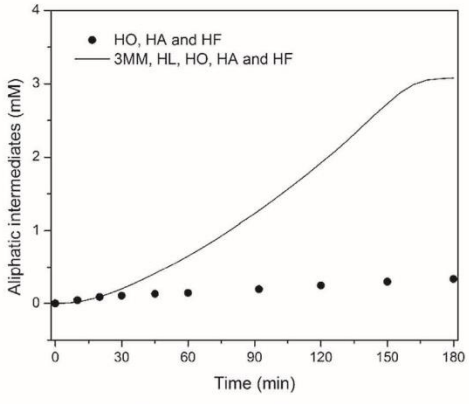

Fig. 7. Evolution of aliphatic reaction intermediates concentration with time. Solid line: model prediction. $[PC]_0 = 0.5$ mM, $[H_2O_2]_0 = 5$ mM. Abbreviations in Fig. 1.

The concentrations of H_2O_2 and TOC, and pH were measured throughout the experiment and predicted using the kinetic model (Figs. 8–10). Despite some differences, the model adequately predicts trends in H_2O_2 concentration (Fig. 8) and pH (Fig. 9). Previous studies have calculated pH changes during this type of experiment by assuming that the target organics are completely converted into carbon dioxide (Crittenden et al., 1999; Rojas et al., 2010). In our study, a significant drop in pH was observed in the 3-h experiment. However, the drop of pH was due to the formation of organic acids. The lack of CO_2 production (that is, complete mineralization of the target) is evident in the TOC results (Fig. 10) since TOC does not change appreciably during the experiments, as predicted by our model.

3.4. Model predictions: 4-Methylcatechol degradation

Experiments were carried out with 4-methylcatechol as the initial substrate at different initial hydrogen peroxide concentrations. As anticipated, degradation rate was directly related to the initial hydrogen peroxide concentration within the range of experiments (Fig. 11). Agreement between experimental data and model simulations is observed at 0.2 mM H_2O_2 but the model tends

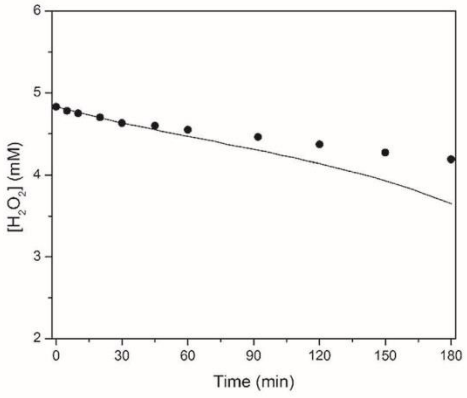

Fig. 8. Evolution of H_2O_2 concentration with time. Solid line: model prediction. $[PC]_0 = 0.5$ mM, $[H_2O_2]_0 = 5$ mM.

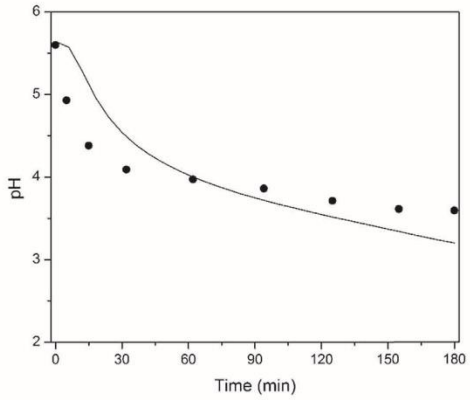

Fig. 9. Evolution of pH with time. Solid line: model prediction. $[PC]_0$ = 0.5 mM, $[H_2O_2]_0$ = 5 mM.

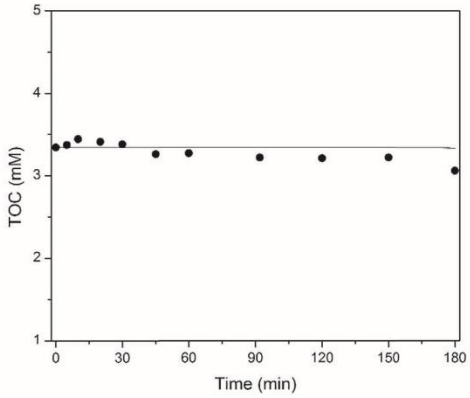

Fig. 10. Evolution of TOC with time. Solid line: model prediction. $[PC]_0$ = 0.5 mM, $[H_2O_2]_0$ = 5 mM.

to over-estimate degradation rates at higher H_2O_2 concentrations.

4. Concluding remarks

A comprehensive kinetic model was developed to quantify the oxidation of *p*-cresol by UV/H_2O_2 AOP in a batch reactor. The model was based on known elementary chemical and photo-chemical reactions of the UV/H_2O_2 photolysis system, together with experimentally established direct photolysis reactions and proposed OH-radical reactions with intermediates. The kinetics of *p*-cresol decomposition, as well as the main reaction intermediate (4-methylcatechol) was successfully simulated throughout a wide range of operating conditions. The approach employed shows that the full reaction mechanism needs to be considered to evaluate process performance. In particular, reaction intermediates, especially those formed before ring cleavage, play an important role in the quenching of hydroxyl radicals and, consequently, those compounds must be considered in kinetic models of AOP degradation of phenolic compounds.

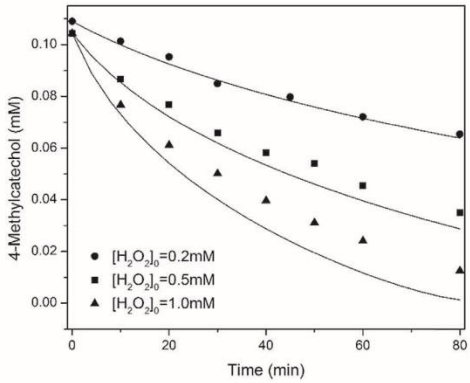

Fig. 11. Degradation of 4-methylcatechol in aqueous solution by UV/H_2O_2 advanced oxidation as a function of initial H_2O_2 concentrations. Solid lines: model predictions. [4 MC]$_0$ = 0.1 mM.

Appendix A. Supplementary data

Supplementary data related to this article can be found at http://dx.doi.org/10.1016/j.chemosphere.2016.06.110.

References

Ahel, M., Schaffner, C., Giger, W., 1996. Behaviour of alkylphenol polyethoxylate surfactants in the aquatic environment - III. Occurrence and elimination of their persistent metabolites during infiltration of river water to groundwater. Water Res. 30, 37–46.
Benjamin, M.M., 2002. Water Chemistry. Waleland Press Inc., p. 139
Bielski, B.H.J., Cabelli, D.E., Arudi, R.L., Ross, A.B., 1985. Reactivity of HO_2/O_2 radicals in aqueous solution. J. Phys. Chem. Ref. Data 14, 1041–1100.
Boltz, D., Holwell, J., 1978. Colorimetric Determination of Nonmetals, second ed. John Wiley and Sons, New York.
Boonrattanakij, N., Lu, M., Anotai, J., 2009. Kinetics and mechanism of 2,6-dimethyaniline degradation by hydroxyl radicals. J. Hazard. Mater. 172, 952–957.
Buxton, G.V., Greenstock, C.L., Helman, W.P., Ross, A.B., 1988. Critical review of rate constants for reactions of hydrated electrons, hydrogen atoms and hydroxyl radicals (·OH/·O) in aqueous solution. J. Phys. Chem. Ref. Data 17, 513–886.
Crittenden, J.C., Hu, S., Hand, D.W., Green, S.A., 1999. A kinetic model for H_2O_2/UV process in a completely mixed batch reactor. Wat. Res. 33, 2315–2328.
Davies, M.S., Mile, B., Rowlands, C.C., 1995. Oxidation of 4-methylcatechol by dioxygen studies by ESR spectroscopy. The different regioselectivity of OH and MeO nucleophilic attack and kinetic deuterium isotope effects. Magn. Reson. Chem. 33, 15–19.
De Luis, A., Lombraña, J.I., Menendez, A., 2011. Modeling of the radicalary state in the H_2O_2/UV oxidation system to predict the degradation kinetics of phenolic mixture solutions. AIChE J. 30, 196–207.
Dong, B., Kahl, A., Cheng, L., Vo, H., Ruehl, S., Zhang, T., Snyder, S., Sáez, A.E., Quanrud, D., Arnold, R.G., 2015. Fate of trace organics in a wastewater effluent dependent stream. Sci. Total Environ. 518–519, 479–490.
Eriksen, T.E., Lind, J., Merenyi, G., 1985. On the acid-base equilibrium of the carbonate radical. Radiat. Phys. Chem. 26, 197–199.
Ershov, B.G., Janata, E., Alam, M.S., Gordeev, A.V., 2008. Studies of the reaction of the hydroxyl radical with the oxalate ion in an acidic aqueous solution by pulse radiolysis. Russ. Chem. Bull. Int. Ed. 57, 1189.
Getoff, N., Schworer, F., Markovic, V.M., Sehested, K., Nielsen, S.O., 1971. Pulse radiolysis of oxalic acid and oxalates. J. Phys. Chem. 75, 749–755.
Glaze, W.H., Lay, Y., Kang, J.-W., 1995. Advanced oxidation processes. A kinetic model for the oxidation of 1,2-dibromo-3-chloropropane in water by the combination of hydrogen peroxide and UV radiation. Ind. Eng. Chem. Res. 34, 2314–2323.
Greenwood, N.N., Earnshaw, A., 1997. Chemistry of the Elements, second ed. Butterworth-Heinemann, p. 310.
Gohn, M., Getoff, N., 1977. Pulse radiolysis of 3,4-dihydroxytoluene. J. Chem. Soc. 73, 1207–1215.
Hart, E.J., 1951. Mechanism of the γ-Ray induced oxidation of formic acid in aqueous solution. J. Am. Chem. Soc. 73, 68–73.
Holeman, J., Bjergbakke, E., Sehested, K., 1987. The importance of radical-radical reactions in pulse radiolysis of aqueous carbonate/bicarbonate. Proc. Tihany Symp. Radiat. Chem. 1, 149–153.

Housecroft, C.E., Sharpe, A.G., 2005. Inorganic Chemistry, second ed. Prentice-Pearson-Hall, p. 368.
Huang, D., Zhang, X., Chen, Z.M., Zhao, Y., Shen, X.L., 2011. The kinetics and mechanism of an aqueous phase isoprene reaction with hydroxyl radical. Atoms. Chem. Phys. 11, 7399–7415.
Jin, F., Zhong, H., Cao, J., Cao, J., Kawasaki, K., Kishita, A., Matsumoto, T., Tohji, K., Enomoto, H., 2010. Oxidation of unsaturated carboxylic acids under hydrothermal conditions. Bioresour. Technol. 101, 7624–7634.
Jongberg, S., Gislason, N.E., Lund, M.N., Skibsted, L.H., Waterhouse, A.L., 2011. Thiol-quinone adduct formation in myofibrillar proteins detected by LC-MS. J. Agric. Food Chem. 59, 6900–6905.
Joschek, H.I., Miller, S.I., 1966. Photooxidation of phenol, cresols, and dihydroxybenzenes. J. Am. Chem. Soc. 88 (14), 3273–3281.
Kang, N., Lee, D.S., Yoon, J., 2002. Kinetic modeling of Fenton oxidation of phenol and monochlorophenols. Chemosphere 47, 915–924.
Lay, Y.S., 1989. Oxidation of 1,2-dibromo-3-chloropropane in Groundwater Using Advanced Oxidation Processes. Ph.D. dissertation. University of California, Los Angeles.
Lee, P.-C., Lee, W., 1996. In vivo estrogenic action of nonylphenol in immature female rates. Bull. Environ. Contam. Toxicol. 57, 341–348.
Leitner, N.K.V., Dore, M., 1997. Mechanism of the reaction between hydroxyl radicals and glycolic, glyoxylic, acetic and oxalic acids in aqueous solution: consequence on hydrogen peroxide consumption in the H_2O_2/UV and O_3/H_2O_2 systems. Water Res. 31, 1383–1397.
Liao, C.-H., Gurol, M., 1995. Chemical oxidation by photolytic decomposition of hydrogen peroxide. Environ. Sci. Technol. 29, 3007–3014.
Loyo-Rosales, J.E., Rice, C.P., Torrents, A., 2007. Fate of octyl- and nonylphenol ethoxylates and some carboxylated derivatives in three American wastewater treatment plants. Environ. Sci. Technol. 41, 6815–6821.
Lye, C.M., Frid, C.L.J., Gill, M.E., Cooper, D.W., Jones, D.M., 1999. Estrogenic alkylphenols in fish tissues, sediments, and waters from the UK. Tyne Tees Estuaries. 33, 1009–1014.
MacDonald, B.C., Lvin, S.J., Patterson, H., 1997. Correction of fluorescence inner filter effects and the partitioning of pyrene to dissolved organic carbon. Anal. Chim. Acta 338, 155–162.
Matsuura, T., Omura, K., 1974. Photochemical hydroxylation of aromatic compounds. Synthesis 3, 173–184.
Moreira, J., Serrano, B., Ortiz, A., de Lasa, H., 2012. A unified kinetic model for phenol photocatalytic degradation over TiO_2 photocatalysts. Chem. Eng. Sci. 78, 186–203.
Murcia, M.D., Vershinin, N.O., Briantceva, N., Gomez, M., Gomez, E., Cascales, E., Hidalgo, A.M., 2015. Development of a kinetic model for the UV/H_2O_2 photodegradation of 2,4-dichlorophenoxiacetic acid. Chem. Eng. J. 266, 356–367.
Nagarnaik, P.M., Boulanger, B., 2011. Advanced oxidation of alkylphenol ethoxylates in aqueous systems. Chemosphere 85, 854–860.
Neta, P., Huie, R.E., Ross, A.B., 1988. Rate constants for reactions of inorganic radicals in aqueous solution. J. Phys. Chem. Ref. Data. 17, 1027–1284.
Olariu, R.I., Klotz, B., Barnes, I., Becker, K.H., Mocanu, R., 2002. FT-IR study of the ring-retaining products from the reaction of OH radicals with phenol, *o*-, *m*-, and *p*-cresol. Atmos. Environ. 36, 3685–3697.
Omura, K., Matsuura, T., 1968. Photo-induced reactions-IX: the hydroxylation of phenols by the photo-decomposition of hydrogen peroxide in aqueous media. Tetrahedron 24, 3475–3487.
Perry, R., Green, D., Maloney, J., 1981. Perry's Chemical Engineerings' Handbook, fifth ed. McGraw-Hill, New York.
Pospisil, J., Ettel, V., Skola, V., 1957. Pyrocatechol oxidation to muconic acid. Chem. Prumysl. 7, 244–248.
Rojas, M.R., Perez, F., Whitley, D., Arnold, R.G., Sáea, A.E., 2010. Modeling of advanced oxidation of trace organic contaminants by hydrogen peroxide photolysis and Fenton's reaction. Ind. Eng. Chem. Res. 49, 11331–11343.
Rojas, M.R., Leung, C., Whitley, D., Zhu, Y., Arnold, R.G., Sáea, A.E., 2011. Advanced oxidation of trace organics in water by hydrogen peroxide solar photolysis. Ind. Eng. Chem. Res. 50, 12479–12487.
Scheck, C.K., Frimmel, F.H., 1995. Degradation of phenol and salicylic acid by ultraviolet radiation/hydrogen peroxide/oxygen. Wat. Res. 29, 2346–2352.
Scullion, S.D., Clench, M.R., Cooke, M., Ashcroft, A.E., 1996. Determination of surfactants in surface water by solid-phase extraction, liquid chromatography and liquid chromatography-mass spectrometry. J. Chromatogr. A 733, 207–216.
Sehested, K., Corfitzen, H., Christensen, H.C., Hart, E.J., 1975. Rates of reaction of O^-, OH and H with methylated benzenes in aqueous solution. Optical spectra of radicals. J. Phys. Chem. 79, 310–315.
Soto, A.M., Justicia, H., Wray, J.W., Sonnenschein, C., 1991. *p*-Nonyl-phenol: an estrogenic xenobiotic released from "modified" polystyrene. Environ. Health Perspect. 92, 167–173.
Stefan, M.I., Hoy, A.R., Bolton, J.R., 1996. Kinetics and mechanism of the degradation and mineralization of acetone in dilute aqueous solution sensitized by the UV photolysis of hydrogen peroxide. Environ. Sci. Technol. 30, 2382–2390.
Song, W., Ravindran, V., Pirbazari, M., 2008. Process optimization using a kinetic model for the ultraviolet radiation-hydrogen peroxide decomposition of natural and synthetic organic compounds in groundwater. Chem. Eng. Sci. 63, 3249–3270.
Sun, W., Saeys, M., 2008. First principles study of the reaction of formic and acetic acids with hydroxyl radicals. J. Phys. Chem. A 112, 6918–6928.
Swartz, C.H., Reddy, S., Benotti, M.J., Yin, H., Barber, L.B., Brownawell, B.J., Rudel, R.A., 2006. Steroid estrogens, nonylphenol ethoxylate metabolites, and other wastewater contaminants in groundwater affected by a residential septic system on Cape Cod, MA. Environ. Sci. Technol. 40, 4894–4902.
Volman, D.H., Chen, J.C., 1959. The photochemical decomposition of hydrogen peroxide in aqueous solutions of allyl alcohol at 2537 Å. J. Am. Chem. Soc. 81 (16), 4141–4144.
Waite, J.H., 1976. Calculating extinction coefficients for enzymatically produced *O*-quinones. Anal. Biochem. 75, 211–218.
Wang, K., Hsieh, Y., Chen, L., 1998. The heterogeneous photocatalytic degradation, intermediates and mineralization for the aqueous solution of cresols and nitrophenols. J. Hazard. Mater. 59, 251–260.
Waters, W.A., 1964. Mechanism of Oxidation of Organic Compounds. Methuen, p. 132.
Weinstein, J., Bielski, B.H.J., 1979. Kinetics of the interaction of perhydroxyl and superoxide radicals with hydrogen peroxide. The Haber-Weiss reaction. J. Am. Chem. Soc. 101, 58–62.
Wojnárovits, L., Foldiak, G., D'angelantonio, M., Emmi, S.S., 2002. Mechanism of OH radical-induced oxidation of p-cresol to p-methylphenolxyl radical. Res. Chem. Intermed. 28, 373–386.

Supporting Information

A. Model of UV/H_2O_2 oxidation of *p*-cresol

In this section, we present the full system of equations that were solved for the kinetic model described in the manuscript. Acronyms are defined in Figure 1.

$$\frac{d[H_2O_2]}{dt} = -\phi_{H_2O_2} f_{H_2O_2} I_0 (1 - e^{-2.303A}) - k_2[^\bullet OH][H_2O_2] + k_8[^\bullet OH]^2 - k_{10}\gamma_{\pm1}[O_2^{\bullet-}][H_2O_2] + k_{13}[HO_2^\bullet]^2 - k_{14}[HO_2^\bullet][H_2O_2] \quad \text{(S1)}$$

$$- k_{15}\gamma_{\pm1}[CO_3^{\bullet-}][H_2O_2] - k_{18}[H_2O_2] + k_{18r}\gamma_{\pm1}[HO_2^-]\gamma_{\pm1}[H^+]$$

$$\frac{d[HO_2^-]}{dt} = -k_3[^\bullet OH]\gamma_{\pm1}[HO_2^-] + k_{12}[HO_2^\bullet]\gamma_{\pm1}[O_2^{\bullet-}] - k_{16}\gamma_{\pm1}[CO_3^{\bullet-}]\gamma_{\pm1}[HO_2^-] + k_{18}[H_2O_2] - k_{18r}\gamma_{\pm1}[HO_2^-]\gamma_{\pm1}[H^+] \quad \text{(S2)}$$

$$\frac{d[^\bullet OH]}{dt} = 2\phi_{H_2O_2} f_{H_2O_2} I_0 (1 - e^{-2.303A}) - k_2[H_2O_2][^\bullet OH] - k_3\gamma_{\pm1}[HO_2^-][^\bullet OH] - k_4\gamma_{\pm1}[HCO_3^-][^\bullet OH] - k_5\gamma_{\pm2}[CO_3^{2-}][^\bullet OH] \quad \text{(S3)}$$

$$- k_6[HO_2^\bullet][^\bullet OH] - k_7\gamma_{\pm1}[O_2^{\bullet-}][^\bullet OH] - 2k_8[^\bullet OH]^2 - k_9\gamma_{\pm1}[CO_3^{\bullet-}][^\bullet OH] + k_{10}\gamma_{\pm1}[O_2^{\bullet-}][H_2O_2] + k_{14}[HO_2^\bullet][H_2O_2]$$

$$- k_{23}[PC][^\bullet OH] - k_{25}[4MC][^\bullet OH] - 2k_{26}[4MB][^\bullet OH] - 4k_{27}\gamma_{\pm1}[3MM^-][^\bullet OH] - k_{28}\gamma_{\pm1}[L^-][^\bullet OH]$$

$$- k_{29}\gamma_{\pm1}[Ox^-][^\bullet OH] - k_{30}\gamma_{\pm2}[Ox^{2-}][^\bullet OH] - k_{32}[HA][^\bullet OH] - k_{33}\gamma_{\pm1}[A^-][^\bullet OH] - k_{34}\gamma_{\pm1}[F^-][^\bullet OH]$$

$$\frac{d[HO_2^\bullet]}{dt} = -k_6[^\bullet OH][HO_2^\bullet] - k_{12}\gamma_{\pm1}[O_2^{\bullet-}][HO_2^\bullet] - 2k_{13}[HO_2^\bullet]^2 - k_{14}[H_2O_2][HO_2^\bullet] - k_{19}[HO_2^\bullet] + k_{19r}\gamma_{\pm1}[H^+]\gamma_{\pm1}[O_2^{\bullet-}] \quad \text{(S4)}$$

$$\frac{d[O_2^{\bullet-}]}{dt} = k_2[H_2O_2][^\bullet OH] + k_3\gamma_{\pm1}[HO_2^-][^\bullet OH] - k_7\gamma_{\pm1}[^\bullet OH][O_2^{\bullet-}] - k_{10}\gamma_{\pm1}[H_2O_2][O_2^{\bullet-}] - k_{11}\gamma_{\pm1}[CO_3^{\bullet-}]\gamma_{\pm1}[O_2^{\bullet-}] \quad \text{(S5)}$$

$$- k_{12}[HO_2^\bullet]\gamma_{\pm1}[O_2^{\bullet-}] + k_{15}[H_2O_2]\gamma_{\pm1}[CO_3^{\bullet-}] + k_{16}\gamma_{\pm1}[HO_2^-]\gamma_{\pm1}[CO_3^{\bullet-}] + k_{19}[HO_2^\bullet] - k_{19r}\gamma_{\pm1}[H^+]\gamma_{\pm1}[O_2^{\bullet-}]$$

$$\frac{d[TotCO_3]}{dt} = -k_4[^{\bullet}OH]\gamma_{\pm1}[HCO_3^-] - k_5[^{\bullet}OH]\gamma_{\pm2}[CO_3^{2-}] + k_{11}\gamma_{\pm1}[O_2^{\bullet-}]\gamma_{\pm1}[CO_3^{\bullet-}] + k_{15}\gamma_{\pm1}[CO_3^{\bullet-}][H_2O_2] \quad \text{(S6)}$$

$$+ k_{16}\gamma_{\pm1}[CO_3^{\bullet-}]\gamma_{\pm1}[HO_2^-] + k_{28}\gamma_{\pm1}[L^-][^{\bullet}OH] + 2k_{31}\gamma_{\pm1}[Ox^{\bullet-}]\gamma_{\pm1}[Ox^{\bullet-}] + k_{32}[HA][^{\bullet}OH]$$

$$+ k_{33}\gamma_{\pm1}[A^-][^{\bullet}OH] + k_{34}\gamma_{\pm1}[F^-][^{\bullet}OH]$$

$$\frac{d[CO_2(aq)]}{dt} = k_{28}\gamma_{\pm1}[L^-][^{\bullet}OH] + 2k_{31}\gamma_{\pm1}[Ox^{\bullet-}]\gamma_{\pm1}[Ox^{\bullet-}] + k_{32}[HA][^{\bullet}OH] + k_{33}\gamma_{\pm1}[A^-][^{\bullet}OH] + k_{34}\gamma_{\pm1}[F^-][^{\bullet}OH] \quad \text{(S7)}$$

$$- k_{20}[CO_2(aq)] + k_{20r}[H_2CO_3]$$

$$\frac{d[H_2CO_3]}{dt} = k_{20}[CO_2(aq)] - k_{20r}[H_2CO_3] - k_{21}[H_2CO_3] + k_{21r}[HCO_3^-][H^+] \quad \text{(S8)}$$

$$\frac{d[CO_3^{\bullet-}]}{dt} = k_4\gamma_{\pm1}[HCO_3^-][^{\bullet}OH] + k_5\gamma_{\pm2}[CO_3^{2-}][^{\bullet}OH] - k_9[^{\bullet}OH]\gamma_{\pm1}[CO_3^{\bullet-}] - k_{11}\gamma_{\pm1}[O_2^{\bullet-}]\gamma_{\pm1}[CO_3^{\bullet-}] - k_{15}[H_2O_2]\gamma_{\pm1}[CO_3^{\bullet-}] \quad \text{(S9)}$$

$$- k_{16}\gamma_{\pm1}[HO_2^-]\gamma_{\pm1}[CO_3^{\bullet-}] - 2k_{17}\gamma_{\pm1}^2[CO_3^{\bullet-}]^2$$

$$\frac{d[PC]}{dt} = -\phi_{PC} f_{PC} I_0 (1 - e^{-2.303A}) - k_{23}[PC][^{\bullet}OH] \quad \text{(S10)}$$

$$\frac{d[4MC]}{dt} = -\phi_{4MC} f_{4MC} I_0 (1 - e^{-2.303A}) + k_{23}[PC][^{\bullet}OH] - k_{25}[4MC][^{\bullet}OH] \quad \text{(S11)}$$

$$\frac{d[4MB]}{dt} = k_{25}[4MC][^{\bullet}OH] - k_{26}[4MB][^{\bullet}OH] \quad \text{(S12)}$$

$$\frac{d[3MM^-]}{dt} = k_{26}[4MB][^{\bullet}OH] - k_{27}\gamma_{\pm1}[3MM^-][^{\bullet}OH] \quad \text{(S13)}$$

$$\frac{d[L^-]}{dt} = k_{27}\gamma_{\pm1}[3MM^-][^{\bullet}OH] - k_{28}\gamma_{\pm1}[L^-][^{\bullet}OH] \quad \text{(S14)}$$

$$\frac{d[TotOx]}{dt} = 2k_{27}\gamma_{\pm1}[3MM^-][^{\bullet}OH] - k_{29}\gamma_{\pm1}[Ox^-][^{\bullet}OH] - k_{30}\gamma_{\pm2}[Ox^{2-}][^{\bullet}OH] + k_{31}\gamma_{\pm1}[Ox^{\bullet-}]\gamma_{\pm1}[Ox^{\bullet-}] \quad \text{(S15)}$$

$$\frac{d[Ox^{\bullet-}]}{dt} = k_{29}\gamma_{\pm1}[Ox^-][^{\bullet}OH] + k_{30}\gamma_{\pm2}[Ox^{2-}][^{\bullet}OH] - k_{31}\gamma_{\pm1}[Ox^{\bullet-}]\gamma_{\pm1}[Ox^{\bullet-}] \quad \text{(S16)}$$

$$\frac{d[TotA]}{dt} = k_{28}\gamma_{\pm1}[L^-][^\bullet OH] - k_{32}[HA][^\bullet OH] - k_{33}\gamma_{\pm1}[A^-][^\bullet OH] \quad \text{(S17)}$$

$$\frac{d[F^-]}{dt} = k_{32}[HA][^\bullet OH] + k_{33}\gamma_{\pm1}[A^-][^\bullet OH] - k_{34}\gamma_{\pm1}[F^-][^\bullet OH] \quad \text{(S18)}$$

$$[H^+] = [OH^-] + [HO_2^-] + [O_2^{\bullet-}] + [CO_3^{\bullet-}] + [HCO_3^-] + 2[CO_3^{2-}] + [3MM^-] + [L^-] + [Ox^-] + [Ox^{\bullet-}] + 2[Ox^{2-}] + [A^-] + [F^-] \quad \text{(S19)}$$

$$\gamma_{\pm1}[HCO_3^-] = \frac{[TotCO_3]}{\left\{\frac{\gamma_{\pm1}[H^+]}{k_{20}k_{21}/k_{20r}k_{21r}} + \frac{\gamma_{\pm1}[H^+]}{k_{21}/k_{21r}} + 1 + \frac{K_{37}}{\gamma_{\pm1}[H^+]}\right\}} \quad \text{(S20)}$$

$$\gamma_{\pm2}[CO_3^{2-}] = \frac{K_{37}\gamma_{\pm1}[HCO_3^-]}{\gamma_{\pm1}[H^+]} \quad \text{(S21)}$$

$$\gamma_{\pm1}[Ox^-] = \frac{[TotOx]}{\left\{1 + \frac{K_{35}}{\gamma_{\pm1}[H^+]}\right\}} \quad \text{(S22)}$$

$$\gamma_{\pm2}[Ox^{2-}] = \frac{K_{35}\gamma_{\pm1}[Ox^-]}{\gamma_{\pm1}[H^+]} \quad \text{(S23)}$$

$$[HA] = \frac{[TotA]}{\left\{1 + \frac{K_{36}}{\gamma_{\pm1}[H^+]}\right\}} \quad \text{(S24)}$$

$$\gamma_{\pm1}[A^-] = \frac{K_{36}[HA]}{\gamma_{\pm1}[H^+]} \quad \text{(S25)}$$

where activity coefficients γ are calculated from the Davies Equation

$$\log(\gamma_{\pm1}) = -0.51\left(\frac{\sqrt{I}}{1+\sqrt{I}} - 0.2I\right) \quad \text{(S26)}$$

$$\log(\gamma_{\pm 2}) = -2.04\left(\frac{\sqrt{I}}{1+\sqrt{I}} - 0.2I\right) \quad \text{(S27)}$$

and I is ionic strength of the solution, which is calculated from the concentration of all ionic species in terms of the charge number for each species, z_i, by

$$I = \frac{1}{2}\sum [C_i] z_i^{\,2} \quad \text{(S28)}$$

Model calculations yield concentration of all species as a function of time. For radicals, the concentration found is a volume-averaged concentration.

B.

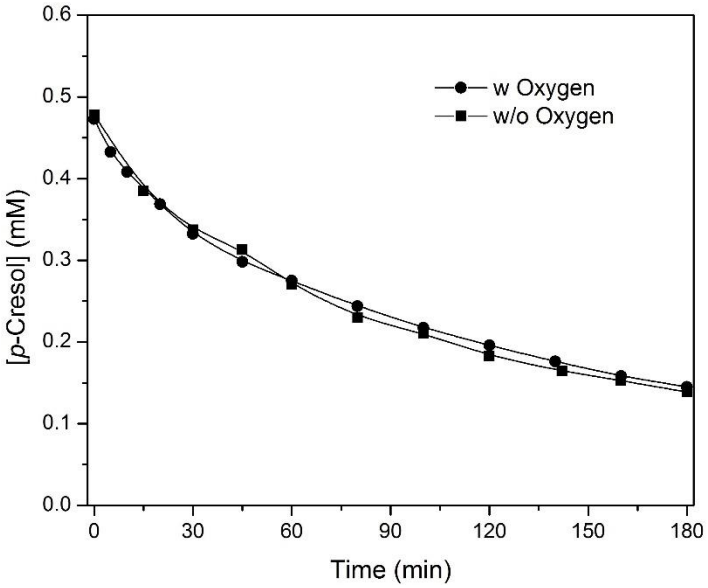

Figure S1. Degradation of *p*-cresol in aqueous solution by UV/H_2O_2 advanced oxidation in the presence/absence of oxygen. $[PC]_0$ = 0.5 mM, (b) $[H_2O_2]_0$ = 1 Mm

APPENDIX E

SUSTAINABLE STRUVITE CONTROL USING CARBON DIOXIDE

This article has been published in the Journal of Environmental Engineering (2018).

Sarah E. Moore[1], Lin Ma[2], Matthew Potzler[3], Jerry Bish[4], Vasiliki Karanikola, Ph.D.[5], Jeff Prevatt, Ph.D.[6], Robert G. Arnold, Ph.D., P.E.[7], A. Eduardo Sáez, Ph.D.[8,*]

[1] Ph.D. Student, Department of Chemical and Environmental Engineering, The University of Arizona, 1133 E. James E. Rogers Way, Harshbarger 108, Tucson, AZ 85721, United States

[2] Ph.D. Student, Department of Chemical and Environmental Engineering, The University of Arizona, 1133 E. James E. Rogers Way, Harshbarger 108, Tucson, AZ 85721, United States

[3] Ph.D. Student, Department of Chemical and Environmental Engineering, The University of Arizona, 1133 E. James E. Rogers Way, Harshbarger 108, Tucson, AZ 85721, United States

[4] Senior Consultant, Greeley and Hansen, 4400 E. Broadway Blvd, Suite 600E, Tucson, AZ 85711

[5] Research Professor, Department of Chemical and Environmental Engineering, The University of Arizona, 1133 E. James E. Rogers Way, Harshbarger 108, Tucson, AZ 85721, United States

[6] Regulatory Compliance Manager, Pima County Wastewater Reclamation, 201 N. Stone Ave., 8th Fl., Tucson, AZ 85701, United States

[7] Professor, Department of Chemical and Environmental Engineering, The University of Arizona, 1133 E. James E. Rogers Way, Harshbarger 108, Tucson, AZ 85721, United States

[8] Professor, Department of Chemical and Environmental Engineering, The University of Arizona, 1133 E. James E. Rogers Way, Harshbarger 108, Tucson, AZ 85721, United States

Sustainable Struvite Control Using Carbon Dioxide

Sarah E. Moore[1]; Lin Ma[2]; Matthew Potzler[3]; Jerry Bish[4]; Vasiliki Karanikola[5]; Jeff Prevatt[6]; Robert G. Arnold, M.ASCE[7]; and A. Eduardo Sáez[8]

Abstract: Struvite ($MgNH_4PO_4 \cdot 6H_2O$) scaling in wastewater treatment plants causes significant processing issues. Struvite formation can be controlled by acid addition since struvite solubility increases as pH decreases. Carbon dioxide from anaerobic digester gas can be used to lower the pH of wastewater to prevent struvite formation. In this work, bench-scale carbon dioxide injection illustrated the feasibility of using carbon dioxide to lower the pH of digester centrate for prevention of struvite formation. A pilot study was conducted to evaluate alternative designs for full-scale process application. Mixing a centrate stream with centrate that was presaturated with carbon dioxide reduces the pH to levels necessary to prevent struvite formation and was more effective than application of gaseous carbon dioxide. Experimental results validated an equilibrium model, which was adapted to produce a design protocol for implementation of this technology. Design parameters include measurable water quality parameters, including alkalinity and concentrations of struvite components. This work demonstrates that carbon dioxide is a sustainable alternative to traditional methods of struvite control and provides a simple methodology for full-scale implementation. **DOI: 10.1061/(ASCE)EE.1943-7870.0001466.**

Introduction

Struvite ($MgNH_4PO_4 \cdot 6H_2O$) is a relatively insoluble mineral that forms in waters rich in magnesium, ammonia, and phosphate, such as digester supernatant or centrate in wastewater treatment plants. Struvite precipitation in processing equipment clogs pipes and coats pump impellers and mixers. Struvite precipitation results in reduced system capacity and inefficiencies that oftentimes require expensive cleaning and temporary plant shutdown (Doyle and Parsons 2002). Traditional methods for prevention of struvite formation focus on formation of phosphate complexes to reduce phosphate availability or on pH reduction via addition of strong acid (Doyle and Parsons 2002). Buchanan et al. (1994) studied twenty commercial antiscaling products and their ability to delay struvite formation and reduce the mass of scale formed. They found that seven of the products tested inhibited struvite formation in deionized water containing magnesium, ammonium, and phosphate at concentrations representative of wastewater lagoons. They ranked the seven products based on their cost and health or environmental risk. Notable among this list is ferric chloride, which ranked sixth out of seven due to its relatively high risk and cost. Nevertheless, addition of ferric chloride or other Fe(III)-containing salts is the most common method for preventing struvite scaling in wastewater treatment plants today (Sharp et al. 2013). Disadvantages of ferric chloride use include cost, negative environmental impacts, health and safety risks, equipment corrosion, and increased sludge production. Furthermore, ferric chloride addition interferes with the downstream precipitation of struvite for nutrient recovery (Mayer et al. 2016). Uysal et al. (2010) demonstrated that many metals, including iron, appear in minerals recovered from anaerobic digesters. This is of concern, as iron-bound phosphate is poorly bioavailable (Mayer et al. 2016), suggesting that alternative methods for struvite control may be preferable. Doyle et al. (2003) investigated several alternative antiscaling and chelating agents in digester centrate. Of all agents tested, only ethylenediaminetetraacetic acid (EDTA) successfully prevented struvite formation, but EDTA is poorly degraded in the environment and should be removed from treated water prior to discharge.

Biogas produced during anaerobic digestion of solids in conventional wastewater treatment plants is composed of methane, carbon dioxide, and trace gases. In some plants, high purity methane is recovered from the biogas before the residual gas, which is rich in carbon dioxide, is vented to the atmosphere (Sun et al. 2015). In this study, we investigate the feasibility of using residual carbon dioxide from biogas to lower the pH of digester centrate and prevent struvite precipitation. At downstream points in the centrate treatment system, CO_2 can be stripped from solution, raising the pH for struvite recovery under controlled conditions (Jordaan et al. 2013; Birnhack et al. 2015). The use of CO_2 for struvite control uses a process waste product (biogas) to solve process problems sustainably and can generate a nutrient-rich byproduct that is in short supply.

Carbon dioxide has been successfully used as an alternative to strong acid for neutralizing high-pH water derived from tunnel construction (Garmo and Escudero 2014). Although industrial carbon

[1]Ph.D. Student, Dept. of Chemical and Environmental Engineering, Univ. of Arizona, 1133 E. James E. Rogers Way, Harshbarger 108, Tucson, AZ 85721.

[2]Ph.D. Student, Dept. of Chemical and Environmental Engineering, Univ. of Arizona, 1133 E. James E. Rogers Way, Harshbarger 108, Tucson, AZ 85721.

[3]Ph.D. Student, Dept. of Chemical and Environmental Engineering, Univ. of Arizona, 1133 E. James E. Rogers Way, Harshbarger 108, Tucson, AZ 85721.

[4]Senior Consultant, Greeley and Hansen, 4400 E. Broadway Blvd., Suite 600E, Tucson, AZ 85711.

[5]Research Professor, Dept. of Chemical and Environmental Engineering, Univ. of Arizona, 1133 E. James E. Rogers Way, Harshbarger 108, Tucson, AZ 85721.

[6]Regulatory Compliance Manager, Pima County Wastewater Reclamation, 201 N. Stone Ave., 8th Floor, Tucson, AZ 85701.

[7]Professor, Dept. of Chemical and Environmental Engineering, Univ. of Arizona, 1133 E. James E. Rogers Way, Harshbarger 108, Tucson, AZ 85721.

[8]Professor, Dept. of Chemical and Environmental Engineering, Univ. of Arizona, 1133 E. James E. Rogers Way, Harshbarger 108, Tucson, AZ 85721 (corresponding author). Email: esaez@email.arizona.edu

Note. This manuscript was submitted on March 27, 2018; approved on June 5, 2018; published online on September 27, 2018. Discussion period open until February 27, 2019; separate discussions must be submitted for individual papers. This paper is part of the ***Journal of Environmental Engineering***, © ASCE, ISSN 0733-9372.

dioxide is used for struvite control in a few wastewater treatment plants and use of biogas byproducts for pH control has been suggested (Sharp et al. 2013), the use of carbon dioxide generated during wastewater treatment for scale prevention remains beyond the current state of practice.

The objective of this study is to investigate the feasibility of using carbon dioxide in residual biogas to prevent struvite formation in centrate lines. The equilibrium behavior of centrate upon carbon dioxide addition was investigated. Equilibrium models were developed to (1) identify the pH at which struvite formation is infeasible, and (2) predict equilibrium pH as a function of carbon dioxide partial pressure. The latter model was validated experimentally using digester centrates from several locations. A pilot system was built to investigate alternative methods for introducing CO_2 into wastewater treatment process fluids. A design protocol was developed and generalized to support the use of carbon dioxide for struvite prevention in waste streams derived from municipal wastewater treatment. The protocol requires only easily measurable water quality parameters. This work demonstrates the feasibility of using carbon dioxide from digester gas to prevent struvite formation and provides a straightforward design methodology for process application at any wastewater treatment plant facing struvite scaling problems.

Methods

Materials

Samples of the supernatant from the centrifugation of anaerobically digested sludge (centrate) were collected from the Tres Rios Water Reclamation Facility in Tucson, Arizona, and stored at 4°C. Titrations and bench-scale CO_2 injection experiments were conducted on the Tres Rios centrate as well as samples from other wastewater treatment plants in Phoenix, Arizona; Portland, Oregon; and Chicago, Illinois, to show that methods developed here can be usefully applied to prevent struvite precipitation despite significant differences in water quality. Samples were shipped overnight on ice and stored at 4°C upon receipt. Prior to experimentation, the total dissolved concentrations of struvite components—ammonia, magnesium, and orthophosphate—were measured at the Tres Rios Water Reclamation Facility using standardized methods (O'Dell 1993a, b; Martin et al. 1994) and electrical conductivity was measured using a Eutech Oakton PC650 electrical conductivity probe.

Struvite Precipitation Modeling Methods

A model was developed to (1) anticipate precipitation of various minerals in centrate, (2) confirm that struvite is the mineral most likely to precipitate in the pH ranges of interest, and (3) determine the pH range over which mineral formation can be avoided. The reactions considered in the model include acid/base reactions involving Mg^{2+}, PO_4^{3-}, and NH_4^+, as well as formation of magnesium/phosphate complexes (Table S1). Other complexation reactions may occur in centrate due to the variety of metals and ligands present. Neglecting these additional reactions leads to underestimation of the mineral solubility so that results may be considered a worst-case representation of pH values necessary to prevent solid-phase precipitation.

In the model calculations, all equilibrium constants were expressed in terms of activities, which were calculated as a function of the measured species concentrations and the ionic strength of the solution, which was estimated from the measured electrical conductivity (Snoeyink and Jenkins 1980). Details are given in the Supplemental Data. In all, the possibility of precipitation of four different minerals was considered, as described by Ohlinger et al. (1998). Minerals considered in the model included struvite ($MgNH_4PO_4 \cdot 6H_2O_{(s)}$), $MgOH_{2(s)}$, $MgHPO_{4(s)}$, and $Mg_3(PO_4)_{2(s)}$ (Table S2). The supersaturation index (SI), defined by Eq. (1), was calculated as a function of solution pH for centrate samples containing measured concentrations of total soluble magnesium, ammonia, and orthophosphate

$$\mathrm{SI} = \frac{\prod \{A\}^a}{K_{sp,\mathrm{mineral}}} \tag{1}$$

where $K_{sp,\mathrm{mineral}}$ values are respective solubility products, reported in Table S2, and brackets denote activity. The numerator is the product of the activities of the chemical dissociation products in the same table, raised to powers derived from their respective stoichiometric coefficients. Their activities are calculated assuming that no precipitate forms despite SI values >1.0. Details of this calculation are provided in the Supplemental Data. The mineral with the highest SI value in the pH range of interest was considered most likely to form. Additionally, the pH below which mineral precipitation was not expected (SI = 1) was identified. The target pH for CO_2 addition was then taken to be 0.3 units below the pH at which SI = 1, in order to provide a safety margin while preventing precipitation reactions.

Titration

Titration Experimental Methods

Titrations were performed to expose acid/base characteristics of the fluids of interest. Standardized hydrochloric acid (1.89 M) was incrementally added to the centrate samples, and pH was measured after each acid addition.

Titration Modeling Methods

An equilibrium model was developed to represent the behavior of centrate upon the addition of strong acid. Calculations showed that the buffering capacity of the centrate was adequately accounted for by consideration of carbonate alone. Ionic species present that do not act as buffers may include strong base cations or strong acid anions. Relevant reactions are given in Table 1. The parameters k_c and k_{-c} are the forward and reverse rate constants for the reaction between carbon dioxide and water to form carbonic acid, K_{C1} and K_{C2} are the first and second acid dissociation constants for the carbonic acid system, and K_W is the acid dissociation constant for water.

A charge balance must be satisfied during titration

$$[\mathrm{H^+}] + \sum c_B = [\mathrm{HCO_3^-}] + 2[\mathrm{CO_3^{2-}}] + [\mathrm{OH^-}] + \sum c_A + [\mathrm{Cl^-}]_{\mathrm{Added}} \tag{2}$$

Table 1. Reactions describing acid/base properties of centrate and equilibrium constants

Reaction	Equilibrium or rate constant	References
$CO_{2(aq)} + H_2O \leftrightarrow H_2CO_3$	$k_c = 0.0423\ s^{-1}$, $k_{-c} = 25.6\ s^{-1}$	Wang et al. (2010)
$H_2CO_3 \leftrightarrow HCO_3^- + H^+$	$K_{C1} = 10^{-3.5}$	
$HCO_3^- \leftrightarrow CO_3^{2-} + H^+$	$K_{C2} = 10^{-10.329}$	Benjamin (2015)
$H_2O \leftrightarrow H^+ + OH^-$	$K_W = 10^{-14}$	

Note: Equilibrium constants are defined in noted equation number.

Square brackets denote species concentrations, Σc_B and Σc_A represent the sum of equivalents of strong base cations and strong acid anions in the original solution, respectively, and $[Cl^-]_{Added}$ is the total molar concentration of HCl added to reach respective points on the titration curve. The titration curve is represented in terms of pH versus $[Cl^-]_{Added}$. In this model, it is assumed that the total carbonate concentration is constant (closed system), so that $[HCO_3^-]$ and $[CO_3^{2-}]$ may be calculated as a function of total carbonate and pH.

Note that the composition of the centrate is treated as unknown: $\Sigma c_B - \Sigma c_A$, and the total carbonate concentrations are not initially known. A mass balance on carbonate species (assuming the system is closed during the titration) and equilibrium constants were used to express each species in Eq. (2) as a function of $[H^+]$, thermodynamic constants, bulk properties of the solution ($TotCO_3$ and $\Sigma c_B - \Sigma c_A$) [Eq. (3)]. Details are provided in the Supplemental Data

$$[Cl^-]_{Added} = [H^+] + \sum c_B - \sum c_A - \left(\frac{K_{C1}}{\gamma^2[H^+]} + 2\frac{K_{C1}K_{C2}}{\gamma^6[H^+]^2}\right) \times \left(\frac{TotCO_3}{\frac{k_{-c}}{k_c} + 1 + \frac{K_{C1}}{\gamma^2[H^+]} + \frac{K_{C1}K_{C2}}{\gamma^6[H^+]^2}}\right) - \frac{K_W}{\gamma^2[H^+]} \quad (3)$$

Here, γ is an activity coefficient for a monovalent ion calculated as a function of the ionic strength of the solution using the Davies equation [Eq. (S2) in the Supplemental Data]. Values of $TotCO_3$ and $\Sigma c_B - \Sigma c_A$ were selected to best fit the titration data. The mineral alkalinity, $\Sigma c_B - \Sigma c_A$, was used in modeling the equilibrium pH upon the addition of carbon dioxide at elevated pressures, as described next.

Elevated Pressure CO_2 Injection

Bench-Scale CO_2 Injection Methods

A reactor was constructed to expose centrate samples to pure CO_2 gas at various pressures (Fig. S1). The reactor consisted of a 7.6-cm, schedule 40 PVC pipe capped on both ends. The pipe was fitted with a gas inlet and outlet and a pH probe port. A 10.2-cm GT-DJ Steam Serializable pH sensor from Innovative Sensors (Mississauga, Ontario, Canada) was used to measure pH. The gas inlet was attached to a CO_2 cylinder, a needle valve for flow control, a rotameter, and a glass-bonded silica diffuser (AS2 Pentair Aquatic Eco-Systems Sweetwater Air Diffuser (Apopka, Florida) with 140-μm pore size) placed at the bottom of the reactor. The gas outlet was attached to a pressure gauge and a needle valve used to control the pressure in the reactor.

To conduct experiments under atmospheric pressure, 1,500-mL centrate samples were added to the reactor through the gas outlet port. The temperature of the centrate was recorded. The CO_2 cylinder was opened, and the needle valve was adjusted so that the gas flow rate was 1 L/min. Gas was allowed to escape until CO_2 had replaced all air in the headspace while maintaining atmospheric pressure within the reactor. The pH was measured every 0.1 s using a Neulog data logger until the pH was stable for at least 15 min. Next, the gas outlet valve was closed completely, and the pressure was allowed to increase to 136 kPa (absolute pressure). Once the pressure reached the set point, the outlet valve was opened, and the inlet and outlet needle valves were adjusted until the flow rate was 1 L/min and the pressure was stable at 136 kPa. Again, the pH was measured every 0.1 s for 30 min, or until the pH was stable for at least 15 min. This was repeated for headspace pressures of 170 and 205 kPa. The steady pH was plotted against the headspace pressure.

CO_2 Injection Modeling Methods

The equilibrium titration model previously described was adapted to predict the steady state pH upon the injection of CO_2 at elevated pressures. A charge balance is given by Eq. (4)

$$[H^+] + \sum c_B = [HCO_3^-] + 2[CO_3^{2-}] + [OH^-] + \sum c_A \quad (4)$$

At equilibrium, the aqueous-phase carbon dioxide concentration was calculated as a function of pressure using Henry's Law [Eq. (S38) in the Supplemental Data, Sander 2017]. This was substituted into Eq. (4), along with other equilibrium expressions, to calculate equilibrium pH as a function of the pressure of CO_2 [Eq. (5)]. Details are provided in the Supplemental Data

$$[H^+] + \sum c_B = \left(\frac{K_{C1}}{\gamma^2[H^+]} + 2\frac{K_{C1}K_{C2}}{\gamma^6[H^+]^2}\right)\left(\frac{k_c}{k_{-c}}\frac{P_{CO_2}}{H_c}\right) + \frac{K_W}{\gamma^2[H^+]} + \sum c_A \quad (5)$$

Pilot-Scale Experiment Methods

A pilot-scale system was constructed at the Tres Rios Wastewater Reclamation Facility in Tucson, Arizona, to investigate the scalability of the struvite prevention strategy and analyze design alternatives. First, the system described as follows was used to investigate the feasibility of applying carbon dioxide in various forms, including gaseous and aqueous CO_2. Second, the system was used to investigate the effect of various operational parameters on the final pH and the ability of the system to prevent struvite formation. Finally, the pilot data were used to validate a pilot model, which was adapted into a generalized design protocol for struvite prevention at any wastewater treatment plant.

Pilot System Description

The pilot system is shown in Fig. 1 and a detailed schematic is provided in the Supplemental Data (Fig. S2). It included a 3,800-L, 3.7-m tall, and 1.2-m diameter steel tank. The tank was connected to a 34.1-m long test section, constructed of 5-cm clear PVC, with sampling ports for measurement of pH as a function of distance from the injection point. Sampling ports were installed 0.9, 1.8, 3.7, 6.7, and 7.3 m from the injection point. Additionally, an in-line Vernier Go Wireless (Beaverton, Oregon) pH probe was installed at tank outlet to measure the pH of pretreated centrate at the tank exit. Another in-line pH probe was installed at the end of the test section, along with a pressure gauge and a gate valve to conduct experiments at elevated pressures in the test section. A 1,500-W AMT pump supplied centrate to the tank, and a 750-W AMT pump supplied the centrate bypass line. A Pentair Point Four microbubble, ultrafine pore ceramic diffuser was placed at the bottom of the tank to produce bubbles with diameters of 100–500 μm. The diffuser was connected to a CO_2 cylinder. A pressure gauge, thermometer, and rotameter were installed in the gas line to quantify CO_2 flow rates. Gas flow was controlled by a gas regulator mounted on the CO_2 cylinder. Centrate flow rate was controlled through union ball valves. Digital flow meters were installed at the tank inlet, tank outlet, and centrate bypass line to measure flow rates of centrate. Tank pressure was controlled by a pressure relief valve mounted on top of the tank.

Feasibility Study

A feasibility study was conducted to determine the optimal method of CO_2 application. The system was operated in one of two modes. In the first mode, gaseous CO_2 was injected directly into the test

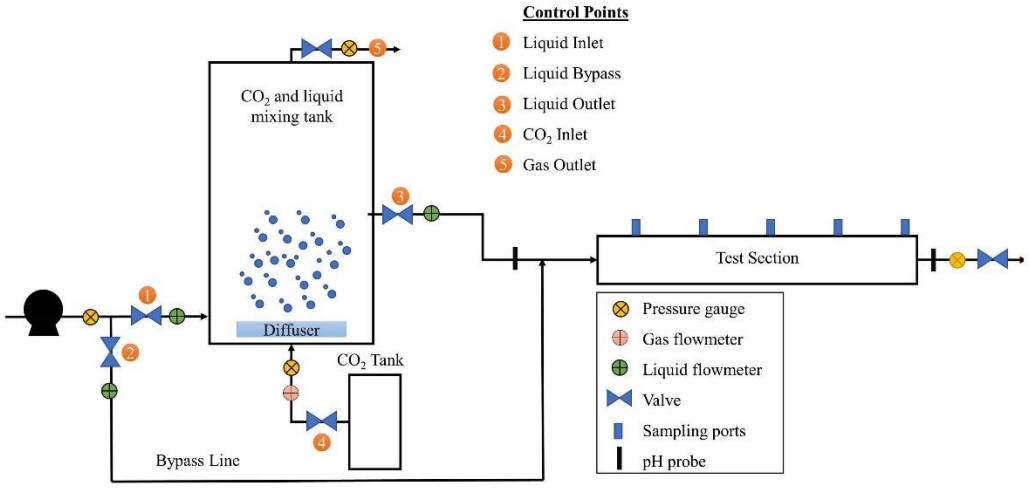

Fig. 1. Aqueous CO_2 injection pilot system.

section (Fig. S3). In the second mode (Fig. 1), aqueous CO_2 was generated by presaturating centrate with CO_2 in the tank. Subsequently, the aqueous-phase CO_2 was injected into the test section.

In the feasibility study, the liquid flow rate was maintained at 18.9 L/min (resulting in a Reynolds number of 8,990, indicating turbulent flow), and CO_2 flow rate was varied from 4 to 10 L/min. Samples were collected from sampling ports along the test section and measured off-line using a bench-scale pH probe. Results demonstrated that injection of gaseous CO_2 is not effective, so this operational mode was not considered further. Details are provided in the "Results" section.

In the second operational mode, the feed tank was filled with centrate (Fig. 1). Carbon dioxide gas was injected into the tank at a flow rate controlled by the regulator installed on the CO_2 tank (Control point 4, Fig. 1). The pressure in the tank was maintained at its set point by adjusting the gas outlet valve (Control point 5, Fig. 1). The centrate in the tank was pretreated in this manner for 1.5 h, or until the pH measured from the online pH probe installed at the tank outlet was steady. At that point, the tank was converted to continuous operation. The inlet and outlet valves were opened and adjusted to maintain the flow rate at the set point (Control points 1 and 3, Fig. 1). Finally, the bypass valve was opened and used to set the bypass flow rate (Control point 2, Fig. 1). After 5 min, the pH profile was established across the test section by collecting samples at each sampling port or using the in-line pH probes.

In the feasibility study, CO_2-saturated centrate was generated under 101 kPa (1 atm) of CO_2. The pretreated centrate was mixed with untreated centrate at various flow rates so that the percent of treated centrate in the final mixture was equal to 16.7%, 37.5%, and 50.0%. The flow rate of centrate varied from 22.7 to 37.8 L/min, while the presaturated centrate flowrate varied from 7.6 to 22.7 L/min. The flowrate of CO_2 gas varied from 5 to 20 L/min. The pH profiles generated were referenced to the mixing point. As discussed next, results demonstrated the feasibility of the methodology, so this operational mode was used in the study described next.

Characterization of Aqueous CO_2 Injection

After confirming that the operational model shown in Fig. 1 is feasible, additional studies were conducted to quantify the effect of operational parameters on the final pH. The mineral alkalinity was measured via a strong acid titration so that the data could be used to validate the pilot model, described next. Centrate was then presaturated with CO_2 at 304 kPa in batch conditions. After the pH in the tank reached steady state, the tank was converted to a continuous stirred tank reactor (CSTR) system by opening the liquid inlet and outlet valves (Control points 1 and 3, Fig. 1). The system was again allowed to reach steady state. The flow rate through the CSTR was 37.9 L/min, resulting in a residence time of approximately 100 min. The flow rate of CO_2 was maintained at 2.16 mol/min. Next, the centrate presaturated with CO_2 in the CSTR was mixed with untreated centrate at various blend ratios (flow rate of treated centrate over total mixed flow). Treated centrate was fed through the test section (blend ratio of one); the pH was measured at end of the test section. Next the bypass valve (Control point 2, Fig. 1) was opened. Treated and untreated flow rates were adjusted to achieve various blend ratios so that the final flow rate of the mixed centrate was 75.6 L/min. The pH was measured as a function of distance along the test section for various blend ratios.

Steady State Model for CO_2 Injection in a Continuous Flow Reactor

The preceding pilot system was modeled by considering two processes in series: a CSTR followed by mixing in a closed system. A model was developed to predict the steady state pH upon the injection of carbon dioxide into centrate in a CSTR. In this case, it was assumed that the system reaches equilibrium, or that the CO_2 concentration may be calculated from Henry's Law. Mass balances result in Eqs. (6) and (7). A charge balance is shown in Eq. (8). Details of the derivation are provided in the Supplemental Data

$$0 = \frac{Q_l}{V}([CO_2]_{in} - [CO_2]) - k_c[CO_2] + k_{-c}[H_2CO_3] \quad (6)$$

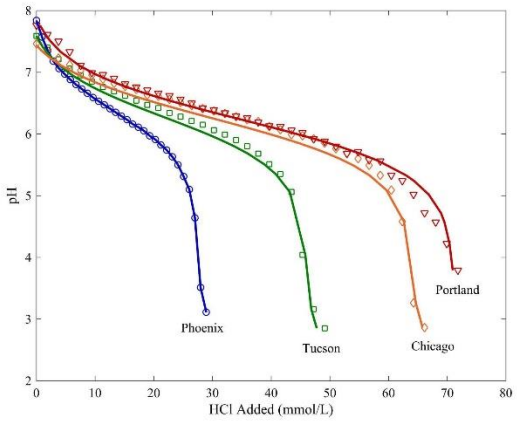

Fig. 2. Experimental and calculated results for equilibrium pH in centrate samples as a function of CO_2 partial pressure. Experimental data are indicated by points and calculated data are indicated by solid lines. Average relative square error varied between 1.83×10^{-5} and 6.69×10^{-4}.

$$0 = \frac{Q_l}{V}\left\{[H_2CO_3]_{in} + \frac{K_{c1}}{\gamma^2[H^+]_{in}}[H_2CO_3]_{in} + \frac{K_{c2}K_{c1}}{\gamma^6[H^+]^2_{in}}[H_2CO_3]_{in} - [H_2CO_3] - \frac{K_{C1}}{\gamma^2[H^+]}[H_2CO_3] - \frac{K_{C1}K_{C2}}{\gamma^6[H^+]^2}[H_2CO_3]\right\} + k_c[CO_2] - k_{-c}[H_2CO_3] \quad (7)$$

$$0 = [H^+] + \sum c_B - \sum c_A - \left(\frac{K_{C1}}{\gamma^2[H^+]} + 2\frac{K_{C1}K_{C2}}{\gamma^6[H^+]^2}\right)[H_2CO_3] - \frac{K_W}{\gamma^2[H^+]} \quad (8)$$

Here, Q_l is the flow rate of liquid through the CSTR and V is the volume of the CSTR. Eqs. (6)–(8) were solved simultaneously to calculate the equilibrium pH of centrate exiting the CSTR (ahead of the mixing point for the CO_2-saturated and untreated centrate flows, shown in Fig. 2).

Steady State Model for Mixing Presaturated and Untreated Centrate

A model was developed to predict the pH after a mixing point in which centrate presaturated with CO_2 was mixed with untreated centrate. It is assumed that the mixing process occurs in a closed system, much like the titration model; the total carbonate in the two streams is conserved [Eq. (9)], and proton transfer must be accounted for when equilibrium is reestablished. A mass balance was performed on total carbonate during mixing and was solved for $TotCO_{3f}$, as shown in Eq. (9)

$$TotCO_{3_f} = \frac{Q_u TotCO_{3_u} + Q_t TotCO_{3_t}}{Q_f} \quad (9)$$

In Eq. (9), $TotCO_3$ is the total carbonate concentration in each stream and Q_i is the stream-specific volumetric flow rate. Subscript u is for the untreated centrate, t represents the centrate treated with CO_2 and f is the final mixed stream. For convenience, the blend ratio, R is defined in Eq. (10)

Table 2. Concentrations of struvite components and target pH for centrate samples from various locations

Sample	$TotMg$ (mM)	$TotNH_3$ (mM)	$TotPO_4$ (mM)	pH for SI = 1	Target pH for struvite control
Phoenix	2.2	20.4	ND	N/A	N/A
Tucson	0.926	89.9	3.6	6.66	6.36
Chicago	1.3	72.1	1.4	6.89	6.59
Portland	1.1	82.1	4.0	6.62	6.32

Note: ND = not detected.

$$R = \frac{Q_t}{Q_f} \quad (10)$$

Because Q_f is the sum of Q_u and Q_t, using this definition, Eq. (9) can be rewritten as follows:

$$TotCO_{3_f} = (1 - R)TotCO_{3_u} + RTotCO_{3_t} \quad (11)$$

Eq. (11) and a charge balance calculated for a closed system can be used to determine the pH beyond the mixing point. This is identical for the titration curve charge balance, but with $[Cl^-]_{Added}$ equal to zero [Eqs. (2) and (3)]. Models presented here were validated experimentally and used to develop a design protocol for CO_2-based struvite prevention systems.

Results and Discussion

Precipitation Model Results

Measured total concentrations of magnesium ($TotMg$), ammonia ($TotNH_3$), and orthophosphate ($TotPO_4$) were as indicated (Table 2). The pH-dependent supersaturation indexes for compounds of potential interest in Tucson centrate are shown in Fig. S4. Calculations confirm that in the pH range of interest ($5.6 < pH < 8$), struvite is the precipitate of primary concern (highest supersaturation index − SI). The range of pH over which struvite solubility is exceeded in the Tucson centrate is $pH > 6.6$. Similar results were obtained for centrates originating at other locations. The results are summarized in Table 2.

Titration Results

Centrate titration data and model results are shown in Fig. 3. Values for fitted parameters are summarized in Table 3. All titrations were conducted in duplicate but little variability was observed (differences were less than 0.1 pH units). Despite significant differences in centrate buffering capacities, agreement between model and measurement was excellent in all cases (average relative square error < 0.05). It is apparent that acid/base conversions in the pH range of relevance to struvite precipitation can be adequately modeled by assuming that bicarbonate is the predominant contributor to centrate buffering.

As expected, samples with higher mineral alkalinity generally required more acid to lower pH to target levels. However, the amount of acid required to reach the target pH is a function of both the mineral alkalinity (Table 3) and the concentration of struvite components (Table 2). For example, the Tucson sample requires more acid to reach the target pH than the Chicago sample, even though its mineral alkalinity is lower. This is because the Tucson centrate has a lower target pH due to higher concentrations of ammonia and phosphate. The Portland centrate requires the highest

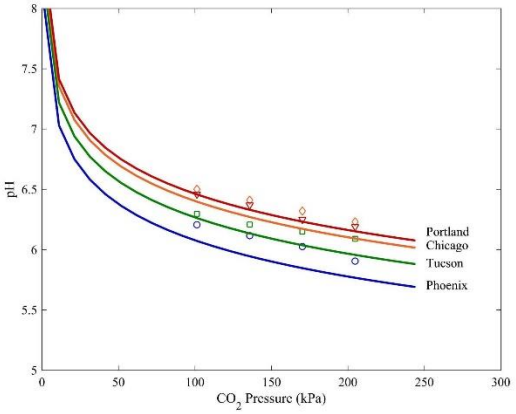

Fig. 3. Experimental and calculated titration curves for four centrate samples. Experimental data are indicated by points and calculated data are indicated by solid lines. Average relative square error varied between 0.00942 and 0.0337.

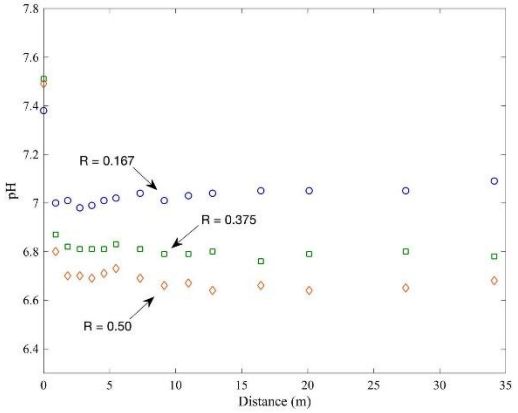

Fig. 4. Change of pH with distance in test section after mixing of CO_2 presaturated (101 kPa) centrate and untreated centrate at various mixing ratios (R).

Table 3. Fitted parameters from titration experiments, strong acid, and pressure of CO_2 (P_{CO_2}) required to reach target pH

Sample	$\sum c_B - \sum c_A$ (mM)	$TotCO_3$ (mM)	Acid required to reach target pH (mM)	P_{CO_2} to reach target pH at equilibrium (kPa)
Phoenix	28	29	N/A	N/A
Tucson	46	48	19.3	80.9
Chicago	64	68	17.4	65.4
Portland	71	72	31.3	139

acid addition to prevent struvite formation due to its high mineral alkalinity and high concentrations of struvite components.

Bench-Scale CO_2 Injection Results

Measured and predicted equilibrium pH values for the four centrates obtained and analyzed (Table 2) are provided as a function of the partial pressure of carbon dioxide (Fig. 3). Results indicate that determination of mineral alkalinity is sufficient to support prediction of the equilibrium pH upon CO_2 addition (average relative square error < 0.001). At worst, the model underpredicted the experimental pH by 0.2 pH units. Additionally, Fig. 3 results were used to identify the CO_2 partial pressure required to reach the target pH for each sample (Table S1).

All partial pressures reported in Table S1 are achievable in practice, suggesting that the use of CO_2 to prevent struvite formation is feasible. Furthermore, many samples require a CO_2 partial pressure of less than 101 kPa (1 atm). For example, the Chicago centrate requires only 65 kPa of CO_2 to reach the target pH. This is similar to the typical partial pressure of CO_2 in biogas (Sun et al. 2015). In this case, use of untreated biogas, as opposed to residual biogas, may be feasible for struvite prevention. In fact, bubbling biogas through centrate to reduce the pH would also result in removal of CO_2 and other water-soluble components from biogas and may serve as an initial water-washing step in a methane recovery process. This is similar to recycling biogas wash water for struvite control, as suggested by Sharp et al. (2013). Overall, CO_2 is an effective method of controlling struvite formation. Additionally, it is safer and more sustainable than previously studied scale inhibitors (Buchanan et al. 1994; Doyle et al. 2003) and those commonly used today (Sharp et al. 2013), especially if the CO_2 is derived from a waste product (biogas).

Pilot-Scale Experimental Results

Feasibility Study Results

Carbon dioxide gas was injected into a centrate line through a diffuser at the head-end of the test section at various flow rates. The pH was measured as a function of distance, as previously described. Results show that higher gas flow rates resulted in lower pHs, as expected. However, the pH changed slowly as a function of distance and did not reach the target pH after 35 m as shown in Fig. S5 of the Supplemental Data. The injected CO_2 gas accumulates at the top of the pipe, resulting in stratified flow. This minimizes the area available for mass transfer, which results in slow pH changes. Since the Reynolds number was high in this experiment (8,990), it is suspected that stratified flow will exist in a typical pipe. Because of this, direct gas injection into transport lines was determined to be infeasible for the purpose intended. However, addition of baffles or other devices to promote mixing may improve mass transfer, so additional investigation may be warranted.

Centrate presaturated with pure CO_2 was produced in the feed tank at atmospheric pressure until steady state pH was reached. This pretreated centrate had a pH equal to 6.23. Pretreated centrate and untreated centrate were then mixed at various ratios. The pH was measured in samples obtained along the test section. The flow rate of CO_2 presaturated centrate was set to 7.6 L/min or 22.7 L/min, and the flow rate of untreated centrate was maintained at 37.9 L/min to achieve 16.7% and 37.5% of CO_2 presaturated centrate in the mixtures. In order to raise the percentage of CO_2 presaturated centrate in total flow to 50%, CO_2 presaturated centrate and untreated centrate were both set to 18.9 L/min. Results are presented in Fig. 4. It is apparent that pH in the mixture reaches equilibrium almost immediately after the mixing point and that injection of centrate pretreated with CO_2 represents a more feasible alternative than introduction of gaseous CO_2.

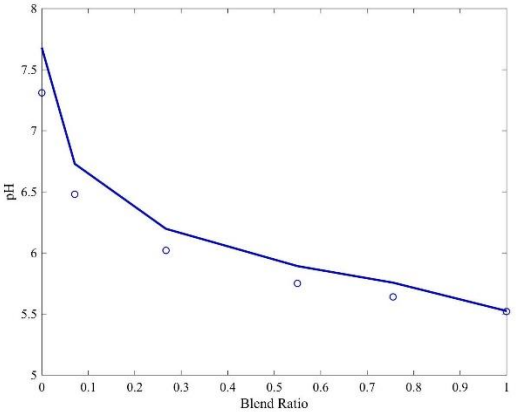

Fig. 5. Calculated and experimental equilibrium pH in Tres Rios centrate as a function of blend ratio presaturated with CO_2 at 300 kPa. Experimental data are indicated by points and calculated data are indicated by solid lines. Average relative square error was 9.88×10^{-4}.

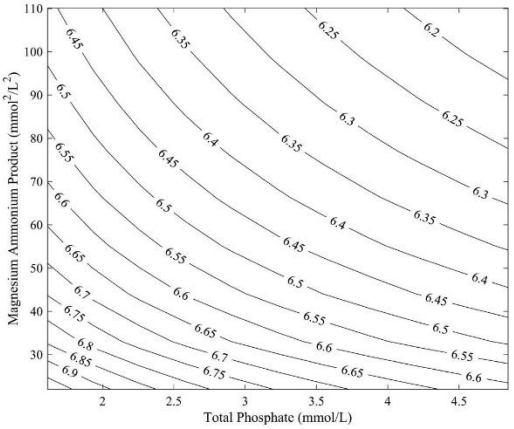

Fig. 6. Precipitation model calculations: Contours of constant target pH as a function of total phosphate and product of total magnesium and ammonia concentrations.

System Characterization and Model Validation

A pilot experiment was performed to validate the mixing model previously described. First, a titration was performed to measure the mineral alkalinity of the centrate immediately prior to experimentation. This was necessary due to day-to-day variation in the composition of digester centrate available at the Tres Rios plant. The mineral alkalinity was determined to be 15 mM. This is only about 30% of the 46 mM measured in a previous sample.

A series of mixing experiments were conducted in which a fraction of the total centrate flow was equilibrated with gas-phase CO_2 in the CSTR before it was recombined with untreated centrate for measurement of pH, as described in the "Methods" section. The pressure in the CSTR was 304 kPa and the total centrate flow rate after recombination was 75.6 L/min. Mixing ratio was the independent variable, and the equilibrium pH in each mixture was predicted and indicated in the modeling section. Note that there is good agreement between data and model (Fig. 5, average relative square error < 0.001), supporting extension of modeling results under reasonably similar physical conditions. The point at R = 1 corresponds to the CSTR liquid only (no mixing). The fact that this point is well predicted validates the CSTR model (relative square error of 6.07×10^{-7}), which is based on attainment of equilibrium with gas-phase CO_2. Results show that the residence time in this experiment (100 min) was long enough to ensure that equilibrium is reached, and the two chemistry simulations—equilibrium with gas-phase CO_2 and mixing models can be combined to design for pH control using CO_2 addition.

Design Protocol

The results of experiments and simulations presented here were used to develop a protocol for the design of struvite prevention systems using CO_2 addition for pH control. The protocol uses measurable parameters to identify design alternatives for centrates of arbitrary initial quality. The blending of CO_2 presaturated centrate with the main centrate flow was used as the basis for design. This methodology is more feasible than direct addition of gas-phase CO_2 as it resulted in rapid achievement of near-equilibrium pH values and thus protection from struvite formation over greater pipe lengths.

Input data for the design protocol include the centrate concentrations of magnesium, ammonia, and phosphate, the initial centrate pH, and strong-acid titration results. These are necessary to determine the target pH for struvite control and the centrate mineral alkalinity. The protocol discussed next can then be used to find combinations of P_{CO_2} during centrate presaturation and mixing ratio that are capable of producing target pH for struvite control in the recombined centrate. Steps are outlined in greater detail in what follows.

The pH at which struvite formation is incipient (SI = 1) should first be calculated. The target pH is then calculated by subtracting a safety factor from the pH at which formation is prevented. An arbitrary safety factor of 0.3 pH units was used here. This is greater than the maximum error observed in the modeling efforts presented here and provides a reaction quotient that is below the stability constant for struvite formation by a factor of two. Absent equilibrium data, Fig. 6 can be used to estimate the pH for which $SI = 1$. In producing the figure, it was assumed that $[Mg^{2+}]$ is about equal to $TotMg$ and $[NH_4^+]$ dominates total ammonia nitrogen and that both concentrations are independent of pH in the relevant pH range. Thus, the product of total magnesium and ammonia concentrations (both in mol/L) is represented on the y-axis and the total phosphate concentration is on the x-axis. Values within the field in Fig. 6 can be used to find target pH values. These will be used along with the mineral alkalinity (see the next paragraph), to identify design or operational alternatives for CO_2 addition (P_{CO2} values and mixing ratios) necessary to reach the pH target in the blended centrates.

In the second step, a strong acid titration is carried out. Titrations should be performed for several samples taken over a period of months to characterize normal variability in the mineral alkalinity of the centrate. The titration model described in the methods is then used to represent the titration data. Values for $TotCO_3$ and the mineral alkalinity ($\Sigma c_B - \Sigma c_A$) are selected to best fit the titration curve. Mineral alkalinity may be roughly estimated from the amount of strong acid added to consume the buffering capacity of the test solution. The mineral alkalinity is then used to identify design alternatives—combinations of centrate blending (raw and

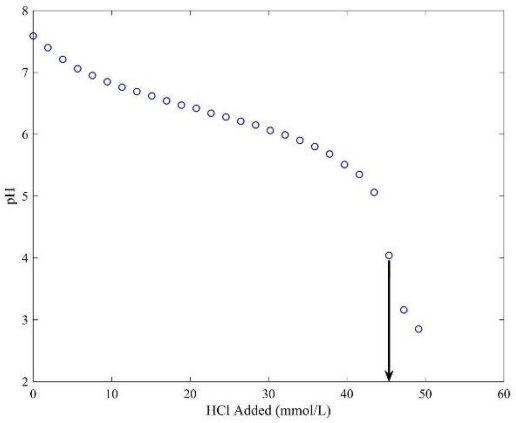

Fig. 7. Tres Rios centrate titration curve. Arrow estimates mineral alkalinity from point at which alkalinity is exhausted.

presaturated centrates) and P_{CO_2} during presaturation of centrate—to reach the target pH.

Design Protocol Example

In this section, the preceding outlined protocol is used to design for struvite prevention in centrate from the Tres Rios Wastewater Reclamation Facility in Tucson.

1. *Calculate a target pH from chemical data* (Fig. 6). Total concentrations of struvite components are reported in Table 2. The product of total ammonium and magnesium concentrations is 83.2 $mmol^2/L^2$. Use of Fig. 6 and the total orthophosphate concentration yields a pH of 6.6, the pH below which struvite should not precipitate. Application of the safety factor (0.3 pH units) leads to a target pH of 6.3.
2. *Estimate mineral alkalinity from the titration curve* (Fig. 7). The mineral alkalinity is estimated as the concentration of strong acid required to exhaust the buffering capacity of the centrate—indicated by the arrow in Fig. 7. The estimated mineral alkalinity is 46 mmol/L, which is nearly the value determined from fitting the titration model (Table S1).
3. *Identify potential system designs—CO_2 partial pressure and blend ratio* (Fig. 8). The target pH and mineral alkalinity are used with Fig. 8 to identify potential system designs. Fig. 8 was generated by the mixing model for a target pH of 6.3; design curves for other centrate-specific targets are provided in the Supplemental Data [Figs. (S6–S16)]. The mineral alkalinity is located on the horizontal in the top and bottom portions of Fig. 8. From the lower figure, it is evident that 43 mmol/L of CO_2 must be added per liter of centrate to reach the target pH. This can be achieved using various combinations of P_{CO_2} and blending ratio, as indicated by the line in the top portion of Fig. 8. When P_{CO_2} equals 101 kPa (1 atm), for example, injection of CO_2 under atmospheric pressure will achieve the target pH if all the centrate is fed through the CSTR. However, this may lead to an unacceptably large feed tank volume or footprint to achieve a residence time of 100 min, so smaller blending ratios may be desired. The CSTR volume can be reduced by half by decreasing the blending ratio to 0.5. In this case, pressure of 250 kPa in the feed tank is required to reach the target pH.

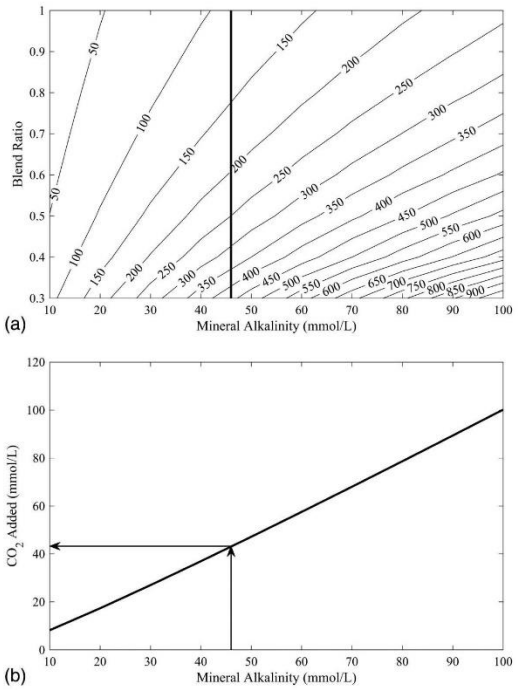

Fig. 8. (a) Contours of CO_2 pressure (kPa) required to reach a target pH of 6.3 as a function of mixing ratio and mineral alkalinity. Line indicates possible design alternatives for Tucson centrate; and (b) CO_2 addition required to reach a target pH of 6.3 as a function of mineral alkalinity. Arrows indicate CO_2 requirement for Tucson centrate.

Further economic optimization and analysis of safety considerations are necessary to decide among the alternatives identified, including consideration of economic tradeoffs associated with a large tank size and operating at high pressures. However, it may be the case that, even with large pressures and small blend ratios, that the CSTR is infeasibly large. In this case, alternative configurations, such as injection of gaseous CO_2 into pipes with baffles, should be considered.

However, note that the CO_2 requirement represents the amount of CO_2 that must be *transferred* to the fluid to reach the target pH. This will be less than the amount of CO_2 that flows through the CSTR, as some CO_2 may fail to dissolve and escape the CSTR. For example, the CO_2 required to reach the target pH determined from Fig. 8 is 43 mmol/L. However, during the pilot experiment 57 mmol of CO_2 were applied per liter of solution fed into the CSTR. This implies that about 75% of the CO_2 applied was absorbed; the remaining 25% was vented to the atmosphere or accumulated in the headspace. It follows that the value determined using the universal design curve should be divided by 0.75 (in this case) to estimate the mass of CO_2 to be applied. Note, however, that the amount of gas that dissolves is a function of gas flow rate, bubble size, fluid properties, and reactor configuration. Additional studies are needed to understand mass transfer effects in detail.

The CO_2 requirement previously determined may also be used to evaluate the feasibility of supplying CO_2 from biogas.

For example, the Tucson plant will need to treat 0.37 million gallons of centrate per day. This will require 60,200 mol of CO_2 per day to reach a concentration of 43 mmol/L. However, the plant produces 390,200 mol of CO_2 per day. If the struvite prevention system transfers CO_2 to the liquid phase with greater than 15% efficiency, all CO_2 may be supplied by the biogas.

Conclusions

Bench- and pilot-scale experiments conducted in this study demonstrate the feasibility of using carbon dioxide for struvite management. First, an equilibrium model was developed and used to (1) demonstrate that struvite is the mineral most likely to form under chemical conditions downstream from anaerobic sludge dewatering operations and (2) identify the pH below which precipitation is prevented. As inputs, the model requires the concentrations of struvite components in, for example, digester centrate. Next, equilibrium models were developed to predict the pH in centrate as a function of the strong acid (titration) or carbon dioxide added to solution. The models were validated using experimental data from several locations. It was shown that (1) CO_2 injection into centrate can produce pH values low enough to prevent struvite formation and (2) pH can be predicted from the mineral alkalinity (titration data) alone.

A pilot study was conducted to evaluate alternatives for implementation of a CO_2 struvite prevention system. Injection of gaseous CO_2 resulted in a slow pH change that left long distances of pipe unprotected. However, by mixing streams of centrate pretreated with CO_2 with untreated centrate, scale formation can be prevented immediately below the mixing point. The equilibrium model validated via bench-scale studies was used to model the aqueous injection pilot system and validated using experimental data. Finally, the model was used to develop a user-friendly, three-step design protocol for a CO_2 struvite prevention system that depends only on conveniently measured water quality parameters.

Several aspects of this study require further investigation. First, the effect of trace gases present in residual biogas deserves attention. This study considered only injection of pure CO_2. While this is a close approximation of residual biogas after methane separation, which is at least 97% CO_2, additional work is needed to investigate interference and/or safety considerations arising from trace gases present in biogas, including hydrogen sulfide and methane. These compounds are not expected to negatively affect process chemistry.

Acknowledgments

The authors wish to thank Water Environment & Reuse Foundation (WERF) for their financial support; Phoenix, Chicago, and Portland Wastewater Reclamation Facilities for providing samples for testing, and the following individuals for their contribution to this work: Dean Moulis, Kalin Denton, Guiherme Gomes, Erica Vanover, Umur Yenal, James Hackett, Meagan Marquard, Lauren Peckler, and Rosanna Salazar.

Supplemental Data

Eqs. (S1)–(S49), Tables S1 and S2, and Figs. S1–S16 are available online in the ASCE Library (www.ascelibrary.org).

References

Benjamin, M. M. 2015. *Water chemistry*. Long Grove, IL: Waveland Press.

Birnhack, L., O. Nir, M. Telzhenski, and O. Lahav. 2015. "A new algorithm for design, operation and cost assessment of struvite (MgNH4PO4) precipitation processes." *Environ. Technol.* 36 (15): 1892–1901. https://doi.org/10.1080/09593330.2015.1015455.

Buchanan, J. R., C. R. Mote, and R. B. Robinson. 1994. "Struvite control by chemical treatment." *Transactions* 37 (4): 1301–1308. https://doi.org/10.13031/2013.28211.

Doyle, J. D., K. Oldring, J. Churchley, C. Price, and S. A. Parsons. 2003. "Chemical control of struvite precipitation." *J. Environ. Eng.* 129 (5): 419–426. https://doi.org/10.1061/(ASCE)0733-9372(2003)129:5(419).

Doyle, J. D., and S. A. Parsons. 2002. "Struvite formation, control and recovery." *Water Res.* 36 (16): 3925–3940. https://doi.org/10.1016/S0043-1354(02)00126-4.

Garmo, O., and C. Escudero. 2014. "Using CO2-gas to lower the pH of tunnelling waste water: Laboratory test and assessment of toxic potential." Accessed February 16, 2018. https://www.vegvesen.no/fag/publikasjoner/Publikasjoner/Statens+vegvesens+rapporter/_attachment/622363?_ts=145d09f1610&download=true&fast_title=Using+CO2-gas+to+lower+the+pH+of+tunnelling+waste+water+%3A+laboratory+test+and+assessment+of+toxic+potential.

Jordaan, E. M., B. Rezania, and N. Cicek. 2013. "Investigation of chemical-free nutrient removal and recovery from CO2-rich wastewater." *Water Sci. Technol.* 67 (10): 2195–2201. https://doi.org/10.2166/wst.2013.116.

Martin, T. D., C. A. Brockhoff, and J. T. Creed. 1994. "Method 200.7: Determination of metals and trace elements in water and wastes by inductively coupled plasma-atomic emission spectrometry." Accessed February 16, 2018. https://www.epa.gov/sites/production/files/2015-08/documents/method_200-7_rev_4-4_1994.pdf.

Mayer, B. K., et al. 2016. "Total value of phosphorus recovery." *Environ. Sci. Technol.* 50 (13): 6606–6620. https://doi.org/10.1021/acs.est.6b01239.

O'Dell, J. W. 1993a. "Method 350.1: Determination of ammonia nitrogen by semi-automated colorimetry." Accessed February 16, 2018. https://www.epa.gov/sites/production/files/2015-06/documents/epa-350.1.pdf.

O'Dell, J. W. 1993b. "Method 365.1: Determination of phosphorous by semi-automated colorimetry." Accessed February 16, 2018. https://www.epa.gov/sites/production/files/2015-08/documents/method_365-1_1993.pdf.

Ohlinger, K. N., T. M. Young, and E. D. Schroeder. 1998. "Predicting struvite formation in digestion." *Water Res.* 32 (12): 3607–3614. https://doi.org/10.1016/S0043-1354(98)00123-7.

Sander, R. 2017. "Carbon dioxide: Henry's law data." Accessed February 16, 2018. http://webbook.nist.gov/cgi/cbook.cgi?ID=C124389&Mask=10.

Sharp, R., E. Vadiveloo, R. Fergen, M. Moncholi, D. Wankmuller, and R. Latimer. 2013. "A theoretical and practical evaluation of struvite control and recovery." *Water Environ. Res.* 85 (8): 675–686. https://doi.org/10.2175/106143012X13560205145253.

Snoeyink, V. L., and D. Jenkins. 1980. *Water chemistry*. New York: Wiley.

Sun, Q., H. Li, J. Yan, L. Liu, Z. Yu, and X. Yu. 2015. "Selection of appropriate biogas upgrading technology—A review of biogas cleaning, upgrading and utilisation." *Renewable Sustainable Energy Rev.* 51: 521–532. https://doi.org/10.1016/j.rser.2015.06.029.

Uysal, A., Y. D. Yilmazel, and G. N. Demirer. 2010. "The determination of fertilizer quality of the formed struvite from effluent of a sewage sludge anaerobic digester." *J. Hazard. Mater.* 181 (1–3): 248–254. https://doi.org/10.1016/j.jhazmat.2010.05.004.

Wang, X., W. Conway, R. Burns, N. McCann, and M. Maeder. 2010. "Comprehensive study of the hydration and dehydration reactions of carbon dioxide in aqueous solution." *J. Phys. Chem.* 114 (4): 1734–1740. https://doi.org/10.1021/jp909019u.

SUPPLEMENTAL DATA

ASCE *Journal of Environmental Engineering*

Sustainable Struvite Control Using Carbon Dioxide

Sarah E. Moore, Lin Ma, Matthew Potzler, Jerry Bish, Vasiliki Karanikola, Jeff Prevatt, Robert G. Arnold, and A. Eduardo Sáez

DOI: 10.1061/(ASCE)EE.1943-7870.0001466

Sustainable Struvite Control Using Carbon Dioxide

Sarah E. Moore,[1] Lin Ma,[2] Matthew Potzler,[3] Jerry Bish,[4] Vasiliki Karanikola,[5] Jeff Prevatt,[6] Robert G. Arnold,[7] A. Eduardo Sáez[8]

[1] Ph.D. Student, Department of Chemical and Environmental Engineering, University of Arizona, 1133 E. James E. Rogers Way, Harshbarger 108, Tucson, AZ 85721.
[2] Ph.D. Student, Department of Chemical and Environmental Engineering, University of Arizona, 1133 E. James E. Rogers Way, Harshbarger 108, Tucson, AZ 85721.
[3] Ph.D. Student, Department of Chemical and Environmental Engineering, University of Arizona, 1133 E. James E. Rogers Way, Harshbarger 108, Tucson, AZ 85721.
[4] Senior Consultant, Greeley and Hansen, 4400 E. Broadway Blvd, Suite 600E, Tucson, AZ 85711.
[5] Research Professor, Department of Chemical and Environmental Engineering, University of Arizona, 1133 E. James E. Rogers Way, Harshbarger 108, Tucson, AZ 85721.
[6] Regulatory Compliance Manager, Pima County Wastewater Reclamation, 201 N. Stone Ave., 8th Fl., Tucson, AZ 85701.
[7] Professor, Department of Chemical and Environmental Engineering, University of Arizona, 1133 E. James E. Rogers Way, Harshbarger 108, Tucson, AZ 85721.
[8] Professor, Department of Chemical and Environmental Engineering, University of Arizona, 1133 E. James E. Rogers Way, Harshbarger 108, Tucson, AZ 85721. Corresponding author: esaez@email.arizona.edu

Activity Calculation

As described in the models in the main text and elaborated upon here, activities of relevant compounds are calculated using the methods described below. Activity of any compound A may be calculated as a function of concentration and activity coefficient, γ_A, as in Eq. S1.

$$\{A\}=\gamma_A[A] \tag{S1}$$

Activity coefficients were calculated using the Davies equation, as shown in Eq. S2 (Doyle and Parsons 2002).

$$\log_{10}\gamma_A = -0.509 z_A^2\left(\frac{\sqrt{I}}{1+\sqrt{I}} - 0.3I\right) \tag{S2}$$

I is the ionic strength of the solution and z_A is the valence of compound A. Eq. S2 can be rewritten as Eq. S3.

$$\gamma_A=\gamma^{z_A^2} \quad \text{(S3)}$$

γ, which is only a function of the ionic strength of the solution and a constant for all compounds, is given by Eq. S4.

$$\gamma=10^{-0.509\left(\frac{\sqrt{I}}{1+\sqrt{I}}-0.3I\right)} \quad \text{(S4)}$$

Eq. S3 was substituted into Eq. S1 to develop a convenient relationship between activity, concentration, valence, and solution ionic strength, shown in Eq. S5. This equation was used in models described subsequently.

$$\{A\}=\gamma^{z_A^2}[A] \quad \text{(S5)}$$

Precipitation Modeling Methods

As described in the main text, a model was developed to predict precipitation of various minerals in centrate. Equilibrium reactions considered are listed in Table S1. Mass balances were performed and used to calculate the concentration of relevant species as a function of pH. Mass balances on ammonia, phosphate, and magnesium are given in Eqs. S6-S8.

$$\text{TotNH}_3=[NH_4^+]+[NH_3] \quad \text{(S6)}$$

$$\text{TotPO}_4=[H_3PO_4]+[H_2PO_4^-]+[HPO_4^{2-}]+[PO_4^{3-}]+[MgPO_4^-]+[MgHPO_4]+[MgH_2PO_4^+] \quad \text{(S7)}$$

$$\text{TotMg}=[Mg^{2+}]+[MgOH^+]+[MgPO_4^-]+[MgHPO_4]+[MgH_2PO_4^+] \quad \text{(S8)}$$

Activities in equilibrium constant definitions were replaced with concentrations using Eq. S5 and solved to express all components in terms of *[NH_4^+]*, *[H_3PO_4]*, and *[Mg^{2+}]*. The results are shown in Eqs. S9-S16.

$$[NH_3]=\frac{K_N}{[H^+]}[NH_4^+] \tag{S9}$$

$$[H_2PO_4^-]=\frac{K_{P1}}{\gamma^2[H^+]}[H_3PO_4] \tag{S10}$$

$$[HPO_4^{2-}]=\frac{K_{P1}K_{P2}}{\gamma^6[H^+]^2}[H_3PO_4] \tag{S11}$$

$$[PO_4^{3-}]=\frac{K_{P1}K_{P2}K_{P3}}{\gamma^{12}[H^+]^3}[H_3PO_4] \tag{S12}$$

$$[MgPO_4^-]=\frac{K_{P1}K_{P2}K_{P3}}{K_{MgPO_4}[H^+]^3}[Mg^{2+}][H_3PO_4] \tag{S13}$$

$$[MgHPO_4]=\frac{\gamma^2K_{P1}K_{P2}}{K_{MgHPO_4}[H^+]^2}[Mg^{2+}][H_3PO_4] \tag{S14}$$

$$[MgH_2PO_4^+]=\frac{\gamma^2K_{P1}}{K_{MgH_2PO_4}[H^+]}[Mg^{2+}][H_3PO_4] \tag{S15}$$

$$[MgOH^+]=\frac{\gamma^2[OH^-]}{K_{MgOH}}[Mg^{2+}] \tag{S16}$$

Eqs. S9-S16 were substituted into Eqs. S6-S8 and solved for *[NH_4^+]*, *[H_3PO_4]*, and *[Mg^{2+}]*, respectively. The results are shown in Eqs. S17-S19.

$$[NH_4^+]=\frac{TotNH_3}{1+\frac{K_N}{[H^+]}} \tag{S17}$$

$$[H_3PO_4]=\frac{TotPO_4}{1+\frac{K_{P1}}{\gamma^2[H^+]}+\frac{K_{P1}K_{P2}}{\gamma^6[H^+]^2}+\frac{K_{P1}K_{P2}K_{P3}}{\gamma^{12}[H^+]^3}+\left\{\frac{K_{P1}K_{P2}K_{P3}}{K_{MgPO_4}[H^+]^3}+\frac{\gamma^2K_{P1}K_{P2}}{K_{MgHPO_4}[H^+]^2}+\frac{\gamma^2K_{P1}}{K_{MgH_2PO_4}[H^+]}\right\}[Mg^{2+}]} \quad \text{(S18)}$$

$$[Mg^{2+}]=\frac{TotMg}{1+\frac{\gamma^2[OH^-]}{K_{MgOH}}+\left\{\frac{K_{P1}K_{P2}K_{P3}}{K_{MgPO_4}[H^+]^3}+\frac{\gamma^2K_{P1}K_{P2}}{K_{MgHPO_4}[H^+]^2}+\frac{\gamma^2K_{P1}}{K_{MgH_2PO_4}[H^+]}\right\}[H_3PO_4]} \quad \text{(S19)}$$

Eq. S17 was solved directly for $[NH_4^+]$. Eqs. S18 and S19 were solved simultaneously for $[H_3PO_4]$, and $[Mg^{2+}]$. The possibility of precipitation of four different minerals was considered. The minerals and their dissolution reactions are listed in Table S2. The supersaturation index (SI), defined in Eq. 1 in the main text, was calculated as a function pH and solution composition. Solubility products were substituted into Eq. 1 and activities were replaced with concentrations, again using Eq. S5. The results are shown in Eqs. S20-S23.

$$SI_{Struvite}=\frac{\gamma^{14}[Mg^{2+}][NH_4^+][PO_4^{3-}]}{K_{sp,Struvite}} \quad \text{(S20)}$$

$$SI_{MgOH2}=\frac{\gamma^6[Mg^{2+}][OH^-]^2}{K_{sp,MgOH_2}} \quad \text{(S21)}$$

$$SI_{MgHPO4}=\frac{\gamma^8[Mg^{2+}][HPO_4^{2-}]}{K_{sp,MgHPO_4}} \quad \text{(S22)}$$

$$SI_{Mg3(PO4)2}=\frac{\gamma^{30}[Mg^{2+}]^3[PO_4^{3-}]^2}{K_{sp,Mg_3(PO_4)_2}} \quad \text{(S23)}$$

As described in the main text, *SI* was determined as a function of pH for each mineral (Figure S4). The mineral with the largest *SI* value in the pH range of interest was considered most likely

to form. Additionally, a target pH was identified for which mineral precipitation was not expected.

Table S1. Aqueous-phase Reactions and Corresponding Equilibrium Constants

Reaction	Equilibrium Constant
$H_3PO_4 \leftrightarrow H^+ + H_2PO_4^-$	[a]$K_{P1}=10^{-2.148}$
$H_2PO_4^- \leftrightarrow H^+ + HPO_4^{2-}$	[a]$K_{P2}=10^{-7.198}$
$HPO_4^{2-} \leftrightarrow H^+ + PO_4^{3-}$	[a]$K_{P3}=10^{-12.375}$
$MgOH^+ \leftrightarrow Mg^{2+} + OH^-$	[b]$K_{MgOH} = 10^{-2.58}$
$MgPO_4^- \leftrightarrow Mg^{2+} + PO_4^{3-}$	[b]$K_{MgPO_4}=10^{-4.80}$
$MgHPO_4 \leftrightarrow Mg^{2+} + HPO_4^{2-}$	[b]$K_{MgHPO_4}=10^{-2.91}$
$MgH_2PO_4^+ \leftrightarrow Mg^{2+} + H_2PO_4^-$	[b]$K_{MgH_2PO_4}=10^{-0.45}$
$NH_4^+ \leftrightarrow H^+ + NH_3$	[a]$K_N=10^{-9.244}$

[a]From (Benjamin 2015).
[b]From (Doyle and Parsons 2002).

Table S2. Precipitation Reactions and Corresponding Solubility Products

Reaction	Solubility Product[a]
$MgNH_4PO_{4(s)} \leftrightarrow Mg^{2+} + NH_4^+ + PO_4^{3-}$	$K_{sp,Struvite}=10^{-13.26}$
$MgOH_{2(s)} \leftrightarrow Mg^{2+} + 2OH^-$	$K_{sp,MgOH_2}=10^{-2.58}$
$MgHPO_{4(s)} \leftrightarrow Mg^{2+} + HPO_4^{2-}$	$K_{sp,MgHPO_4}=10^{-2.91}$
$Mg_3(PO_4)_{2(s)} \leftrightarrow 3Mg^{2+} + 2PO_4^{3-}$	$K_{sp,Mg_3(PO_4)_2}=10^{-4.80}$

[a]Data from Ohlinger et al. (1998).

Titration Modeling Methods

An equilibrium model was developed to predict the steady state behavior of centrate upon the addition of a strong acid, as described in the main text. The activity was substituted into equilibrium constants to develop equilibrium relationships in terms of concentration instead of activity (Eqs. S24 through S27).

$$k_c[CO_2]=k_{-c}[H_2CO_3] \quad \text{(S24)}$$

$$K_{C1}=\frac{\gamma^2[HCO_3^-][H^+]}{[H_2CO_3]} \quad \text{(S25)}$$

$$K_{C2}=\frac{\gamma^4[CO_3^{2-}][H^+]}{[HCO_3^-]} \quad \text{(S26)}$$

$$K_W=\gamma^2[H^+][OH^-] \quad \text{(S27)}$$

For the solution to maintain electroneutrality, a charge balance must be satisfied at each point in the titration. This is represented by Eq. S28.

$$[H^+]+\sum c_B=[HCO_3^-]+2[CO_3^{2-}]+[OH^-]+\sum c_A+[Cl^-]_{Added} \quad \text{(S28)}$$

Σc_B represents the summed concentrations of all strong base cations, Σc_A represents all strong acid anions in the original solution, and $[Cl^-]_{Added}$ is the molar concentration of strong acid added to reach respective points on the titration curve. The titration curve is represented in terms of pH vs. $[Cl^-]_{Added}$. Note that the composition of the centrate is unknown, so Σc_B, Σc_A, and the total amount of carbonate are not known initially. The total amount of carbonate may be expressed as a mass balances on carbonate, shown in Eq. S29.

$$TotCO_3=[CO_2]+[H_2CO_3]+[HCO_3^-]+[CO_3^{2-}] \quad \text{(S29)}$$

TotCO₃ represents the total concentration of carbonate in the solution in mol/L. It is assumed to be constant throughout the titration and is treated as a fitted parameter. The compounds appearing in Eq. S29 were put in terms of *[H₂CO₃]* using the Eqs. S24 through S27. The results are summarized below (Eqs. S30 through S32).

$$[CO_2]=\frac{k_{-c}}{k_c}[H_2CO_3] \tag{S30}$$

$$[HCO_3^-]=\frac{K_{C1}}{\gamma^2[H^+]}[H_2CO_3] \tag{S31}$$

$$[CO_3^{2-}]=\frac{K_{C1}K_{C2}}{\gamma^6[H^+]^2}[H_2CO_3] \tag{S32}$$

Eqs. S30 through S32 were substituted into Eq. S29, which was solved for *[H₂CO₃]* (Eq. S33).

$$[H_2CO_3]=\frac{TotCO_3}{\frac{k_{-c}}{k_c}+1+\frac{K_{C1}}{\gamma^2[H^+]}+\frac{K_{C1}K_{C2}}{\gamma^6[H^+]^2}} \tag{S33}$$

Eq. S33 was substituted in Eqs. S31 and S32, which were substituted into Eq. S28. Eq. S27 was solved for *[OH⁻]* and substituted into Eq. S28 as well. The resulting equation was rearranged to Eq. S34 to express $[Cl^-]_{Added}$ as a function of *[H⁺]*, thermodynamic constants, bulk properties of the solution (*TotCO₃* and Σc_B - Σc_A).

$$[Cl^-]_{Added}=[H^+]+\sum c_B-\sum c_A- \tag{S34}$$

$$\left(\frac{K_{C1}}{\gamma^2[H^+]}+2\frac{K_{C1}K_{C2}}{\gamma^6[H^+]^2}\right)\left(\frac{TotCO_3}{\frac{k_{-c}}{k_c}+1+\frac{K_{C1}}{\gamma^2[H^+]}+\frac{K_{C1}K_{C2}}{\gamma^6[H^+]^2}}\right)-\frac{K_W}{\gamma^2[H^+]}$$

γ, which is a function of ionic strength, is given by Eq. S4. The ionic strength at each point in the titration curve is represented by Eq. S35.

$$I=0.5\left(\sum c_B+\sum c_A+[HCO_3^-]+4[CO_3^{2-}]+[H^+]+[OH^-]+[Cl^-]_{Added}\right) \quad (S35)$$

As before, $[HCO_3^-]$ and $[CO_3^{2-}]$ are given by Eqs. S31, S32, and S33, and $[OH^-]$ is given by Eq. S27. Eq. S35 was substituted into Eq. S4. For each point in the titration curve, Eqs. S4 and S34 were solved simultaneously for $[Cl^-]_{Added}$ and γ. Note that, in this model, the dependent and independent variables (pH and $[Cl^-]_{Added}$) are switched for mathematical simplicity. Values of $TotCO_3$ and $\Sigma c_B - \Sigma c_A$ were selected to best fit the titration curve.

Note that the ionic strength (Eq. S35) is difficult to calculate; $\Sigma c_B - \Sigma c_A$ is selected, but $\Sigma c_B + \Sigma c_A$ is not known. However, the conductivity measured prior to the titration may be used to calculate the initial ionic strength, as in Eq. S36 (Snoeyink and Jenkins 1980).

$$I=0.0160\text{Conductivity} \quad (S36)$$

Conductivity is given in mS/cm and I is given in M. This value was calculated and substituted into Eq. S35. Eq. S35 was solved for $\Sigma c_B + \Sigma c_A$. $\Sigma c_B + \Sigma c_A$ was assumed to be constant throughout the titration, and was used in Eq. S35 to calculate activities and concentrations in the titration model.

Elevated Pressure CO_2 Injection Equilibrium Model

An equilibrium model was developed to predict the steady state pH upon the injection of CO_2 at elevated pressures, as described in the methods section in the main manuscript. A charge balance is given by Eq. S37.

$$[H^+]+\sum c_B=[HCO_3^-]+2[CO_3^{2-}]+[OH^-]+\sum c_A \quad (S37)$$

As in the titration curve model, Σc_B represents the summed concentrations of all strong base cations, Σc_A represents all strong acid anions in the original solution. The value of Σc_B - Σc_A was determined by fitting the titration curve and may be used here to predict the steady state pH under CO_2 injection. At equilibrium, the aqueous carbon dioxide concentration may be calculated as a function of pressure using Henry's Law as shown in Eq. S38.

$$[CO_2]=\frac{P_{CO_2}}{H_c} \tag{S38}$$

H_c is Henry's Law constant for carbon dioxide was calculated as a function of temperature (in K). It is given by Eq. S39 in the units of atm/M (Sander 2017).

$$H_C=\frac{1}{0.034e^{2400\left[\frac{1}{T}-\frac{1}{298.15}\right]}} \tag{S39}$$

Eq. S38 may be substituted into Eq. S30 and solved for $[H_2CO_3]$, yielding Eq. S40.

$$[H_2CO_3]=\frac{k_c}{k_{-c}}\frac{P_{CO_2}}{H_c} \tag{S40}$$

Eq. S40 was substituted into Eqs. S31 and S32 to yield Eqs. S41 and S42.

$$[HCO_3^-]=\frac{K_{C1}}{\gamma^2[H^+]}\frac{k_c}{k_{-c}}\frac{P_{CO_2}}{H_c} \tag{S41}$$

$$[CO_3^{2-}]=\frac{K_{C1}K_{C2}}{\gamma^6[H^+]^2}\frac{k_c}{k_{-c}}\frac{P_{CO_2}}{H_c} \tag{S42}$$

Eqs. S41 and S42 were substituted into Eq. S37 to yield Eq. S43.

$$[H^+]+\sum c_B=\left(\frac{K_{C1}}{\gamma^2[H^+]}+2\frac{K_{C1}K_{C2}}{\gamma^6[H^+]^2}\right)\left(\frac{k_c}{k_{-c}}\frac{P_{CO_2}}{H_c}\right)+\frac{K_W}{\gamma^2[H^+]}+\sum c_A \tag{S43}$$

As in the titration curve model, Eqs. S43 and S4 were solved simultaneously to determine the steady state pH as a function of the applied pressure of CO_2.

Steady State Model for CO_2 Injection in a Continuous Reactor

A model was developed to predict the steady state pH upon the injection of carbon dioxide into centrate in a continuous stirred tank reactor (CSTR). Mass balances on CO_2, H_2CO_3, HCO_3^-, and CO_3^{2-} give Eqs. S44 through S47 below. Note that all are equal to zero because the reactor is at steady state.

$$\frac{d[CO_2]}{dt}=\frac{Q_l}{V}\left([CO_2]_{in}-[CO_2]\right)-k_c\{CO_2\}+k_{-c}\{H_2CO_3\}=0 \tag{S44}$$

$$\frac{d[H_2CO_3]}{dt}=\frac{Q_l}{V}\left([H_2CO_3]_{in}-[H_2CO_3]\right)+k_c\{CO_2\}-k_{-c}\{H_2CO_3\}- k_1\{H_2CO_3\}+k_{-1}\{HCO_3^-\}\{H^+\}=0 \tag{S45}$$

$$\frac{d[HCO_3^-]}{dt}=\frac{Q_l}{V}\left([HCO_3^-]_{in}-[HCO_3^-]\right)+k_1\{H_2CO_3\}-k_{-1}\{HCO_3^-\}\{H^+\}- k_2\{HCO_3^-\}+k_{-2}\{CO_3^{2-}\}\{[H^+]\}=0 \tag{S46}$$

$$\frac{d[CO_3^{2-}]}{dt}=\frac{Q_l}{V}\left([CO_3^{2-}]_{in}-[CO_3^{2-}]\right)+k_2\{HCO_3^-\}+k_{-2}\{CO_3^{2-}\}\{H^+\}=0 \tag{S47}$$

It was assumed that the carbon dioxide concentration may be calculated from Henry's Law. Eqs. S45 to S47 were added and *[HCO_3^-]* and *[CO_3^{2-}]* were substituted using Eqs. S31 and S32 to yield Eq. S48.

$$0=\frac{Q_l}{V}\left\{[H_2CO_3]_{in}+\frac{K_{c1}}{\gamma^2[H^+]_{in}}[H_2CO_3]_{in}+\frac{K_{c2}K_{c1}}{\gamma^6[H^+]_{in}^2}[H_2CO_3]_{in}-[H_2CO_3]-\frac{K_{C1}}{\gamma^2[H^+]}[H_2CO_3]-\frac{K_{C1}K_{C2}}{\gamma^6[H^+]^2}[H_2CO_3]\right\}+k_c[CO_2]-k_{-c}[H_2CO_3] \tag{S48}$$

A charge balance is given in Eq. S49. Eqs. S4, S44, S48, and S49 were solved simultaneously to calculate the steady state pH at the outlet of the CSTR.

$$0=[H^+]+\sum c_B-\sum c_A-\left(\frac{K_{C1}}{\gamma^2[H^+]}+2\frac{K_{C1}K_{C2}}{\gamma^6[H^+]^2}\right)[H_2CO_3]-\frac{K_W}{\gamma^2[H^+]} \quad \text{(S49)}$$

Supplementary Figures: Pilot Design

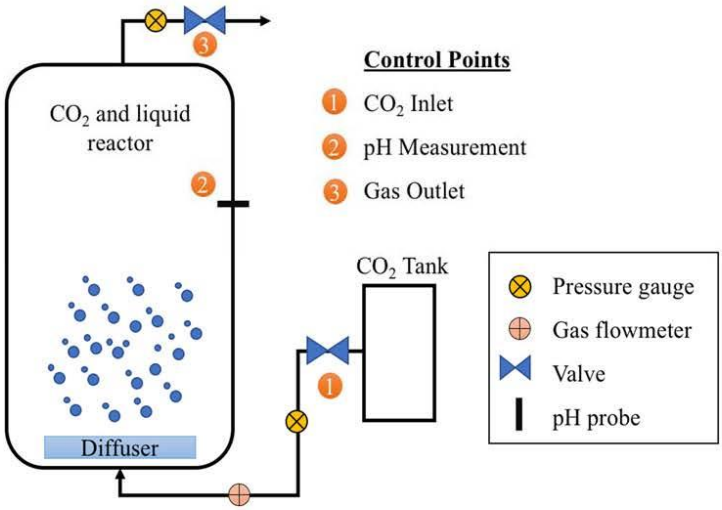

Fig. S1. Bench scale CO_2 injection reactor schematic.

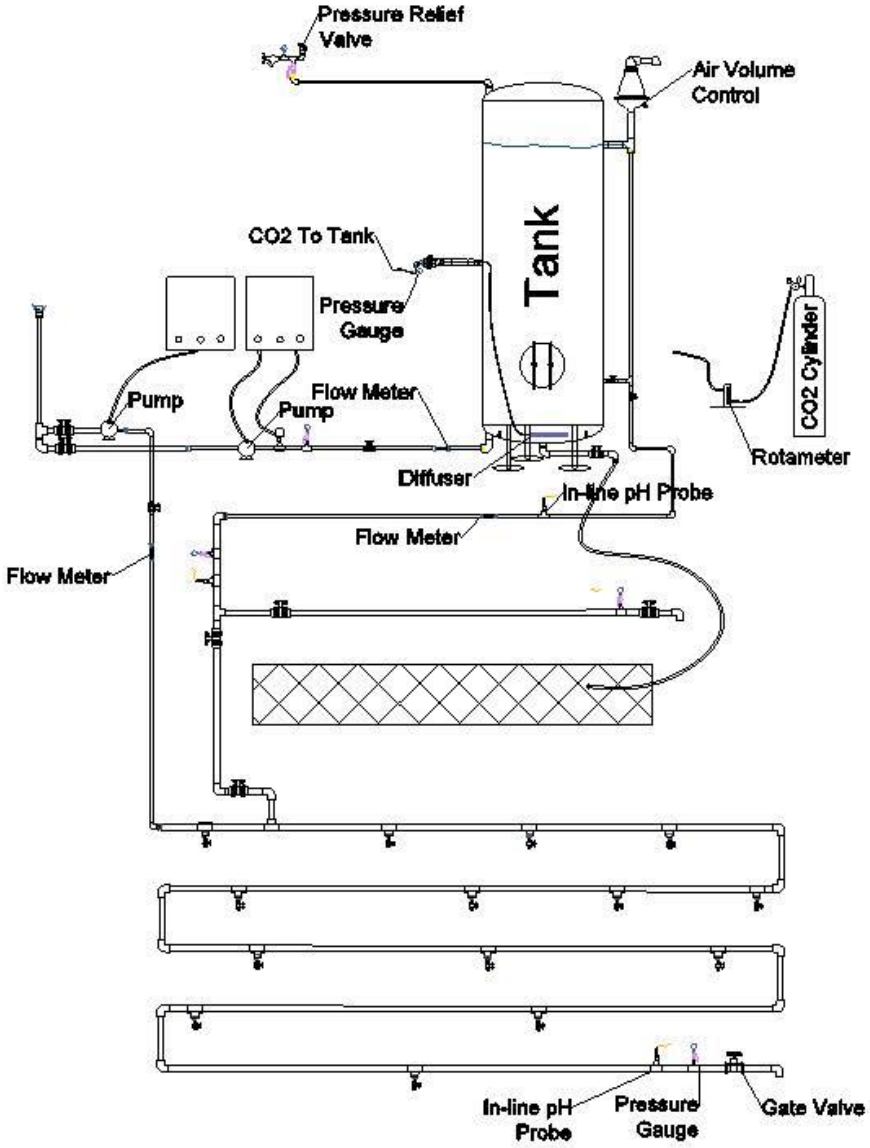

Fig. S2. Detailed schematic of pilot plant.

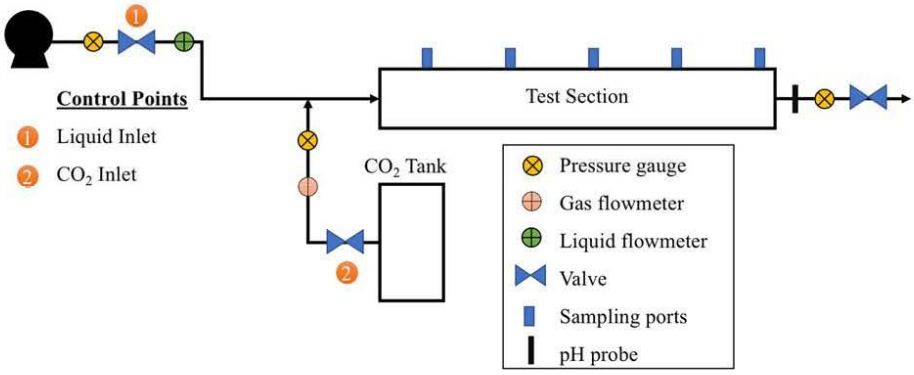

Fig. S3. In-line CO_2 injection pilot system schematic.

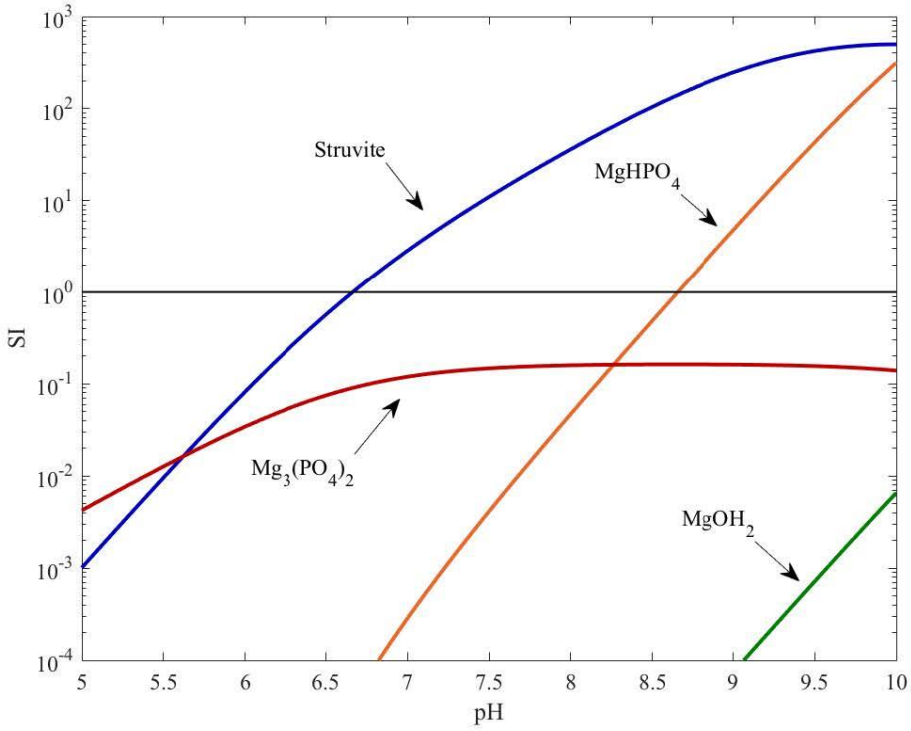

Fig. S4. Calculated supersaturation index (SI) as a function of pH for candidate minerals in Tucson centrate (*TotMg* = 0.926 mM, $TotNH_3$ = 89.9 mM, $TotPO_4$ = 3.6 mM).

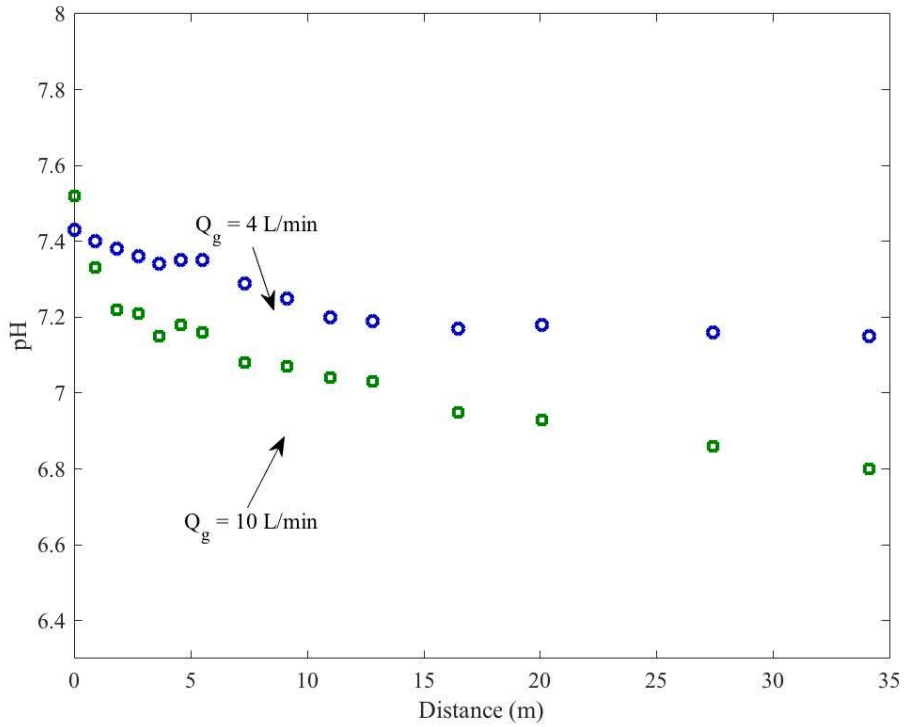

Fig. S5. Centrate pH as a function of distance in the test section (Fig. S3) following the injection of gas-phase CO_2 directly into the centrate line.

Design Curves for Various Target pHs

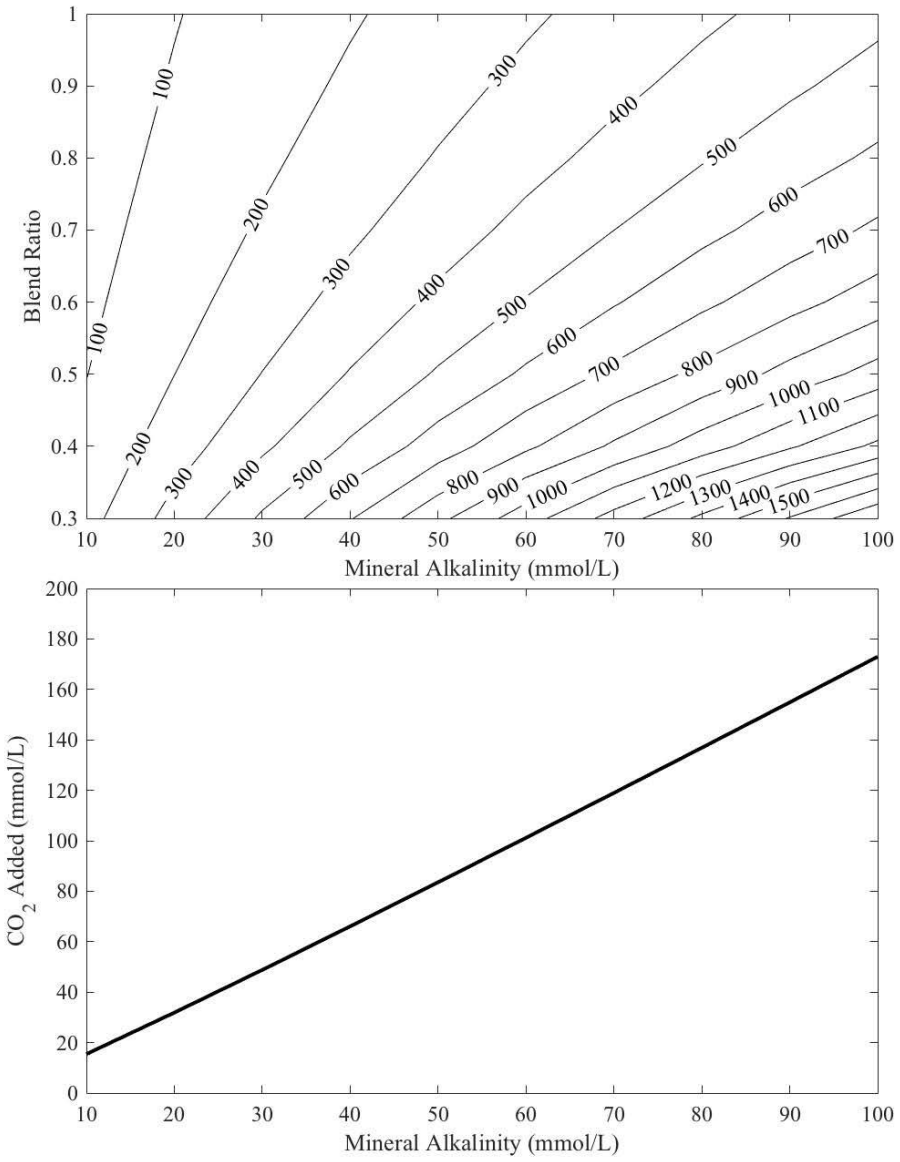

Fig. S6. Design curve for target pH of 6.0. Contours show P_{CO2} (kPa).

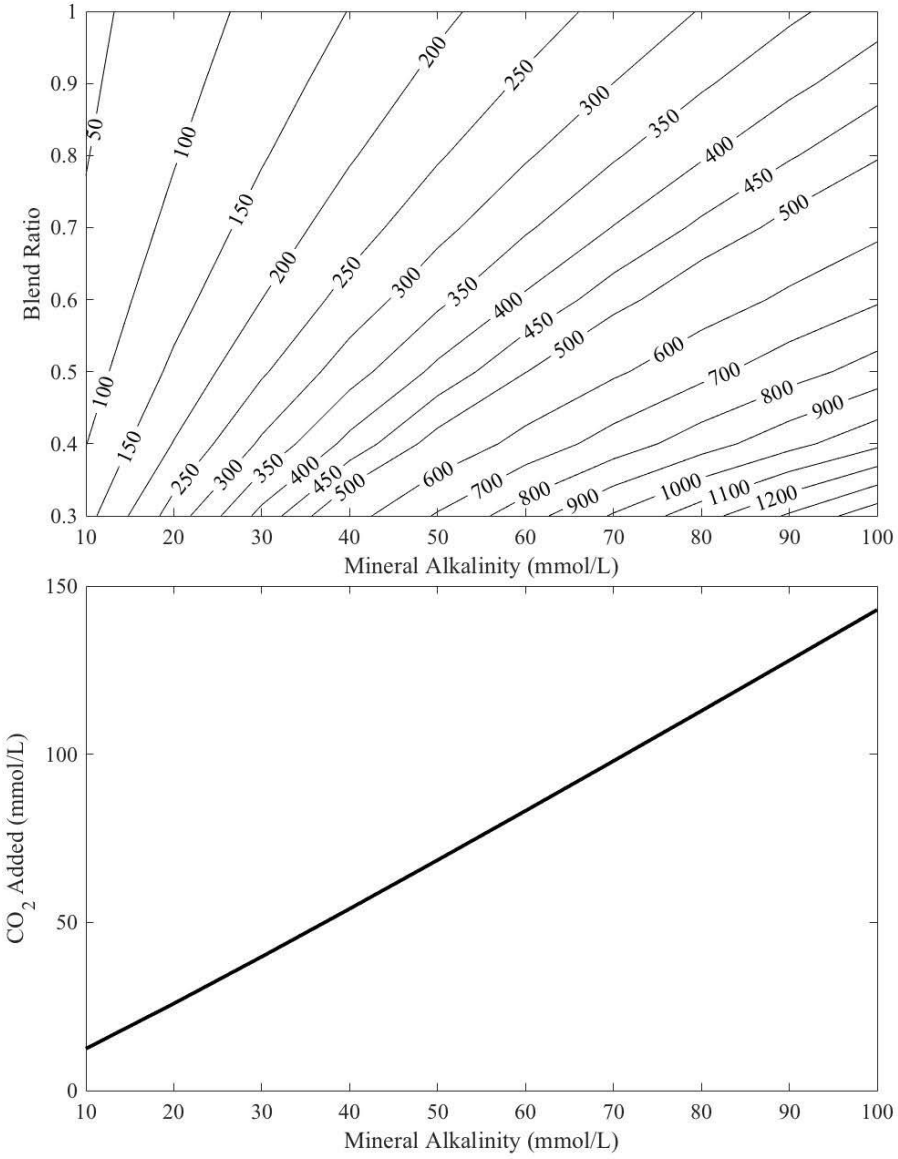

Fig. S7. Design curve for target pH of 6.1. Contours show P_{CO2} (kPa).

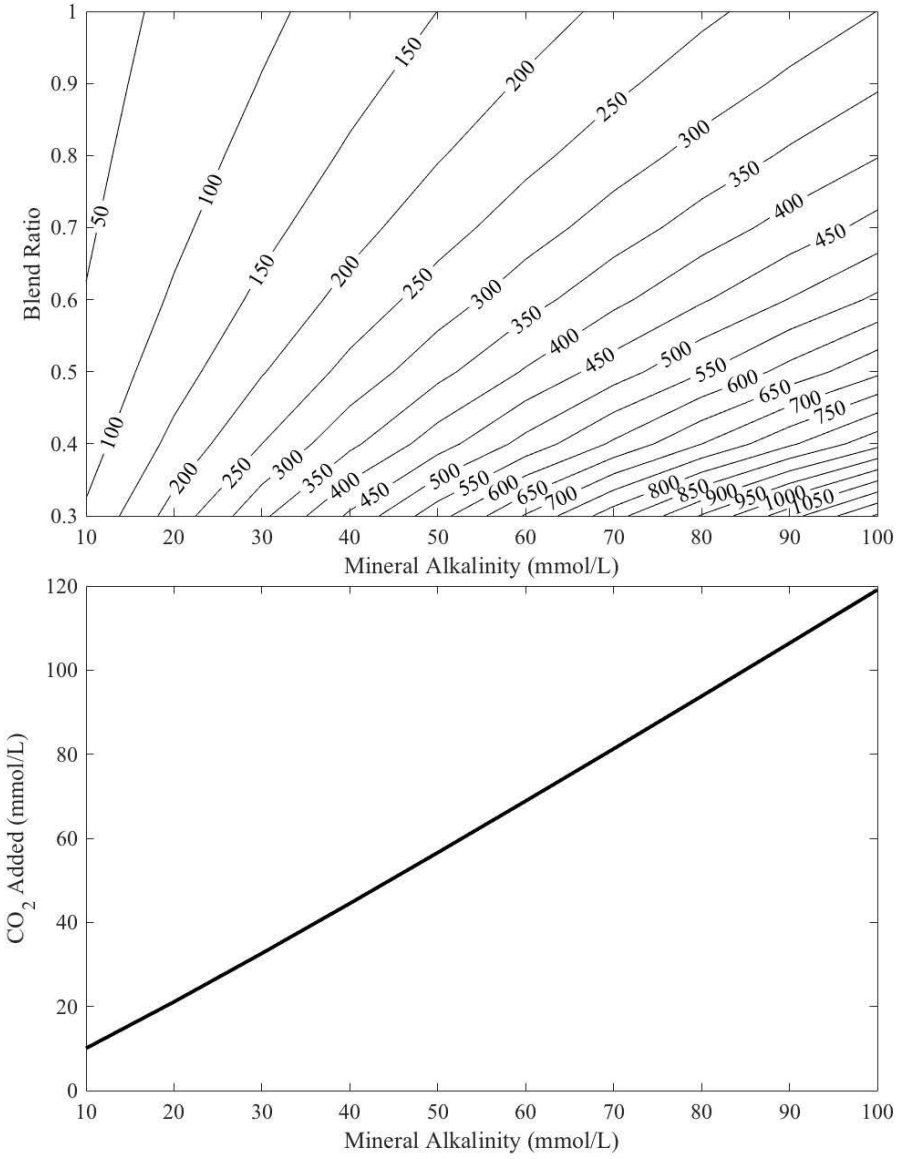

Fig. S8. Design curve for target pH of 6.2. Contours show P_{CO2} (kPa).

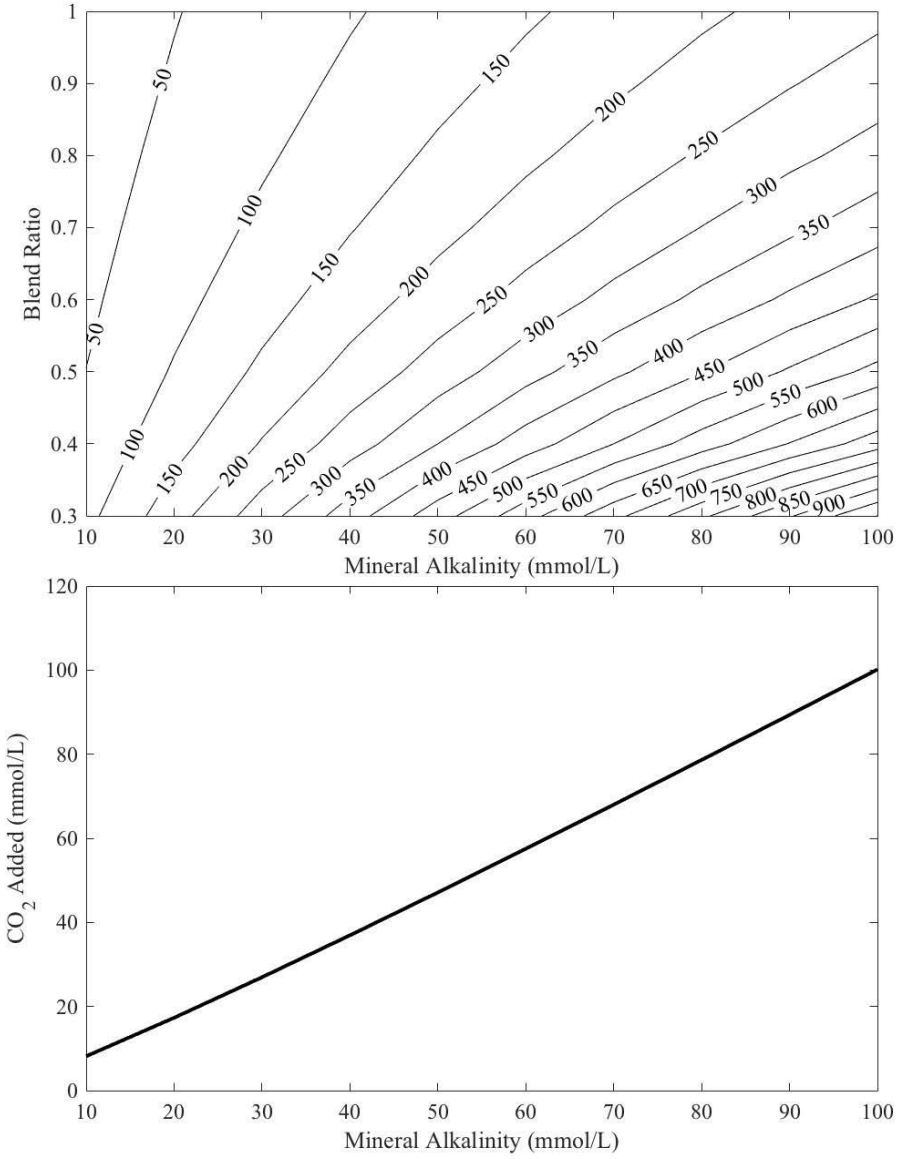

Fig. S9. Design curve for target pH of 6.3. Contours show P_{CO2} (kPa).

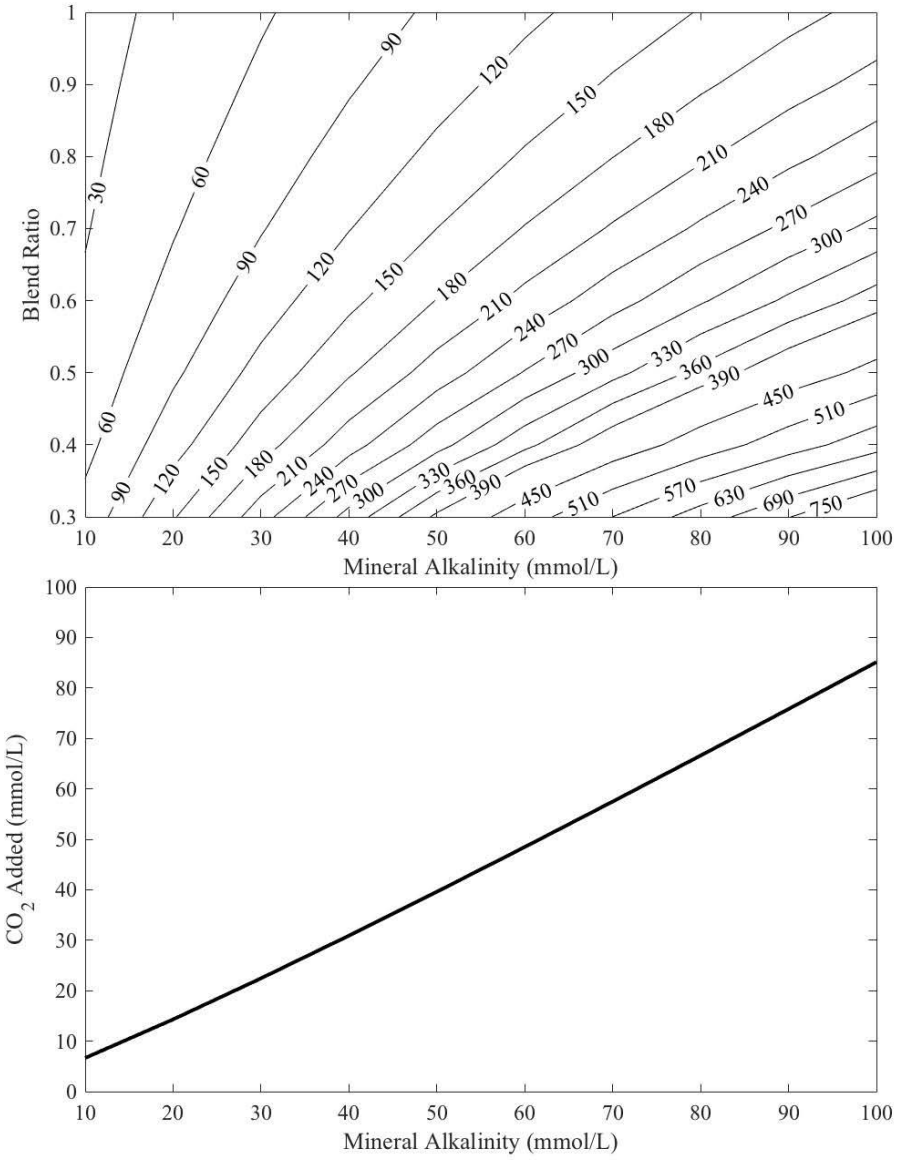

Fig. S10. Design curve for target pH of 6.4. Contours show P_{CO2} (kPa).

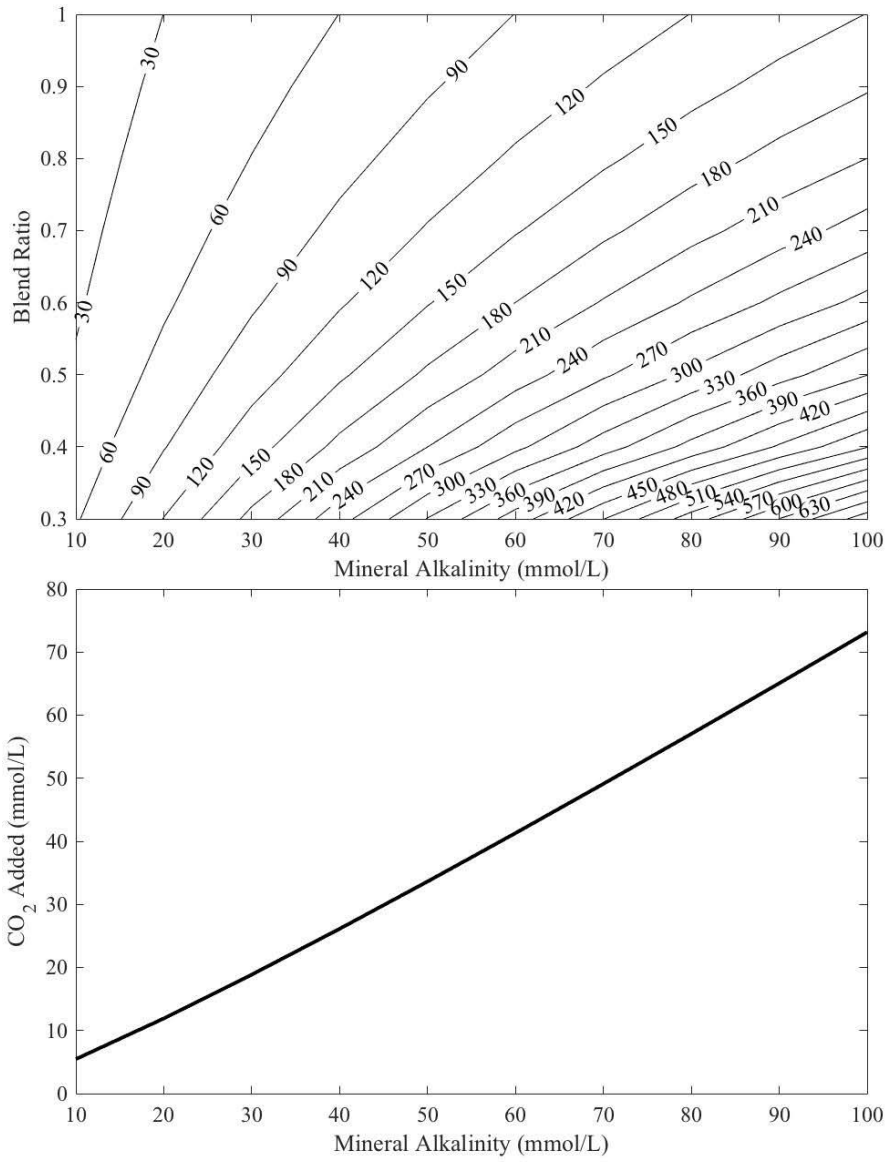

Fig. S11. Design curve for target pH of 6.5. Contours show P_{CO2} (kPa).

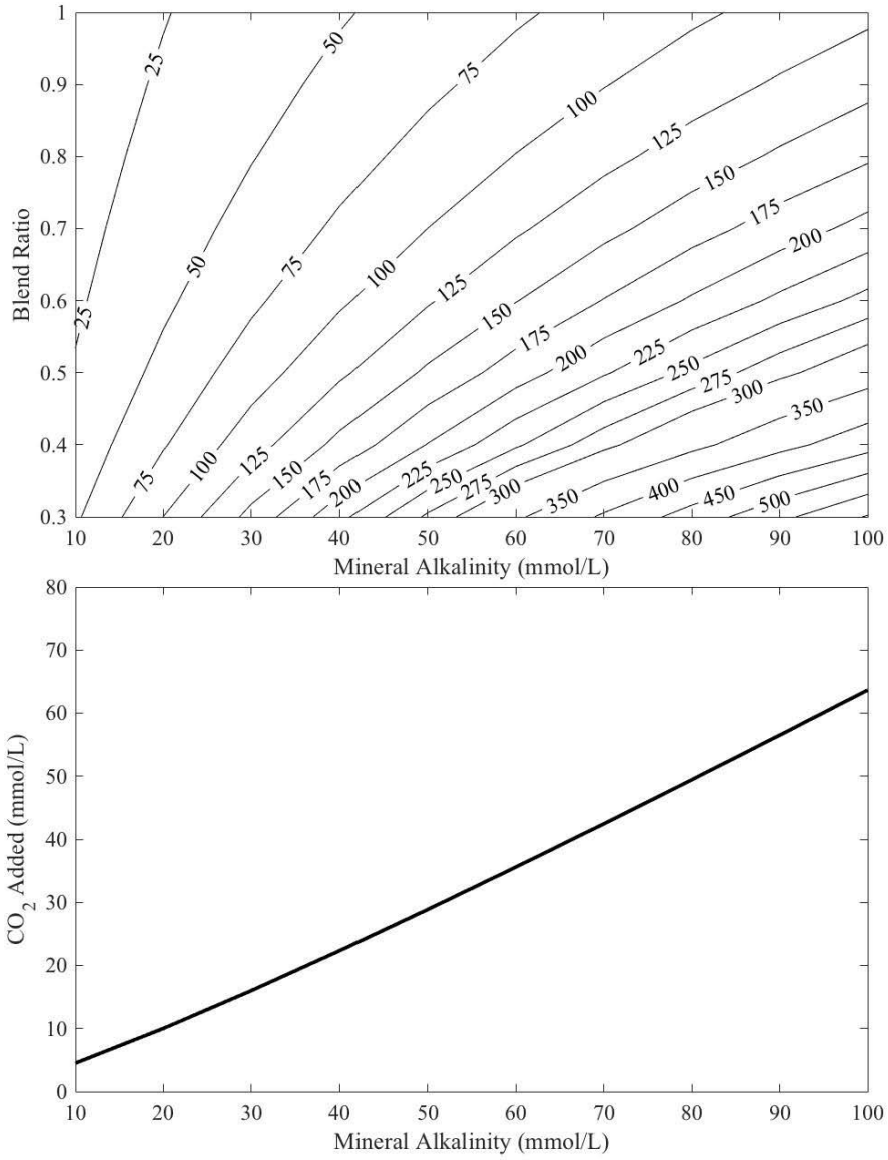

Fig. S12. Design curve for target pH of 6.6. Contours show P_{CO2} *(kPa)*.

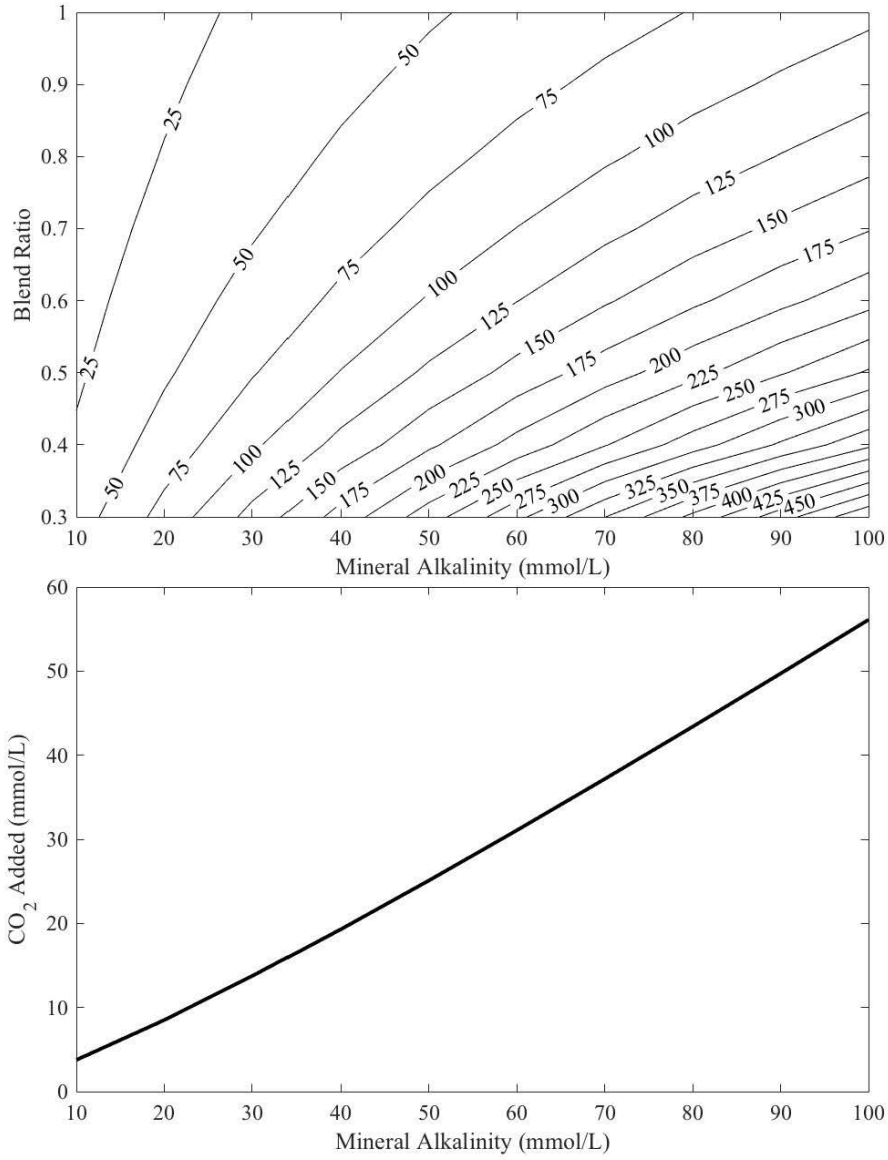

Fig. S13. Design curve for target pH of 6.7. Contours show P_{CO2} (kPa).

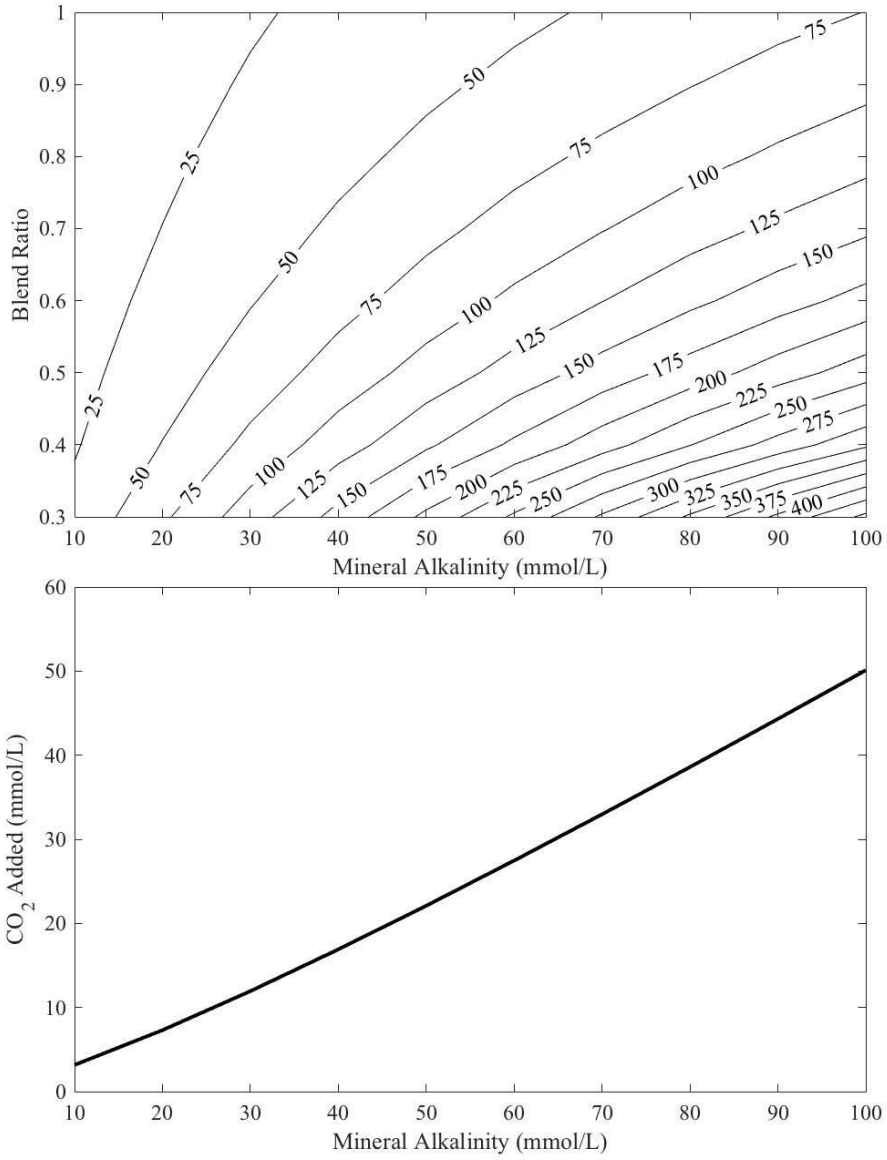

Fig. S14. Design curve for target pH of 6.8. Contours show P_{CO2} (kPa).

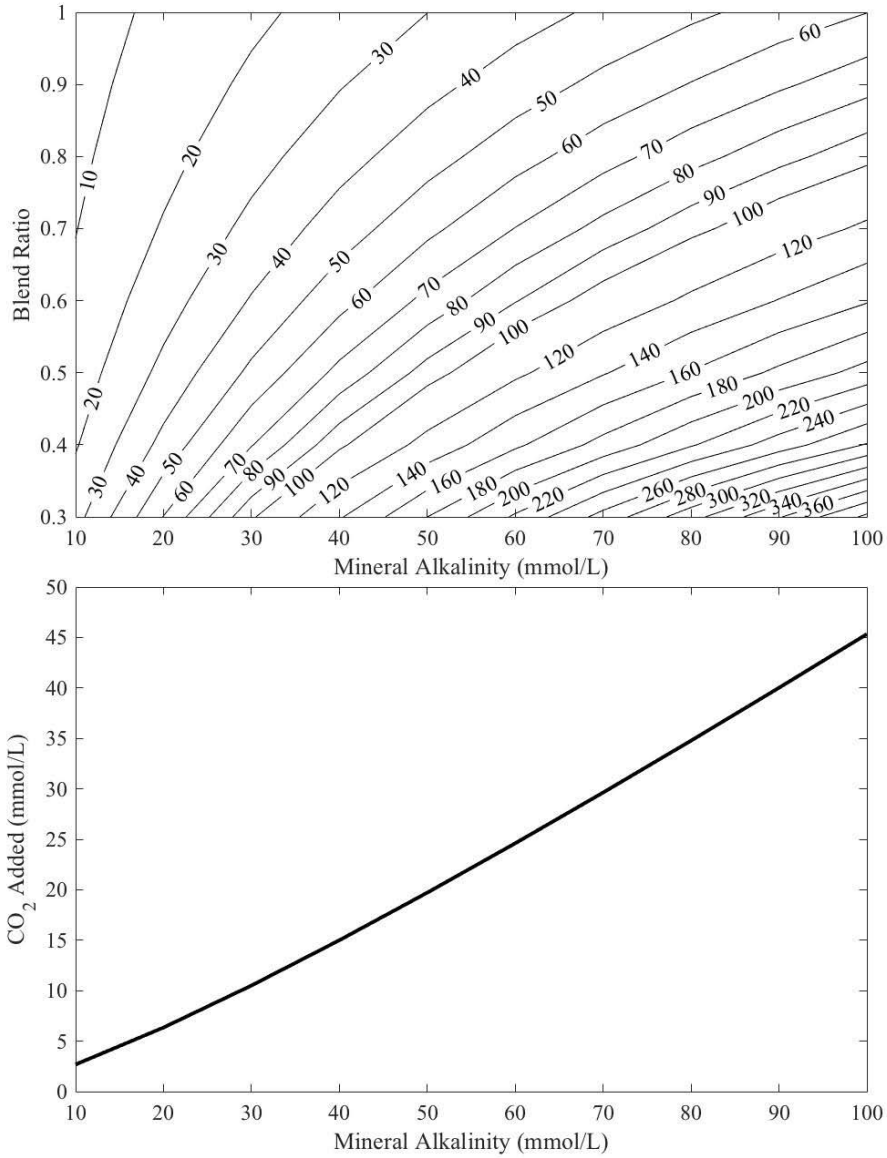

Fig. S15. Design curve for target pH of 6.9. Contours show P_{CO2} (kPa).

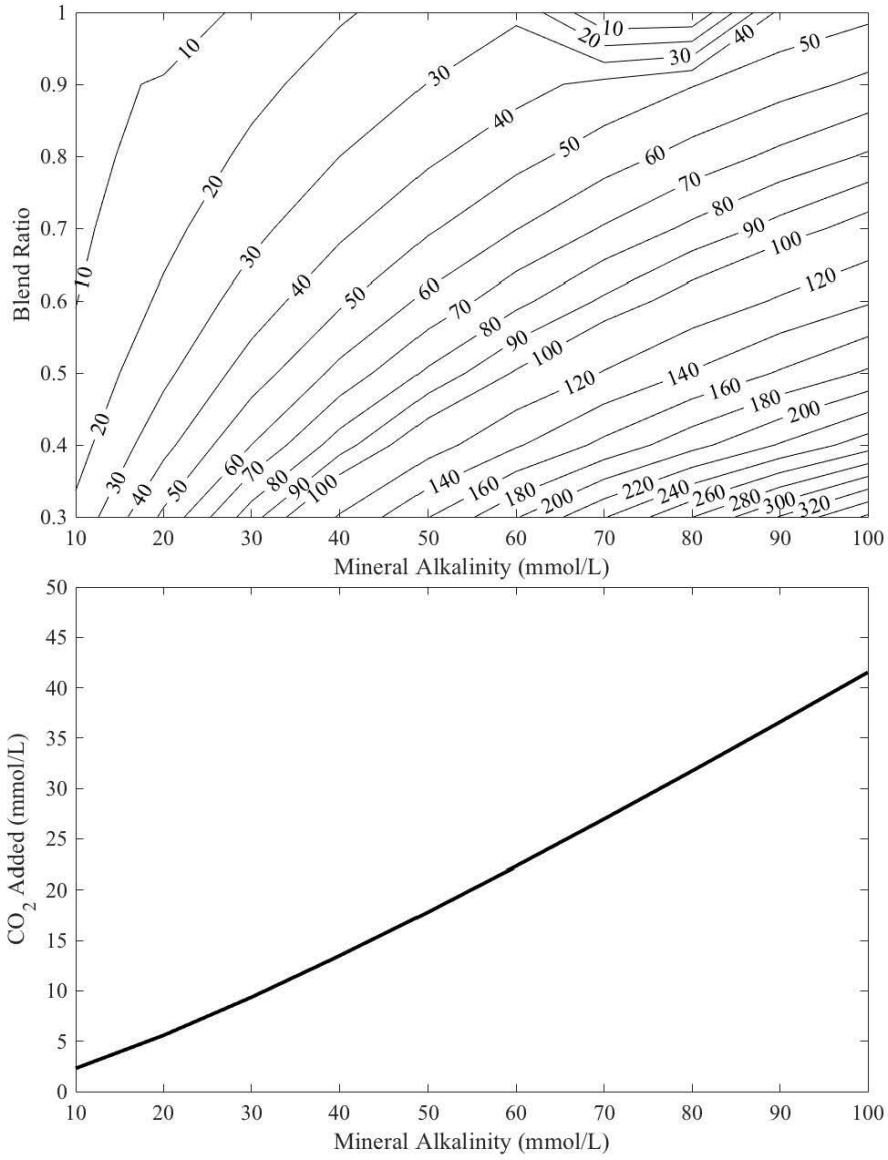

Fig. S16. Design curve for target pH of 7.0. Contours show P_{CO2} (kPa).

Notation

The following symbols are used in this paper:

$[A]$ = Concentration of any compound A;

$\{A\}$ = Activity of any compound A;

I = Ionic strength;

H_c = Henry's Law Constant;

K_{C1} = First acid dissociation constant for H_2CO_3;

K_{C2} = Second acid dissociation constant for H_2CO_3;

$K_{MgH2PO4}$ = Equilibrium constant for the reaction $MgH_2PO_4^+ \leftrightarrow Mg^{2+} + H_2PO_4^-$;

K_{MgHPO4} = Equilibrium constant for the reaction $MgHPO_4 \leftrightarrow Mg^{2+} + HPO_4^{2-}$;

K_{MgOH} = Equilibrium constant for the reaction $MgOH^+ \leftrightarrow Mg^{2+} + OH^-$;

K_{MgPO4} = Equilibrium constant for the reaction $MgPO_4^- \leftrightarrow Mg^{2+} + PO_4^{3-}$;

K_N = Acid dissociation constant for NH_4^+;

K_{P1} = First acid dissociation constant for H_3PO_4;

K_{P2} = Second acid dissociation constant for H_3PO_4;

K_{P3} = Third acid dissociation constant for H_3PO_4;

$K_{sp,Mg3(PO4)2}$ = Solubility product for $Mg_3(PO_4)_2$;

$K_{sp,MgHPO4}$ = Solubility product for $MgHPO_4$;

$K_{sp,MgOH2}$ = Solubility product for $MgOH_2$;

$K_{sp,Struvite}$ = Solubility product for struvite;

K_W = Acid dissociation constant for water;

k_{-c} = Reaction rate constant for $H_2CO_3 \leftrightarrow CO_2 + H_2O$;

k_c = Reaction rate constant for $CO_2 + H_2O \leftrightarrow H_2CO_3$;

REFERENCES

Alexander, B., Park, R.J., Jacob, D.J., Gong, S., 2009. Transition metal-catalyzed oxidation of atmospheric sulfur: Global implications for the sulfur budget. Journal of Geophysical Research: Atmospheres 114.

Baghurst, P.A., McMichael, A.J., Wigg, N.R., Vimpani, G.V., Robertson, E.F., Roberts, R.J., Tong, S.-L., 1992. Environmental exposure to lead and children's intelligence at the age of seven years: the Port Pirie Cohort Study. New Engl J Med 327, 1279-1284.

Blanco, A., De Tomasi, F., Filippo, E., Manno, D., Perrone, M.R., Serra, A., Tafuro, A.M., Tepore, A., 2003. Characterization of African dust over southern Italy. Atmos Chem Phys 3, 2147-2159.

Bobbink, R., Hornung, M., Roelofs, J.G., 1998. The effects of air-borne nitrogen pollutants on species diversity in natural and semi-natural European vegetation. Journal of ecology 86, 717-738.

Boltz, D. F., & Howell, J. A. (1978). Colorimetric Determination of Nonmetals, Second Edition. New York: John Wiley & Sons Inc.

Buchanan, J. R., Mote, C. R., & Robinson, R. B. (1994). Struvite Control by Chemical Treatment. Transaction of the Americal Society of Agricultural Engineers, 37(4), 1301-1308.

Carballa, M.; Fink, G.; Omil, F.; Lema, J.M.; Ternes, T. Determination of the SolidWater Distribution Coefficient (KD) for Pharmaceuticals, Estrogens and Musk Fragrances in Digested Sludge. Water Res. 2008, 2, 287.

Chen, S., Xu, L., Zhang, Y., Chen, B., Wang, X., Zhang, X., Zheng, M., Chen, J., Wang, W., Sun, Y., 2017. Direct observations of organic aerosols in common wintertime hazes in

North China: insights into direct emissions from Chinese residential stoves. Atmos Chem Phys 17, 1259-1270.

Chen, W., Westerhoff, P., Leenheer, J.A., Booksh, K., 2003. Fluorescence excitation− emission matrix regional integration to quantify spectra for dissolved organic matter. Environ Sci Technol 37, 5701-5710.

Conner, T.L., Norris, G.A., Landis, M.S., Williams, R.W., 2001. Individual particle analysis of indoor, outdoor, and community samples from the 1998 Baltimore particulate matter study. Atmos Environ 35, 3935-3946.

Csavina, J., Landázuri, A., Wonaschütz, A., Rine, K., Rheinheimer, P., Barbaris, B., Conant, W., Sáez, A.E., Betterton, E.A., 2011. Metal and metalloid contaminants in atmospheric aerosols from mining operations. Water, Air, & Soil Pollution 221, 145-157.

Dadashazar, H., Ma, L., Sorooshian, A., 2019. Sources of pollution and interrelationships between aerosol and precipitation chemistry at a central California site. Sci Total Environ 651, Part 2, 2019, 1776-1787. https://doi.org/10.1016/j.scitotenv.2018.10.086

Dong, B., Kahl, A., Cheng, L., Vo, H., Ruehl, S., Zhang, T., Snyder, S., Sáez, A.E., Quanrud, D., Arnold, R.G., 2015. Fate of trace organics in a wastewater effluent dependent stream. Sci Total Environ 518, 479-490.

Dorfman, L.M.; Adams, G.E. Reactivity of the Hydroxyl Radical in Aqueous Solutions, National Standard Reference System. Monograph NSRDS-NBS 46. National Bureau of Standards, Washington DC, 1973.

Doyle, J. D., & Parsons, S. A. (2002). Struvite formation, control and recovery. *Water Research, 36*, 3925-3940.

Doyle, J. D., Oldring, K., Churchley, J., Price, C., & Parsons, S. A. (2003). Chemical Control of Struvite Precipitation. Journal of Environmental Engineering, 129, 419-426.

Driscoll, C.T., Whitall, D., Aber, J., Boyer, E., Castro, M., Cronan, C., Goodale, C.L., Groffman, P., Hopkinson, C., Lambert, K., 2003. Nitrogen pollution in the northeastern United States: sources, effects, and management options. BioScience 53, 357-374.

Fassi-Fihri, A., Suhre, K., Rosset, R., 1997. Internal and external mixing in atmospheric aerosols by coagulation: Impact on the optical and hygroscopic properties of the sulphate-soot system. Atmos Environ 31, 1393-1402.

Font, A., de Hoogh, K., Leal-Sanchez, M., Ashworth, D.C., Brown, R.J.C., Hansell, A.L., Fuller, G.W., 2015. Using metal ratios to detect emissions from municipal waste incinerators in ambient air pollution data. Atmos Environ 113, 177-186.

Hu, T., Cao, J., Shen, Z., Wang, G., Lee, S., Ho, K., 2012. Size differentiation of individual atmospheric aerosol during winter in Xi'an, China. Aerosol and Air Quality Research 12, 951-960.

Imai, A., Fukushima, T., Matsushige, K., Kim, Y.-H., Choi, K., 2002. Characterization of dissolved organic matter in effluents from wastewater treatment plants. Water research 36, 859-870.

IPCC (2013): Stocker, T., Qin, D., Plattner, G., Tignor, M., Allen, S., Boschung, J., Nauels, A., Xia, Y., Bex, V., Midgley, P., 2013. IPCC, 2013: summary for policymakers in climate change 2013: the physical science basis, contribution of working group I to the fifth assessment report of the intergovernmental panel on climate change. Cambridge University Press, Cambridge.

Khanal, S.K.; Xie, B.; Thompson, M.L.; Sung, S.; Ong, S.K.; Van Leeuwen J.H. Fate, Transport and Biodegradation of Natural Estrogens in the Environment and Engineered Systems. Environ. Sci. Technol. 2006, 40, 6537.

Kochevar, I.E., Redmond, R.W., 2000. [2] Photosensitized production of singlet oxygen, Methods in enzymology. Elsevier, pp. 20-28.

Kristell S. Le Corre, E. V.-J. (2005). Impact of calcium on struvite crystal size, shape and purity. Journal of Crystal Growth.

Lee, E., Glover, C.M., Rosario-Ortiz, F.L., 2013. Photochemical formation of hydroxyl radical from effluent organic matter: role of composition. Environ Sci Technol 47, 12073-12080.

Li, N., Xia, T., Nel, A.E., 2008. The role of oxidative stress in ambient particulate matter-induced lung diseases and its implications in the toxicity of engineered nanoparticles. Free Radical Bio Med 44, 1689-1699.

Li, W., Wang, T., Zhou, S., Lee, S., Huang, Y., Gao, Y., Wang, W., 2013. Microscopic observation of metal-containing particles from Chinese continental outflow observed from a non-industrial site. Environ Sci Technol 47, 9124-9131.

Li, Z., Zhao, S., Edwards, R., Wang, W., Zhou, P., 2011. Characteristics of individual aerosol particles over Ürümqi Glacier No. 1 in eastern Tianshan, central Asia, China. Atmospheric research 99, 57-66.

MacDonald, A.B., Dadashazar, H., Chuang, P.Y., Crosbie, E., Wang, H., Wang, Z., Jonsson, H.H., Flagan, R.C., Seinfeld, J.H., Sorooshian, A., 2018. Characteristic vertical profiles of cloud water composition in marine stratocumulus clouds and relationships with precipitation. Journal of Geophysical Research: Atmospheres 123, 3704-3723.

MacDonald, B.C., Lvin, S.J., Patterson, H., 1997. Correction of fluorescence inner filter effects and the partitioning of pyrene to dissolved organic carbon. Anal Chim Acta 338, 155-162.

Mateos, A.C., Amarillo, A.C., Carreras, H.A., Gonzalez, C.M., 2018. Land use and air quality in urban environments: Human health risk assessment due to inhalation of airborne particles. Environ Res 161, 370-380.

Mayer, B. K., Baker, L. A., Boyer, T. H., Drechsel, P., Gifford, M., Hanjra, M. A., . . . Rittmann, B. E. (2016). Total Value of Phosphorus Recovery. Environmental Science & Technology, 50, 6606-6620.

Morata, D., Polvé, M., Valdés, A., Belmar, M., Dinator, M.I., Silva, M., Leiva, M., Aigouy, T., Morales, J.R., 2008. Characterisation of aerosol from Santiago, Chile: an integrated PIXE–SEM–EDX study. Environmental Geology 56, 81-95.

Norris, G., Duvall, R., Brown, S., Bai, S., 2014. Epa positive matrix factorization (pmf) 5.0 fundamentals and user guide prepared for the us environmental protection agency office of research and development, washington, dc. Washington, DC.

Paatero, P., Tapper, U., 1994. Positive matrix factorization: A non-negative factor model with optimal utilization of error estimates of data values. Environmetrics 5, 111-126.

Pardo, L.H., Fenn, M.E., Goodale, C.L., Geiser, L.H., Driscoll, C.T., Allen, E.B., Baron, J.S., Bobbink, R., Bowman, W.D., Clark, C.M., 2011. Effects of nitrogen deposition and empirical nitrogen critical loads for ecoregions of the United States. Ecological Applications 21, 3049-3082.

Pósfai, M., Gelencsér, A., Simonics, R., Arató, K., Li, J., Hobbs, P.V., Buseck, P.R., 2004. Atmospheric tar balls: Particles from biomass and biofuel burning. Journal of Geophysical Research: Atmospheres 109.

Quaranta, M.L., Mendes, M.D., MacKay, A.A., 2012. Similarities in effluent organic matter characteristics from Connecticut wastewater treatment plants. Water research 46, 284-294.

Ryan, C.C., Tan, D.T., Arnold, W.A., 2011. Direct and indirect photolysis of sulfamethoxazole and trimethoprim in wastewater treatment plant effluent. Water research 45, 1280-1286.

Satsangi, P., Yadav, S., 2014. Characterization of PM 2.5 by X-ray diffraction and scanning electron microscopy–energy dispersive spectrometer: its relation with different pollution sources. International Journal of Environmental Science and Technology 11, 217-232.

Sharp, R., Vadiveloo, E., Fergen, R., Moncholi, M., Wankmuller, D., & Latimer, R. (2013). A Theoretic and Practical Evaluation of Struvite Control and Recovery. Water Environment Research, 85(8), 675-686.

Srivastava, A., Jain, V., Srivastava, A., 2009. SEM-EDX analysis of various sizes aerosols in Delhi India. Environ Monit Assess 150, 405.

Sun, Q., Li, H., Yan, J., Liu, L., Yu, Z., & Yu, X. (2015). Selection of appropriate biogas upgrading technology-a review of biogas cleaning, upgrading and utilisation. Renewable and Sustainable Energy Reviews, 51, 521-532.

Talbi, A., Kerchich, Y., Kerbachi, R., Boughedaoui, M., 2018. Assessment of annual air pollution levels with PM1, PM2. 5, PM10 and associated heavy metals in Algiers, Algeria. Environmental Pollution 232, 252-263.

Uysal, A., Yilmazel, Y. D., & Demirer, G. N. (2010). The determination of fertilizer quality of the formed struvite from effluent of sewage sludge anaerobic digester. Journal of Hazardous Materials, 181, 248-2454.

Valavanidis, A., Fiotakis, K., Vlachogianni, T., 2008. Airborne Particulate Matter and Human Health: Toxicological Assessment and Importance of Size and Composition of Particles for Oxidative Damage and Carcinogenic Mechanisms. J Environ Sci Heal C 26, 339-362.

Wenk, J., Von Gunten, U., Canonica, S., 2011. Effect of dissolved organic matter on the transformation of contaminants induced by excited triplet states and the hydroxyl radical. Environ Sci Technol 45, 1334-1340.

Zeb, B., Alam, K., Sorooshian, A., Blaschke, T., Ahmad, I., Shahid, I., 2018. On the morphology and composition of particulate matter in an urban environment. Aerosol and air quality research 18, 1431.